The Dissertation Committee for Paul Mikhaël Sayar Certifies that this is the approved version of the following dissertation:

Development of Effective Medium Models for Quantification of Elastic Properties and Modeling of Velocity Dispersion of Saturated Rocks

Committee:

Carlos Torres-Verdín, Supervisor

Kyle T. Spikes

Hugh Daigle

Jon Olson

Kamy Sepehrnoori

Development of Effective Medium Models for Quantification of Elastic Properties and Modeling of Velocity Dispersion of Saturated Rocks

by

Paul Mikhaël Sayar, M.S.E.

Dissertation

Presented to the Faculty of the Graduate School of

The University of Texas at Austin

in Partial Fulfillment

of the Requirements

for the Degree of

Doctor of Philosophy

The University of Texas at Austin

December, 2015

Dedication

To my family, for their unconditional support.

Acknowledgements

I want to thank my advisor, Dr. Carlos Torres-Verdín. I am immensely grateful to him for giving me a chance to be a member of his research group for the last 4 years. He has had an incommensurable influence on my way of thinking, and taught me the importance of producing meticulous scientific work. Special thanks to Dr. Kyle T. Spikes, whose expertise in rock physics has proved to be extremely valuable. I would like to acknowledge the members of my dissertation committee, Dr. Jon Olson, Dr. Hugh Daigle, and Dr. Kamy Sepehrnoori, for their time, support, and reviews of this dissertation.

My gratitude goes to Dr. Mark Chapman for his time, kindness, and help when I was working on his model.

Special thanks to Rey Casanova for his administrative support at the formation evaluation research consortium. I want to thank Frankie Hart in the Petroleum Engineering department for her help and patience when taking care of my administrative questions. I am thankful to Roger Terzian for his incredibly helpful computer support. I am grateful to the petroleum engineering department at the University of Texas at Austin, for providing travel and financial grants to attend professional and industry conferences.

I thank Nigel Quayle and Sylviane Wignacourt of the Ecole Centrale de Lille for helping me join this program. They gave me invaluable help and support at the beginning of my educational experience.

For their never-failing support, I thank my parents Georges and Agnès, and my siblings Marie, Antoine, Bernadette, and Matthieu. They have always encouraged me to give the best I could. I am grateful for their love, their advice, and their prayers.

Klarissa, many thanks for your generosity, your infinite patience, and your presence at my side through the most difficult moments. Your love and your friendship gave me the strength to complete this journey.

I am extremely grateful to Antoine. Thanks for the laughs, the triple-Bs, your inestimable advice, and your selfless hospitality during my internship and so many week-ends.

Special thanks to the Bsaibes family for their warm welcome and skillful guidance when I moved to Austin.

I would like to thank my fellow students and office mates. I am particularly grateful to Shaina Kelly, Elsa Maalouf, Mathild Luycx, Vivek Ravi, Siddharth Mishra, Wilbert Herrera, Elton Ferreria, Shan Huang, Essi Kwabi, and Ben Voss.

The work reported in this dissertation was funded by The University of Texas at Austin's Research Consortium on Formation Evaluation, jointly sponsored by Anadarko, Aramco, Baker-Hughes, BG, BHP Billiton, BP, Chevron, COSL, ConocoPhillips, DEA Deutsche Erdoel AG, Det Norske, ENI, ExxonMobil, Halliburton, Hess, Maersk Oil, Paradigm, Petrobras, PTTEP, Repsol, Southwest Energy, Schlumberger, Shell, Statoil, Total, Weatherford, Wintershall and Woodside Petroleum Limited.

« Pour un esprit scientifique, toute connaissance est une réponse à une question. S'il n'y a pas eu de question, il ne peut y avoir connaissance scientifique. Rien ne va de soi. Rien n'est donné. Tout est construit. »

- Gaston Bachelard,
- *La Formation de l'Esprit Scientifique (1934)*

Development of Effective Medium Models for Quantification of Elastic Properties and Modeling of Velocity Dispersion of Saturated Rocks

Paul Mikhaël Sayar, Ph.D.

The University of Texas at Austin, 2015

Supervisor: Carlos Torres-Verdín

Elastic effective medium theory (EMT) relates to quantitative rock physics modeling that calculates macroscopic properties of a mixture by incorporating the individual elastic properties, the volume fractions, and the spatial arrangement of the constituents that make up the rock. Despite the valuable merits of effective medium models, these theories exhibit limitations that require further investigation. Common instances are the non-unique configurations of the rock's elements that give rise to identical wave velocities and the limiting assumption that rocks are purely elastic materials. Consequently, direct applications of classical EMTs can yield inaccurate and non-unique estimates of rock fabric properties that directly affect the assessment of elastic properties.

The primary purpose of this dissertation is to improve the reliability of rock physics models based on the use of effective medium theories. In the first part, a rock physics model is developed for reliable estimation of velocities and elastic properties for sandstone-shale laminated rocks that are assumed to be vertical transverse isotropic (VTI). The new model is concerned with the reproduction of typical geological features and petrophysical properties of such formations that exhibit complex rock fabric. Isotropic and anisotropic versions of the self-consistent approximation and the differential effective medium theory,

and Backus average are invoked to compute the effective medium's stiffness tensor. The rock is separated into volumes of sandstone (regarded as isotropic) and shale (regarded as VTI), which are treated separately to reliably reproduce the spatial arrangement of the individual components included in the rock. Shale volumes enclose penny-shaped cracks and clay platelets aligned in the horizontal direction. Total porosity is divided into percolating porosity, isolated pores, and aligned fractures. The new simulation method is implement in three wells in the Haynesville shale and the Barnett shale. Estimates of elastic properties are verified when calculated velocities and sonic logs are in agreement. All relative differences between simulated and measured velocities are below 5.4%. To reduce non-uniqueness, electrical resistivity is calculated with modified effective medium theories and a procedure to compute Stoneley velocity is combined with the rock physics model. A method is advanced to calculate stress distribution and fracture initiation pressure around potential wellbores drilled horizontally in VTI rocks from the stiffness tensor obtained with the improved rock physics model. Effects of degree of anisotropy and elastic properties on fracture initiation pressure are investigated to determine a criterion to locate optimal depths along a vertical well to place a horizontal well.

In the second part of the dissertation, an effective medium model is developed for reproduction of four of the main mechanisms of dispersion and attenuation of acoustic waves in saturated rocks. Simple and practical alternatives are introduced for effective medium modeling that account for dispersion mechanisms due to fluid flow inside the pore space. Biot's flow and squirt flow effects are simulated by the calculation of frequency-dependent equivalent bulk and shear moduli for the solid background of the rock. When equal to the static moduli of minerals that compose the matrix of a rock at low frequencies, dynamic moduli of the solid background become complex at high frequencies and their absolute value increases. Frequency-dependent solid moduli are used as elastic properties

of the matrix material in which fluid-filled porous inclusions are then added with dynamic self-consistent approximations for replication of acoustic scattering phenomena due to stiff pores and cracks. Resulting elastic features of the saturated medium calculated with the frequency-dependent effective medium model display viscoelastic behavior. Velocity predictions are conducted on synthetic examples to investigate conditions where dynamic rock physics modeling is necessary to obtain accurate elastic properties.

Table of Contents

List of Tables

List of Figures

Chapter 1: Introduction

This dissertation introduces new rock physics models built on effective medium theories for quantitative estimation of macroscopic features and prediction of dynamic behavior of porous rocks.

First, I develop a method based on existing effective medium theories (EMTs) for accurate representation of rock fabric parameters for hydrocarbon-bearing laminated sandstone-shale rocks. Supplemental schemes are proposed for limitation of the non-uniqueness solutions for more reliable assessment of stiffness attributes in such formations. As a secondary objective, a procedure is advanced for using the estimates of elastic properties obtained with the improved rock physics model to calculate fracturing pressure around horizontal boreholes. Second, models involving self-consistent equations and frequency-dependent solid properties are devised for simulation of dispersive mechanisms due to solid/fluid interactions in isotropic rocks. Previously developed models for reproduction of acoustic scattering effects are then combined, and a dynamic effective medium model for joint prediction of fluid-related and geometrical effects on wave propagation in isotropic rocks is introduced in this dissertation.

1.1 Background and Problem Statement

Rocks targeted for hydrocarbon production present a wide variety of solid compositions, types and volumes of porous space, shapes of constituents, and types of saturating fluids, to cite only a few characteristics. Having knowledge of the characteristics and volumetric fraction of individual components of a porous medium rarely guarantees accurate insight into its effective properties. In fact, rocks with identical composition but different rock fabrics can exhibit highly different elastic properties. Rock fabric pertains to

the manner in which individual rock elements are structurally arranged. Elastic EMTs allow for the incorporation of the respective elastic properties, the volume fractions, and the spatial arrangement of the rock's constituents to calculate the macroscopic elastic properties of the mixture.

Many theories have been developed to estimate elastic properties of rocks from their composition. Wyllie's time-average equation (Wyllie et al., 1956, 1958), for example, is an empirical relation used for assessing sonic velocities from solid composition. Velocities can then be invoked to calculate elastic properties. However, this method is overly simplistic and can lead to erroneous estimations even in isotropic and homogeneous rocks. EMTs are more complex models that often lead to more rigorous assessment of elastic properties. Hashin and Shtrikman (1963) derived lower and upper bounds for the value of bulk and shear moduli in isotropic rocks. Any estimate of elastic properties should be verified by ensuring that they fall within Hashin and Shtrikman's bounds. Kuster and Toksöz's (1974) theory to approximate compressional- and shear-wave velocities has been widely utilized, but it requires small fractions of inclusions for its validity with the Hashin-Shtrikman bounds. The self-consistent approximation (SCA) is a theory developed to be suitable for higher concentrations of inclusions (Budiansky, 1965; Hill, 1965; Wu, 1966). This effective medium model integrates the deformation of inclusions in a background medium of unknown effective elastic properties calculated by subsequent iterations. The differential effective medium (DEM) theory is another model developed originally by Bruggeman (1935) to assess elastic properties of a rock in which a host material is considered load-bearing. Combinations of the self-consistent approximation and the differential effective medium have been shown to represent composites comprising two percolating phases (Sheng, 1990, 1991).

Multiple Hydraulic fracturing and horizontal drilling gave access to large energy sources by increasing formation exposure and improving reservoir stimulation (King, 2010). Fracturability, the ability of fractures to initiate and propagate, typically correlates with the elastic characteristics of a rock (Britt and Schoeffler, 2009). Therefore, it is of great interest to estimate elastic properties of such formations to optimize hydraulic stimulation. Due to complex solid composition, various types of porosity, alignment of clay platelets, thin laminations, and other anisotropic features, it becomes critical to identify and quantify rock fabric parameters of highly laminated shales to estimate their elastic properties accurately. All the effective medium models described above assume isotropic composites and do not describe the effects of anisotropic inclusions, which cannot be dismissed in organic shales because of the complexity of their rock fabric and their great impact on elastic properties.

Anisotropic versions of these models have been developed subsequently. For example, Hudson (1980) constructed a model to estimate the impact of penny-shaped inclusions, but it can only be applied to an isotropic background. This prevents the addition of more than one type of anisotropic inclusion, which is a restrictive impediment when reproducing the rock fabric of laminated shale formations because observations often show multiple types of oriented and aligned inclusions. Nishizawa (1982) proposed a vertical transverse isotropic version of the DEM theory, and Willis (1977) formulated anisotropic equations for the self-consistent approximation. However, all of these theories, taken individually, are idealistic, and they cannot be used to represent accurate configurations of individual elements of complex formations such as organic shales.

Some studies attempted to reproduce true features of unconventional formations by combining existing effective medium theories. Jakobsen et al. (2000) developed a theoretical scheme using both DEM and SCA theories to relate elastic properties of

hydrate-bearing sediments to their porosity, mineralogy, and microstructural features, among others. Hornby et al. (1994) established a model based on combinations of the same EMTs to model an aligned biconnected clay-fluid medium to estimate anisotropic elastic characteristics of shale formations. Previously described models still neglect some key properties of typical hydrocarbon-bearing shales such as the presence of fractures or fine laminations. To my knowledge, a rock physics model that accounts for a complete and reliable representation of the geological features, petrophysical, and rock fabric parameters commonly encountered in laminated shaly sandstones has not yet been developed.

An important limitation of rock physics models based on EMTs is the non-uniqueness of solutions (Farmer, 2002; Fjar et al., 2008). Different sets of assumed rock fabric parameters can lead to the same velocity estimations. Montaut (2012) found a need for more field data to reduce the number of possible rock fabric parameters that give rise to the reproduction of sonic logs. This impediment, characteristic of effective medium modeling, has rarely been addressed in the literature.

Furthermore, acoustic properties of most rocks depend on the presence of fluid-filled pores because they represent heterogeneous material within the medium and the possibility of wave-induced fluid flow. Thus, fluid-saturated rocks should be described as viscoelastic media. Properties of viscoelastic composites vary with the frequency of passing waves that experience dispersion and attenuation. Classical elastic EMTs, such as the self-consistent approximation and the differential effective medium theory, fail to take into account dispersion and attenuation phenomena that cannot be neglected in fluid-saturated rocks exhibiting sufficiently high porosity (Tod, 2003). The dynamic behavior of rocks is associated with parameters such as porosity, permeability, fluid viscosity (Parra, 1997), shape and size of pores (Valdiviezo-Mijangos and Nicolás-Lopez, 2014), and microcracks (Chapman et al., 2002). Consequently, accurate prediction of the magnitude

of dispersion and increase of velocity at all frequencies is of high interest for estimating crucial parameters of rocks.

Biot's flow and squirt flow are the two principal mechanisms related to fluid-flow dispersion (Dvorkin and Nur, 1993). Biot (1956a, 1956b, 1962) derived theoretical formulas for predicting the frequency-dependent velocities of saturated rocks. Biot's equations reproduce the impact of some viscous and inertial interactions between the pore fluid and the solid matrix of the rock. Berryman (1998) developed a poroelastic model to integrate Biot's flow effects into the development of frequency-dependent SCA and DEM theories, but he ignored some of the parameters found in Biot's original equations. Tod (2003) formulated a more complete effective medium model for Biot's flow using the method of smoothing and following Hudson's (1994) model to approximate the wavefield within an inclusion. Mavko and Jizba (1991) devised a quantitative model to estimate the effect of squirt flow on the rock's elastic properties by calculating frequency-dependent frame moduli. Ghosh and Sen's (2011) modified version of the DEM includes a pressure term obtained from Chapman et al. (2002) and allows one to account for squirt flow in the computation of effective elastic parameters of a rock containing multiple types of inclusions. The models by Tod and by Ghosh and Sen are demonstrated rigorously, but both disregard one of the fluid-related dispersion mechanisms. Yao et al. (2015) developed the concept of frequency-dependent dynamic fluid modulus to reproduce poroelasticity behavior of heterogeneous rocks. Jakobsen and Chapman (2009) extended the T-matrix approach to a unified theory of global (Biot) and squirt flow, but the complexity of the equations makes their solution arduous to implement. None of the models described above can integrate the dispersion and attenuation caused by heterogeneities encountered by a propagating wave.

Whenever the wavelength has the same dimension as the diameter or length of porous inclusions, the dispersion mechanism referred to as multiple scattering of waves occurs. This phenomenon has been extensively reviewed, and many models based on the effective medium theory reproduce the effects of acoustic scattering on the stiffness of rocks (Sabina and Willis, 1988; Kanaun, 1996; Kanaun, 1997; Kanaun and Levin, 2003). All these studies have one characteristic in common. They invoke different self-consistent schemes. However, no published effective medium model that simulates acoustic scattering behavior effects and includes fluid-related dispersion mechanisms exists. Jakobsen and Hudson (2003) developed an alternative form for the transition matrix included in their T-matrix solution, which accounts for joint effects of poroelasticity and acoustic scattering. However, the dynamic framework this equation established remains unsolved since it was proposed, probably because of its mathematical complexity.

Therefore, the challenge remains to construct an uncomplicated and efficient effective medium model to reproduce poroelastic and geometric mechanisms of velocity dispersion and attenuation at any frequency in isotropic fluid-saturated rocks.

1.2 RESEARCH OBJECTIVES

The main thrust of this dissertation is to develop rock physics models based on effective-medium modeling that (1) explicitly account for typical geometrical features of laminated shales while limiting non-uniqueness and (2) reproduce the effects of main sources of dispersion and attenuation on effective elastic properties in saturated isotropic rocks. Both models are intended to calculate effective elastic properties and enable at the same time the estimation of additional rock fabric and petrophysical parameters. The detailed objectives of the dissertation are as follows:

- To develop a new rock physics model to quantify several rock fabric parameters affecting elastic properties of laminated hydrocarbon-bearing shales. To meet this objective, a new combination of isotropic and anisotropic EMTs is advanced to reproduce fabric and petrophysical features typically exhibited by such formations.
- To develop a procedure for calculation of additional outputs to be adjoined to the rock physics model. Additional outputs produced by the improved model aim at decreasing the number of matching solutions in order to improve the reliability of elastic properties estimates.
- To verify the accuracy of the developed combined rock physics model using field examples. Estimated properties are compared to measurements conducted in vertical and deviated wells drilled in two different shale formations.
- To develop a method to interpret the quantified elastic properties in order to assess suitable zones for drilling horizontal wells in vertical transverse isotropic rocks. This method will be based on a minimal fracture initiation pressure criterion calculated from the stiffness tensor obtained using the improved rock physics model.
- To introduce the concept of complex-valued and frequency-dependent equivalent elastic properties for the solid background to account for dispersion and attenuation caused by fluid-related dispersion mechanisms.
- To develop two semi-empirical effective medium models to reproduce Biot's flow and squirt flow effects on velocity and attenuation of compressional and shear waves. In conjunction with the dynamic equivalent solid moduli, the new frequency-dependent EMTs are constructed using the classical self-consistent approximation. A simple and practical procedure is advanced to combine both models for simulation of effects due to wave-induced pore fluid flow.

- To develop a new dynamic model to account for fluid-related and geometrical mechanisms of dispersion simultaneously. The model will account for accurate representation of velocities over large ranges of frequencies and quantification of key rock properties not included in classical EMTs.

1.3 METHOD OVERVIEW

In the first part of the dissertation, I develop a rock physics model to reproduce features typically exhibited by shales such as alignment of clay particles, alignment of penny-shaped pores and fractures, and thin laminations.

The first step in the construction of the model consists of dividing quartz concentration of each layer into two parts: one included in the sandstone volume of the layer, and the other added in the shale volume as silt matrix. Calcite and the first fraction of quartz are mixed together using the isotropic version of the DEM, and they constitute the background of the sandstone volume of the layers. The isotropic DEM is also invoked to add gas-saturated porosity as spherical pores within a kerogen matrix to reconstruct the total organic content, which is then incrementally incorporated in the quartz-calcite medium with the same effective medium theory. Next, sand porosity is included in two steps: first the percolating porosity using a combination of the SCA and the DEM, then the isolated porosity utilizing only the DEM. Sand volumes are assumed to be isotropic and therefore, all solid and porous inclusions are spherical. Next, shale volumes are constructed by first adding oblate spheroidal, horizontally-aligned clay particles in a background made of silt by invoking the anisotropic version of the DEM. Shale porosity, considered water saturated, is also included in the silt-clay matrix as horizontally-aligned spheroids. Percolating porosity is added with a combination of the anisotropic versions of the SCA

and the DEM, and finally isolated porosity is incorporated using only the anisotropic DEM. Individual stiffness tensors of shale and sandstone volumes of the layers are then averaged in order to estimate the effective medium's VTI stiffness tensor using the Backus average. I then introduce two methods to further constrain evaluation of rock fabric and petrophysical parameters obtained with the rock physics model. Stoneley velocity is approximated in addition to compressional and shear velocity using estimates of stiffness properties. Simultaneously with the construction of the stiffness tensor, anisotropic electrical conductivity is also computed in the vertical and horizontal directions with an effective medium model. Resulting calculations are plotted against Stoneley-wave sonic logs, and electrical resistivity measurements conducted along wells drilled in the Haynesville and Barnett shales. Obtained elastic properties are invoked to compute velocities for comparison with sonic logs and for validation of the model.

A two-step analysis is then performed to identify the optimal places for horizontal well placement along the vertical wells where the rock physics model has been implemented. First, stress concentration around horizontal boreholes is calculated the analytical solutions developed by Fairhurst (1968). It depends on in-situ stresses and borehole pressure. Stiffness parameters obtained with the rock physics model become inputs for stress calculations. Second, fracturing pressure is obtained when the pressure in the well overcomes the hoop stress. A relationship between the ratio of horizontal to vertical Young's modulus and fracturing pressure is found, and rocks having a high degree of anisotropy are recommended as sites for drilling of horizontal wells.

The second part of the dissertation is independent and describes a new effective medium model that takes into account the viscoelastic behavior exhibited by real rocks. It is applicable to isotropic composites with a homogeneous solid matrix. I assume the medium to exhibit a dual porosity distribution consisting of idealized spherical pores with

uniform diameter and penny-shaped cracks with all cracks having the same length and aspect ratio.

First, I formulate two new semi-empirical effective medium schemes built on the self-consistent approximation that accurately duplicate the results predicted by Biot's (1956a, 1956b) and Chapman et al.'s (2002) dispersion theories for wave-induced fluid flow. I define the new concept of frequency-dependent equivalent solid bulk and shear moduli. Two bulk moduli are calculated separately for incident compressional and shear waves. Dynamic equivalent elastic properties are used as stiffness parameters of the matrix material in which fluid-filled porous inclusions are then added with Wu's (1966) version of the SCA. Effective elastic features obtained in this manner represent properties of the saturated medium and display behavior that also varies with frequency. They are then invoked to reproduce compressional- and shear-wave velocities affected by Biot's flow and squirt flow effects. New effective medium models for fluid-related dispersion mechanisms are extensively benchmarked against original theories of Biot and Chapman et al. with synthetic examples. I propose a simple scheme to combine Biot's flow and squirt flow effects using the same version of the SCA and computing joint frequency-dependent solid moduli.

I develop a complete model for geometric and fluid-related dispersion effects with SCA theories for scattering mechanisms, which are used to add cracks and stiff pores into a solid background with frequency-dependent elastic properties that incorporates Biot's flow and squirt flow mechanisms. I derive equations of the dynamic SCA for inclusion cracks oriented in all directions. Finally, the model is applied to a variety of cases, and a discussion is presented on the possibility of quantifying petrophysical and rock physics parameters such as presence and shape of porous inclusions, permeability, and fluid viscosity, from seismic, sonic, and ultrasonic measurements.

1.4 OUTLINE OF THE DISSERTATION

This dissertation consists of two parts of equal importance divided into four principal chapters. Following this introductory chapter, the first part of the dissertation comprises Chapters 2 and 3. Chapter 2 establishes a new rock physics model constructed on a combination of existing isotropic and anisotropic effective medium theories. This model will account for accurate reproduction of rock fabric and estimation of elastic properties of laminated organic shaly sandstone formations.

Subsequently, Chapter 3 introduces and validates new procedures to calculate Stoneley-wave velocity and anisotropic electrical resistivity using effective medium theories, giving rise to the development of an original joint electrical/sonic model. The main contribution is the improvement in accuracy of rock properties and limitation of non-uniqueness of solutions. Chapter 3 also proposes a method to calculate stress distribution and fracture initiation pressure around potential wellbores drilled horizontally in laminated rocks from the stiffness tensor obtained using the rock physics model.

Chapter 4 is the first chapter of the second part of this dissertation. It formulates two semi-empirical effective medium models that reproduce fluid-related mechanisms (Biot's flow and squirt flow) that affect dispersion and attenuation of waves propagating in saturated isotropic rocks. Equations for the calculation of frequency-dependent equivalent bulk and shear moduli for the solid background are formulated in this chapter. A method is established to integrate the new models to account for combined effects of Biot's flow and squirt flow on velocities.

Chapter 5 describes dynamic self-consistent equations used to replicate the geometrical effect of idealized spherical and spheroidal porous inclusions on passing waves. The chapter introduces a frequency-dependent effective medium model that associates four wave-attenuation sources in saturated isotropic rocks: wave-induced flow

of the pore fluid, and acoustic scattering caused by spherical pores and randomly-oriented penny-shaped cracks.

Finally, Chapter 6 summarizes the general conclusions and main contributions of the dissertation and details recommendations for future research work.

Chapter 2: Rock Physics Model for Computation of Elastic Properties of Highly Laminated Organic Shale Formations

Due to their spatially complex nature, shales often exhibit large seismic anisotropy. The directional dependence of the velocity of sonic waves in shale formations is generally the result of an average of anisotropic rock fabric features occurring at multiple scales. Rock fabric anisotropy generates anisotropic elastic properties that can be quantified by rock physics modeling. This chapter introduces a new rock physics model for reliable estimation of velocities and elastic properties for sandstone-shale laminated rocks based on a combination of existing isotropic and anisotropic effective medium theories.

A multi-mineral inversion method is used first to assess rock solid composition, porosity, fluid types, and fluid saturations. Once rock composition is known, the rock fabric of studied laminated shale formations is reconstructed using the new rock physics model. At each depth where measurements are available, the rock is separated into volumes of sandstone and shale that are treated individually to reliably reproduce the spatial arrangement of the rock's individual components. Sandstone volumes are assumed to be isotropic and modeled as such, whereas shale volumes exhibit vertical transverse isotropy (VTI) and contain horizontally aligned clay platelets and cracks. The rock physics model also differentiates percolating porosity from isolated porosity—both porosities are included separately in sandstone and shale volumes—and from fracture porosity, which is added at the last stage within the effective medium. Distinction between percolating and isolated porosity is an important constraint on the final estimates of elastic properties of the mixture. Rock fabric parameters remain constant in vertically homogeneous areas. In vertically heterogeneous formations, the depth interval of interest is divided into rock types, based on solid composition, and each rock type is associated with a specific fabric. Backus average is then invoked to compute the effective elastic properties of the medium

composed of alternating layers of sandstone and shales. The rock physics model is implemented in wells in the Haynesville shale and in the Barnett shale, giving rise to accurate estimates of wave velocities, with errors lower than 5.4% for wells in the Haynesville shale and a 4.3% difference for the wells in the Barnett shale.

2.1 INTRODUCTION

Laminated shales often exhibit elastic anisotropy, as observed in the field (Banik, 1984) and in laboratory measurements (Jones and Wang, 1981; Johnston and Christensen, 1995; Wang, 2002). The elastic behavior of a rock is described by its stiffness tensor. Laminated sedimentary formations comparable to hydrocarbon-bearing shales can be described as vertically transversely isotropic (VTI) rocks (Walsh et al., 2006), which implies that five independent elastic constants are needed to determine the complete stiffness tensor. Physical properties of a VTI rock are symmetric about a vertical axis that is normal to alternating planes of isotropy. The spatial anisotropy is in fact a manifestation of the fine layering of shale and sandstone layers, and the alignment in the horizontal plane of different heterogeneities such as non-spherical pores and clay minerals, micro-cracks, and natural fractures (Bandyopadhyay, 2009). Distinct vertical and horizontal stiffnesses can then be calculated in the form of two dynamic Young's moduli that are functions of the constants of the stiffness tensor.

Although mineralogy can be estimated with multi-mineral nonlinear inversion of conventional well logs (Heidari et al., 2012), this method does not provide information on how individual components are spatially arranged and how they contribute to a rock's elastic properties. Rock fabric designates the shape and the spatial arrangement of the different components of the rock. Due to the spatially intricate and highly anisotropic

nature of hydrocarbon-bearing shales, rock fabric can have a great impact on their elastic features (Montaut et al. 2013). In shale formations, the ability to initiate and grow hydraulic fractures through the near-wellbore region commonly correlates with elastic properties (Britt and Schoeffler, 2009). Hence, developing a rock physics model that identifies and quantifies rock fabric parameters of shales is a practical approach to improve accuracy of the estimates of elastic properties, which is in turn valuable for the enhancement of hydrocarbon production from such formations. Other parameters, including in-situ stress, pore pressure, and temperature, may affect rock elastic properties, but they are not studied in this chapter. I assume that rock elastic properties only vary with rock composition and rock fabric.

Many effective medium theories have been developed to estimate rock elastic properties (Hashin and Shtrikman, 1963; Berryman, 1980b; Sheng, 1990), but they generally neglect the anisotropic spatial arrangement of the rock's constituents that are often encountered in shale formations. An effective medium theory, called the self-consistent approximation (SCA), was developed to describe the elastic deformation caused by inclusions in a background medium of yet-to-be-known elastic properties (Budiansky, 1965; Hill, 1965). The differential effective medium (DEM) theory is another model developed originally by Bruggeman (1935) to assess elastic properties of a rock considered to be composed of a load-bearing phase and an inclusion phase. Isolated inclusions are infinitesimally added into the host material and at each step of increment the new effective medium becomes the host background. These two theories, which are often used in rock physics models, assume isotropic rocks and do not describe the effects of anisotropic inclusions, which cannot be dismissed in organic shales because of the complexity of their rock fabric and their great impact on elastic properties. Anisotropic versions of these models have been developed subsequently; for example, Hornby et al. (1994) proposed an

anisotropic formulation for the SCA and the DEM. Another model established by Hudson (1980) investigated the effects of aligned, thin, penny-shaped cracks in an isotropic medium. Hudson's theory can be used to calculate anisotropic elastic properties due to the anisotropic distribution of inclusions, which can be either mineral inclusions or fluid-filled cracks. The latter method was extended to describe heavily faulted structures by Hudson and Liu (1999). Combinations of anisotropic effective medium models, such as those described above, have been shown to describe elastic properties of unconventional formations reliably by accurately accounting for the combined effects of mineral concentration and grain and pore shapes (Xu and White, 1995).

In this chapter, the relationship between elastic properties and sonic and density logs is detailed for isotropic and VTI rocks. Isotropic effective medium theories and their anisotropic versions invoked in the rock physics model are described, as well as the Backus average used to estimate the effective medium's stiffness tensor from individual stiffness tensors of shale and sandstone volumes. I develop a new rock physics model to improve the method finalized by Montaut et al. (2013) and to quantify several rock fabric parameters affecting elastic properties of laminated hydrocarbon-bearing shales by reproducing features typically exhibited by such formations.

For verification purposes, sonic wave-velocities calculated from estimated elastic properties of the studied formations are compared to sonic logs. Rock fabric is validated when simulations match sonic logs within an acceptable margin of error (below 10%). Differences above 10% indicate erroneous simulation parameters, unexpected rock fabric at a certain location, or an incorrect model.

2.2 ANISOTROPY IN LAMINATED SHALES

Elastic anisotropy in a laminated shale formation is a manifestation of the aligned heterogeneities at scales smaller than the scale of measurements. At sub-seismic scale, the following kinds of textural alignments are usually observed in shales (Bandyopadhyay, 2009):

- Alignment of penny-shaped clay minerals,
- Alignment of non-spherical pores and micro-cracks,
- Alignment of fractures at scales larger than the scale of pore and grains, but smaller than the seismic scale,
- Fine-scale lamination of shaly materials, silty materials, and organic materials.

Several of these types of alignment are often encountered together because they are intertwined. For example, strongly aligned platy clay minerals, because of their geometry, cause the pores to be thin and strongly aligned, thus generating further anisotropy in the rock. **Figure 2.1** shows an example of the complex structure and fabric of a typical shale. This instance, from the Barnett shale, is a laminated siliceous mudstone comprising clay, quartz, carbonate material, and other minerals in minor amounts. Magenta lines represent micro-fractures (natural and induced), both parallel and perpendicular to the horizontal bedding plane. Horizontal alignment of mineral inclusions can be easily observed in **Figure 2.1**.

Petrophysical properties of laminated shales are difficult to quantify because of their complex composition and the high spatial variability of the rock components. Heidari et al. (2012) developed a deterministic nonlinear multi-mineral inversion method that allows for the assessment of the solid composition of shales. Heidari et al.'s method is based on conventional logs such as density, neutron porosity, photoelectric factor, and spectral gamma ray. The method was improved by Adiguna (2012), who proposed a

practical workflow to estimate rock solid composition, porosity, fluid types, and fluid saturation.

The method was successfully applied to measurements acquired in wells drilled in the Haynesville and Barnett shales. Results were validated by comparison to core measurements and neutron capture spectroscopy logs.

2.3 ELASTIC CONSTANTS AND SONIC LOGS

The modern theory of elasticity generalizes Hooke's law to describe the relation between stress and strain of a solid. Its general form for an anisotropic, linear, and elastic solid is given by

$$\boldsymbol{\varsigma} = \mathbf{C}\mathbf{e}, \tag{2.1}$$

where $\boldsymbol{\varsigma}$ is the stress tensor, $\mathbf{e}$ is the strain tensor, and $\mathbf{C}$ is the elastic stiffness tensor.

2.3.1 Isotropic Media

For an isotropic rock, the stiffness tensor can be described in the following matrix form using Voigt's notation:

$$\mathbf{C} = \begin{bmatrix} c_{11} & c_{12} & c_{12} & 0 & 0 & 0 \\ c_{12} & c_{11} & c_{12} & 0 & 0 & 0 \\ c_{12} & c_{12} & c_{11} & 0 & 0 & 0 \\ 0 & 0 & 0 & c_{44} & 0 & 0 \\ 0 & 0 & 0 & 0 & c_{44} & 0 \\ 0 & 0 & 0 & 0 & 0 & c_{44} \end{bmatrix}, \tag{2.2}$$

where $c_{12} = c_{11} - 2c_{44}$. It can be noted that the isotropic stiffness tensor contains only two independent entries. Bulk modulus of the medium is given by

$$K = c_{11} - \tfrac{4}{3} c_{44}, \tag{2.3}$$

shear modulus by

$$\mu = c_{44}, \tag{2.4}$$

and Lamé parameter by

$$\lambda = K - \tfrac{2}{3}\mu. \tag{2.5}$$

Mechanical properties of linear elastic materials are usually defined by Young's modulus and Poisson's ratio calculated, respectively, as follows:

$$E = \frac{9K\mu}{3K + \mu}, \tag{2.6}$$

and

$$\nu = \frac{3K - 2\mu}{2\left(3K + \mu\right)}. \tag{2.7}$$

Velocities are functions of elastic properties and bulk density, ρ, of the rock. For isotropic formations, compressional- and shear-wave velocities, V_p and V_s, respectively, are calculated using the formulas

$$V_p = \sqrt{\frac{c_{11}}{\rho}} = \sqrt{\frac{K + \tfrac{4}{3}\mu}{\rho}}, \tag{2.8}$$

and

$$V_s = \sqrt{\frac{c_{44}}{\rho}} = \sqrt{\frac{\mu}{\rho}}. \tag{2.9}$$

2.3.2 VTI Media

In a vertical transverse isotropic medium, the elastic stiffness tensor consists of five independent parameters and can be expressed using Voigt's notation:

$$\mathbf{C} = \begin{bmatrix} c_{11} & c_{12} & c_{13} & 0 & 0 & 0 \\ c_{12} & c_{11} & c_{13} & 0 & 0 & 0 \\ c_{13} & c_{13} & c_{33} & 0 & 0 & 0 \\ 0 & 0 & 0 & c_{44} & 0 & 0 \\ 0 & 0 & 0 & 0 & c_{44} & 0 \\ 0 & 0 & 0 & 0 & 0 & c_{66} \end{bmatrix}, \tag{2.10}$$

where $c_{66} = \frac{1}{2}(c_{11} - c_{12})$ and where the axis of symmetry lies along the vertical x_3-axis.

Frydman (2010) gives the values for vertical and horizontal Young's modulus in a VTI formation, E_v and E_h, respectively, as functions of the stiffness constants:

$$E_v = c_{33} - 2\frac{c_{13}^2}{c_{11} + c_{12}}, \tag{2.11}$$

$$E_h = \frac{(c_{11} - c_{12})(c_{11}c_{33} - 2c_{13}^2 + c_{12}c_{33})}{c_{11}c_{33} - c_{13}^2}. \tag{2.12}$$

Similarly, two values for Poisson's ratio can be calculated as

$$\nu_v = \frac{c_{13}}{c_{11} + c_{12}}, \tag{2.13}$$

in the vertical plane and

$$\nu_h = \frac{c_{33}c_{12} - c_{13}^2}{c_{11}c_{33} - c_{13}^2}, \tag{2.14}$$

in the horizontal plane of isotropy.

In transverse isotropic media, one compressional-wave velocity exists as well as one vertically-polarized and one horizontally-polarized shear-wave velocity, denoted by V_{sv} and V_{sh}, respectively; they can be explicitly calculated as follows (Mavko et al., 2009):

$$V_p = \left(c_{11}\sin^2\theta + c_{33}\cos^2\theta + c_{44} + \sqrt{M}\right)^{1/2}(2\rho)^{-1/2}, \tag{2.15}$$

for compressional velocity,

$$V_{sv} = \left(c_{11}\sin^2\theta + c_{33}\cos^2\theta + c_{44} - \sqrt{M}\right)^{1/2}(2\rho)^{-1/2}, \tag{2.16}$$

for vertically-polarized shear velocity (also referred to as slow shear velocity),

$$V_{sh} = \left(c_{66}\sin^2\theta + c_{44}\cos^2\theta\right)^{1/2}(\rho)^{-1/2}, \tag{2.17}$$

for the horizontally-polarized shear velocity (or fast shear velocity). In the previous equations M is given by

$$M = \left[\left(c_{11} - c_{44}\right)\sin^2\theta - \left(c_{33} - c_{44}\right)\cos^2\theta\right]^2 + \left(c_{13} + c_{44}\right)^2\sin^2 2\theta, \tag{2.18}$$

and θ is the angle between the wave vector and the vertical x_3-axis of symmetry.

2.4 ROCK PHYSICS MODELS FOR EFFECTIVE ELASTIC PROPERTIES IN POROUS MEDIA

In this section I describe some of the rock physics modeling tools invoked in the different models developed in this dissertation for estimating the effective elastic moduli of composites or porous elastic materials.

2.4.1 Isotropic Effective Medium Models

2.4.1.1 Isotropic Differential Effective Medium Model

The differential effective medium (DEM) theory estimates bulk and shear moduli of a two-component mixture. One of the components forms the background of a composite and remains topologically connected regardless of concentration. The other component is incrementally added as inclusions into the background, or host, material until it reaches its desired concentration, x_2. The effective elastic moduli obtained at each step are used as

the properties of the background material in the next step. Berryman (1992) gives the following formulation for the DEM differential equations for an isotropic medium:

$$(1-x)\frac{d}{dx}\left[K_{\mathbf{DEM}}(x)\right]=(K_2-K_{\mathbf{DEM}})P_{\mathbf{DEM}\_2}(x)\,, \tag{2.19}$$

and

$$(1-x)\frac{d}{dx}\left[\mu_{\mathbf{DEM}}(x)\right]=(\mu_2-\mu_{\mathbf{DEM}})Q_{\mathbf{DEM}\_2}(x)\,, \tag{2.20}$$

where x is the volumetric concentration of the inclusion phase and subscripts 1 and 2 refer to host and inclusion materials, respectively. $K_{\mathbf{DEM}}$ and $\mu_{\mathbf{DEM}}$ are the effective bulk and shear moduli of the mixture, respectively. P and Q are geometric factors and subscript $\mathbf{DEM}\_2$ indicate that coefficients P and Q are calculated for an inclusion of material 2 in a background medium with effective elastic properties $K_{\mathbf{DEM}}$ and $\mu_{\mathbf{DEM}}$. **Table 2.1** summarizes P and Q formulas for three different shapes of inclusions: spheres, prolate spheroids (needle-shaped cracks), and oblate spheroids (penny-shaped cracks). Spheroid inclusions are characterized by their aspect ratio, γ, which is the ratio of short to long axes. Aspect ratio is larger than 1 for prolate spheroids and lower than 1 for oblate spheroids. Equation (2.19) and (2.20) are coupled and are to be solved by simultaneous iterations with initial conditions $K_{\mathbf{DEM}}(x=0) = K_1$ and $\mu_{\mathbf{DEM}}(x=0) = \mu_1$. If a medium is composed of more than two phases, the mixture's effective elastic properties can be calculated in several steps, adding one type of inclusion after another. The order in which inclusions are added does not necessarily reflect the true geological evolution of the rock (Mavko et al., 2009).

2.4.1.2 Isotropic Self-Consistent Approximation Models

Wu's (1966) self-consistent modulus estimates for two-component composites is expressed as

$$K_{\mathbf{SCA}} = K_1 + x_2 \left(K_2 - K_1 \right) P_{\mathbf{SCA}\_2} \left(x \right) , \tag{2.21}$$

and

$$\mu_{\mathbf{SCA}} = \mu_1 + x_2 \left(\mu_2 - \mu_1 \right) Q_{\mathbf{SCA}\_2} \left(x \right) . \tag{2.22}$$

Berryman (1995) develops a more general formulation of the self-consistent approximation (SCA) for a mixture of N phases, given by

$$\sum_{i=1}^{N} x_i \left(K_i - K_{\mathbf{SCA}} \right) P_{\mathbf{SCA}\_i} = 0 \ , \tag{2.23}$$

and

$$\sum_{i=1}^{N} x_i \left(\mu_i - \mu_{\mathbf{SCA}} \right) Q_{\mathbf{SCA}\_i} = 0 \ , \tag{2.24}$$

where i refers to the i-th material and x_i represents its volumetric concentration. In equations (2.21) to (2.24), $K_{\mathbf{SCA}}$ and $\mu_{\mathbf{SCA}}$ are the effective bulk and shear moduli of the mixture, respectively. P and Q are identical to those of the differential effective medium theory, and their expressions can be found in **Table 2.1**. Subscripts $\mathbf{SCA}\_2$ and $\mathbf{SCA}\_i$ mean that coefficients P and Q are calculated for an inclusion of material *2* or i, respectively, in a background medium with effective bulk modulus $K_{\mathbf{SCA}}$ and shear modulus $\mu_{\mathbf{SCA}}$.

The difference between Wu's and Berryman's theories lies in how the roles of the components of the effective medium are treated. Wu's (1966) formulation considers one constituent to be host material or matrix and the other an inclusion component, whereas there is no preferential approach between the components of the rock in Berryman's (1995)

equations. It is interesting to note that even though these models treat the role of the matrix differently, they yield identical estimates of effective properties when the inclusions are spherical (Kim, 2010). Unless otherwise stated, I used Berryman's self-consistent equations when the SCA theory is invoked in subsequent rock physics models.

2.4.2 Anisotropic Effective Medium Models

2.4.2.1 Anisotropic Differential Effective Medium Model

Nishizawa (1982) showed that the change in stiffness in an anisotropic medium due to an increase in volume of the inclusion component, dx, is given by

$$d\mathbf{C}_{\mathbf{DEM}} = \frac{dx}{1-x}\left(\mathbf{C}_2 - \mathbf{C}_{\mathbf{DEM}}\right)\mathbf{Q}_2, \tag{2.25}$$

where x is the volume of inclusion added into x the background, $\mathbf{C}_2$ and $\mathbf{C}_{\mathbf{DEM}}$ are the stiffness tensors of the inclusion component and of the effective medium at each step of the iteration, respectively, and $\mathbf{Q}_2$ is calculated using the expression

$$\mathbf{Q}_2 = \left[\mathbf{I} + \mathbf{G}_2\mathbf{C}_{\mathbf{DEM}}\left(\mathbf{C}_2 - \mathbf{C}_{\mathbf{DEM}}\right)\right]^{-1}, \tag{2.26}$$

where $\mathbf{I}$ is the identity tensor and $\mathbf{G}_2$ is a fourth-rank tensor computed from the response of an unbounded matrix of the effective medium (Mura, 1982). The expression for $\mathbf{G}_2$ for spheroidal inclusions is given in **Appendix A**.

2.4.2.2 Anisotropic Self-Consistent Approximation Model

This effective medium theory describes the elastic deformation of inclusions in a background medium. The interaction of inclusions is calculated by replacing the background material with the effective medium of not yet known elastic properties. Willis (1977) gave the expression for the effective stiffness tensor in the self-consistent approximation (SCA) model for a two-component composite as follows:

$$\mathbf{C}_{\mathbf{SCA}} = \left[(1-x_2)\mathbf{C}_1\mathbf{Q}_1 + x_2\mathbf{C}_2\mathbf{Q}_2\right]\left[(1-x_2)\mathbf{Q}_1 + x_2\mathbf{Q}_2\right]^{-1}, \tag{2.27}$$

where x_2 is the volumetric concentration of the second component composing the effective medium, $\mathbf{C}_1$ and $\mathbf{C}_2$ are the stiffness tensors of the two components, and $\mathbf{Q}_1$ and $\mathbf{Q}_2$ are the same tensors as the tensor $\mathbf{Q}_2$ defined above and are associated with the first and second component of the composite material, respectively.

Neither the SCA nor the DEM theory individually can be used to describe the elastic behavior of rocks that exhibit several topologically connected phases over wide ranges of concentrations. However, a combination of the SCA and the DEM theories provides a solution to this problem, as shown by Sheng (1990, 1991). In fact, if two materials of volumetric concentration between 40% and 60% are mixed using the self-consistent approximation, the two phases become connected within the effective medium. The DEM model is subsequently invoked to adjust the relative concentrations of the two materials. Using a combination of it with the SCA and the DEM theory, one can therefore estimate elastic properties of mixtures exhibiting more than one topologically connected, or percolating, component.

2.4.3 Backus Average

In the case of a medium consisting of thin superpositions of isotropic and VTI layers, Backus (1962) showed that it becomes effectively a VTI medium in the long wavelength limit. Computing window-moving averages of properties of layered volumes weighted by their respective volumetric concentration with the Backus average allows for the estimation of average VTI tensors of a laminated formation as sensed by the measurements. The details for calculation of the averaged stiffness tensor of a VTI medium with its axis of symmetry perpendicular to alternating fine layers are shown in **Appendix B**.

2.5 ELASTIC PROPERTIES OF INDIVIDUAL ROCK COMPONENTS

Table 2.2 shows the assumed elastic moduli and density of individual solid components and elastic moduli, density, and viscosity of fluid components of a rock. The values are used in every rock physics model described in this dissertation.

Field cases studied in this chapter and Chapter 3 contain only two fluids: water and gas. Elastic properties of the fluid mixture are defined by its bulk modulus estimate with Reuss's (1929) formula:

$$K_{fl} = \left(\frac{s_w}{K_w} + \frac{(1 - s_w)}{K_g} \right)^{-1}, \tag{2.28}$$

where K_w and K_g are the bulk modulus of water and gas, respectively, and s_w represents water saturation. Shear modulus of individual fluid components and any fluid mixture are set to zero.

2.6 ROCK PHYSICS MODEL

The objective of the new rock physics model is to reproduce features typically exhibited by shales such as alignment of clay particles (Aplin et al., 2006), alignment of penny-shaped pores (Reed et al., 2012) and fractures, and thin laminations (Gale et al., 2014). The model is based on the separate treatment of sandstone and shale volumes for each horizontal thin layer of a studied laminated shale formation and of the different types of porosity. More precisely, it is a quintuple porosity model with percolating and isolated porosity included individually in both sandstone and shale volumes and fluid-filled fractures added at the last stage of the reconstruction of the effective medium to reproduce the wide variety of pore types observed in shale formations (Pommer and Milliken, 2015). Presence and orientation of natural fractures is inferred from the observation of borehole

images. Shale porosity is based on total porosity readings for pure shale layers in the formation of interest and is assumed constant throughout a particular formation. The remaining porosity is included in the sandstone part of the layers.

2.6.1 Sandstone Volume of Thin Layers

The first step in the construction of the model consists of dividing the quartz concentration of each layer into two parts: one included in the sandstone volume of the layer, the other is added in the shale volume as silt matrix. A layer refers to a specific depth along a well where measurements were acquired, and volumetric concentration of solid and fluid constituents were estimated with a multi-mineral inversion method. Relative amount of silt particles with respect to clay concentration is derived from the mineral composition of pure shale zones within the formation of interest. Calcite and the first fraction of quartz are mixed together using the isotropic version of the DEM, and they constitute the background of the sandstone volume of the layers. Depending on relative concentrations, the host background can be either quartz or calcite. The component that exhibits the higher concentration becomes the host material. The isotropic DEM is also invoked to add gas-saturated porosity as spherical pores within a kerogen matrix to reconstruct the total organic content (TOC), which is then incrementally incorporated in the quartz-calcite medium using the same effective medium theory. Next, sand porosity, constituted of isotropic inclusions, is added in two steps: the percolating porosity first using a combination of the SCA and the DEM —which has been shown to successfully model rocks with two connected phases—and then the isolated porosity utilizing only the DEM. **Figure 2.2** describes the process of reconstruction of the sandstone volume of each layer. At this point, all the inclusions are spherical and have no preferred orientation, indicating

that the sandstone volume of the layers is isotropic. After the completion of this last step, every sandstone volume of each layer is associated with its own isotropic stiffness tensor.

2.6.2 Shale Volume of Thin Layers

Elastic anisotropy in shales is a manifestation of aligned heterogeneities at scales smaller than the scale of the measurements. Aligned platy clay minerals and cracks are the types of textural features that are usually encountered within shale layers. To reproduce such characteristics, I reconstruct shale volumes by first adding oblate spheroidal, horizontally-aligned clay particles in a background made of silt by invoking the anisotropic version of the DEM, as shown in **Figure 2.3**. Next, shale porosity, assumed water saturated, is also included in the silt-clay matrix as horizontally-aligned spheroids. Percolating porosity is added with a combination of the anisotropic versions of the SCA and the DEM, and finally isolated porosity is incorporated using only the anisotropic DEM. Every shale component of the layers is then described by its own VTI stiffness tensor. Individual stiffness tensors of shale and sandstone volumes of the layers are then averaged in order to estimate the effective medium's stiffness tensor using the Backus average, as explained below.

2.6.3 Backus Average of Thin Layers

Sonic tools are composed of several transmitters and an array of receivers. For instance, in the field examples considered below in this chapter, the array includes 13 receivers spaced at 0.5 ft intervals. In fact, at the measurement scale, sonic tools average elastic properties of the rock and cannot distinguish individual layers. Therefore, velocities and elastic properties of a laminated formation calculated from sonic/density logs represent averaged in-situ rock properties. Simulated elastic properties must be vertically averaged so that velocities are consistently compared to sonic logs. It is assumed that there are no

sources of intrinsic energy dissipation and layer thickness is much smaller than acoustic wavelength, so that the Backus average can be applied in the model.

Properties of sand and shale volumes previously reconstructed are weighted by the volumetric fraction that the volumes occupy within a layer of the rock. Window-moving averages of elastic properties are then computed with the Backus average to estimate VTI stiffness tensors of a laminated formation as sensed by the measurements.

2.6.4 Addition of Fractures

Information about fractures, such as orientation and aspect ratio is inferred from the examination of borehole images, when available. Presence of fractures is then simulated with the anisotropic DEM. Because the effective medium is assumed to exhibit VTI anisotropy, vertical fractures are defined as prolate spheroids (aspect ratio larger than 1) and horizontal fractures as oblate spheroids (aspect ratio lower than 1). The final stiffness tensor for every layer of the effective reconstructed rock has now been determined after this last step of the rock physics model. Using equations (2.15) to (2.17) compressional-, fast shear-, and slow shear-wave velocities can be calculated and plotted against the available sonic measurements to verify the validity of the elastic properties as predicted by the model.

2.7 Simulation Results: Field Case Examples

This section describes the application of the previously described rock physics model in two wells in the Haynesville shale formation and two intervals of the same vertical well in the Barnett shale. The Haynesville shale is one of the major shale gas fields in the United States, and the Barnett shale is one of the first shale formations in which horizontal drilling and hydraulic fracturing permitted economical production of hydrocarbons.

2.7.1 Simulation Results in the Haynesville Shale

The Haynesville shale, located in east Texas and northwest Louisiana, is a black, organic-rich shale (Hammes et al., 2011). Its deposition occurred during the Late Jurassic, approximately 150 million years ago. It is bounded by the Bossier shale above, and the Haynesville limestone and Smackover formation below. The simulation method developed in this chapter is applied to two wells in the Haynesville shale, referred to as Well H1 and Well H2. Two distinct intervals of Well H1 are considered: a vertical section and a deviated section, or transition section between the vertical and horizontal parts of the well. The angle of the studied deviated part of the well varies between 45° and 80°. Only a vertical interval of Well H2 is available for study.

Conventional well logs are available in Wells H1 and H2 and are used to estimate rock solid composition, porosity, fluid types, and fluid saturation. One compressional and one shear velocity log were acquired in both vertical wells, whereas one compressional and two shear velocities were measured in the deviated portion of Well H1. In fact, due to the anisotropy of the Haynesville shale formation, a splitting between vertically- and horizontally-polarized shear waves is observed in the transition interval. Velocities are simulated based on assumed rock composition and fabric with the rock physics model. First, the method is implemented in the vertical section of Well H1, and rock physics parameters needed for the model such as fraction of percolating porosity, aspect ratios of inclusions, etc., are determined before it is applied to the deviated section of the well. Rock fabric parameters similar to the ones determined with the rock physics model in the first well are then invoked in Well H2. Extrapolating the inputs of the rock physics model from one interval of a well to another and from one well to the other allows one to verify the model because the wells penetrate the same geologic formation. Estimated velocities are compared to sonic logs to validate the rock fabric parameters assumed in the model.

Rock fabric is assumed constant throughout the entire simulation interval. As described previously, each layer is divided into a sandstone volume and a shale volume. In the sandstone volumes, the load-bearing matrix is assumed to be made of quartz or calcite, depending on which one has the higher concentration in each bed. Solids and fluids are then included in the sandstone volumes using either a combination of SCA and DEM for connected phases or simply the DEM model. In the shale volumes, the load-bearing matrix is assumed to be composed of silt. Therefore, the first step is to invoke the VTI DEM to model penny-shaped horizontally-aligned clay particles into a background matrix that consists of quartz. Percolating shale porosity is included within the latter background using also the joined VTI versions of the SCA and DEM theory before isolated water-saturated cracks are added with the VTI DEM. Averages of elastic properties of the laminated medium are calculated with the Backus average, and the effective rock is completed by embedding horizontal fractures into the mixture (refer to Gale et al., 2014).

Table 2.3 shows the rock fabric and properties estimated in the vertical Well H1 from the application of the rock physics model. Properties of sandstone volumes are, among others, 50% of sand porosity modeled as connected porosity and kerogen porosity of 10%. Shale volumes contain 35% of silt minerals, shale porosity is found to be 6% with 3% of shale porosity that percolates, aspect ratio of spheroidal pores aligned in the horizontal direction is 0.25, and aspect ratio of clay platelets is 0.2. Percentage of total porosity modeled as horizontal fractures is 9% and their aspect ratio is 0.05. **Figure 2.4** shows the velocities calculated with the rock physics model in the vertical section, plotted alongside sonic measurements. In the vertical section, measured sonic logs are one compressional and one shear wave velocity. The mean (2.7% for V_p and 2.3% for V_s) and the median (2.1% for V_p and 1.7% for V_s) of absolute relative differences between calculated and field velocities indicate that estimated velocities accurately reproduce sonic

logs. **Table 2.4** summarizes the estimated rock fabric properties in deviated Well H1. Both portions of the well penetrate the same topological section, consequently the rock physics model applied to the deviated part is almost identical to the one applied to the vertical section. Sandstone volumes have the same composition and rock fabric properties than in the vertical section. Differences are found only in shale volumes, where porosity is predicted to be 6.5% instead of 6%. In **Figure 2.5**, I describe the calculated velocities obtained with the application of the rock physics model in the deviated section of Well H1 along the available sonic measurements, including compressional, vertically -polarized, and horizontally -polarized shear-wave velocities. The mean (3% for V_p, 5.9% for V_{sv}, and 4% for V_{sh}) and the median (2.7% for V_p, 5.2% for V_{sv}, and 3.4% for V_{sh}) of absolute relative differences are all lower than 6%, and they indicate an accurate reproduction of sonic logs by estimated velocities. The match between simulated and field velocities in both intervals of Well H1 suggests that the assumed rock fabric parameters and, *a fortiori*, the obtained estimates of elastic properties are accurate.

If the rock physics model is applied to Well H2 with the same rock fabric parameters determined in Well H1, small discrepancies between sonic logs and simulated velocities are visible. The mismatch is explained by differences in composition and fabric of shale layers between Wells H1 and H2. Track 3 of **Figure 2.6** shows that pure shale layers, located for example at xx125 ft and xx225 ft, contain similar volumetric concentrations of quartz and clay and exhibit higher porosity (about 9%) than in the first well. Consequently, 50% of the solid background of shale volumes is modeled to be made of silt minerals and shale porosity is assumed to be 9%. All other characteristics of shale volumes remain unchanged from Well H1. Apart from percentage of percolating sand porosity, increased from 50% to 65%, properties of sandstone volumes are identical to those estimated in the first well. **Table 2.5** summarizes the estimated rock fabric properties

and **Figure 2.6** shows the final calculation results of compressional- and shear-wave velocities in Well H2. Both simulated velocities are in agreement with sonic logs, the mean of absolute relative differences is 3.6% for V_p and 2.8% for V_s, and the median, 3.2% for V_p and 2.5% for V_s, which implies that estimated elastic properties in Well H2 inferred from rock fabric and composition are valid.

2.7.2 Simulation Results in the Barnett Shale

Barnett shale was deposited during the Mississippian. In the northern and northeastern regions, it overlies the Viola/Simpson group, a stiff limestone formation that acts as a fracture barrier. Opposite to that in the southern and southwestern regions, the Barnett shale overlies the Chappel limestone or the Ellenburger dolomite/limestone (Montgomery et al., 2005). The latter formation is porous and water-saturated, and is avoided during hydraulic stimulation to prevent water production and aquifer contamination. The rock physics model developed previously is tested in two intervals of the same vertical well drilled in the Barnett shale separated by a limestone formation that acts as fracture barrier. The two intervals of well are designated as Upper and Lower Well B2.

Using identical rock fabric along the entire depth interval of a formation yields accurate estimations of elastic properties and velocities in the Haynesville shale wells H1 and H2. However, in vertically heterogeneous formations such as the Barnett shale, the depth interval of interest is to be divided into areas exhibiting similar properties. The different areas are called rock types, and each rock type is associated with a specific fabric. In other words, rock fabric varies with rock composition, which is commonly observed in shale formations. Rock typing in this chapter is based on solid volumetric composition of the formation, more specifically on volumetric concentration of kerogen, quartz, and

calcite. The method is applied to the vertical Well B2, in which three rock types are defined. **Table 2.6** summarizes the average volumetric concentrations of quartz, calcite, and kerogen in the solid phase of the rock for each rock type in Well B2.

Conventional well logs are available and are used to estimate rock solid composition, porosity, fluid types, and fluid saturation. Compressional- and shear-wave logs are available in both studied intervals of Well B2. Velocities are calculated based on rock composition and rock fabric with the rock physics model in the upper part of the well first. They are compared to sonic logs to validate the assumed properties chosen as input to the model. Once rock fabric parameters of Upper Well B2 are verified, similar properties are then assumed in Lower Well B2 in which the rock physics model is applied. Disparities between simulated and measured velocities are corrected by slightly adapting assumed parameters.

As described above, layers are separated between sandstone volumes and shale volumes. In sandstone volumes, the load-bearing matrix is assumed to be made of quartz or calcite, depending on which one exhibits the higher concentration. The rest of the solids are then included in the sandstone volumes using the isotropic version of the DEM model. Percolating porosity is added with a combination of isotropic SCA and DEM before isolated porosity is embedded in the background with the DEM only. In shale volumes, the first step is to invoke the VTI DEM to model a background matrix that is made of quartz with spheroidal, horizontally aligned clay particles. Connected shale porosity is included within this two-phase background using a combination of VTI SCA and DEM theories and isolated pores are added next with the VTI version of the DEM. In the Barnett shale, modeling vertical fractures provides the best fit with sonic logs, and they are embedded in the previously reconstructed background as prolate spheroidal, or needle-shaped, inclusions fractures with the VTI DEM model.

In the upper section of Well B2, the percentage of porosity in sandstone volumes modeled as percolating porosity is 45%, 80%, and 90% for rock types 1, 2, and 3, respectively, as shown in **Table 2.7**. Kerogen porosity is 10% for all rock types. In shale volumes, porosity is found to be 8% for rock type 1, 6.5% for rock type 2, and 1% for rock type 3, the aspect ratio of spheroidal pores aligned in the horizontal direction is 0.25 while the aspect ratio of clay platelets is 0.1 for all rock types. The percentage of total porosity modeled as vertical fractures is 15% for rock type 1, 16% for rock type 2, and 8% for rock type 3. Fracture aspect ratio is 20 for all rock types. **Figure 2.7** shows the velocities calculated with the rock physics model in Upper Well B2, plotted along with sonic logs. The mean (3.8% for V_p and 3.4% for V_s) and the median (2.9% for V_p and 2.7% for V_s) of relative differences between calculated and measured velocities indicate that estimated velocities accurately reproduce sonic measurements. In Lower Well B2, most of rock physics features determined in the upper interval of the well remain unaffected. The only difference is a lower percentage of connected porosity within shale volumes in Lower Well B2 (30%) for all rock types than in the first part of the well. The values for rock parameters are summarized in **Table 2.8**. **Figure 2.8** illustrate the accuracy of the velocity simulations. The mean of relative differences is 4.2% for V_p and 4.3% for V_s, and the median, 3.3% for V_p and 3.7% for V_s. The agreement between simulated and field acoustic waves in both intervals of Well B2 suggests that the rock fabric parameters and the resulting elastic properties estimated along well trajectories are accurate.

2.8 SUMMARY AND DISCUSSION

The reason for performing rock physics modeling based on effective medium theory is to estimate elastic properties of studied formations, and therefore to incorporate

these insights into formation evaluation. Elastic properties of shale formations have a great impact on fracturability, which quantifies how efficiently a fracture forms and propagates in a rock. Montaut et al. (2013) finalized a rock physics model that produced accurate estimates of compressional- and shear-wave velocities in vertical Wells H1 and H2 and in both sections of Well B2. This method had, however, several limitations and I develop a model that leads to accurate and more constrained assessment of rock fabric parameters and thus of elastic properties of laminated shale formations.

First, Montaut et al. (2013) invoked Hudson's (1980) method in their model to add anisotropic inclusions into the background of a composite. Hudson's model, however, can only be applied to an isotropic background, which prevented the addition of more than one type of anisotropic inclusion. This is a restrictive impediment when reproducing the rock fabric of laminated shale formations because observations often show multiple types of oriented and aligned inclusions. The rock physics model introduced in this chapter is built on combinations of anisotropic effective medium theories, namely the VTI version of the SCA and DEM, and accounts for anisotropy due to specific rock fabric attributes such as shape of constituents, presence of anisotropic pores, and their orientation. The effective medium theories incorporated into this model allow the addition of multiple anisotropic inclusions within the background matrix, thereby leading to the reconstruction of realistic rock fabrics for shale formations. Moreover, reconstruction of porosity is an essential improvement of this new model: fluid inclusions are treated separately and are added as isolated porosity, percolating porosity, or fluid-filled fractures. The reconstruction of a thinly layered medium using the Backus average method ensures a reliable representation of laminated shales.

Second, Montaut et al.'s (2013) method was implemented and tested in vertical wells alone, thus the sonic velocities calculated from the reconstructed elastic properties of

the formations only accounted for waves propagating in the vertical direction. Only some of the elements of the estimated elastic stiffness tensor were used when computing vertically-propagating velocities and therefore, other elastic components were estimated but never verified against in-situ measurements. For example, there is only one visible shear wave that propagates in a vertical well in a VTI formation, whereas in deviated wells a splitting can be observed of fast and slow shear velocities. The value of the two shear velocities depends on different elements of the stiffness tensor. The new rock physics model was applied to the deviated section of Well H1 in addition to the vertical Well H1. This ensures that all elastic properties are utilized for the calculation of the velocity of both sonic waves and provides additional control over the estimated elastic properties.

2.9 CONCLUSIONS

I have described available effective medium theories that I incorporate into a new rock physics model to determine elastic properties of highly laminated organic shale formations. This method introduces a new way to estimate rock fabric from sonic logs to reconstruct constituents of a VTI rock and to account for anisotropy due to specific rock fabric attributes. I particularly focused on reproducing realistic porosity distribution by distinguishing between sandstone porosity, shale porosity, and fractures and specific features of laminated unconventional formations such as the alignment of cracks and solid particles.

Based on the very close match between simulated and measured sonic logs—the average of errors are lower than 2.7% in the vertical wells in the Haynesville shale, 5.9% in the deviated well in the Haynesville shale, and 4.3% in the wells in the Barnett shale—the rock physics model seems to provide reliable estimations of elastic properties.

Parameters such as stress, pore pressure, temperature, and dispersive behavior affect rock elastic properties and are not taken into account by the model. Moreover, I realize that a VTI medium under different directional stresses may become orthorhombic or monoclinic, but the study was conducted assuming that it remained transversely isotropic.

Parameters estimated with effective medium theories are rock fabric properties such as rock component shapes, fraction of percolating porosity, and aspect ratio and orientation of cracks. The only outputs produced by the estimation are compressional- and shear-wave velocities. Therefore, reproducing sonic logs with the method developed in this chapter may give rise to several solutions. Rock physics modeling requires further consideration of non-uniqueness, which is an inherent flaw of most effective medium theories. The contributions in this chapter encourage further improvement of the rock physics model with joint estimation of petrophysical and rock fabric parameters from usual sonic measurements and other well logs to reduce the number of possible results.

Inclusion shape	P_{b_i}	Q_{b_i}
Sphere	$\dfrac{K_b + 4/3\,\mu_b}{K_i + 4/3\,\mu_b}$	$\dfrac{\mu_b + \zeta_b}{\mu_i + \zeta_b}$
Needle-shaped crack	$\dfrac{K_b + \mu_b + 1/3\,\mu_i}{K_i + \mu_b + 1/3\,\mu_i}$	$\dfrac{1}{5}\left[\dfrac{4\mu_b}{\mu_b + \mu_i} + 2\dfrac{\mu_b + \Gamma_b}{\mu_i + \Gamma_b} + \dfrac{K_i + 4/3\,\mu_b}{K_i + \mu_b + 1/3\,\mu_i}\right]$
Penny-shaped crack	$\dfrac{K_b + 4/3\,\mu_i}{K_i + 4/3\,\mu_i + \pi\gamma\beta_b}$	$\dfrac{1}{5}\left[1 + \dfrac{8\mu_b}{4\mu_i + \pi\gamma\left(\mu_b + 2\beta_b\right)} + 2\dfrac{K_i + 2/3\left(\mu_i + \mu_b\right)}{K_i + 4/3\,\mu_i + \pi\gamma\beta_b}\right]$

where

$$\Gamma = \frac{\left(3K + \mu\right)}{\left(3K + 7\mu\right)},\ \ \beta = \mu\frac{\left(3K + \mu\right)}{\left(3K + 4\mu\right)},\ \text{and}\ \ \zeta = \frac{\mu}{6}\frac{\left(9K + 8\mu\right)}{\left(K + 2\mu\right)}.$$

Table 2.1: P and Q coefficients used in the differential effective medium theory and self-consistent approximation for spherical and spheroidal (needle and penny crack) shapes. K and μ are bulk and shear moduli, respectively. γ is the crack aspect ratio. Subscripts b and i designate the background and inclusion material, respectively (Berryman, 1980b; Mavko et al., 2009).

Solid properties

Solid component	Bulk Modulus K (GPa)	Shear Modulus μ (GPa)	Density ρ (kg/m^3)
Quartz[1]	36.6	45	2650
Calcite[1]	76.8	32	2710
Clay[1]	21	7	2600
Kerogen[2]	8	4	1300

Fluid properties

Fluid component	Bulk Modulus K (GPa)	Shear Modulus μ (GPa)	Density ρ (kg/m^3)	Viscosity η (Pa.s)
Water	2.25	0	1100	7.5×10^{-4}
Oil	1.5	0	750	10×10^{-3}
Gas	0.21	0	120	2.2×10^{-5}

[1] Mavko et al. (2009)

[2] Ahmadov et al. (2009)

Table 2.2: Summary of elastic properties of individual solid components and elastic properties and viscosity of fluids assumed in the estimation of rock elastic properties in synthetic and field cases throughout the entire dissertation.

Sandstone volumes	% of sand porosity that percolates	50
	Kerogen porosity (%)	10
Shale volumes	Shale porosity (%)	6
	% of shale porosity that percolates	30
	% of silt within shale layers	35
	Aspect ratio of clay platelets	0.2
	Crack aspect ratio	0.25
Fractures	% of total porosity modeled as horizontal fractures	9
	Aspect ratio	0.05

Table 2.3: Summary of the rock fabric parameters determined in the vertical section of Well H1 using the rock physics model.

Sandstone volumes	% of sand porosity that percolates	50
	Kerogen porosity (%)	10
Shale volumes	Shale porosity (%)	6.5
	% of shale porosity that percolates	30
	% of silt within shale layers	35
	Aspect ratio of clay platelets	0.2
	Crack aspect ratio	0.25
Fractures	% of total porosity modeled as horizontal fractures	9
	Aspect ratio	0.05

Table 2.4: Summary of the rock fabric parameters in the deviated section of Well H1 determined using the rock physics model.

Sandstone volumes	% of sand porosity that percolates	65
	Kerogen porosity (%)	10
Shale volumes	Shale porosity (%)	9
	% of shale porosity that percolates	55
	% of silt within shale layers	35
	Aspect ratio of clay platelets	0.2
	Crack aspect ratio	0.25
Fractures	% of total porosity modeled as horizontal fractures	9
	Aspect ratio	0.05

Table 2.5: Summary of the rock fabric parameters in Well H2 determined using the rock physics model.

Rock types	RT 1	RT 2	RT 3
Quartz concentration (%)	50	36	13
Kerogen concentration (%)	8	6	0.5
Calcite concentration (%)	21	40	8

Table 2.6: Average volumetric concentration of quartz, kerogen, and calcite in the solid part of the rock for each rock type in Well B2.

	Rock types	RT 1	RT 2	RT 3
Sandstone volumes	% of sand porosity that percolates	45	80	90
	Kerogen porosity (%)	10	10	10
Shale volumes	Shale porosity (%)	8	6.5	1
	% of shale porosity that percolates	55	55	55
	% of silt within shale layers	70	70	75
	Aspect ratio of clay platelets	0.1	0.1	0.1
	Crack aspect ratio	0.25	0.25	0.25
Fractures	% of total porosity modeled as horizontal fractures	15	16	9
	Aspect ratio	20	20	20

Table 2.7: Summary of the rock fabric parameters in the upper section of Well B2 determined with the rock physics model.

	Rock types	RT 1	RT 2	RT 3
Sandstone volumes	% of sand porosity that percolates	45	80	90
	Kerogen porosity (%)	10	10	10
Shale volumes	Shale porosity (%)	8	6.5	1
	% of shale porosity that percolates	30	30	30
	% of silt within shale layers	70	70	75
	Aspect ratio of clay platelets	0.1	0.1	0.1
	Crack aspect ratio	0.25	0.25	0.25
Fractures	% of total porosity modeled as horizontal fractures	15	16	9
	Aspect ratio	20	20	20

Table 2.8: Summary of the rock fabric parameters determined in the lower section of Well B2 with the rock physics model in.

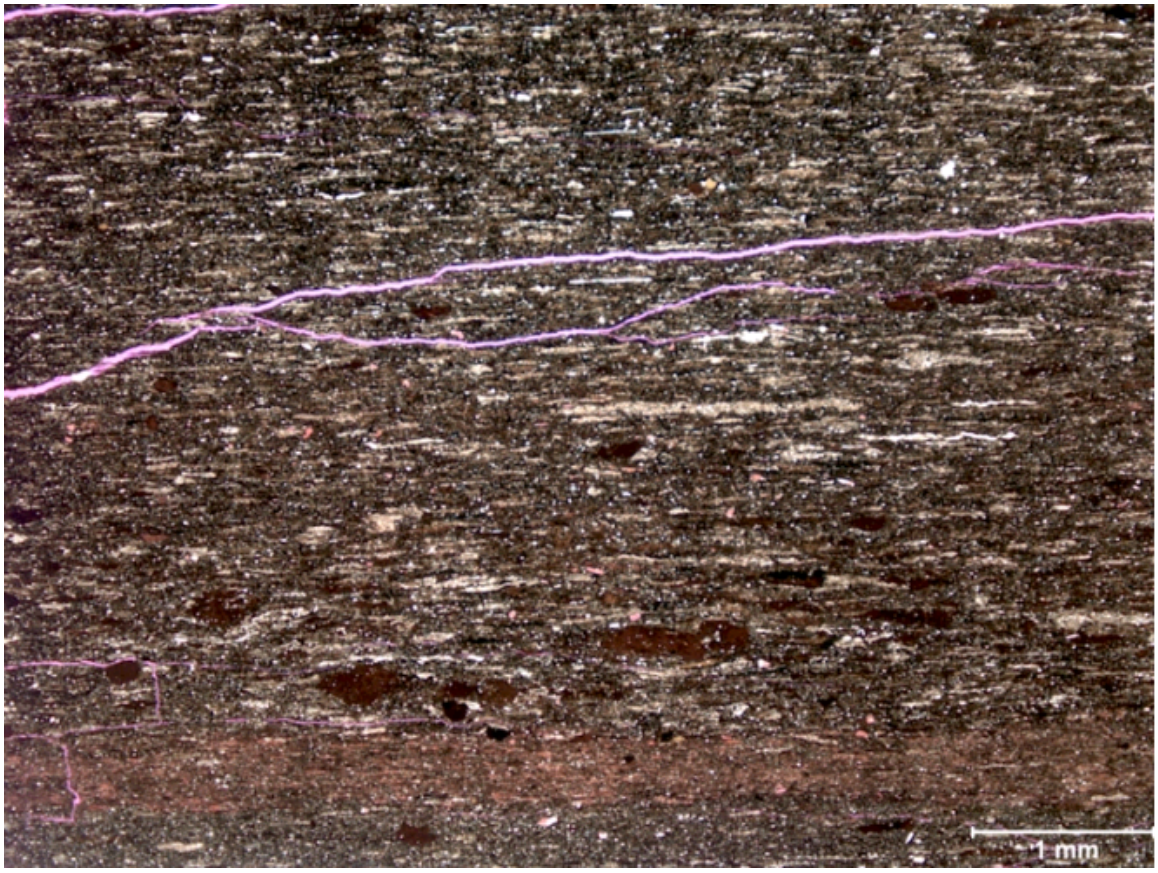

Figure 2.1: Thin section from the Barnett (courtesy of ConocoPhillips) shale showing fine-scale laminations and horizontal alignment of mineral inclusions. Magenta lines identify micro-fractures. Main constituents in this rock are quartz, calcite, clay, and kerogen.

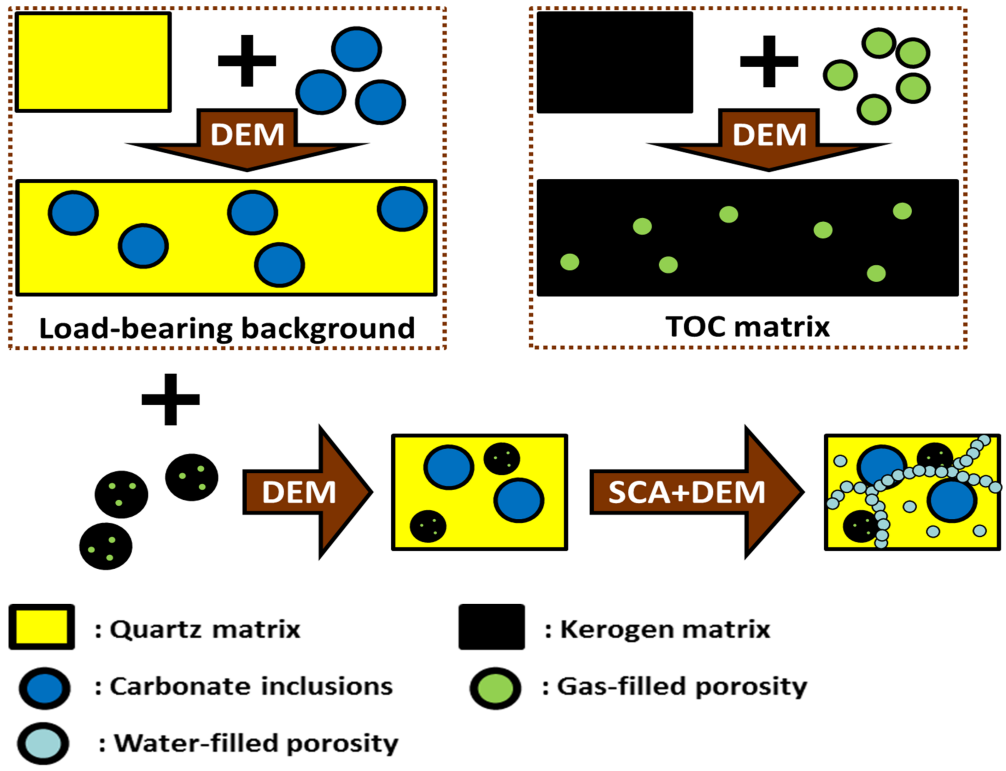

Figure 2.2: Illustration of the reconstruction of sand layers based on isotropic effective medium theories. Quartz and calcite are mixed together using the differential effective medium theory (DEM) and form the background of the sandstone component of each layer. Gas-saturated porosity is then added within the kerogen matrix to reconstruct the total organic content (TOC), which is then incrementally incorporated into the quartz-calcite medium with the DEM. Next, sand porosity is included in two steps: the percolating porosity first, using a combination of the self-consistent approximation (SCA) and the DEM, and then the isolated porosity utilizing only the DEM.

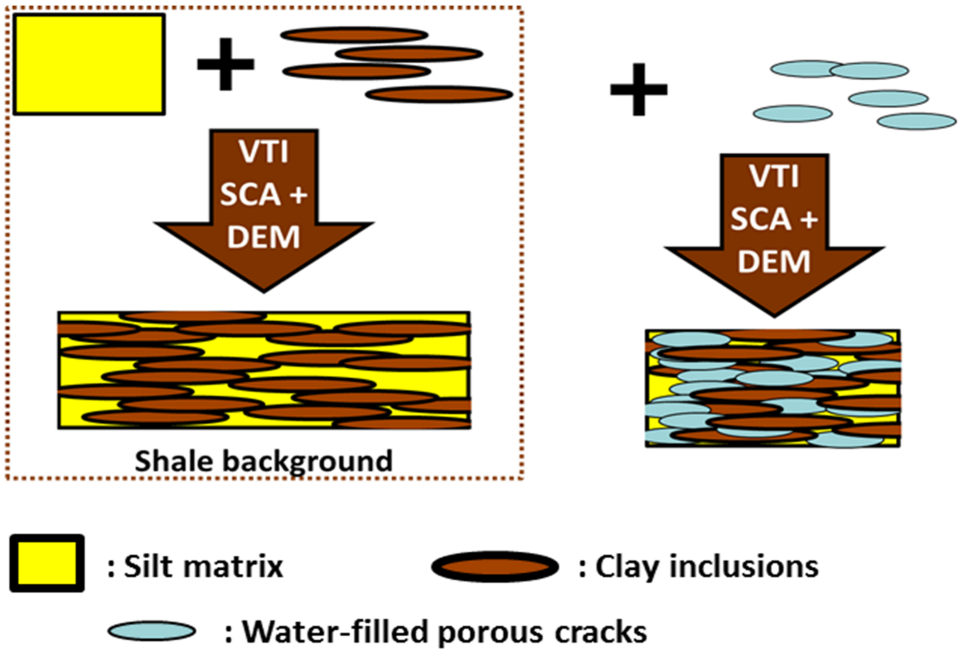

Figure 2.3: Illustration of the reconstruction of shale layers using vertical transverse isotropic (VTI) effective medium theories. Penny-shaped, horizontally-aligned clay particles are added in a background made of silt by invoking the VTI version of the DEM. Next, shale porosity, assumed fully water saturated, is included in the model. Percolating porosity is added with a combination of the anisotropic versions of the SCA and the DEM, and finally isolated porosity is incorporated in the model using only the VTI DEM.

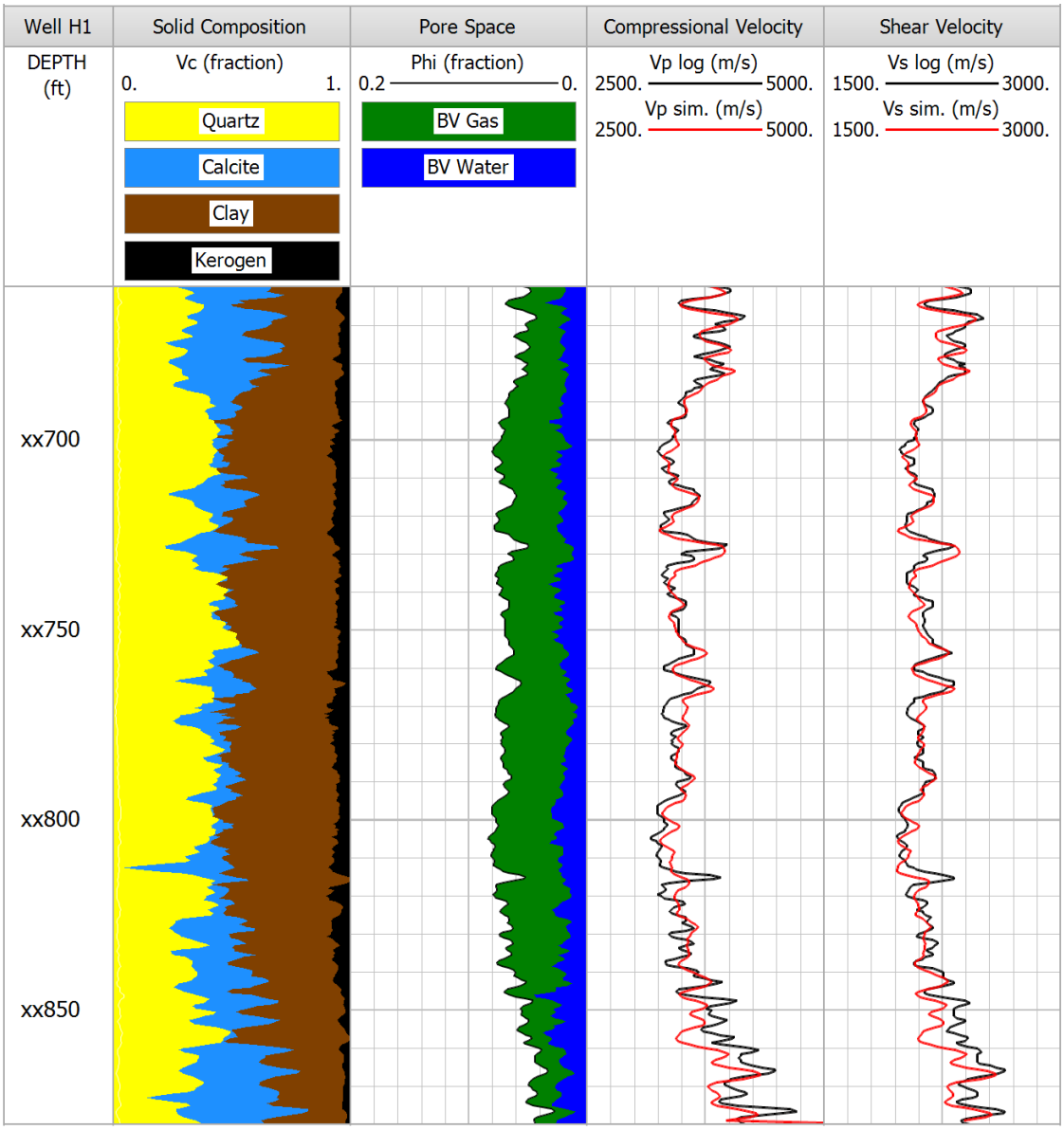

Figure 2.4: Velocity estimation in vertical Well H1. Track 1: solid composition. Track 2: porosity and bulk volume of fluids. Track 3: compressional velocity. Track 4: shear velocity. In tracks 3 and 4, black and red curves identify measured and calculated velocity, respectively.

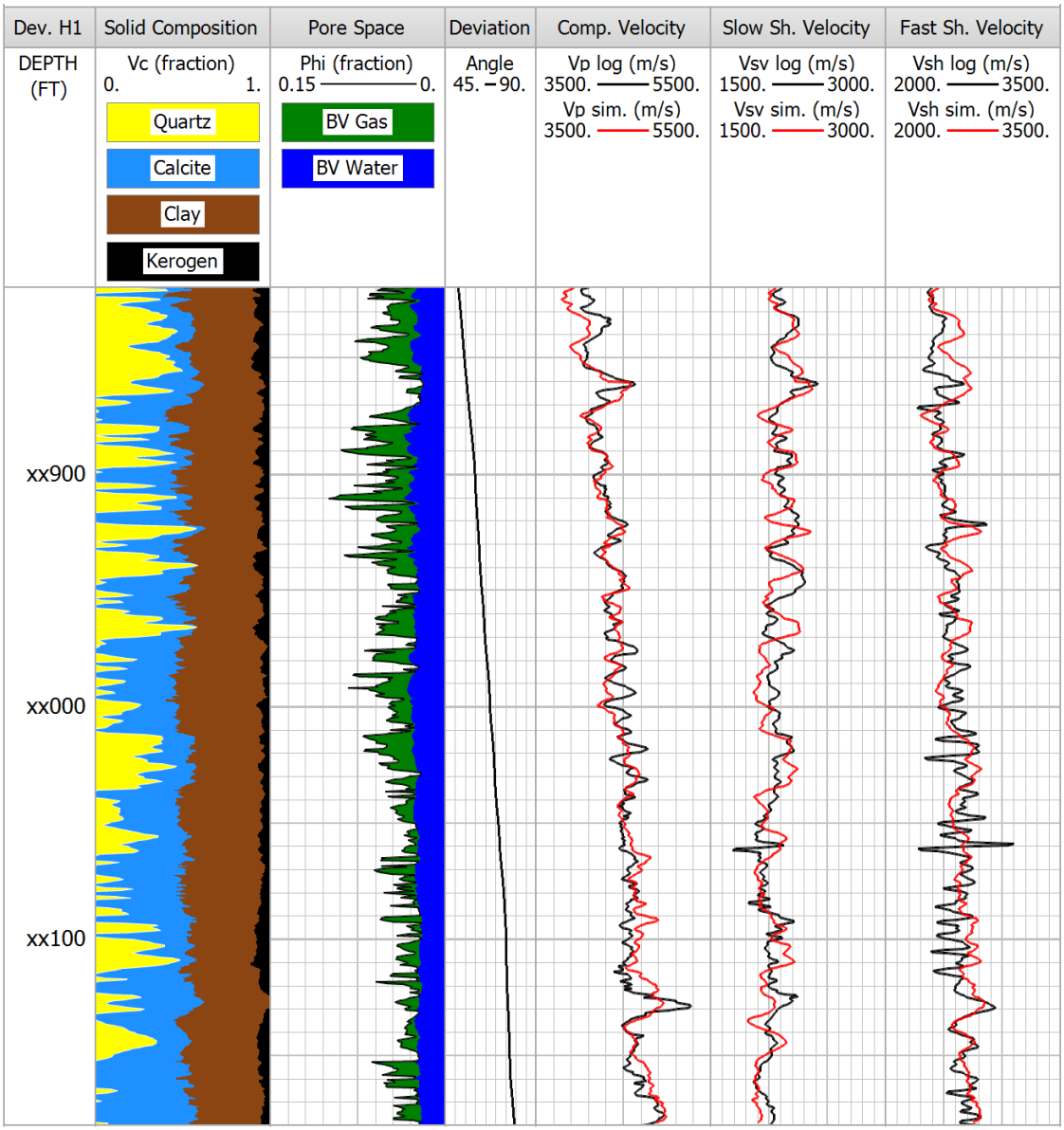

Figure 2.5: Velocity estimation in deviated Well H1. Track 1: solid composition. Track 2: porosity and bulk volume of fluids. Track 3: deviation angle. Track 4: compressional velocity. Track 5: slow (vertically-polarized) shear velocity. Track 6: fast (horizontally-polarized) shear velocity. In tracks 4, 5, and 6, black and red curves identify measured and calculated velocity, respectively.

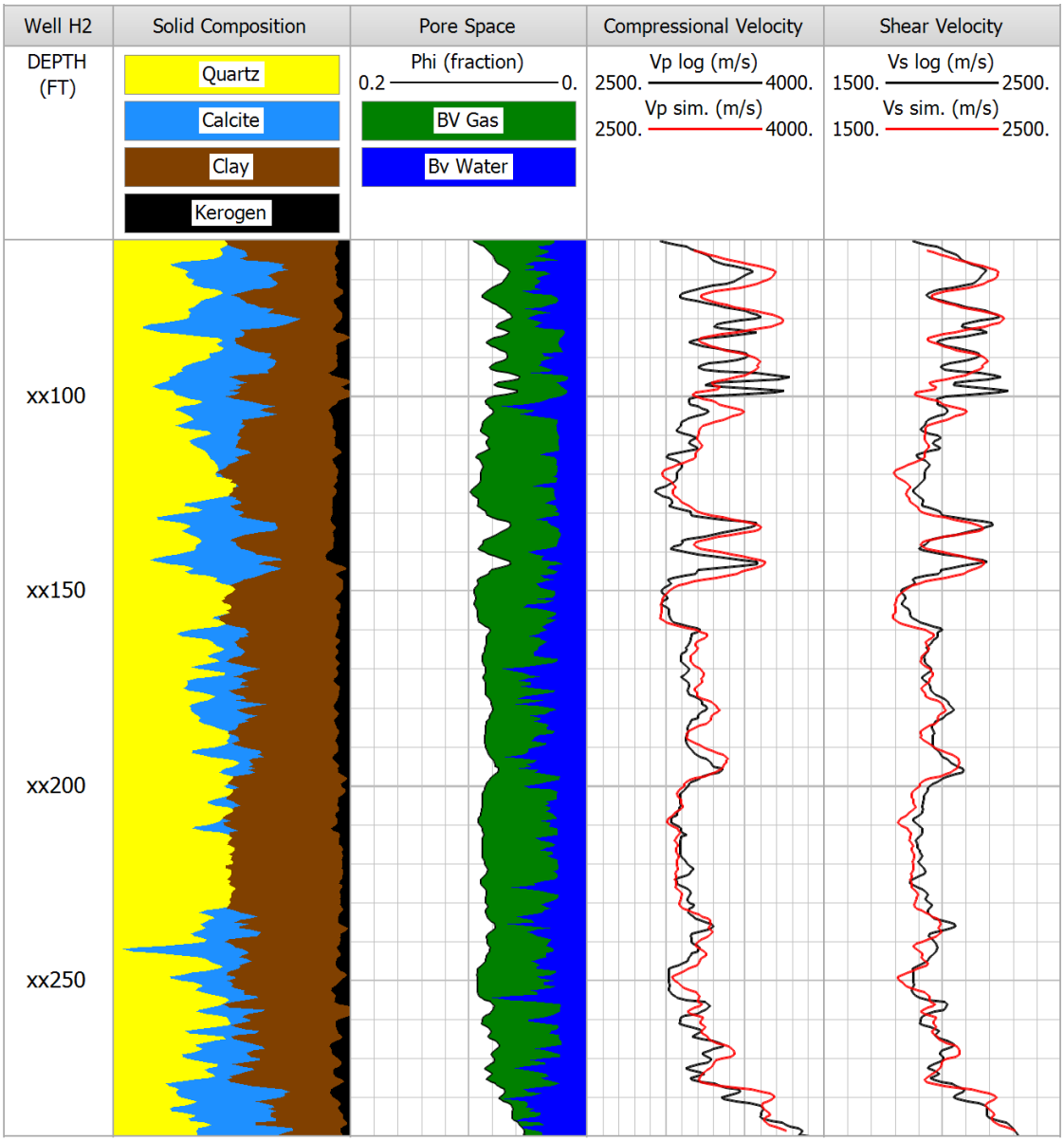

Figure 2.6: Velocity estimation in Well H2. Track 1: solid composition. Track 2: porosity and bulk volume of fluids. Track 3: compressional velocity. Track 4: shear velocity. In tracks 3 and 4, black and red curves identify measured and calculated velocity, respectively.

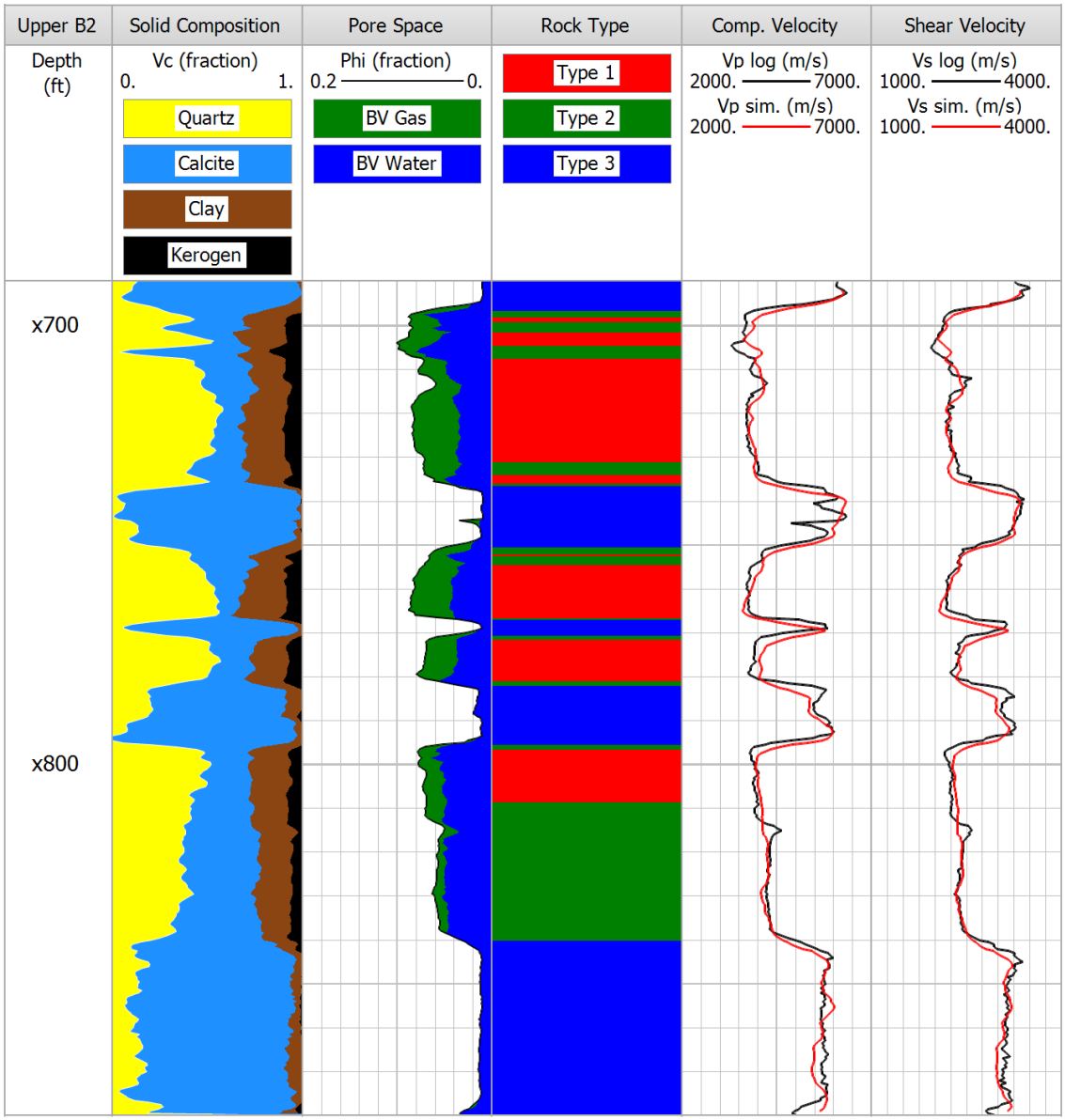

Figure 2.7: Velocity estimation in the upper section of Well B2. Track 1: solid composition. Track 2: porosity and bulk volume of fluids. Track 3: rock types. Track 4: compressional velocity. Track 5: shear velocity. In tracks 4 and 5, black and red curves identify measured and calculated velocity, respectively.

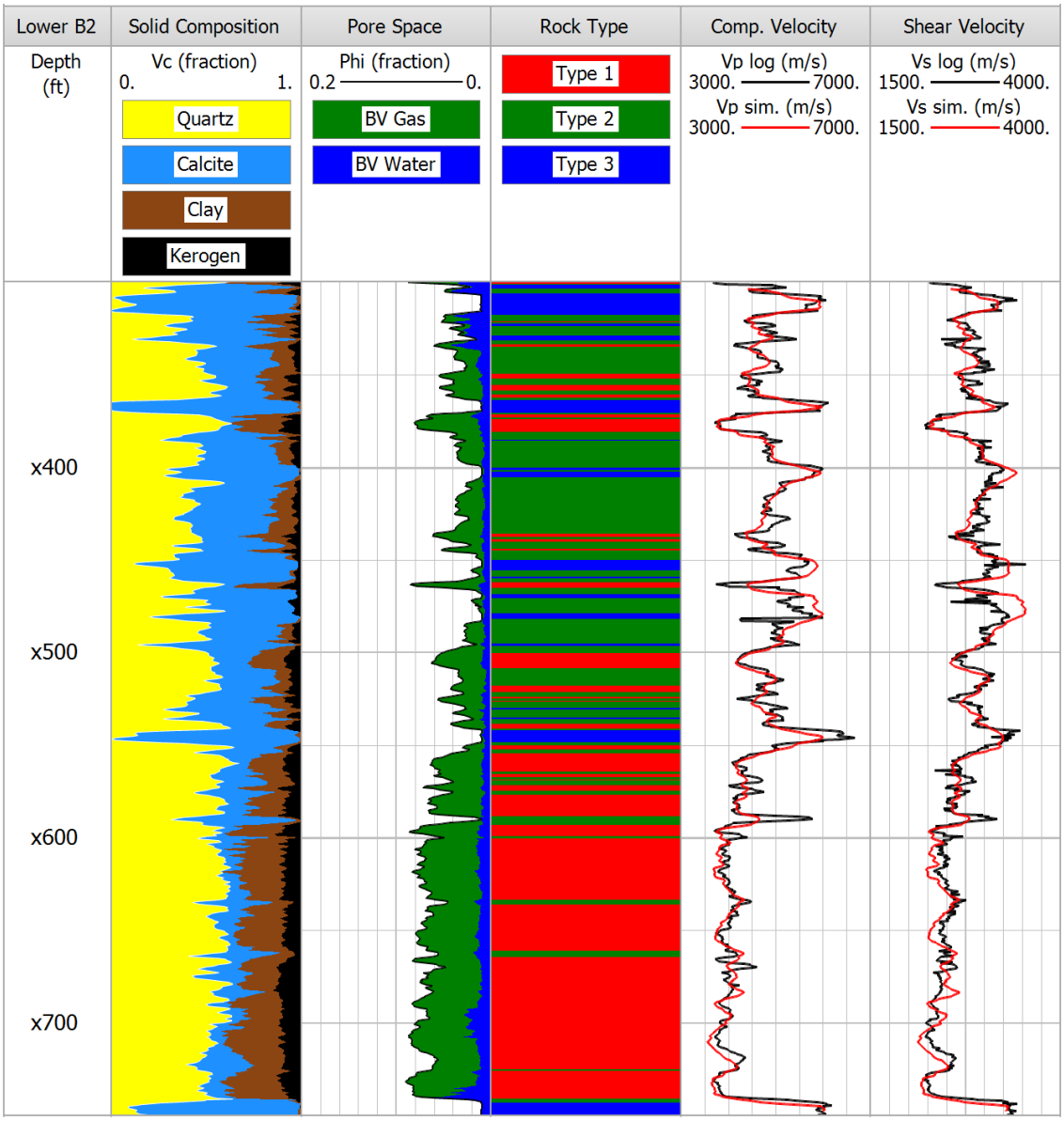

Figure 2.8: Velocity estimation in the lower section of Well B2. Track 1: solid composition. Track 2: porosity and bulk volume of fluids. Track 3: rock types. Track 4: compressional velocity. Track 5: shear velocity. In tracks 4 and 5, black and red curves identify measured and calculated velocity, respectively.

Chapter 3: Identification of Optimum Locations for Horizontal Well Placement in a VTI formation with a Joint Electrical/Sonic Effective Medium Model

In unconventional reservoirs such as organic shales, rock fabric can substantially affect the elastic properties because of the complex and highly anisotropic internal grain/clay structure of shales. Elastic features not only have a great influence on stress concentration around the wellbore, they also affect fracture initiation. Therefore, measuring the type and degree of rock fabric anisotropy is of utmost importance when attempting to locate optimum depths along a vertical well trajectory to drill a horizontal well. The main limitation of effective medium models is that they can give rise to non-unique solutions when estimating rock fabric parameters. New procedures are introduced in this chapter to verify the calculation of the stiffness tensor of such formations while limiting non-uniqueness. Elastic characteristics evaluated with the rock physics models constructed in the previous chapter are invoked to compute Stoneley velocity. In addition, modified effective medium theories are combined to simulate anisotropic electrical resistivity. Simulations continue to assume vertical transverse isotropy and are implemented in the same wells in the Haynesville and Barnett shale formations. Estimates of elastic properties are further verified by the comparison of newly computed properties against Stoneley velocity, when available, and resistivity logs. The rock physics model becomes then more constrained and reliable than previously developed methods.

Once the stiffness of the rock has been estimated it can be used as input into analytical solutions to calculate stress distribution around possible horizontal wells drilled at different depths along the vertical well. Rock stiffness can also be employed to study the variations of fracture initiation pressure with the degree of anisotropy. Thus, accurate

assessment of the elastic properties of a formation enable identification of areas where the rock is most easily susceptible to experience controlled shear failure.

3.1 INTRODUCTION

Prior to the advent of modern technologies related to multiple hydraulic well-stimulation combined with horizontal drilling, economically viable hydrocarbon production from organic shale formations was impossible because of the very low permeability, heterogeneous mineralogy, and complex arrangement of solid and fluid constituents in shales. These technologies gave access to large energy sources by increasing formation exposure and improving reservoir stimulation (King, 2010). Nevertheless, designing and drilling horizontal wells and performing effective hydraulic fracturing remain a challenge for the oil industry.

Designing a horizontal well and optimizing hydraulic stimulation are difficult processes that require detection and quantification of many factors. Among others, mechanical brittleness and fracture initiation pressure are key parameters that require special consideration.

Brittle rocks, defined as exhibiting high static Young's moduli, are more suited for efficient hydraulic-fracture initiation and growth than are ductile rocks. When drilling horizontal wells, brittle rocks are also preferable because they are resistant to collapse and fracture closure (Montaut et al., 2013). Static and dynamic Young's moduli tend to be linearly related in shale formations (Britt and Schoeffler, 2009). Young's moduli estimated from the entries of a stiffness tensor are, as a result, reliable for the identification of recommended zones to place horizontal wells and initiate fracturing. Although non-uniqueness is a problem widely known to be associated with the assessment of rock fabric

properties achieved with effective medium theories (Farmer, 2002; Fjar et al., 2008), this issue has rarely been addressed in the past. In order to provide greater reliability in horizontal well location selection it is necessary to establish the accuracy of elastic features obtained with the rock physics model.

The first objective of this chapter is to complete the rock physics model presented in Chapter 2 by limiting non-uniqueness in order to quantify the strength of a studied rock as closely as possible to its true value. Montaut (2012) recommended to use more field data to reduce the number of possible rock fabric parameters that lead to the reproduction of sonic logs. I introduce the simulation of Stoneley wave as an additional output of the rock physics model to verify calculations of elastic properties further and to control more efficiently the values of estimated rock fabric parameters. In fact, in wells where Stoneley wave propagation was acquired, up to four velocity curves can then be simulated and compared to in-situ measurements. In the same manner, effective medium theories for electrical resistivity are jointly invoked with the rock physics model to reduce non-uniqueness. Aspect ratio value of porous inclusions and percentage of percolating porosity are rock fabric parameters that have an influence on both mechanical and electrical properties. Consequently, simulating and matching electrical resistivity measurements increases the number of outputs and limits the possible solutions, leading to more reliable estimations of rock elastic properties.

Prediction of pressures required to initiate fracturing from the borehole is crucial for profitable hydraulic fracturing simulation. Rock fabric anisotropy directly influences stress distribution around the wellbore, therefore affecting fracture initiation pressure. Stress concentration around a borehole is often derived using Kirsch's solution (1898), but it is only valid for elastic and isotropic rocks. Hossain et al. (2000) extended calculations for the fracture initiation pressure to wells of varying trajectories drilled in isotropic rocks.

Stress analysis assuming rock isotropy in shale formations can lead to inaccurate estimations of fracturing pressure (Zoback, 2007). Amadei (1983) and Lekhnitskii (1981) calculated the stress distribution around boreholes with different deviation angles and drilled in formations that exhibited general anisotropy. However, the solution they proposed is not reliable in the case of simpler anisotropy, such as vertical transverse isotropy, because the corresponding simplifications lead to undefined mathematical expressions. Several studies, such as Serajian and Ghassemi (2011) and Gaede et al. (2012), applied Amadei and Lekhnitskii's solutions to wells drilled in VTI formations but ignored the resulting mathematical errors.

The second objective is thus to establish a procedure to calculate stress distribution and fracture initiation pressure around potential wellbores drilled horizontally in VTI rocks from the stiffness tensor obtained with the improved rock physics model. The analytical solutions developed by Fairhurst (1968) are first used to compute the effective hoop stress from assumed in-situ stresses and pore pressure, and estimated elastic features. Fracture initiation pressure is then defined as the borehole pressure at which the effective hoop stress reduces to zero. Effects of degree of anisotropy and elastic properties on fracture initiation pressure are investigated, and a relationship is found between fracturing pressure and ratio of horizontal to vertical Young's modulus. Identification of recommended zones to drill horizontal wells at various depths along the studied vertical well is then discussed based on these observations

3.2 IMPROVEMENT OF THE ROCK PHYSICS MODEL

In this section, I introduce two models to further constrain evaluation of rock fabric and petrophysical parameters obtained with the rock physics model established in Chapter

2. Stoneley velocity is approximated in addition to compressional and shear velocity using estimates of stiffness properties. Simultaneously with the construction of stiffness tensor, anisotropic electrical conductivity is also computed in the vertical and horizontal directions with an effective medium model. Resulting calculations are plotted against Stoneley and electrical resistivity measurements conducted along the wells drilled in the Haynesville and Barnett shales as was described in the previous chapter.

3.2.1 Calculation of Stoneley Velocity

At low frequencies, the Stoneley wave velocity, V_{Sto}, is expressed as (Norris, 1990)

$$V_{Sto} = \sqrt{\frac{K_{bor}}{\rho_{fl}}}, \tag{3.1}$$

where ρ_{fl} is the density of the borehole fluid and K_{bor} is the effective bulk modulus of the borehole, given by

$$K_{bor} = \left[\frac{1}{K_{fl}} + \frac{1}{1-r}\left(\frac{1}{\mu_{fm}} + \frac{r}{\mu_r} \right) \right]^{-1}, \tag{3.2}$$

where K_{fl} is the bulk modulus of the borehole fluid, r is the volume fraction the tool occupies in the borehole, and μ_{fm} and μ_r are the effective formation and tool shear modulus, respectively. An approximate formula for the effective formation shear modulus, μ_{fm}, as a function of well deviation and stiffness parameters in a VTI formation has been determined by Chi and Tang (2003) as

$$\begin{aligned} \mu_{fm} = c_{44}\sin^2\theta + c_{66}\cos^2\theta + \frac{1}{4}(\varepsilon-\delta)c_{33}\sin^4\theta \\ -\frac{1}{2f}(\varepsilon-\delta)\left(\varepsilon\sin^2\theta + \delta\cos^2\theta\right)c_{33}\sin^6\theta, \end{aligned} \tag{3.3}$$

where $\varepsilon = \frac{c_{11} - c_{33}}{2c_{33}}$ and $\delta = \frac{\left(c_{13} + c_{44}\right)^2 - \left(c_{33} + c_{44}\right)^2}{2c_{33}\left(c_{33} - c_{44}\right)}$ are Thomsen's (1986) parameters and $f = 1 - \frac{c_{44}}{c_{33}}$. The c_{ij} terms represent entries of the VTI stiffness tensor as defined in Chapter 2.

The average value of Stoneley velocity is controlled by the properties of the mud in the borehole when measurements were acquired. On the other hand, variations around the mean speed value are mainly influenced by the effective shear modulus. The value of μ_{fm} directly depends on the elastic properties described in the stiffness tensor of the formation but in a distinctive manner than that of V_p, V_{sv}, and V_{sh} (refer to equations (2.15), (2.16), and (2.17)). Hence, comparing calculated Stoneley velocity with in-situ surveys provides additional verification of the estimated elastic properties—and rock fabric features—that is not redundant with comparisons between simulations and measurements of other sonic logs.

3.2.1.1 Simulation Results in the Haynesville Shale

Stoneley wave is a type of large-amplitude surface wave generated by the sonic tool. It propagates along the walls of a fluid-filled borehole, and its speed depends greatly on the size of the borehole and on the volume fraction the tool occupies in the borehole. Consequently, in depth zones where caliper logs show washouts, measured Stoneley wave are often highly noisy and impracticable. This is the case for the interval of interest in vertical Well H1. By contrast, measurements of Stoneley waves performed in the deviated portion of Well H1 and in Well H2 are more stable and exploitable for comparisons with calculations.

Results of Stoneley wave simulation are plotted alongside velocity measurements in **Figure 3.1** for deviated Well H1 and in **Figure 3.2** for Well H2. Qualitative comparisons

of velocities show that the rock physics model based on a combination of VTI effective medium theories gives rise to accurate estimation of the elastic properties invoked in Stoneley calculation for both wells of the Haynesville shale. The mean and median of relative differences between simulated and field velocities are 0.24% and 0.18% in deviated Well H1, and 0.32% and 0.24% in Well H2, respectively.

There is one depth zone in the deviated well, between xx040 ft and xx060 ft, where the velocity log and computed speed do not agree. This is due to a washout observed on the caliper log (refer to track 1 of **Figure 3.1**). For this reason, sonic measurements at this depth are not suitable for validation of the rock fabric parameters assumed for the formation.

3.2.1.2 Simulation Results in the Barnett Shale

In the case of the wells in the Barnett shale, a Stoneley velocity log was only reliable in the upper part of Well B2. Note the good agreement between computed and measured Stoneley wave speed in **Figure 3.3**. The mean and median of relative differences between simulated and field velocities in the upper Well B2 are 0.52% and 0.39%, respectively, indicating that stiffness properties evaluated with the rock physics model are accurate.

3.2.2 Effective Medium Modeling of Electrical Resistivity

Hornby et al. (1993) showed that a modification and combination of the SCA and DEM equations could be used to calculate the electrical properties of anisotropic systems. The modified SCA for electrical conductivity computation reduces to the following pair of coupled equations:

$$-\frac{x_s\sigma_V}{1-\Lambda_V\sigma_V}+\frac{x_{fl}\left[\sigma_{fl}-\sigma_V\right]}{1+\Lambda_V\left[\sigma_{fl}-\sigma_V\right]}=0, \tag{3.4}$$

and

$$-\frac{x_s\sigma_H}{1-\Lambda_H\sigma_H}+\frac{x_{fl}\left[\sigma_{fl}-\sigma_H\right]}{1+\Lambda_H\left[\sigma_{fl}-\sigma_H\right]}=0, \tag{3.5}$$

where x_s is the volume fraction of non-conducive phase (solids and isolated pores), x_{fl} is the volume fraction of the conductive and connected fluid phase, σ_V and σ_H are the effective vertical and horizontal electrical conductivities, respectively, and σ_{fl} is the electrical conductivity of the pore fluid. The above equations are coupled through the quantities $\Lambda_V \equiv L_V/\sigma_V$ and $\Lambda_H \equiv L_H/\sigma_H$, where L_V and L_H are depolarization factors that are prescribed functions of the ratio $\lambda = \sigma_V/\sigma_H$. More precisely, if the porous inclusions are defined as horizontally-aligned oblate spheroids and the direction of the effective medium coincides with the principal axes of the inclusions, the inclusions are defined by

$$\frac{x_1^2}{\alpha_1^2}+\frac{x_2^2}{\alpha_1^2}+\frac{x_3^2}{\alpha_3^2}\le 1, \tag{3.6}$$

where α_1 and α_3 are the principal semi-axes of the spheroid with $\alpha_3 < \alpha_1$. In that case,

$$L_V=\frac{1+g^2}{g^3}\left[g-\tan^{-1}g\right], \tag{3.7}$$

and

$$L_H=(1-L_V)/2, \tag{3.8}$$

where $g\equiv\left[\lambda\left(\alpha_1/\alpha_3\right)^2-1\right]^{1/2}$. The modified DEM equations for electrical conductivity estimations for the case of fluid-filled porosities less than 50% (which is always the case in shale formations) are given by Hornby et al. (1993) as

$$\frac{d\sigma_V}{\sigma_V}=\frac{dx_{fl}}{x_{fl}}\frac{1}{1-L_V}, \tag{3.9}$$

and

$$\frac{d\sigma_H}{\sigma_H} = \frac{dx_{fl}}{x_{fl}} \frac{1}{1 - L_H}. \tag{3.10}$$

In order for the simulated electrical conductivity not to be zero, the conductive phase needs to be connected throughout the entire effective medium. As described above, the SCA represents an effective medium with both fluid and solid phases that are connected for porosities between 40% and 60% only. To obtain electrical conductivity of a rock with values of porosity outside this range, the solution is to start with a bi-connected medium formed by a 50% porosity SCA composite and to apply the DEM to adjust for the relative concentrations of solids and fluids, which ensures that both phases remain connected throughout the entire process. Vertical and horizontal electrical resistivity are then simulated by calculating the inverse of the simulated vertical and horizontal electrical conductivity, respectively.

The electrical resistivity model developed jointly with the rock physics model reproduces an important feature of sedimentary rocks: bi-continuity of fluid and solid phases. Because all the porous inclusions are assumed to be spherical in the sand volume of the layers, electrical resistivity is isotropic, whereby vertical and horizontal resistivity are equal. On the other hand, it is assumed that porosity in shale layers consists of horizontally-aligned spheroidal cracks (Reed et al., 2012), as described in Chapter 2, generating a preferential path for the electrical current in the horizontal direction. Therefore, anisotropy is observed, and calculated vertical electrical resistivity is higher than horizontal electrical resistivity. Percentage of percolating porosity and aspect ratio of porous inclusions are the only parameters that affect resistivity estimations when applying my effective medium model. Consequently, calculating electrical resistivity and comparison of the measurements provides additional control on the concentration and shape of connected pores. Electrical resistivity is estimated in every sandstone and shale

layer and then averaged using the Backus average to reproduce deep resistivity in-situ measurements.

3.2.2.1 Simulation Results in the Haynesville Shale

Figures 3.4 and **3.5** describe the electrical resistivity estimation results plotted alongside the measured resistivity in the vertical wells H1 and H2. The last tracks in both figures show the estimates of horizontal and vertical electrical resistivity. Because the shale formation is assumed to be VTI, the layering is perpendicular to a vertical axis of symmetry in this configuration. Therefore, in vertical wells, the simulated horizontal resistivity matches the resistivity measured with an induction tool.

In the deviated section of Well H1, an average between simulated vertical and horizontal resistivity, weighted by the sine and cosine of the deviation angle respectively, is calculated and then compared to resistivity logs. **Figure 3.6** shows vertical and horizontal electrical resistivity simulated with the effective medium model (track 5) as well as the calculated deep resistivity plotted alongside field measurements (track 4).

3.2.2.2 Simulation Results in the Barnett Shale

The last track of **Figures 3.7** and **3.8** shows the estimates of horizontal and vertical electrical resistivity in the upper and lower sections of Well B2, respectively. Tracks 4 of both figures confirm the accurate reproduction of measured electrical resistivity by properties. For the same reasons described in the above section, simulated horizontal resistivity matches the measured resistivity.

The good agreement between calculated and field electrical resistivity seems to validate proportions of isolated and connected porosity for sandstone and shale volumes, and aspect ratio of penny-shaped cracks assumed in both shale formations. This result gives higher credibility to the elastic characteristics obtained by using the rock physics model.

3.2.3 Computational Speed

Complete reconstruction of the rock components and calculation of the elastic properties and electrical resistivity take on average 1.3 seconds at a particular depth using a Windows 7 PC with an Intel i7 3.6 GHz processor. Computational time when applying the joint sonic/electrical rock physics model is about 10 minutes and 18 minutes in the vertical and deviated sections of Well H1, respectively, 10 minutes in Well H2, 8 minutes in upper Well B2, and 19 minutes in lower Well B2.

3.3 PREDICTION OF FRACTURE INITIATION PRESSURE

Most of the wells drilled horizontally to enhance hydrocarbon production penetrate transversely isotropic formations such as laminated shales. A two-step analysis should be performed in these anisotropic formations for hydraulic fracturing design. One should first calculate borehole stresses for VTI rocks; second, one should compute the fracture initiation pressure with a stress-related criterion. The stress distribution estimation around the horizontal boreholes is based on the analytical solutions developed by Fairhurst (1968). Stiffness parameters obtained with the rock physics model become inputs for stress calculations.

3.3.1 Coordinate Systems

Three different coordinate systems are defined for in-situ stress, the formation, and the horizontal well. Let $(\mathbf{x}, \mathbf{y}, \mathbf{z})$ be the coordinate system of the principal stresses so that the maximum horizontal stress, S_H, is aligned with the x-direction, the minimum horizontal stress, S_h, is aligned with the y-direction, and the vertical stress, S_V, is aligned with the z-direction. The coordinate system $(\mathbf{x_1}, \mathbf{x_2}, \mathbf{x_3})$ is defined to describe the VTI rock; the x_1- and x_2-axis are in the plane of elastic isotropy whereas the x_3-axis is the vertical

axis of symmetry that coincides with the z -axis. Furthermore, because the horizontal plane is a plane of isotropy, the orientation of the vectors $\mathbf{x_1}$ and $\mathbf{x_2}$ can be arbitrary. To simplify calculations, I choose $\mathbf{x_1}$ and $\mathbf{x_2}$ to be parallel with vectors $\mathbf{x}$ and $\mathbf{y}$, respectively, so that $(\mathbf{x_1}, \mathbf{x_2}, \mathbf{x_3}) = (\mathbf{x}, \mathbf{y}, \mathbf{z})$. Elastic properties, determined with the rock physics model previously described and used in the stress concentration calculations, are expressed in the $(\mathbf{x_1}, \mathbf{x_2}, \mathbf{x_3})$ system. Finally, $(\mathbf{x_1}', \mathbf{x_2}', \mathbf{x_3}')$ are the coordinates associated with a horizontal well where the -axis is the axis of the borehole and the -axis lies in the plane of isotropy of the rock. **Figure 3.9** describes the position of the horizontal well with respect to in-situ stress and the VTI formation coordinate system. Compression stresses are assumed positive.

3.3.2 Stress Concentration around a Horizontal Wellbore

To conduct calculation of stress distribution around a horizontal borehole with Fairhurst's (1968) solutions, the principal in-situ stresses must be expressed in the coordinate system $(\mathbf{x_1}', \mathbf{x_2}', \mathbf{x_3}')$ associated with the well. The principal stresses in the $\mathbf{x_i}'$ coordinates are then given by

$$\begin{aligned} S_1 &= \sin^2(\psi) S_H + \cos^2(\psi) S_h, \\ S_2 &= S_V, \\ S_3 &= \cos^2(\psi) S_H + \sin^2(\psi) S_h, \end{aligned} \tag{3.11}$$

for normal stresses, and

$$\begin{aligned} \tau_{12} &= \tau_{23} = 0, \\ \tau_{13} &= \cos(\psi)\sin(\psi)\left[S_h - S_H\right], \end{aligned} \tag{3.12}$$

for shear stresses, where ψ is the angle between the axis of the borehole and the direction of maximum horizontal stress.

The stress concentration, expressed as the hoop stress, around a horizontal borehole penetrating a vertically transversely isotropic formation, is then given by Fairhurst (1968) as

$$S_\varphi = \left(S_\varphi\right)_1 + \left(S_\varphi\right)_2, \tag{3.13}$$

where

$$\begin{aligned}\left(S_\varphi\right)_1 = \frac{P_{bor}}{H}\Big[&2k_3\left(k_1+1\right)-2\left(k_1+k_2\right)\\ &-2k_3\left(k_1-1\right)\cos\left(2\varphi\right)-\left(k_1^{\,2}-2k_2+1\right)\cos^2\left(2\varphi\right)\Big],\end{aligned} \tag{3.14}$$

and

$$\begin{aligned}\left(S_\varphi\right)_2 = \frac{1}{H}\Big\{&\left(S_1-S_2\right)\left(k_3+k_1+1\right)\Big[\left(k_1-1\right)-\left(k_1+1\right)\cos\left(2\varphi\right)\Big]\\ &+\left(S_1+S_2\right)\Big[k_3\left(k_1+1\right)+\left(k_1-1\right)^2\\ &-\left(k_3+k_1+1\right)\left(k_1-1\right)\cos\left(2\varphi\right)\Big]\Big\},\end{aligned} \tag{3.15}$$

where φ is the angle around the horizontal wellbore, measured counterclockwise from the horizontal x_1'-direction, P_{bor} is the borehole pressure, and

$$H = \left(k_1^{\,2}+2k_2+1\right)-2\left(k_1^{\,2}-1\right)\cos\left(2\varphi\right)+\left(k_1^{\,2}-2k_2+1\right)\cos^2\left(2\varphi\right), \tag{3.16}$$

$$k_1 = \left(\frac{1-\nu_h^{\,2}}{E_h/E_v-\nu_v^{\,2}}\right)^{1/2}, \tag{3.17}$$

$$k_2 = \left(\frac{E_h/2c_{44}-\nu_v\left(1+\nu_h\right)}{E_h/E_v-\nu_v^{\,2}}\right)^{1/2}, \tag{3.18}$$

and

$$k_3 = \sqrt{2\left(k_1+k_2\right)}. \tag{3.19}$$

In the previous equations, E_v and E_h are vertical and horizontal Young's moduli, respectively, and ν_v and ν_h are vertical and horizontal Poisson's ratios, respectively, defined in Chapter 2. **Figure 3.10** shows the orientation of in-situ stress expressed in the wellbore coordinate system and hoop stress exerted around the wellbore.

3.3.3 Fracture Initiation Pressure

The effective hoop stress is defined as

$$\varsigma_\varphi = S_\varphi - P_\phi, \tag{3.20}$$

where P_ϕ is the pore pressure. Fracture initiation pressure is defined as the borehole pressure at which the effective hoop stress is zero. Stress concentration is directly dependent on the angle around the borehole; therefore, different values of P_{bor} are obtained for different angles. The minimum value of P_{bor} corresponds to the fracturing pressure, P_{frac}, measured at the weakest point around the horizontal wellbore, or fracture initiation point. Note that in some cases, depending of the in-situ stress conditions and well orientation, fracturing pressure might be defined based on the longitudinal stress. These cases are not studied in this dissertation.

3.3.3.1 Effects of Elastic Properties on Fracture Initiation Pressure

In this section, I conduct an analysis of the dependence of the fracturing pressure on the values of Young's moduli and Poisson's ratios. More precisely, the impact of the degree of anisotropy is investigated through the ratios E_v/E_h and ν_v/ν_h. **Table 3.1** describes in-situ stress used for the simulations. The stress regime is assumed to be normal faulting, and drilling depth is 10,000 ft. The different values of elastic properties invoked in the analysis are shown in **Table 3.2**. Vertical Young's modulus and Poisson's ratio remained constant, and horizontal properties vary over large ranges of values so that

$1 \le E_v / E_h \le 2$ and $0.5 \le \nu_v / \nu_h \le 2$. In the simulations, the horizontal Young's modulus is modeled larger than the vertical one because horizontal alignment of penny-shaped solid and porous constituents generates higher stiffness in that direction. The stiffness tensor entry c_{44}, that appears in equation (3.18), is calculated as

$$c_{44} = \frac{E_v}{2(1+\nu_v)}. \tag{3.21}$$

The well is assumed to be drilled along the direction of maximum horizontal stress $(\psi = 0^\circ)$. The calculated fracturing pressures are shown in **Figure 3.11**. The contour zones tend to be vertical, which indicates that the ratio E_v / E_h greatly influences fracturing pressure, whereas the ratio ν_v / ν_h has a limited impact. I observe that for low ratios of horizontal to vertical Young's modulus, in other words, for low degrees of anisotropy, calculated fracturing pressure is higher than when the Young's modulus ratio is high (high degree of anisotropy). Therefore, the fracture initiation pressure and the equivalent fluid pressure necessary to initiate fracturing are higher in layers exhibiting nearly isotropic elastic properties in VTI formations. On the other hand, rock with large discrepancies between vertical and horizontal elastic features enhances the probability of fracturing.

3.3.3.2 Effects of Orientation of the Well within the Horizontal Plane

Figure 3.12 shows how the angle between the axis of the horizontal well and the direction of maximum horizontal stress affects fracturing pressure in VTI rocks. Simulations are conducted assuming the same in-situ stress conditions as described in **Table 3.1** for an isotropic rock, and two VTI rocks with Young's modulus ratios of 1.5 and 2. Ratio of horizontal to vertical Poisson's ratios is taken equal to 1. The observations shown in **Figure 3.11** are confirmed: predicted fracture initiation pressure is lower for formations with a higher degree of anisotropy. Regardless of well orientation, the

differences between fracturing pressures in the distinct rocks remain approximately constant. In this example, the impact of well orientation on fracturing pressures is much larger than the effect of anisotropy, when ψ varies from 0° to 90°, fracturing pressure increases by more than 20 MPa, whereas the difference due to elastic anisotropy is only about 4 MPa. However, if a well is drilled in a region where S_H and S_h exhibit similar values, elastic anisotropy becomes a preponderant factor in fracturing pressure variations. **Figure 3.13** illustrates this phenomenon when the gradient of S_h is changed to 18.8×10^3 Pa.m^{-1}. In this case, maximum variations of fracturing pressure caused by anisotropy and well orientation are about 4 MPa.

3.4 DISCUSSION

3.4.1 Limitation of Non-Uniqueness

By providing validation of elastic properties that are not invoked in the calculation of compressional- and shear-wave velocities, the addition of a means of estimating Stoneley velocity within the model helps to constrain the possible rock fabric parameters. Furthermore, the new model introduces the calculation of vertical and horizontal electrical resistivities based on modified version of the same effective medium theories used to evaluate elastic properties. This enhancement of the model enables the calculation of two additional outputs to compare to measurements for verification of the rock fabric estimates.

Table 3.3 illustrates how two distinct choices of rock fabric properties can give rise to simulated wave velocities that match sonic logs when using the rock physics model. I modify the final values of cracks' aspect ratio determined by the model (see Table 2.3) to 1 to represent spherical pores and transform grains of quartz and calcite originally modeled as spheres into spheroidal inclusions (aspect ratio changed from 1 to 0.125) in vertical Well

H1. As a result, calculated equivalent vertical bulk moduli, c_{33}, (changed from 31.8 GPa to 31.7 GPa), and equivalent vertical shear moduli, c_{44}, (changed from 12 GPa to 12.3 GPa) are almost identical from one simulation to another. Relative errors between sonic logs and simulated velocities calculated with modified rock fabric parameters are still very low: the means are 3.6% for V_p, and 2.6% for V_s, respectively. In the vertical well, calculated velocities agree with sonic logs and estimated elastic properties seem accurate irrespective of the assumed rock fabric features. **Table 3.4** compares averaged entries of the stiffness tensors calculated for both sets of rock fabric parameters that are not invoked in the calculations of velocity of waves propagating in the vertical direction. Although entries of stiffness tensors are dissimilar, sonic logs cannot help determine which values are accurate. Therefore, if the decision for rock fabric parameters is entirely based on the agreement between simulated and measured sonic wave velocities, nothing indicates which values yield correct elastic properties, thus illustrating the non-uniqueness problem typical of effective medium theories.

However, as emphasized in **Figure 3.14**, the new rock physics model allows one to constrain values of rock fabric parameters. This new model shows the calculation of electrical resistivities in the vertical Well H1 based on the rock fabric properties shown in the last column of **Table 3.3**. As can be observed in track 3 of **Figure 3.14**, larger aspect ratios for porous cracks produce higher values of horizontal electrical resistivity and lower values of vertical electrical resistivity. Consequently, estimates of electrical resistivity do not match resistivity measurements (track 4), indicating that this choice of rock fabric parameters is inconsistent and leads to erroneous estimates of elastic properties.

3.4.2 Optimal Placement of Horizontal Wells

The rock physics model introduced in this dissertation produces accurate calculation of the entries of stiffness tensors of organic laminated shaly sandstones that are then used to estimate other elastic properties such as dynamic vertical and horizontal Young's moduli. However, static moduli are commonly used in wellbore stability and in-situ stress applications. Britt and Schoeffler (2009) found that prospective shales tend to fit the linear dynamic-to-static clastic correlations of Young's modulus. Prospective shales are characterized by clay content generally of less than 40% and Young's modulus in excess of 24.1 GPa. The shale formations studied in this dissertation agree with that description and, as a result, identification of best areas to drill a horizontal well can be based on the model's estimates of dynamic Young's moduli. Consequently, estimating elastic properties to locate zones characterized by such properties appears to effectively identify optimum depths along the vertical well trajectory where horizontal wells could be drilled to initiate hydraulic fracturing operations.

Estimates of elastic properties are used for calculation of stress concentration. Although Fairhurst's (1968) analytical solutions have been well established for more than four decades from a theoretical point of view, they have been rarely used in practice, probably because elastic anisotropic material properties are difficult to estimate. The new rock physics model overcomes that shortcoming by providing reliable elastic properties used as inputs in Fairhurst's model to calculate hoop stress around horizontal boreholes, and thereafter to estimate the pressures required to initiate hydraulic fracturing. I observe a correlation between ratios of horizontal to vertical Young's moduli and fracturing pressure: mud weight necessary to initiate hydraulic fracturing is lower in rocks with higher Young's moduli ratios. Therefore, in VTI formations such as laminated shales, horizontal wells should be drilled in depth segments that exhibit a high degree of anisotropy (which

is determined from the calculated elastic properties). Because brittle rocks (defined by high Young's moduli) are more suitable for hydraulic-fracture initiation and growth than are ductile rocks and on the basis of the above observations, I discuss the recommended depth zones for horizontal well placement along the vertical wells in the Haynesville and Barnett shale.

Figures 3.15 and **3.16** show vertical and horizontal Young's moduli as well as the ratio of horizontal to vertical Young's modulus calculated in the vertical portion of Well H1 and Well H2, respectively. In vertical Well H1, Young's modulus ratio reaches a maximum at xx812 ft (track 4) and the rock is brittle with vertical and horizontal Young's moduli above 30 GPa and 48 GPa, respectively (see track 3). The layer at xx761 ft exhibits a lower degree of anisotropy (Young's modulus ratio is around 1.52GPa) but is slightly stiffer (38 GPa and 52 GPa for E_v and E_h), and this layer is situated in the center of the gas-saturated interval. For these reasons, the layer located at xx761 ft should be targeted for horizontal well placement. Estimated clay concentration is higher in Well H2 than in Well H1. Therefore, concentration of aligned clay platelets and penny-shaped cracks associated with shale layers is more important. These characteristics explain the lower stiffness of that formation (refer to track 3 of **Figure 3.15**), and the greater degree of anisotropy (illustrated by larger ratio of horizontal to vertical Young's modulus, as shown on track 4 of **Figure 3.15)**. In Well H2, the recommended depth to drill a horizontal well is located at xx143 ft, in the middle of the gas-saturated organic zones where the rock is stiff and Young's modulus ratio is 1.6.

Figures 3.17 and **3.18** show Young's moduli and Young's modulus ratio estimated in the upper and lower section of Well B2, respectively. In the Barnett shale, there is a clear distinction between rock types. Rock types 1 and 2 are associated with high Young's modulus ratios. Rock type 3, identified by large calcite concentration, is characterized by

ratios close to 1, indicating that the rock is almost isotropic. For these reasons, rock types 1 and 2 are more suitable for hydraulic fracturing but are less stiff than rock type 3. Furthermore, rock type 1 is the most advantageous rock type in terms of hydrocarbon reserves. In upper Well B2, favorable depths to drill a horizontal well are thus found at x775 ft and x814 ft. These layers are some of the stiffest for rock type 1 ($E_v \geq 30\,\text{GPa}$ and $E_h \geq 35\,\text{GPa}$) while exhibiting Young's modulus ratios of between 1.3 and 1.4. The depth interval from x550 ft to x740 ft in the lower portion of Well B2 is the most profitable for production on account of high porosity, high gas saturation, and large volumetric concentration of organic matter. Potential horizontal wells should be drilled in the rock type 2 layers at x630 ft and x662 ft because of their position in the center of the gas-saturated interval, and the large vertical to horizontal Young's moduli ratio (1.38 and 1.3, respectively) and stiffness features ($E_v \geq 30\,\text{GPa}$ and $E_h \geq 35\,\text{GPa}$) that they exhibit.

3.5 CONCLUSIONS

I introduced a new simulation method that postulates a way to estimate rock fabric jointly from sonic and resistivity logs with a combination of effective medium theories. The joint model helps to determine rock fabric attributes that have an influence on elastic and electrical properties: percentage of percolating porosity and the shape of penny-shaped cracks. I demonstrated that obtaining a good fit between simulated and measured velocities, in particular in vertical wells, did not provide enough verification to prove that the elastic estimates were reliable. By adjusting rock fabric parameters such as the aspect ratio of cracks and solid grains, it is possible to reproduce measured wave velocities with relative errors between simulated velocities and sonic logs, consistently below 5%. This non-uniqueness of the solution is an inherent flaw of most effective medium theories that

required further examination and improvement. The introduction of a new calculated velocity, Stoneley-wave velocity, and the calculation of electrical resistivity effectively constrains the rock fabric parameters within the new model. The method helped to decrease the degree of non-uniqueness of solutions, hence contributing to the improved accuracy of the estimates of rock elastic properties.

Optimization of well trajectory depends on many factors including stress regime, rock mechanical property, stress and rock anisotropy, natural fracture orientations, etc. If the minimization of fracturing pressure is the objective pursued, I determined that in-situ stress anisotropy is the most relevant parameter to consider. However, if horizontal drilling is conducted in a region where the difference between minimum and maximum horizontal stress is small, rock anisotropy becomes a predominant component in the choice of well placement along a vertical well. Indeed, rocks with a high degree of anisotropy, expressed as ratio of horizontal to vertical Young's modulus, enhance the ability to initiate hydraulic stimulation. The joint sonic/electrical resistivity rock physics model I describe in this chapter is of great help in determining the degree of anisotropy in terms of elastic properties and can therefore be used to locate optimal depths to drill horizontal wells in highly laminated shale formations.

Vertical stress S_V	**Maximum horizontal stress** S_V	**Minimum horizontal stress** S_h	**Pore pressure** P_ϕ
1 psi.ft^{-1}	0.85 psi.ft^{-1}	0.75 psi.ft^{-1} / 0.83 psi.ft^{-1}	0.5 psi.ft^{-1}
22.6×10^3 Pa.m^{-1}	19.2×10^3 Pa.m^{-1}	17×10^3 Pa.m^{-1} / 18.8×10^3 Pa.m^{-1}	11.3×10^3 Pa.m^{-1}

Table 3.1: Gradients of in-situ stresses and pore pressure assumed for calculations of fracture initiation pressure (from Zoback, 2007).

Young's moduli		**Poisson's ratios**	
E_v (GPa)	20	ν_v	0.2
E_h (GPa)	20-40	ν_h	0.1-0.4

Table 3.2: Elastic properties assumed for investigation of the dependence of fracturing initiation pressure on rock elastic anisotropy.

	Validated rock fabric parameters	Modified rock fabric parameters
Aspect ratio of porous cracks	0.25	1
Aspect ratio of quartz/calcite grains	1	0.125
Averaged equivalent vertical bulk modulus (c_{33}) (GPa)	31.8	31.7
Averaged equivalent vertical shear modulus (c_{44}) (GPa)	12	12.3
Mean of relative error for V_p (%)	3.0	3.6
Mean of relative error for V_s (%)	2.2	2.6

Table 3.3: Illustration of non-uniqueness of solutions introduced by the use of effective medium theories in the rock physics model along the vertical portion of Well H1.

	Validated rock fabric parameters	Modified rock fabric parameters
Aspect ratio of porous cracks	0.25	1
Aspect ratio of quartz/calcite grains	1	0.125
Averaged c_{11} (GPa)	50.4	44.4
Averaged c_{12} (GPa)	11.9	9.9
Averaged c_{13} (GPa)	9.97	9.38
Averaged c_{66} (GPa)	19.3	17.3

Table 3.4: Averaged entries of stiffness tensors non-invoked in the calculation of vertical velocities obtained for two distinct sets of rock fabric parameters along the vertical portion of Well H1.

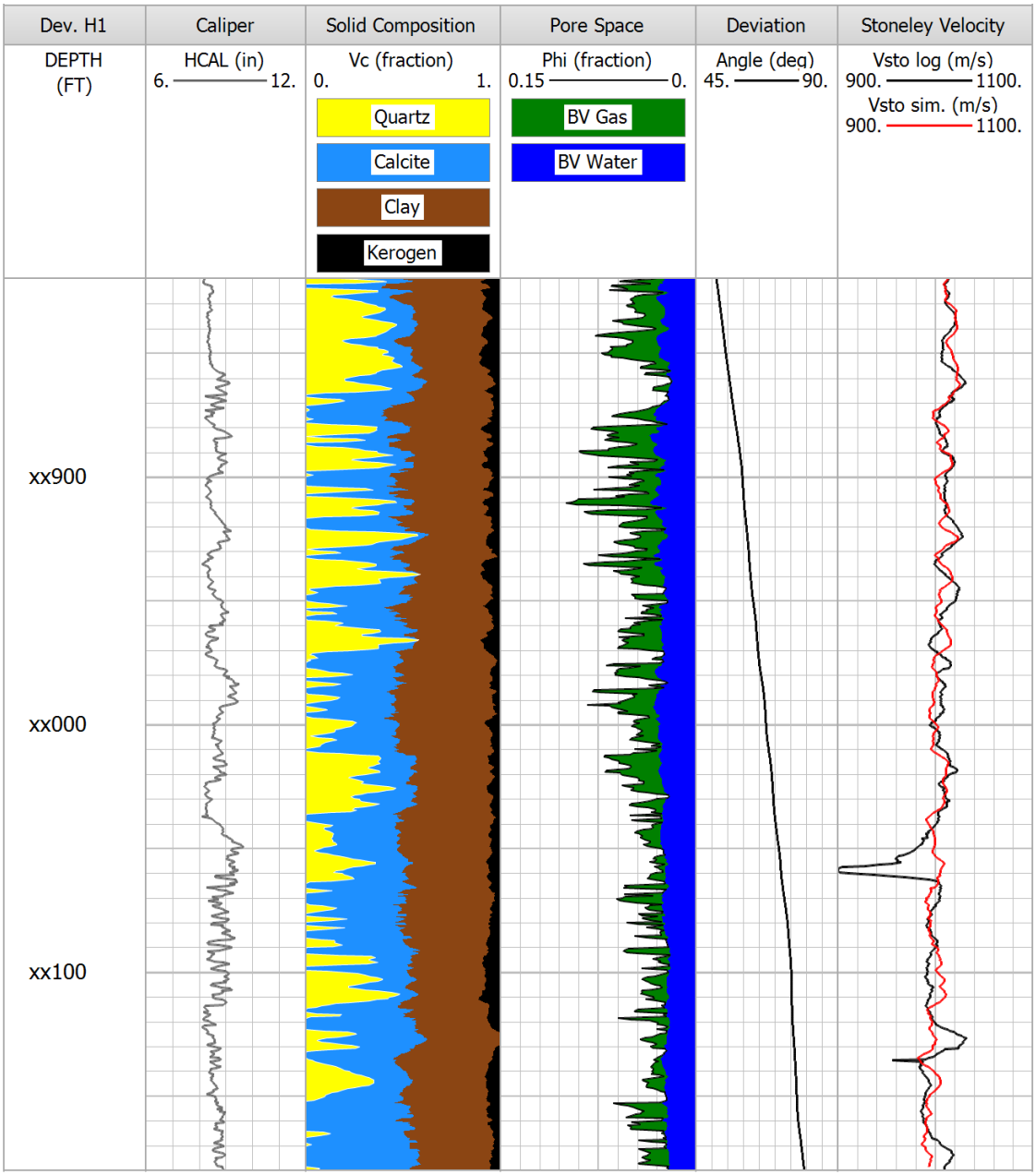

Figure 3.1: Stoneley velocity estimation in deviated Well H1. Track 1: Caliper. Track 2: solid composition. Track 3: porosity and bulk volume of fluids. Track 4: deviation angle. Track 5: Stoneley velocity. In track 5, the black curve identifies measured velocity and the red curve identifies calculated velocity.

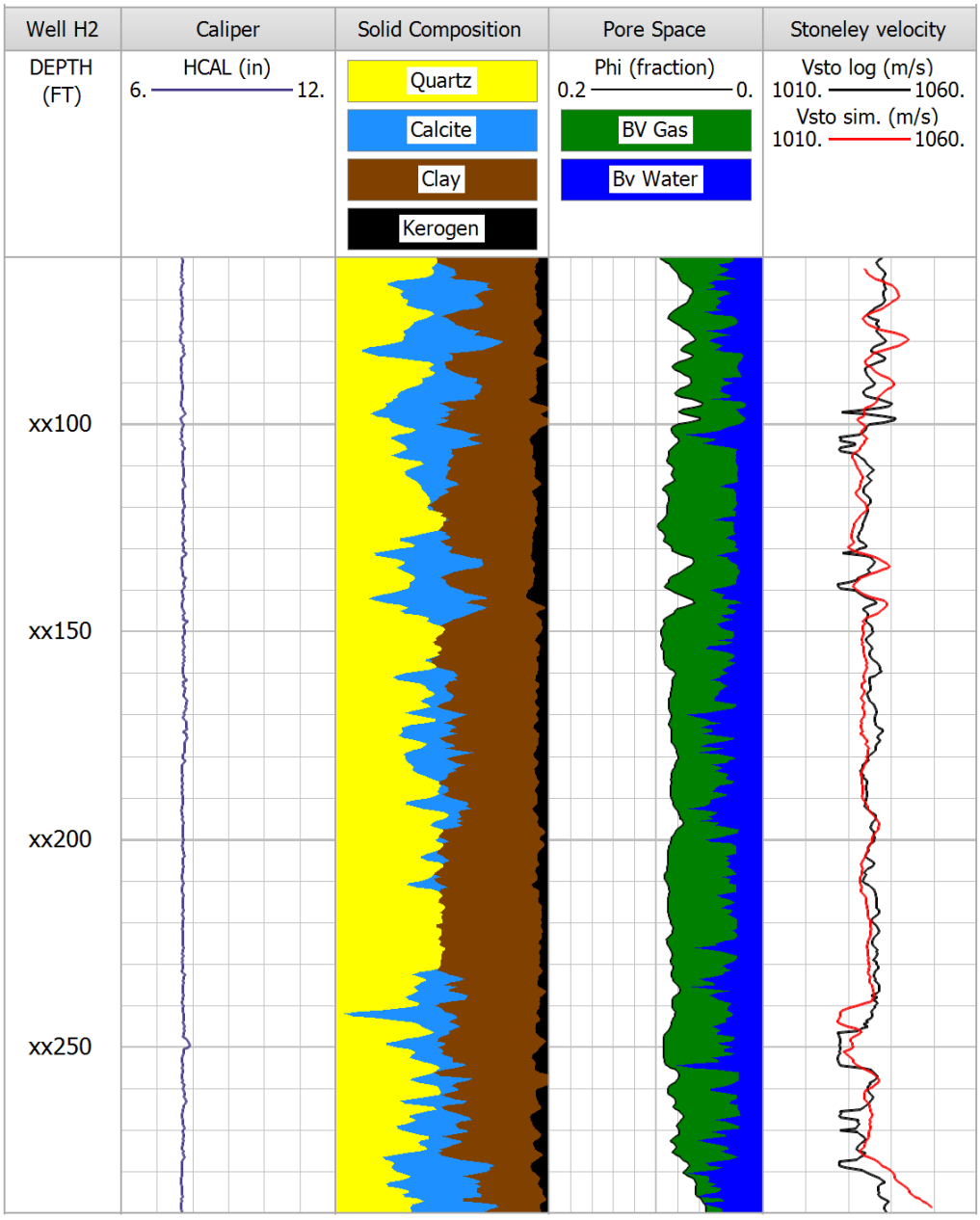

Figure 3.2: Stoneley velocity estimation in Well H2. Track 1: Caliper. Track 2: solid composition. Track 3: porosity and bulk volume of fluids. Track 4: Stoneley velocity. In track 4, the black curve identifies measured velocity and the red curve identifies calculated velocity.

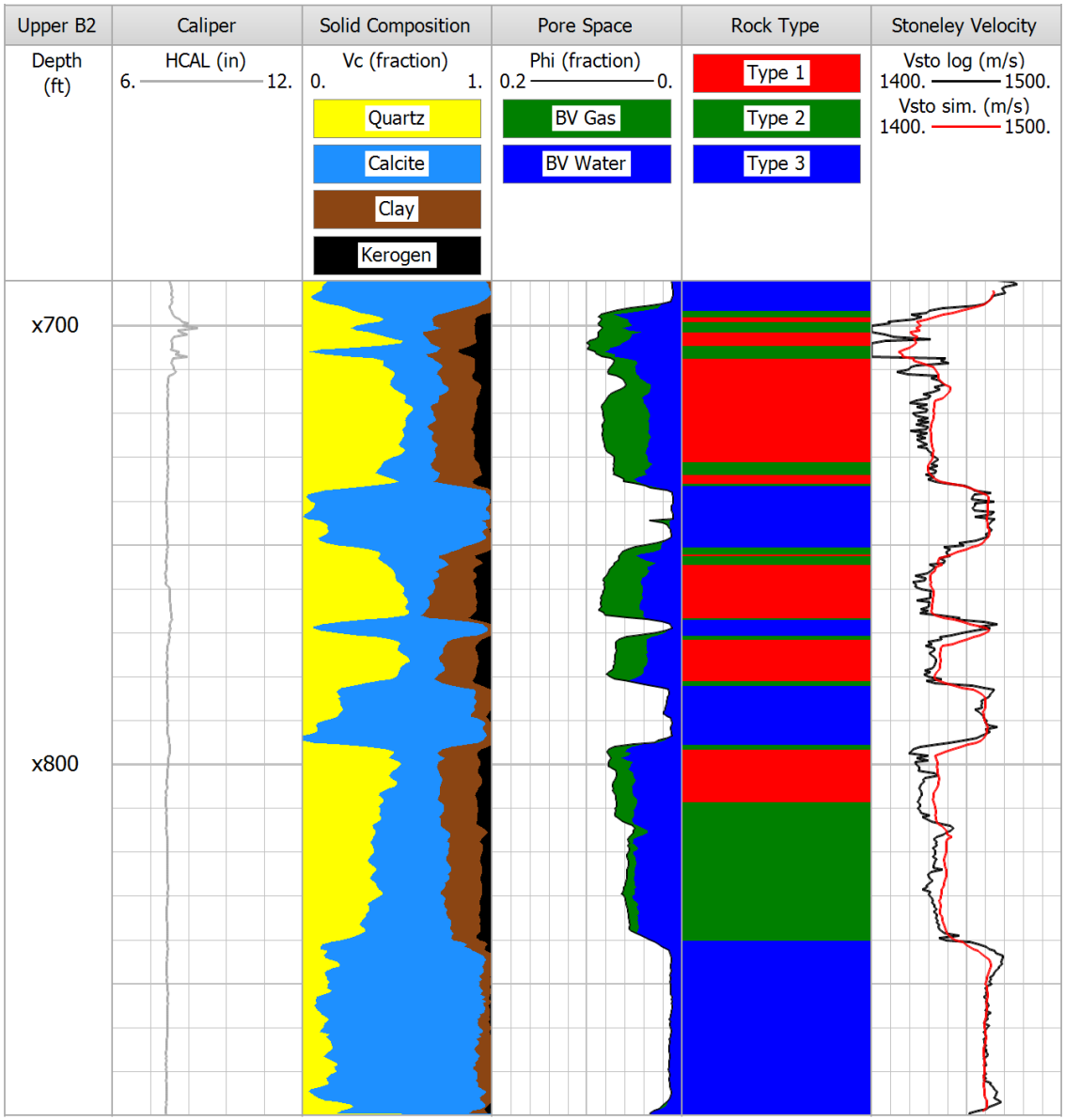

Figure 3.3: Stoneley velocity estimation in the upper section of Well B2. Track 1: Caliper. Track 2: solid composition. Track 3: porosity and bulk volume of fluids. Track 4: rock types. Track 5: Stoneley velocity. In track 5, the black curve identifies measured velocity and the red curve identifies calculated velocity.

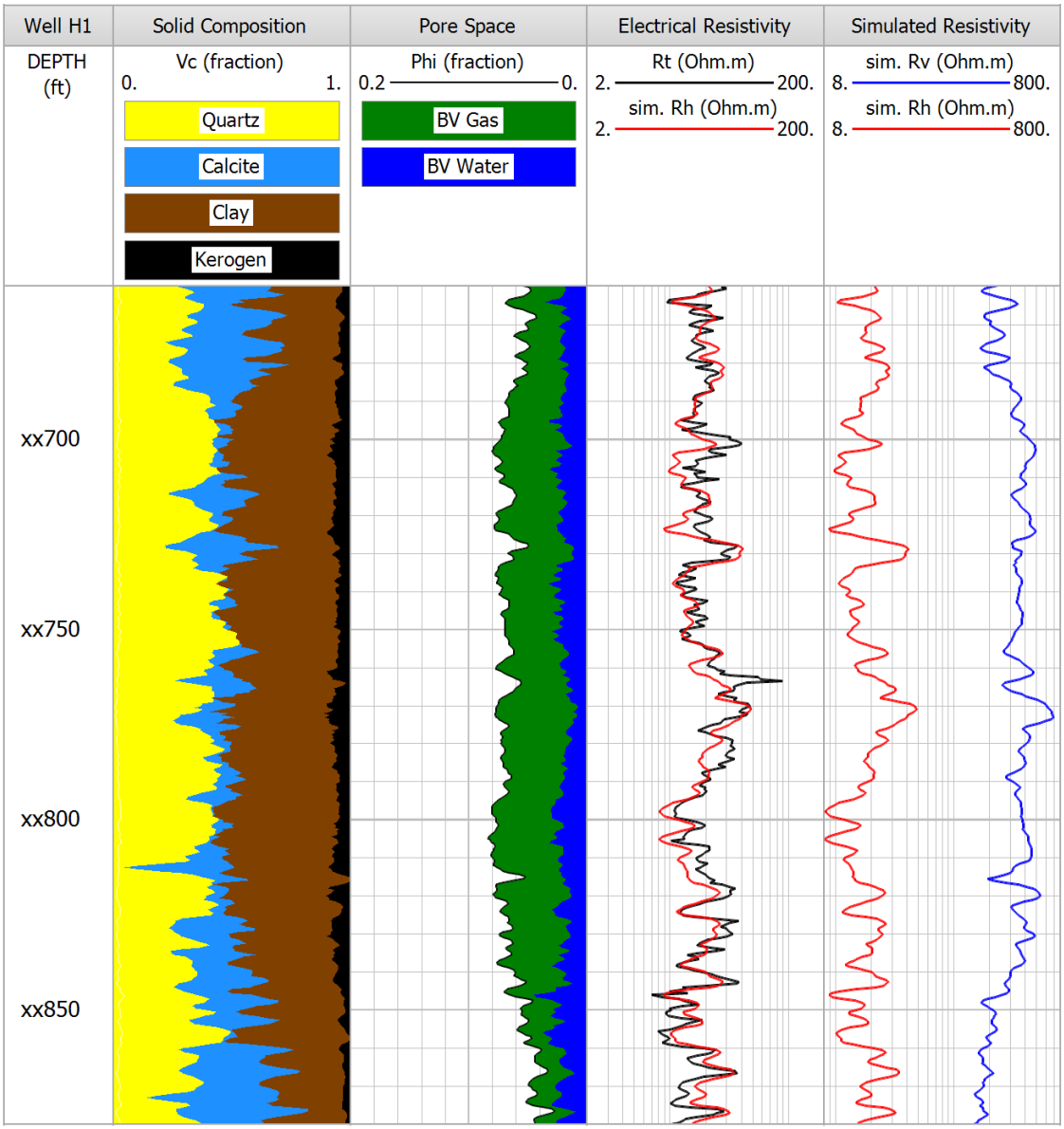

Figure 3.4: Electrical resistivity estimation in Well H1. Track 1: solid composition. Track 2: porosity and bulk volume of fluids. Track 3: deep electrical resistivity. In track 3, black and red curves identify measured and calculated deep resistivity, respectively. Track 4: vertical and horizontal electrical resistivity. In track 4, blue and red curves identify vertical and horizontal resistivity, respectively.

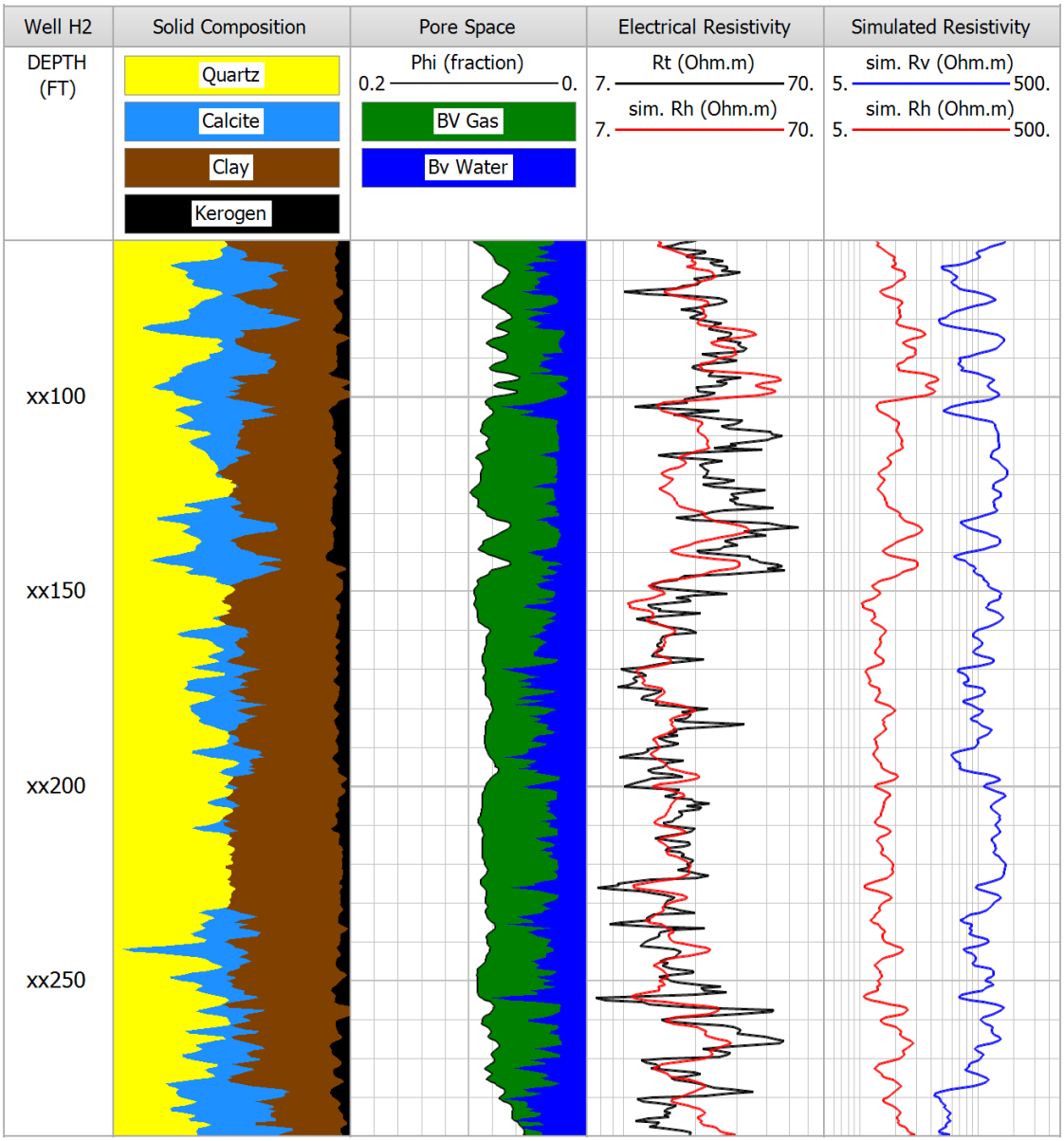

Figure 3.5: Electrical resistivity estimation in Well H2. Track 1: solid composition. Track 2: porosity and bulk volume of fluids. Track 3: deep electrical resistivity. In track 3, black and red curves identify measured and calculated deep resistivity, respectively. Track 4: vertical and horizontal electrical resistivity. In track 4, blue and red curves identify vertical and horizontal resistivity, respectively.

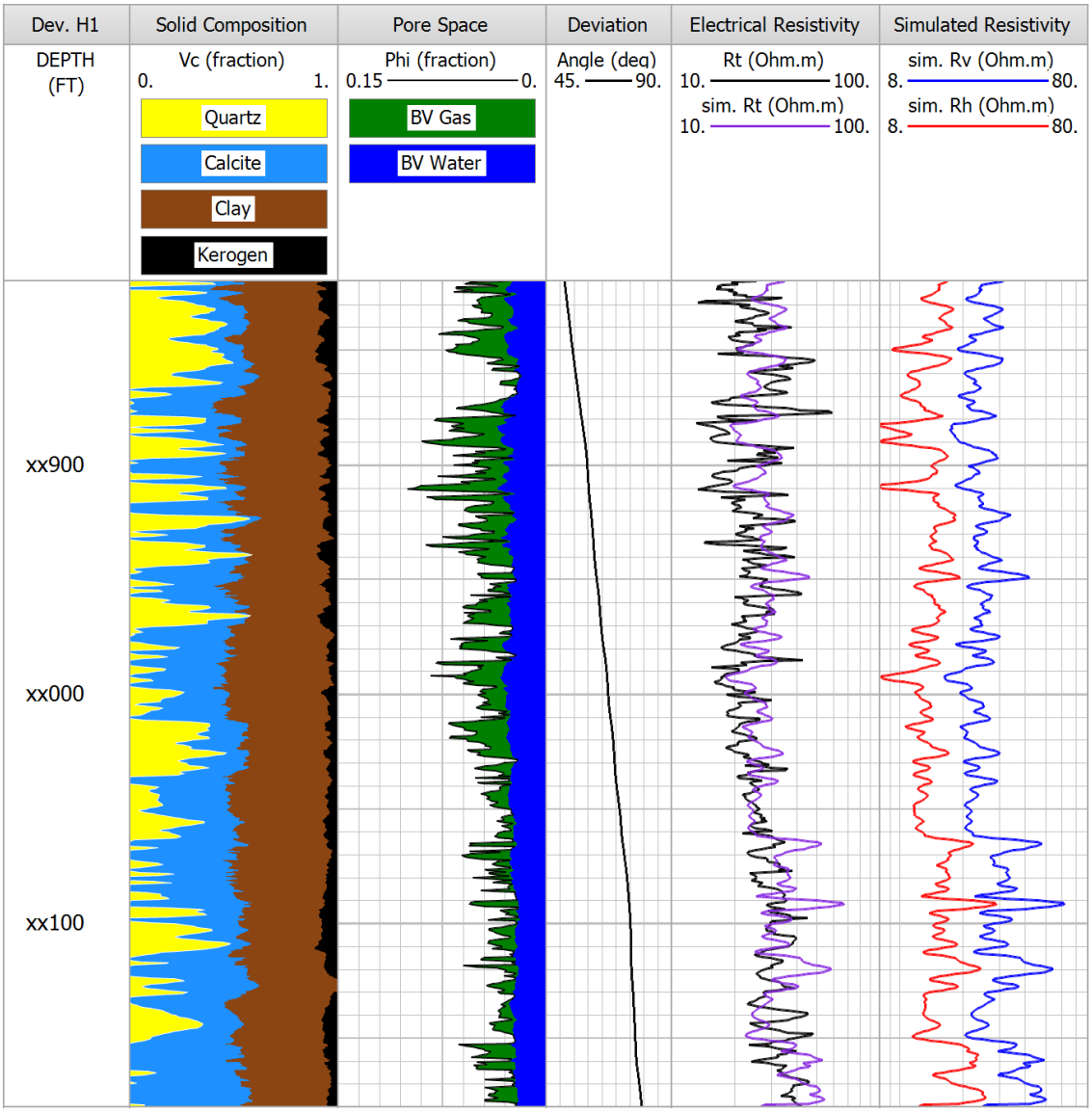

Figure 3.6. Electrical resistivity estimation in deviated Well H1. Track 1: solid composition. Track 2: porosity and bulk volume of fluids. Track 3: deviation angle. Track 4: deep electrical resistivity. In track 4 black and magenta curves identify measured and calculated deep resistivity, respectively. Track 5: vertical and horizontal electrical resistivity. In track 5, blue and red curves identify vertical and horizontal resistivity, respectively.

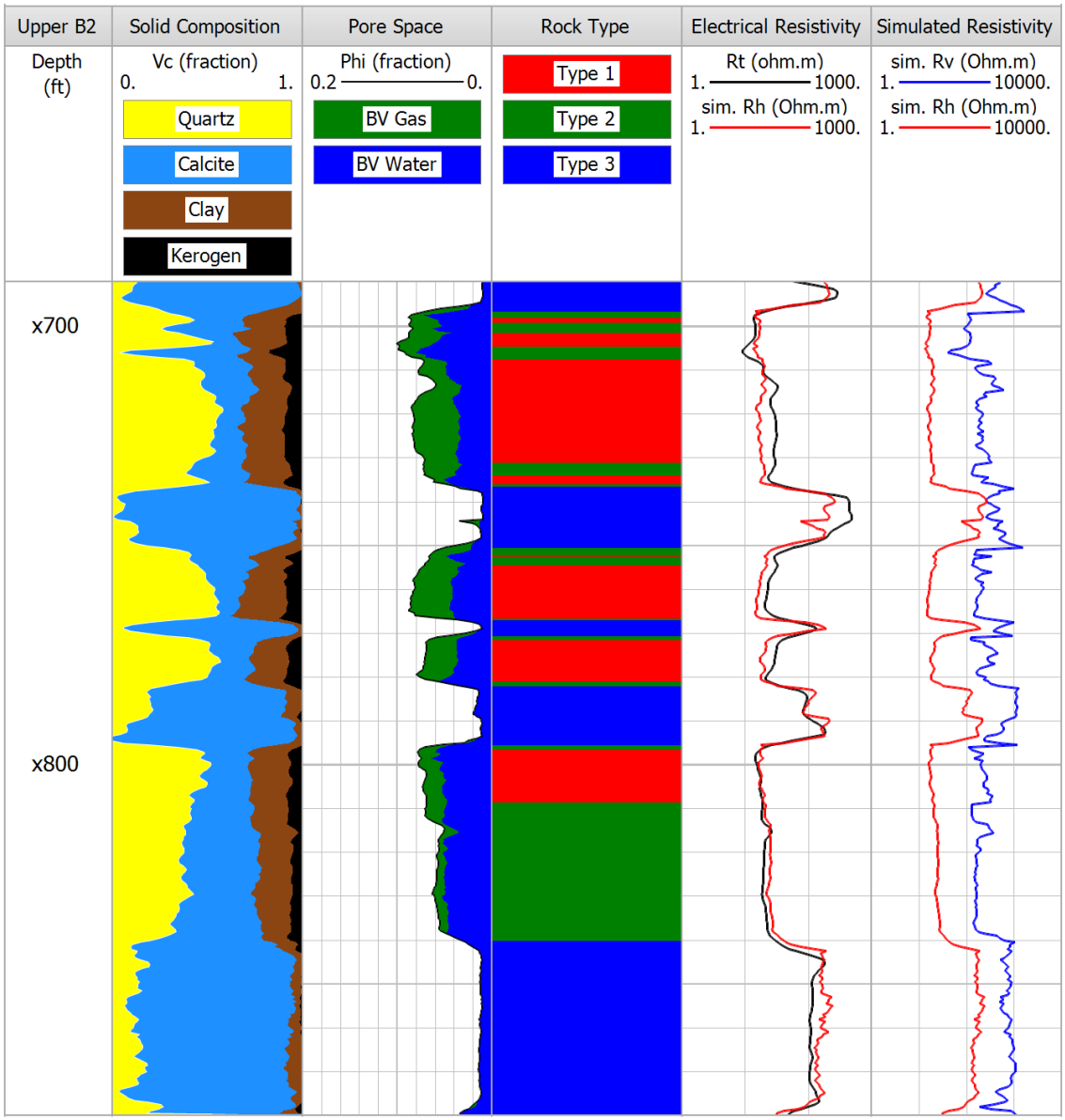

Figure 3.7: Electrical resistivity estimation in the upper section of Well B2. Track 1: solid composition. Track 2: porosity and bulk volume of fluids. Track 3: rock types. Track 4: deep electrical resistivity. In Track 4, black and red curves identify measured and calculated deep resistivity, respectively. Track 5: vertical and horizontal electrical resistivity. In Track 5, blue and red curves identify vertical and horizontal resistivity, respectively.

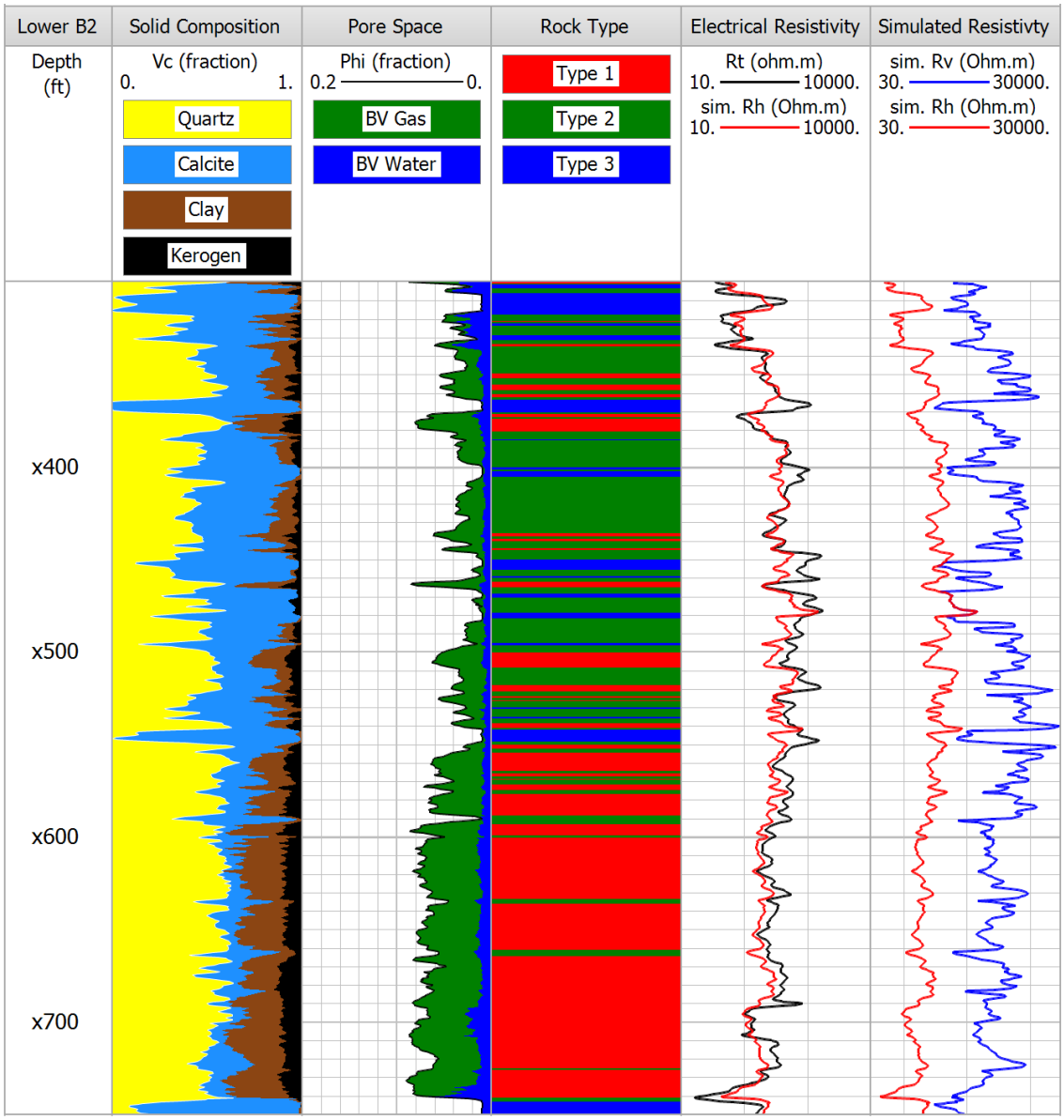

Figure 3.8: Electrical resistivity estimation in the lower section of Well B2. Track 1: solid composition. Track 2: porosity and bulk volume of fluids. Track 3: rock types. Track 4: deep electrical resistivity. In Track 4, black and red curves identify measured and calculated deep resistivity, respectively. Track 5: vertical and horizontal electrical resistivity. In Track 5, blue and red curves identify vertical and horizontal resistivity, respectively.

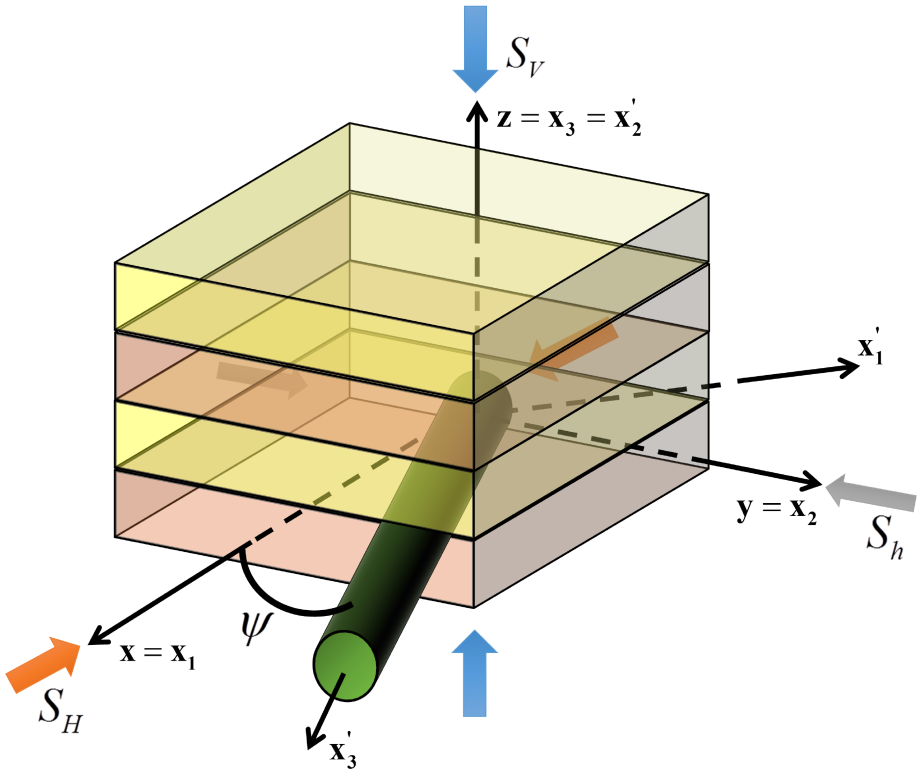

Figure 3.9: Position of the horizontal well with respect to in-situ stress and VTI formation coordinate system. S_V is the vertical stress, S_H is the maximum horizontal stress, and S_h is the minimum horizontal stress. $(\mathbf{x}, \mathbf{y}, \mathbf{z})$ are the coordinates of the principal stresses, $(\mathbf{x}_1, \mathbf{x}_2, \mathbf{x}_3)$ are the coordinates of the VTI material, and $(\mathbf{x}_1', \mathbf{x}_2', \mathbf{x}_3')$ are the coordinates associated with the horizontal well.

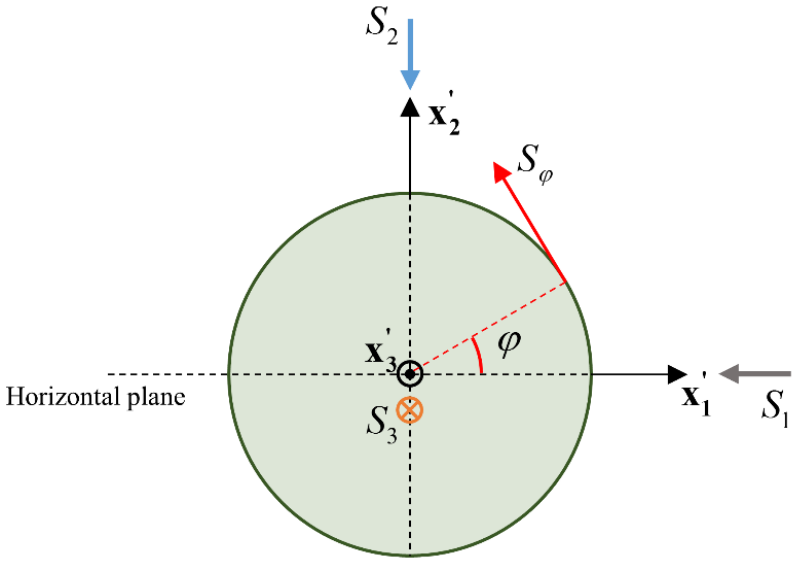

Figure 3.10: Orientation of in-situ stress expressed in the wellbore coordinate system and hoop stress exerted around the wellbore. φ is the angle around the horizontal wellbore from the horizontal plane.

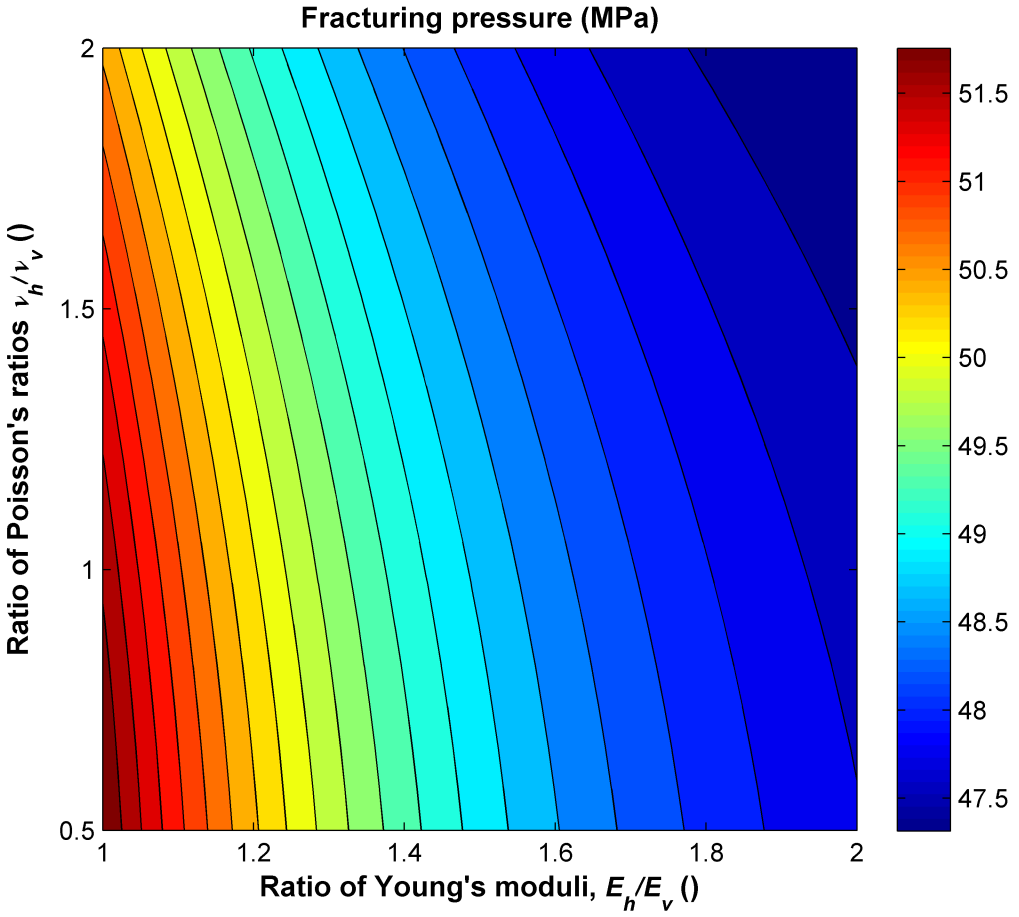

Figure 3.11: Dependence of fracture initiation pressure on degree of elastic anisotropy for a horizontal well drilled in the direction of maximum horizontal stress in in-situ stress conditions described in Table 3.1.

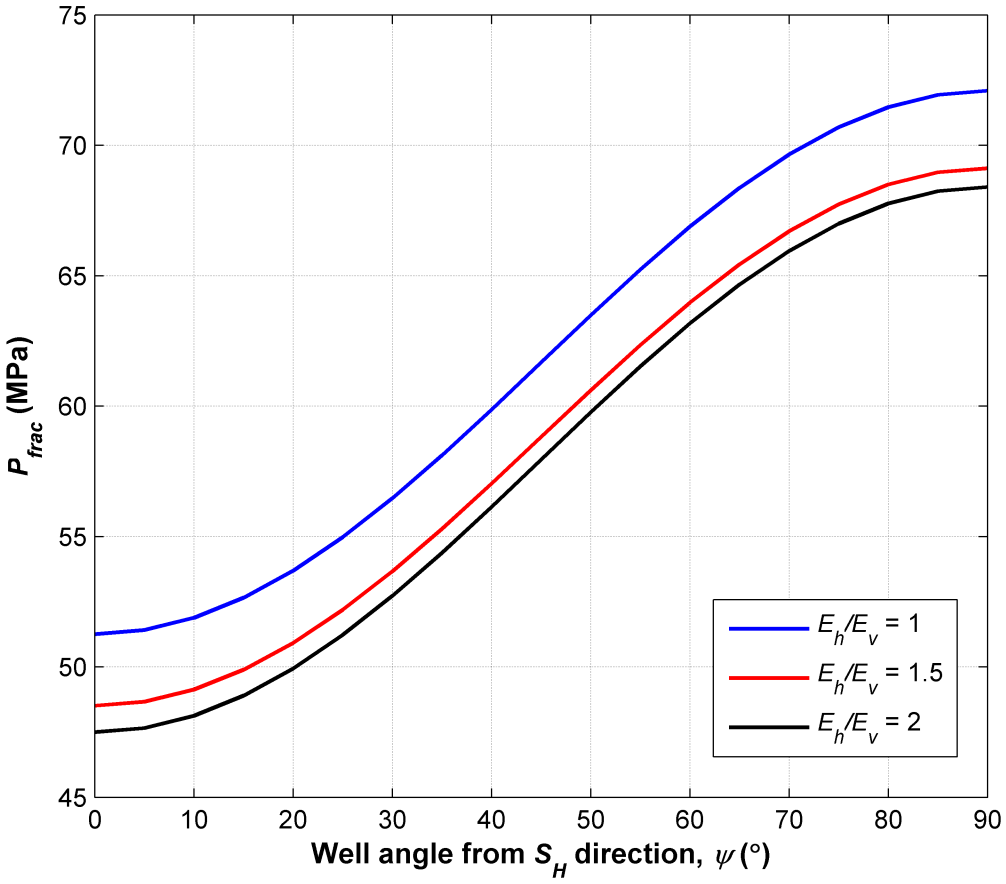

Figure 3.12: Dependence of fracture initiation pressure on ratio of horizontal to vertical Young's modulus and well orientation with respect to direction of maximum horizontal stress for in-situ stress conditions described in Table 3.1.

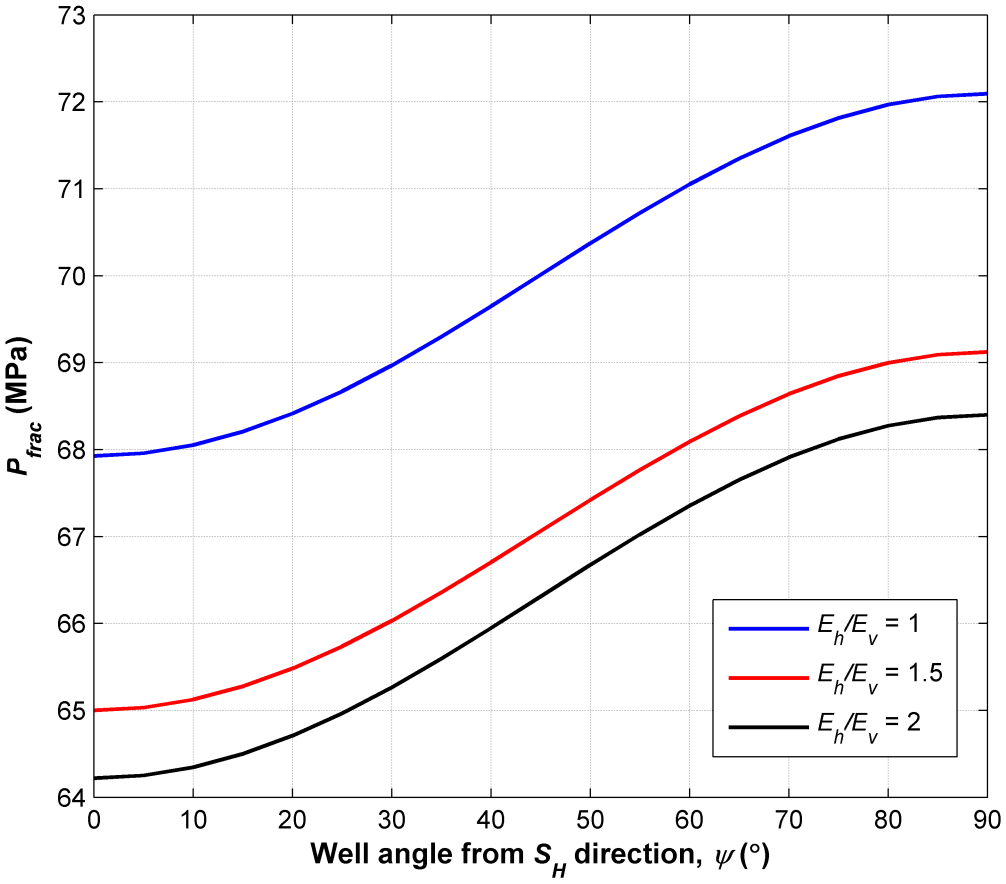

Figure 3.13: Dependence of fracture initiation pressure on ratio of horizontal to vertical Young's modulus and well orientation with respect to direction of maximum horizontal stress. Simulations are performed for in-situ stress conditions described in Table 3.1 where minimum horizontal stress is changed to 18.8 $kPa.m^{-1}$.

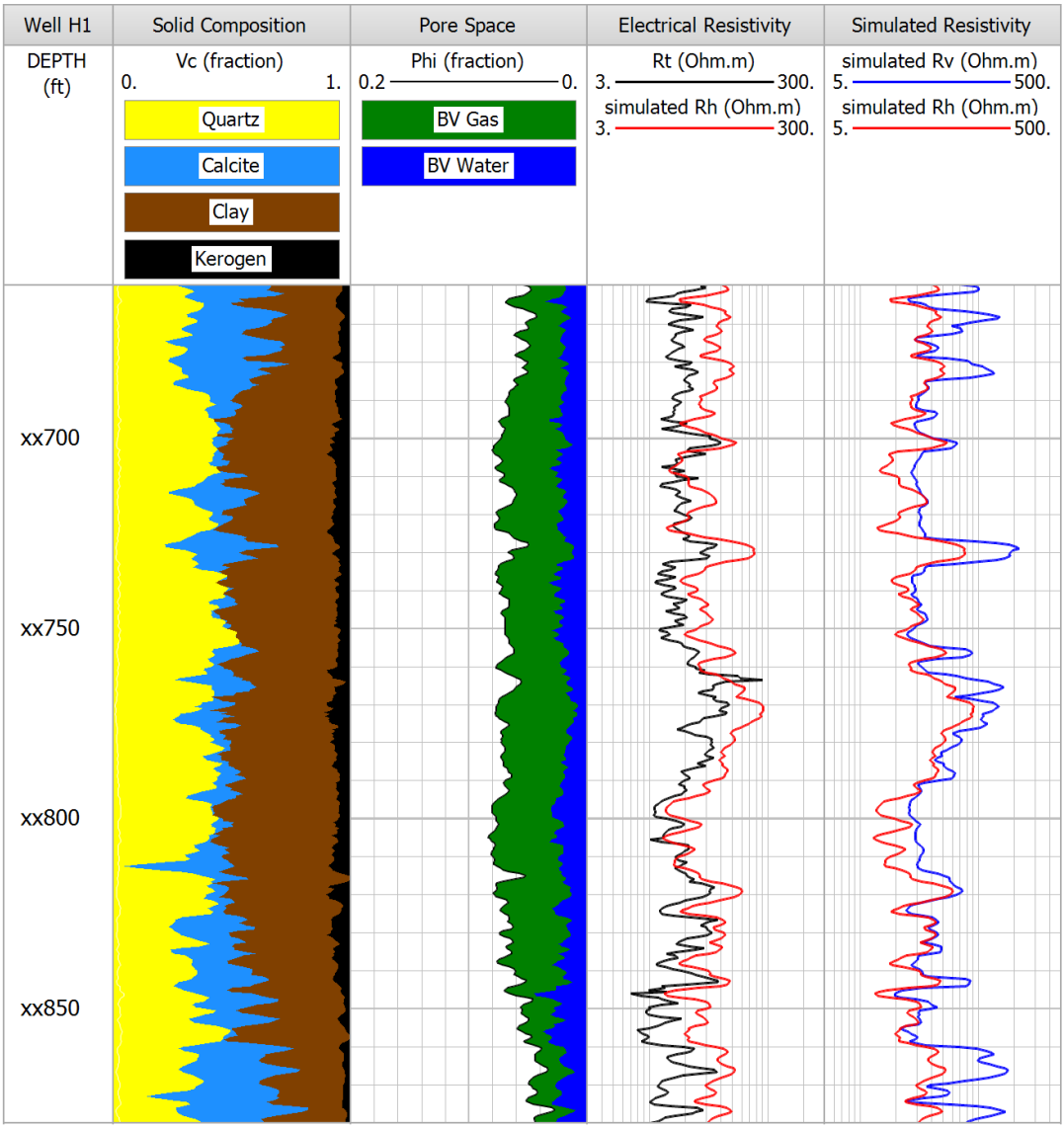

Figure 3.14: Illustration of the limitation of non-uniqueness with the joint sonic/electrical resistivity rock physics model with the estimation of electrical resistivity in the vertical portion of Well H1. The choice of rock fabric parameters that led to a good fit between simulated velocities and sonic logs, as shown in Table 3.3, produces erroneous calculations of electrical resistivities. Track 1: solid composition. Track 2: porosity and bulk volume of fluids. Track 3: deep electrical resistivity. In Track 3, black and red curves identify measured and calculated deep resistivity, respectively. Track 4: vertical and horizontal electrical resistivity. In Track 4, blue and the red curves identify vertical and horizontal resistivity, respectively.

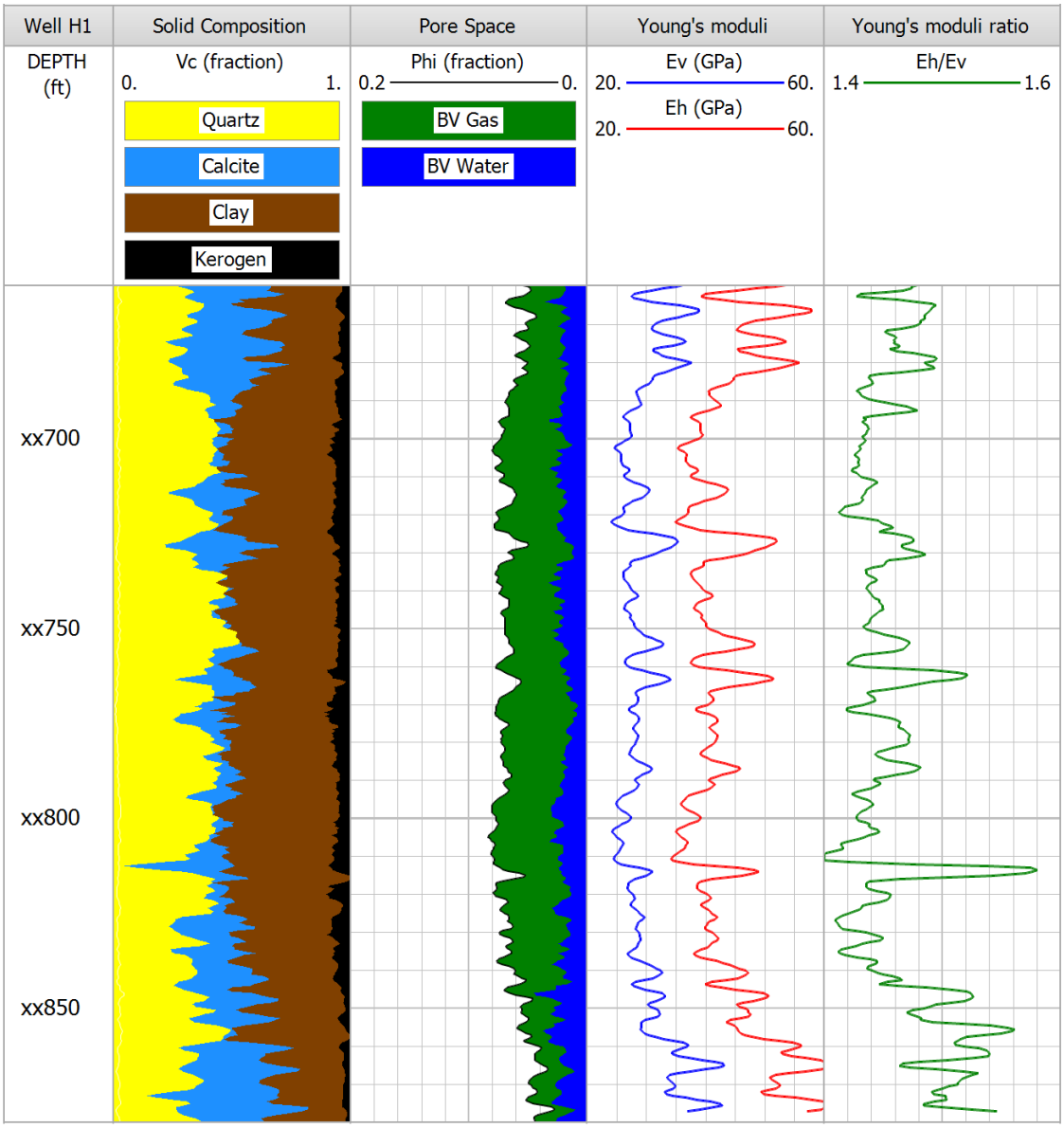

Figure 3.15: Young's moduli calculation in the vertical portion of Well H1. Track 1: solid composition. Track 2: porosity and bulk volume of fluids. Track 3: vertical and horizontal Young's modulus. Track 4: ratio of horizontal to vertical Young's modulus.

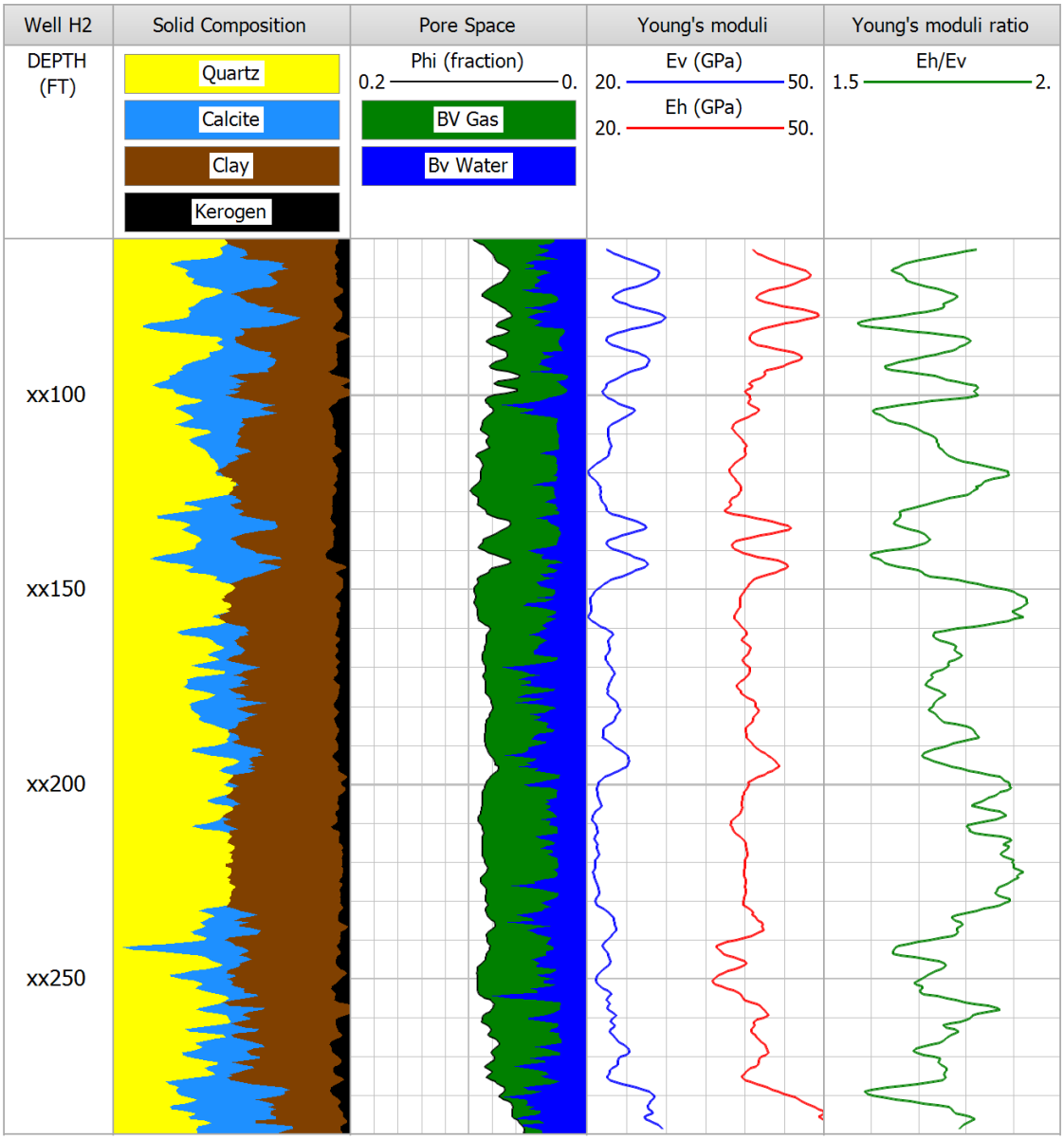

Figure 3.16: Young's moduli calculation in Well H2. Track 1: solid composition. Track 2: porosity and bulk volume of fluids. Track 3: vertical and horizontal Young's modulus. Track 4: ratio of horizontal to vertical Young's modulus.

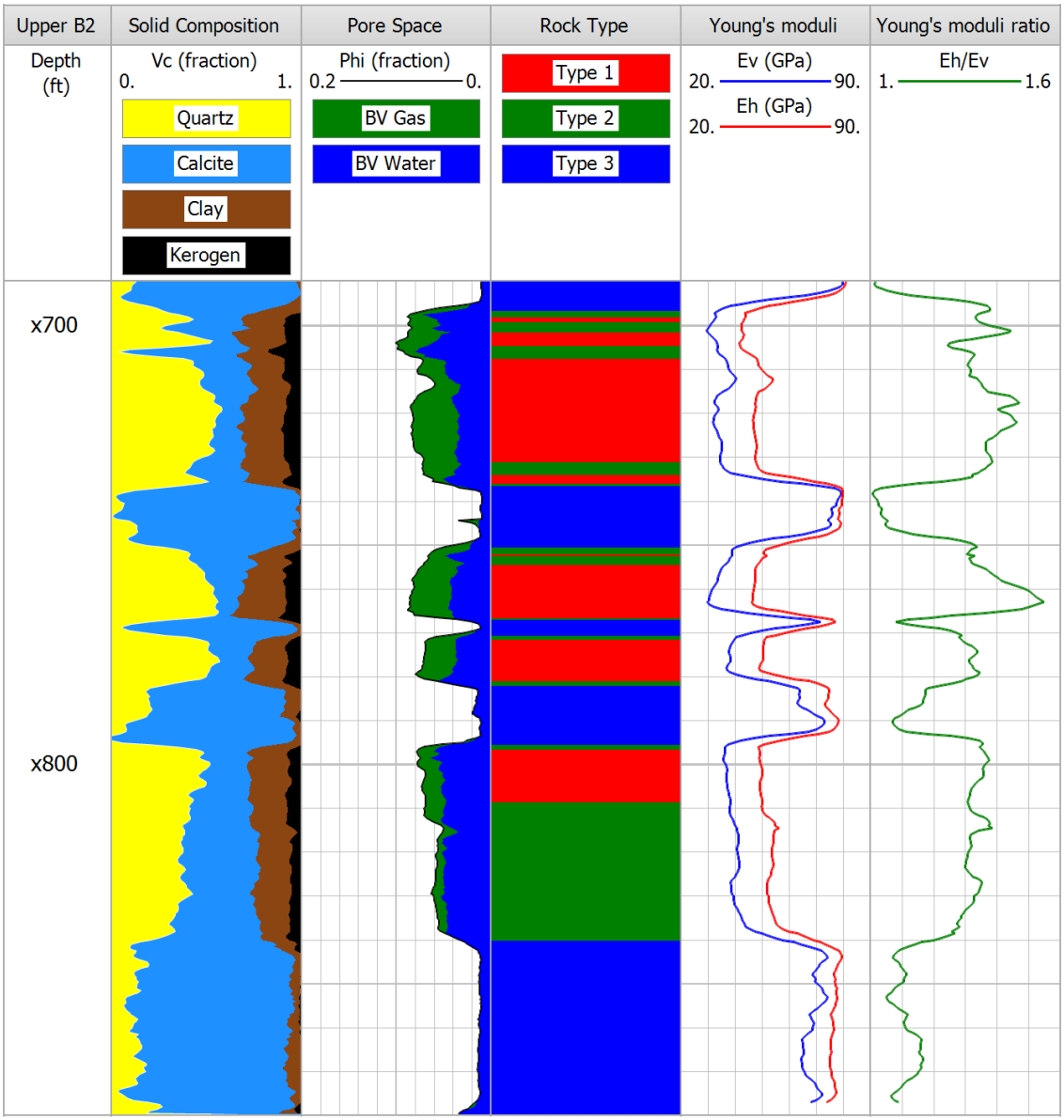

Figure 3.17: Young's moduli calculation in the upper section of Well B2. Track 1: solid composition. Track 2: porosity and bulk volume of fluids. Track 3: rock types. Type 4: vertical and horizontal Young's modulus. Track 5: ratio of horizontal to vertical Young's modulus.

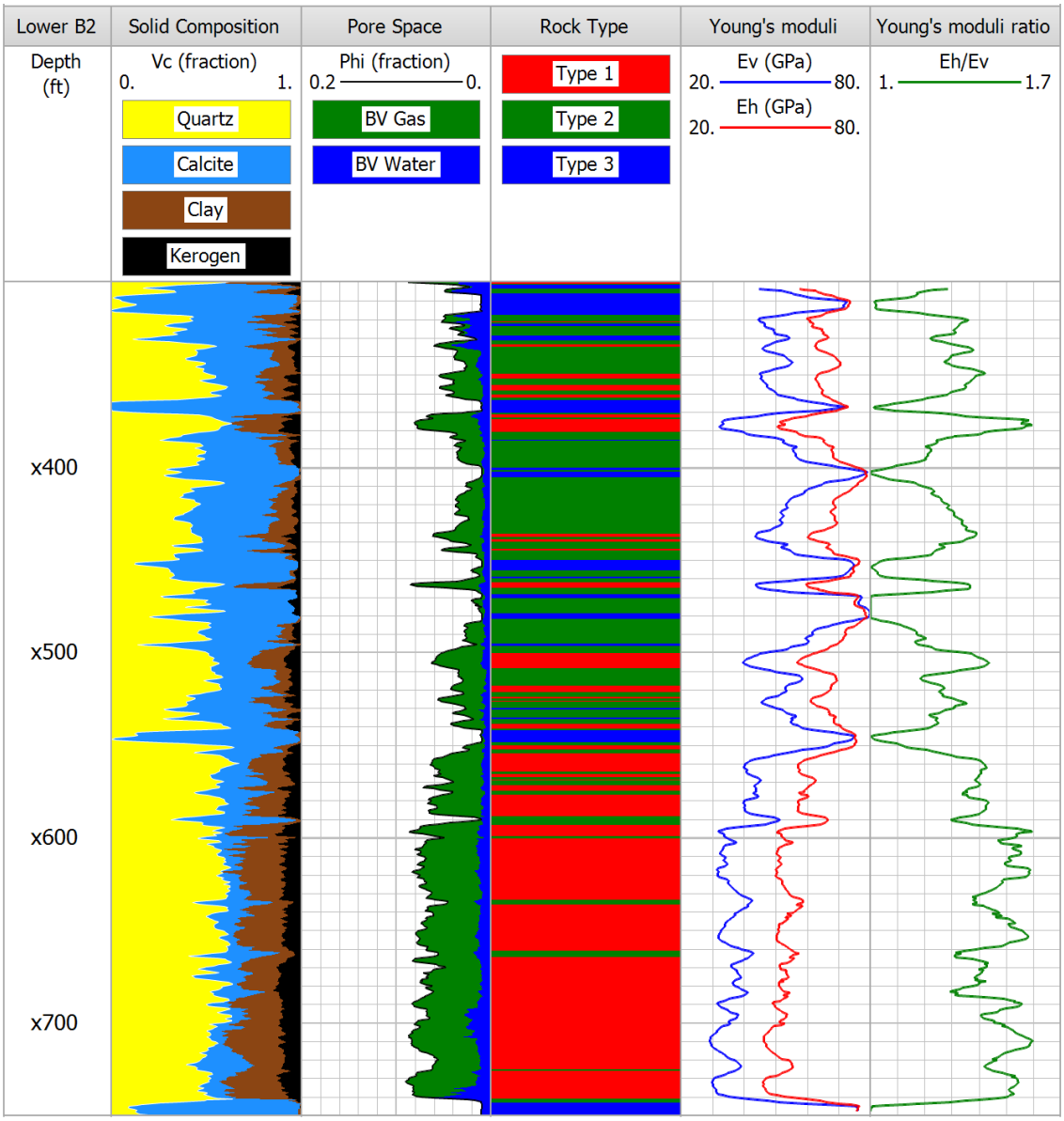

Figure 3.18: Young's moduli calculation in the lower section of Well B2. Track 1: solid composition. Track 2: porosity and bulk volume of fluids. Track 3: rock types. Type 4: vertical and horizontal Young's modulus. Track 5: ratio of horizontal to vertical Young's modulus.

Chapter 4: Reproduction of Fluid-Related Wave Dispersion and Attenuation Mechanisms with Effective Medium Models

Wave-induced flow of fluid inside the porous space of rocks is responsible for large dispersion and attenuation effects. One of the resulting interactions between fluid and solid, referred to as Biot's flow or global flow, is caused by pressure gradients at the scale of the acoustic wavelength and mainly controlled by the permeability of the rock. Another fluid-flow-related mechanism of dispersion, often called local flow or squirt flow, is based upon microscopic fluid motion in which fluid is squeezed out of grain contacts into nearby pores or between adjacent cracks having different orientations. This chapter describes two new effective medium (EM) models that reproduce both causes of dispersion and attenuation of waves propagating in fluid-saturated isotropic rocks. Strengthening of rocks and increase of wave velocities observed at high frequencies are modeled by introducing the concept of complex-valued and frequency-dependent equivalent moduli for the solid background. Complex-valued and frequency-dependent effective moduli of the mixture are calculated by invoking the newly defined dynamic solid moduli into the self-consistent approximation theory. Effective properties are utilized to estimate compressional- and shear-wave velocities that exhibit dispersive behavior. Both new effective medium models are tested and verified by varying main input parameters and plotting obtained velocity and attenuation curves against results predicted by previously validated theories for Biot's and squirt flow. A procedure is devised to efficiently account for the combined influence of the two fluid-related causes of dispersions in isotropic rocks with a joint effective medium model. Consideration is given to the possibility of quantifying key rock properties with the reproduction of combined dispersion phenomena.

4.1 INTRODUCTION

Acoustic properties of most rocks depend greatly on wave-induced flow of fluids contained within the pore space. For that reason, fluid-saturated rocks should be described as poroelastic media. The behavior of waves that propagate within a poroelastic composite differs significantly from that within a purely elastic one, as they are subject to dispersion and attenuation over a wide range of frequencies. Classical elastic effective medium theories are static and fail to take into account fluid-related dispersion and attenuation phenomena that cannot be neglected in fluid-saturated rocks exhibiting sufficiently high porosity (Tod, 2003). New simple and practical schemes are introduced in this chapter for effective medium modeling that incorporate dispersion mechanisms due to fluid flow inside the pore space.

Velocity is affected by two main fluid-related modes in waves propagating in fluid-saturated rocks (Dvorkin and Nur, 1993): Biot or global flow, caused by pressure gradients at the scale of the wavelength, and squirt or local flow, generated by pressure gradients at the scale of the microstructure.

Biot (1956a, 1956b, 1962) derived theoretical formulas for predicting the frequency-dependent velocities of saturated rocks in terms of rock frame features. His formulation incorporates mechanisms of viscous and inertial interaction between the pore fluid and the solid matrix of the rock, and his method has been the support of most investigations of wave speed dispersion in fluid-saturated rocks. At low frequencies, pore fluid and solid are assumed to be moving in phase, attenuation is minimal, and asymptotic velocities are the same as predicted by Gassmann's relations (Gassmann, 1951). At high frequencies, the fluid and mineral matrix are essentially decoupled, velocity is at a maximum and attenuation is low. However, at intermediate frequencies, velocity dispersion occurs and attenuation is at its peak. There are four basic assumptions of Biot's

equations of poroelasticity (Müller et al., 2010). First, the frame of the rock is homogeneous and isotropic. It exhibits uniform porosity, bulk modulus, shear modulus, density, and permeability. The mineral background is made of only one grain type, characterized by diameter, bulk modulus, shear modulus, and density. Second, the rock is fully saturated by only one fluid defined by its shear viscosity, bulk modulus, and density. Third, relative motion between solid and fluid is governed by Darcy's law. And last, the wavelength of the propagating wave is substantially larger than the size of the largest grains or pores.

Biot's theory of poroelasticity enjoys strong experimental support but still is not adequate to describe wave attenuation and dispersion in some cases. Another theory, first proposed by Mavko and Nur (1975), assumes that a propagating wave may induce pore-pressure gradients, thus fluid flow, at a microscopic scale. The theory, referred to as local flow or squirt flow, can predict large velocity dispersion in some rocks where Biot's theory underestimates it. A second problem with Biot's theory is the prediction of velocities decreasing with increasing fluid viscosity when experiments tend to show the opposite (Jones and Nur, 1983; Jones, 1986). Squirt flow theory predicts that velocity increases with increasing fluid viscosity. Squirt flow behavior has since been addressed theoretically in many studies (O'Connell and Budiansky, 1977; Mavko and Jizba, 1991; Dvorkin and Nur, 1993; Dvorkin et al., 1995; Hudson et al., 1996; Pride et al., 2004). Squirt flow is often described as the compression of compliant cracks by passing waves, with an ensuing flow of fluid into adjacent stiffer pores or cracks of different orientations. Until recently, Biot's and squirt flow phenomena had traditionally been treated separately. However, Biot's and squirt flow dispersion mechanisms are intimately interconnected by the pore fluid; a consistent poroelasticity theory should consider both mechanisms simultaneously (Dvorkin et al., 1994).

In this chapter, I describe two previously established fluid-related dispersion theories that approximate effects of Biot's flow and squirt flow, respectively based on Biot's (1956a, 1956b) and Chapman et al.'s (2006) equations. Several errors in Chapman et al.'s (2006) original formulas were found, and their corrected versions are presented below. I introduce new semi-empirical effective medium schemes built on the isotropic version of Wu's (1966) self-consistent approximation that accurately reproduce the results predicted by both dispersion theories. The models are based on the novel definition of frequency-dependent equivalent solid bulk and shear moduli, calculated separately for incident compressional and shear waves, and for which I define explicit equations. When equal to the static moduli of minerals that compose the matrix of a rock at low frequencies, dynamic moduli of the mineral background become complex-valued at higher frequencies, and their absolute value increases. Frequency-dependent solid moduli are used as elastic properties of the matrix material in which fluid-filled porous inclusions are then added with the simple self-consistent approximation. Resulting elastic properties of the saturated medium display behavior that also varies with frequency. They are then invoked to compute P- and S-wave velocities affected by Biot's and squirt flow effects.

The original models and their matching effective medium methods are applied to several synthetic examples to consider the effects of different properties on velocity behavior for each type of flow. The accuracy of frequency-dependent velocities calculated with the new effective medium theories is also validated in this manner. By constructing both methods with a combination of dynamic equivalent grain moduli and the simple SCA, a joint scheme for Biot/squirt flow is readily formulated and subsequently tested on synthetic cases.

4.2 MODELING OF BIOT'S FLOW MECHANISM

This section describes Biot's complete frequency-dependent velocity relations as well as my model developed to simulate Biot's flow mechanism for homogeneous isotropic fluid-saturated rocks. I assume the medium to exhibit a dual porosity distribution consisting of idealized spherical pores exhibiting uniform diameter and penny-shaped cracks with all cracks having the same length and aspect ratio. Cracks are randomly-oriented, thus ensuring that the composite remains isotropic. The background of the rock is composed of a homogeneous mixture of quartz, calcite, and clay varying in concentration, and solid grains are assumed to be spherical. All petrophysical inputs of Biot's (1956a, 1956b) equations are incorporated into the new effective medium theory. First, a low-frequency limiting case is defined using the static self-consistent approximation theory and serves as basis for velocity calculations performed with both Biot's relations and my model at the low-frequency limit. Next, frequency-dependent and complex-valued equivalent solid moduli are calculated by modifying Biot's equations with the addition of correction functions depending on static elastic characteristics of solids and fluid making up the rock. At the low-frequency limit, the frequency-dependent solid moduli tend to their mineral value. Two distinct dynamic bulk moduli are defined, as well as one dynamic solid shear modulus. Finally, the classical self-consistent approximation is invoked to compute complex-valued frequency-dependent elastic moduli of the saturated rock. The dynamic solid moduli are incorporated into the isotropic SCA theory as elastic properties of the background of the effective medium. **Figure 4.1** describes the three main steps of the new model.

4.2.1 Biot's Velocity Relations

The complete frequency dependence of Biot compressional and shear waves is obtained from the roots of dispersion equations (Biot, 1956a, 1956b; Stoll, 1977;

Berryman, 1980a). The complex roots then yield the following expressions for Biot's compressional and shear waves:

$$V_p^{Bi} = \left[\frac{1}{2\left(C^2 - MH\right)} \left(-\left(Hq + M\rho - 2C\rho_{fl} \right) + \sqrt{\left(Hq + M\rho - 2C\rho_{fl} \right)^2 - 4\left(C^2 - MH \right)\left(\rho_{fl}^2 - \rho q \right)} \right) \right]^{-1/2}, \tag{4.1}$$

and

$$V_s^{Bi} = \left(\frac{q\rho - \rho_{fl}^2}{q\mu_{fr}} \right)^{-1/2}, \tag{4.2}$$

where μ_{fr} is the effective shear modulus of the rock frame, ρ is the bulk density of the rock, and ρ_{fl} is the fluid density. The Biot compressional and shear velocities are then calculated by taking the real component of V_p^{Bi} and V_p^{Bi}, respectively. The various terms included in Biot's velocity equations (4.1) and (4.2) are explained in **Appendix C**.

The frequency regime over which dispersion occurs and the magnitude of dispersion and attenuation are mainly controlled by q in equations (4.1) and (4.2), which is defined as

$$q = \frac{\mathrm{T}\rho_{fl}}{\phi} - \frac{i\eta F(z)}{\omega\kappa}, \tag{4.3}$$

where η is the fluid viscosity, κ is the absolute permeability of the rock, ϕ is the total porosity, T is a tortuosity parameter, $F(z)$ is a viscodynamic operator, and ω is the angular frequency of the plane wave.

The tortuosity, T, is a purely geometrical factor. In this chapter Berryman's relation (1981) is used to estimate tortuosity:

$$\mathrm{T} = 1 - \frac{1}{2}\left(1 - \frac{1}{\phi}\right), \tag{4.4}$$

where the coefficient $\frac{1}{2}$ before the parentheses indicates spherical pores. In all synthetic cases defined in this chapter to which Biot's velocity relations are applied, porosity constituted of spherical pores represents at least 95% of total porosity, and equation (4.4) is considered valid on that account.

The operator $F(z)$ incorporates the frequency dependence of viscous drag and is defined in **Appendix C**.

Following Dvorkin et al. (1995), attenuation is estimated as the inverse of the quality factor Q for P- and S-waves, respectively, defined as

$$Q_p^{-1} = \left| \frac{\mathrm{Im}\left(\left(V_p^{Bi}\right)^2\right)}{\mathrm{Re}\left(\left(V_p^{Bi}\right)^2\right)} \right|, \tag{4.5}$$

and

$$Q_s^{-1} = \left| \frac{\mathrm{Im}\left(\left(V_s^{Bi}\right)^2\right)}{\mathrm{Re}\left(\left(V_s^{Bi}\right)^2\right)} \right|. \tag{4.6}$$

4.2.2 Approximation of Biot's Velocities with an Effective Medium Model

I describe here the method and workflow I developed to reproduce poroelastic effects predicted by Biot's (1956a, 1956b) relations based on the calculation of frequency-dependent equivalent mineral bulk and shear moduli for the matrix of the rock.

Anticipating the fact that Biot's flow and squirt flow mechanisms are to be combined in the new model, total porosity is divided into two parts namely, stiff porosity ϕ_p, composed of spherical pores of uniform radius a, and soft porosity ϕ_c, composed of cracks of uniform length a_c, such that

$$\phi = \phi_p + \phi_c, \tag{4.7}$$

with

$$\phi_c = \frac{4}{3}\pi\varepsilon\gamma, \tag{4.8}$$

where ε is the crack density, and γ is the crack aspect ratio. The crack density parameter has the interpretation of the number of cracks times the average axis length, per unit volume of the rock. Related to the in-situ stress, crack density cannot exceed 0.3 (see Chapman et al., 2002). Dividing total porosity in this manner violates Biot's assumption of uniform porosity. However, as explained above, spherical pores make up a large majority of total porosity in all models presented in this chapter. Consequently, the effect of soft porosity on Biot's velocity predictions is always negligible, and the radius of stiff pores is used when a pore-size parameter is invoked in Biot's velocity equations.

4.2.2.1 Low-Frequency Reference Case

A procedure is established (step I in **Figure 4.1**) to ensure that both Biot's formulas and the effective medium theory give rise to the same low-frequency limits of compressional- and shear-wave velocities for every possible combination of petrophysical and rock physics properties. For each particular synthetic instance, the low-frequency limiting case, henceforth referred to as the reference case, is defined by its static bulk and shear moduli estimated with the SCA. Based on assumed mineral composition, the bulk and shear moduli of the uniform homogeneous solid background of the rock, K_{sol} and μ_{sol}, respectively, are calculated with the Voigt-Reuss-Hill average (Hill, 1952). Fluid-saturated penny-shaped cracks are added first to the mineral matrix with Wu's (1966) SCA theory explained in Chapter 2. Spherical pores are included next within the resulting effective medium in the same manner. Outcomes of this first step are the static bulk and shear moduli

of the saturated medium, $K^*_{\mathbf{SCA}}$ and $\mu^*_{\mathbf{SCA}}$, where the superscript * denotes a low-frequency case of reference.

Frame moduli K_{fr} and μ_{fr} of the composite, as invoked in Biot's equations (4.2) and (C.1) to (C.3), are computed with Gassmann's (1951) relations utilizing $K^*_{\mathbf{SCA}}$, $\mu^*_{\mathbf{SCA}}$, K_{sol}, and the bulk modulus of the saturating fluid K_{fl}. By calculating elastic properties of the rock frame from saturated moduli of reference, Biot's low-frequency limiting velocities are the same as the velocities obtained using $K^*_{\mathbf{SCA}}$, and $\mu^*_{\mathbf{SCA}}$ in equations (2.8) and (2.9).

The Biot-Willis parameter calculated as

$$\alpha^* = 1 - K_{fr} \Big/ K_{sol}, \tag{4.9}$$

represents the change in pore volume per unit change in bulk volume under drained conditions (Kümpel, 1991) and is also defined for the low-frequency limit case.

4.2.2.2 Calculation of Frequency-Dependent Solid Moduli

To reproduce Biot's flow effects on velocities, I introduce the concept of complex-valued, frequency-dependent solid moduli (see step II in **Figure 4.1**). One shear modulus is calculated as well as two bulk moduli used distinctively for computation of effective frequency-dependent moduli for a passing P-wave or S-wave.

Using the equations of wave propagation derived by Tod (2003) under the assumption that the material can be described by Biot's equations of poroelasticity, a frequency-dependent Biot-Willis parameter can be expressed as

$$\alpha^{fd} = \alpha^* + \rho_{fl}\Theta, \tag{4.10}$$

and a frequency-dependent equivalent rock density as

$$\rho^{fd} = \rho + \rho_{fl}{}^2\Theta, \tag{4.11}$$

where the superscript fd denotes a frequency-dependent parameter. In the above equations, the function Θ is given by

$$\Theta = -q^{-1}, \tag{4.12}$$

where q is defined in equation (4.3).

For simplicity purposes, I add all attenuation and increase of velocity mechanisms into the new moduli equations of the mineral background instead. By incorporating the effect of Biot's flow on rock density described by equation (4.11), the new frequency-dependent solid shear modulus, μ_{sol}^{Bi}, is calculated as:

$$\mu_{sol}^{Bi} = \mu_{sol}\left(1+\frac{\rho_{fl}^{\ 2}}{\rho}\Theta\right)^{-1}. \tag{4.13}$$

Similarly, the frequency-dependent solid bulk modulus for propagating shear waves, K_{sol-s}^{Bi}, becomes

$$K_{sol-s}^{Bi} = K_{sol}\left(1+\frac{\rho_{fl}^{\ 2}}{\rho}\Theta\right)^{-1}. \tag{4.14}$$

The calculation of the equivalent solid bulk modulus for an incident P-wave is complicated by the need to include some of the assumed rock features in a newly formulated Biot-Willis parameter. By modifying equation (4.10), the frequency-dependent Biot-Willis parameter is now formulated as follows:

$$\alpha^{fd} = \alpha^{*} + \mathrm{f}_1^{Bi}\,\mathrm{f}_2^{Bi}\,\rho_{fl}\Theta, \tag{4.15}$$

where f_1^{Bi} and f_2^{Bi} are correction functions that depend on elastic properties of the rock's solid background and pore fluid, respectively; f_1^{Bi} and f_2^{Bi} are calculated as

$$\mathrm{f}_1^{Bi} = 3.4\times10^{-5}\mu_{sol}^2 - 3.7\times10^{-3}\mu_{sol} + 1.4\times10^{-5}K_{sol}^2 - 2.1\times10^{-3}K_{sol} + 0.23, \tag{4.16}$$

and

$$f_2^{Bi} = -0.14K_{fl}^2 + 1.35K_{fl} - 0.2, \tag{4.17}$$

for relatively incompressible fluids $\left(K_{fl} \geq 0.5 \text{ GPa}\right)$, or

$$f_2^{Bi} = -0.2K_{fl}^2 + 1.5K_{fl} - 0.025, \tag{4.18}$$

for other fluids. Note that in equations (4.16) to (4.18), K_{sol}, μ_{sol}, and K_{fl} are expressed in GPa. The frequency-dependent bulk modulus of the solid matrix for an incident compressional wave is then given by

$$K_{sol-p}^{Bi} = \frac{K_{fr}}{1-\alpha^{fd}}\left(1+\frac{\rho_{fl}^{\ 2}}{\rho}\Theta\right)^{-1}, \tag{4.19}$$

where the frame bulk modulus of the composite, K_{fr}, is assumed to remain constant at all frequencies.

4.2.2.3 Calculation of Frequency-Dependent Effective Moduli

The final step in my method involves estimation of elastic characteristics of the effective medium. Wu's (1966) SCA theory is first invoked to model the presence of porous cavities in a background characterized by frequency-dependent properties K_{sol-s}^{Bi} and μ_{sol}^{Bi} (step III.a in **Figure 4.1**). Randomly-oriented fluid-filled cracks are added into the solid matrix first, fluid-filled spherical pores are included next into the composite in the same manner. Outcomes at this stage of the procedure are effective frequency-dependent bulk and shear moduli of the saturated rock, K_s^{Bi} and μ_s^{Bi}, respectively, for an incident shear wave. Shear-wave velocity affected by Biot's flow effects can be readily estimated at any frequency by using μ_s^{Bi} and the effective density of the rock, ρ, in equation (2.9); S-wave attenuation is then calculated with equation (4.6).

In the same manner, effective elastic properties for a passing P-wave are computed by modeling a medium with solid bulk and shear moduli respectively expressed by K_{sol-p}^{Bi} and μ_{sol}^{Bi} (step III.b in **Figure 4.1**). Adding spheroidal and spherical porous inclusions with the SCA gives rise to the effective parameters K_p^{Bi} and μ_p^{Bi}. Compressional velocity is then approximated from equation (2.8) using K_p^{Bi}, μ_p^{Bi}, and ρ; P-wave attenuation is computed using equation (4.5).

4.2.3 Limitations of the Method

This approach to reproduce Biot's flow effects on velocity exhibits limitations in the instance of soft solid backgrounds. Best results are obtained for solid matrices characterized by $\mu_{sol} \geq 18$ GPa and $K_{sol} \geq 20$ GPa when using the new effective medium method.

Assuming total porosity higher than 35% might also lead to erroneous simulations. However, I believe that the assumption that a rock is composed of 35% or less of porous space is not excessively restrictive (see Manger, 1963).

4.2.4 Application to Synthetic Cases

Table 4.1 describes solid composition, petrophysical properties, and rock physics parameters assumed in the synthetic example defined to investigate the effects of porosity, permeability, and fluid type on velocity behavior and to verify the agreement between Biot's original relations and the new effective medium model. The synthetic case represents a typical sandstone composed of 55% quartz and 20% clay, and solid grains are assumed to have a diameter of 200 μm. Total porosity is relatively high (20%), crack density is 0.1, and permeability is 65 mD. As discussed in the description of the method (section 4.2.2), frequency-dependent and complex-valued solid moduli are calculated at all frequencies. **Figure 4.2** shows real and imaginary parts of the solid shear and bulk moduli.

Note the distinct curves of bulk moduli associated with either an incident compressional or shear wave. There is a clear increase between low and high frequencies of real values of the equivalent elastic properties of the solid background that is consistent with the strengthening of a rock experiencing Biot's flow. It can be easily verified that low-frequency limits of the equivalent solid moduli are the same as the characteristics of the grains that make up the rock matrix, K_{sol} and μ_{sol}, calculated with the Voigt-Reuss-Hill average of the features of the individual solid components described in **Table 2.2**. Imaginary parts of frequency-dependent background moduli tend to zero at low- and high-frequency limits and reach a peak at frequencies where the maximum of amplitude attenuation occurs. Wave behavior with respect to frequency as simulated with Biot's equations and the new effective medium model is depicted in **Figure 4.3**, where P-wave (panel a) and S-wave (panel b) velocities are plotted with their attenuation calculated as Q_p^{-1} (panel c) and Q_s^{-1} (panel d), respectively. My method to reproduce the Biot's flow mechanism leads to valid simulations of acoustic attenuation and wave velocities: percentages of dispersion (relative difference between high- and low-frequency limiting velocities) are 0.994% and 1.59% for V_p and V_s calculated with Biot's equations, respectively, and 0.987% and 1.57% for V_p and V_s calculated with the effective medium model, respectively.

To exhaustively verify the accuracy of my effective medium model, I perform simulations of velocity dispersion and attenuation on several synthetic instances identical to the example specified in **Table 4.1**, where one parameter at a time is varied over an extensive range of values. Velocity and attenuation curves obtained with Biot's equations are plotted along those simulated with the new scheme. Correlations between the different parameters and the dispersive behavior of compressional and shear velocities are also examined in this process.

4.2.4.1 Porosity Variations

Biot's equations and the effective medium model are implemented to three cases with total porosity of 10%, 18%, and 25%. **Figure 4.4** shows compressional velocity (panel a) and attenuation (panel c) as well as shear velocity (panel b) and attenuation (panel d) for the synthetic rock that exhibits 10% of total porosity. Additionally, **Table 4.2** compares the percentages of dispersion computed for velocities simulated with Biot's formulas and my model for the three examples. Qualitatively and quantitatively, the effective medium model accurately reproduces Biot's flow effects on velocity dispersion and attenuation for a large spectrum of porosities.

As expected, porosity greatly affects wave velocity and attenuation. As total porosity increases, dispersion and attenuation effects become larger. A remarkable relationship is observed between total porosity and frequencies at which attenuation reaches its maximum. Assumed total porosities are plotted against frequency of maximum attenuation, denoted f_{att}, for P- and S-waves in **Figure 4.5**. f_{att} increases with total porosity, and a seemingly linear relationship is observed between frequency of maximum attenuation and porosity when f_{att} is plotted on a logarithmic scale.

4.2.4.2 Permeability Variations

Next, I perform simulations on synthetic rocks characterized by different permeabilities. **Figure 4.6** describes wave velocity (panels a and b) and attenuation (panel c and d) estimations obtained with Biot's equations and the effective medium model for three instances described by permeabilities of 1 D, 0.1 D, and 1 mD. I observe good agreement between Biot's original theory and my model. Amplitude of dispersion is not influenced by variations of κ, and both theories generate identical percentages for all synthetic examples (see **Table 4.3**). But, attenuation decreases with lower permeability, particularly when the rock is highly permeable $(\kappa \geq 1\text{D})$; however, peak values of the

inverse quality factors tend to stabilize when permeability is below 1 D. Furthermore, the range of frequency for which variations of velocity are observed increases with decreasing permeability.

Frequency at which dispersion takes place is directly influenced by the permeability of the rock. As observed in **Figure 4.6**, f_{att} increases with decreasing permeability. **Figure 4.7** displays a first-degree relationship between assumed values of κ and corresponding frequency of maximum attenuation, when plotted on a log-log scale, for compressional- and shear- wave velocities.

4.2.4.3 Pore Fluid Variations

Using two additional examples, I investigate the impact of changing fluid elastic properties and viscosity on wave dispersion and attenuation as predicted by Biot's flow theory. Oil and gas are assumed to replace water within the pore space of the synthetic case described in **Table 4.1,** and results are shown in **Figures 4.8** and **4.9,** respectively. In these figures, I juxtapose P- and S-wave velocities (panels a and b), and P- and S-attenuations (panels c and d) obtained with both models for qualitative comparisons. Velocities and attenuations calculated with my model agree with Biot's original relations, regardless of the nature of the fluid saturating the rock. Accuracy of the new effective medium method is demonstrated quantitatively in **Table 4.4**. Percentages of dispersion predicted by both theories concur for all three fluids. It is worth noticing that when the rock is saturated with gas, increase of velocities is almost negligible with percentage of dispersion below 0.2% for both compressional and shear waves.

Viscosity of the saturating fluid has greater repercussions on velocity behavior than its bulk modulus. **Figure 4.10** shows that f_{att} and η are in fact linearly related when

displayed on a log-log plot. It confirms the results observed in **Figures 4.2**, **4.8**, and **4.9**: frequency at which dispersive behavior occurs increases with increasing fluid viscosity.

Further simulations are carried out to validate thoroughly the new effective medium model. Simulated velocities and attenuations are compared to results yielded by Biot's equations while all other parameters that have an influence on Biot's flow mechanism such as solid composition and grain size—or alternatively, pore size—are varied extensively. The effective medium model outputs values that consistently agree well with Biot's predictions, but I do not document them in this dissertation.

4.2.4.4 Fluid Mobility Study

Following observations made about **Figures 4.7** and **4.10**, I consider variations of f_{att} with fluid mobility, computed as

$$M = \frac{\kappa}{\eta}, \tag{4.20}$$

for wide ranges of permeability and fluid viscosity. **Figure 4.11** displays a linear increase of frequency of maximum attenuation with decreasing of fluid mobility for a constant permeability. However, there is no straightforward correlation between M and f_{att} because the effects of κ and η are decoupled in Biot's velocity relations. For instance, for a specific fluid mobility (along any horizontal line in **Figure 4.11**), frequency of maximum attenuation decreases with decreasing permeability before it starts to increase above a certain point. For this reason, estimation of fluid mobility based on measurements performed around frequencies at which dispersion caused by Biot's flow occurs requires *a priori* knowledge of the permeability of the rock or of the viscosity of the fluid that occupies the pore space.

4.3 MODELING OF THE SQUIRT FLOW MECHANISM

Increase of velocity and acoustic attenuation predicted by Biot's flow theory has been experimentally verified, but in some cases it does not accurately describe wave attenuation and dispersion. Squirt flow theory assumes that propagating waves in reservoir rocks may cause pore fluid to flow in directions that differ from those of the waves; thus squirt flow theory can often predict larger velocity dispersion than can Biot's theory of poroelasticity. I consider the local flow scheme proposed by Chapman et al. (2002) and develop a new effective medium model that reproduces the dispersive velocity behavior predicted by this theory. Rocks are defined as porous composites that exhibit the same characteristics described in the first paragraph of section 4.2. For validity of Chapman et al.'s model, aspect ratio of cracks is assumed to be lower than 0.01. A reference case is calculated using the static self-consistent approximation theory, and a procedure is formulated in order for elastic properties computed with Chapman et al.'s equations to tend to values obtained with the SCA at low frequencies. Building on the same concept explained in the previous section, dynamic and complex-valued equivalent moduli for the solid matrix of a medium are calculated by modifying Chapman's et al. relation using correction functions of total porosity and crack density. One dynamic solid shear modulus and two distinct dynamic bulk moduli are defined as well, and Wu's self-consistent approximation is invoked to compute complex-valued frequency-dependent elastic moduli of the saturated rock. **Figure 4.12** summarizes the workflow of the newly produced method for modeling the squirt flow mechanism.

4.3.1 Chapman et al.'s Squirt Flow Model

Chapman et al. (2002) derived a squirt flow or local flow model that considers frequency-dependent, wave-induced exchange of fluid between pores and cracks, as well as between cracks of different orientations. Fluid-related dispersion models are supposed

to be consistent with the evidence in favor of poroelasticity: they should predict the existence of the Biot wave and agree with Gassmann's predictions of velocity in the low-frequency limit. The advantage of Chapman et al.'s (2002) model is that it satisfies these requirements, whereas the BISQ model (Dvorkin and Nur, 1993) or the equant porosity model (Hudson et al., 1996), for example, do not.

In the model, the rock is isotropic, porosity is divided between stiff spherical pores, and soft cracks idealized as oblate spheroids with a small aspect ratio. Penny-shaped cracks are all assumed to exhibit the same length and aspect ratio. At high frequencies the model predicts that unequal pore pressures are induced on the microscale of individual pores. Larger increments are induced in the crack-like porosity and smaller increments in the stiffer pores. If these do not equilibrate, the rock will be stiffer, and the velocities will be faster than the low-frequency velocities. Chapman et al. (2006) described the procedure for calculating the frequency-dependent effective bulk and shear moduli for squirt flow based on Eshelby's (1957) calculations. The equations are based on those of Chapman et al. (2002) but simplified by only considering squirt flow. Note that the equations published in Chapman et al. (2006) presented several errors that I identified. The correct equations are as follows:

$$K^{Sq} = K_{sol} - 4\varepsilon K_{sol}\left\{\frac{K_{sol}(\lambda_{sol}+2\mu_{sol})}{3\mu_{sol}(\lambda_{sol}+\mu_{sol})}\left[1-A(\omega)\right]-4\pi\gamma A(\omega)\right\} - \phi\frac{K_{sol}(\lambda_{sol}+2\mu_{sol})}{4\mu_{sol}}\left[1-9B(\omega)\right], \tag{4.21}$$

for the effective bulk modulus and

$$\mu^{Sq} = \mu_{sol} - \frac{16}{45}\varepsilon\frac{\mu_{sol}\left(\lambda_{sol}+2\mu_{sol}\right)}{\left(3\lambda_{sol}+4\mu_{sol}\right)}\left[2+\frac{1}{1+K_c}\left(K_c+\frac{1}{1+i\omega\tau}\right)\right] - \phi\frac{15\mu_{sol}\left(\lambda_{sol}+2\mu_{sol}\right)}{9\lambda_{sol}+14\mu_{sol}}, \tag{4.22}$$

for the effective shear modulus, where K_{sol}, μ_{sol}, and λ_{sol} are the bulk modulus, shear modulus, and Lamé parameter of the mineral making up the matrix of the rock, respectively, ϕ is the total porosity, ε is the crack density, γ is the crack aspect ratio, τ is a timescale parameter, and ω is the angular frequency of the incident wave. $A(\omega)$ and $B(\omega)$ are frequency-dependent constants given by

$$A(\omega) = \frac{\frac{i\omega\tau}{3(1+K_c)} - \Gamma' i\omega\tau + \frac{1}{\Gamma}(1+i\omega\Gamma\tau)\left[\frac{1}{3(1+K_c)}+\Gamma'\right]}{1+i\omega\tau+\frac{1}{\Gamma}(1+i\omega\Gamma\tau)}, \tag{4.23}$$

and

$$B(\omega) = \frac{(1+i\omega\tau)\left[\frac{1}{3(1+K_c)}+\Gamma'\right] - i\omega\tau\left[\frac{1}{3(1+K_c)}-\Gamma'\right]}{1+i\omega\Gamma\tau+\Gamma(1+i\omega\tau)}, \tag{4.24}$$

where Γ and Γ' and are non-dimensional parameters calculated as

$$\Gamma = \frac{9\phi(\lambda_{sol}+\mu_{sol})(1+K_p)}{16\varepsilon(\lambda_{sol}+2\mu_{sol})(1+K_c)}, \tag{4.25}$$

and

$$\Gamma' = \Gamma\frac{\lambda_{sol}+2\mu_{sol}}{(3\lambda_{sol}+2\mu_{sol})(1+K_p)}. \tag{4.26}$$

In the above equations, K_p and K_c are the pore- and crack-space compressibility parameters, respectively, given by

$$K_p = \frac{4\mu_{sol}}{3K_{fl}}, \tag{4.27}$$

and

$$K_c = \frac{\pi\mu_{sol}\left(\lambda_{sol}+\mu_{sol}\right)\gamma}{K_{fl}\left(\lambda_{sol}+2\mu_{sol}\right)}, \tag{4.28}$$

where K_{fl} is the bulk modulus of the fluid in the pore space. All other parameters being equal, the timescale parameter τ controls the frequency regime over which the dispersion occurs, whereas the crack density ε controls the magnitude of dispersion and attenuation. For small aspect ratios, $\gamma < 0.01$, τ is approximately given by

$$\tau \approx \frac{4\eta a_c^3\left(1-\nu_{sol}\right)}{9\kappa d\,\mu_{sol}}, \tag{4.29}$$

where η is the fluid viscosity, a_c is the crack length, d is a characteristic grain diameter, κ is the permeability, and ν_{sol} is the Poisson's ratio of the solid part of the rock.

In Chapman et al.'s (2002) model, a_c is equal to the radius of the stiff spherical pores, a. To allow for the presence of cracks of lengths different from the pores radius, I modify equation (4.29) by following Chapman's (2003) who incorporated the effect of meso-scale fractures on squirt flow dispersion into the analysis developed by Chapman et al. (2002). The expression for the timescale parameter associated with cracks whose size is different from that of pores becomes

$$\tau \approx \left(\frac{a_c}{a}\right)\frac{4\eta a^3\left(1-\nu_{sol}\right)}{9\kappa d\,\mu_{sol}} = \frac{4\eta a_c a^2\left(1-\nu_{sol}\right)}{9\kappa d\,\mu_{sol}}, \tag{4.30}$$

and all other equations hold.

Squirt compressional- and shear-wave velocities, V_p^{Sq} and V_s^{Sq}, are then simply computed with equations (2.8) and (2.9), respectively, using the frequency-dependent

moduli K^{Sq} and μ^{Sq} in lieu of K and μ, respectively, and taking the real part of the results. The quality factors for P- and S-waves are defined in the same manner as in equations (4.5) and (4.6), respectively.

4.3.2 Approximation of Chapman et al.'s Velocity Relations with an Effective Medium Model

In this section, I describe my new effective medium model that reproduces the dispersion and attenuation behavior of compressional- and shear-wave velocities as predicted by Chapman et al. (2006). Pursuing the reasoning presented in the description of the effective medium model for Biot's velocities, the method is based on the calculation of frequency-dependent equivalent bulk and shear moduli of the solid matrix of the rock.

4.3.2.1 Low-Frequency Reference Case

I first develop a procedure following Chapman et al. (2006) so that low-frequency limits calculated with Chapman et al.'s model and velocities obtained when applying Wu's version of SCA are consistent (step I in **Figure 4.12**). Equations (4.21) and (4.22) given in the section above can be decomposed into the form:

$$\left(K^{Sq}, \mu^{Sq}\right) = \left(K_{sol}, \mu_{sol}\right) - \mathrm{P}\left(K_{sol}, \mu_{sol}, \omega, \tau, \phi, \varepsilon, K_{\mathrm{fl}}\right), \tag{4.31}$$

where the first term represents the elastic properties of the solid background of the composite without inclusions and the second term, P, is the perturbation due to the presence of cracks and pores. A static reference is determined in the same manner as in the Biot's flow section. The elastic properties of the reference case at low frequencies, $K^{*}_{\mathbf{SCA}}$ and are calculated by adding fluid-filled spheroidal and spherical inclusions, in this order, into the solid matrix of properties and with the classical SCA theory. I further define

$$(K^{Sq*}, \mu^{Sq*}) = \left(K^{*}_{\mathbf{SCA}}, \mu^{*}_{\mathbf{SCA}}\right) + \mathrm{P}(K^{*}_{\mathbf{SCA}}, \mu^{*}_{\mathbf{SCA}}, \omega_0, \tau, \phi, \varepsilon, K_{fl}), \tag{4.32}$$

where the superscript Sq designates parameters that describe squirt flow mechanism and ω_0 is an arbitrary angular frequency small enough to be considered in the low-frequency range, e.g. 10 Hz. Next, effective frequency-dependent bulk and shear moduli for squirt flow can be computed as

$$\left(K^{Sq}, \mu^{Sq}\right) = (K^{Sq*}, \mu^{Sq*}) - \mathrm{P}(K^{*}_{\mathbf{SCA}}, \mu^{*}_{\mathbf{SCA}}, \omega, \tau, \phi, \varepsilon, K_{fl}). \tag{4.33}$$

Thus, the final squirt bulk and shear moduli computed with Chapman et al.'s expressions tend to the same values as the moduli of the fluid-saturated rock computed with the classical self-consistent approximation at low frequencies. This procedure also provides conformity to my method for modeling Biot's flow mechanism (as well as conformity to all other frequency-dependent models subsequently described) because they predict identical low-frequency limits. Chapman et al.'s squirt flow velocities are then estimated using K^{Sq} and μ^{Sq} with bulk density ρ in equations (2.8) and (2.9).

4.3.2.2 Calculation of Frequency-Dependent Solid Moduli

As shown in **Figure 4.12** (step II), dynamic elastic properties of the solid matrix of the composite are then calculated for all frequency by modifying Chapman et al.'s equations. Similarly to the method advanced for modeling Biot's flow effects, one shear modulus, μ^{Sq}_{sol}, and two bulk moduli, K^{Sq}_{sol-p} and K^{Sq}_{sol-s}, are calculated to estimate effective frequency-dependent moduli that depend on the nature of the incident wave. The objective is to include all squirt flow mechanisms within the definition of the equivalent solid properties of the rock. Because outcomes of Chapman et al.'s equations are elastic moduli, I use equation (4.21) and adapt it for the calculation of two bulk moduli of the solid matrix with the introduction of correction functions, as follows:

$$K_{sol-p}^{Sq} = K_{sol-p}^{Sq*} - \mathrm{f}_1^{Sq}\,\mathrm{f}_2^{Sq}\left\{4\varepsilon K_{sol}\left[\frac{K_{sol}(\lambda_{sol}+2\mu_{sol})}{3\mu_{sol}(\lambda_{sol}+\mu_{sol})}\left(1-A(\omega)\right)-4\pi\gamma A(\omega)\right]\right.$$
$$\left.-\phi\frac{K_{sol}(\lambda_{sol}+2\mu_{sol})}{4\mu_{sol}}\left(1-9B(\omega)\right)\right\}, \tag{4.34}$$

for the equivalent solid bulk modulus for an incident P-wave and

$$K_{sol-s}^{Sq} = K_{sol-s}^{Sq*} - \mathrm{g}_1^{Sq}\,\mathrm{g}_2^{Sq}\left\{4\varepsilon K_{sol}\left[\frac{K_{sol}(\lambda_{sol}+2\mu_{sol})}{3\mu_{sol}(\lambda_{sol}+\mu_{sol})}\left(1-A(\omega)\right)-4\pi\gamma A(\omega)\right]\right.$$
$$\left.-\phi\frac{K_{sol}(\lambda_{sol}+2\mu_{sol})}{4\mu_{sol}}\left(1-9B(\omega)\right)\right\}, \tag{4.35}$$

for the equivalent solid bulk modulus for an incident S-wave.

The frequency-dependent solid shear modulus is readily calculated by modifying equation (4.22) as

$$\mu_{sol}^{Sq} = \mu_{sol}^{Sq*} - \frac{16}{45}\varepsilon\frac{\mu_{sol}\left(\lambda_{sol}+2\mu_{sol}\right)}{\left(3\lambda_{sol}+4\mu_{sol}\right)}\left[2+\frac{1}{1+K_c}\left(K_c+\frac{1}{1+i\omega\tau}\right)\right]$$
$$-\phi\frac{15\mu_{sol}\left(\lambda_{sol}+2\mu_{sol}\right)}{9\lambda_{sol}+14\mu_{sol}}. \tag{4.36}$$

In equations (4.34), (4.35), and (4.36), K_{sol-p}^{Sq*}, K_{sol-s}^{Sq*}, and μ_{sol}^{Sq*} are solid moduli of reference defined to constrain K_{sol-p}^{Sq}, K_{sol-s}^{Sq}, and μ_{sol}^{Sq} to tend to the corresponding static grain moduli K_{sol} and μ_{sol} at low frequencies. They are expressed as

$$K_{sol-p}^{Sq*} = K_{sol} + \mathrm{f}_1^{Sq}\,\mathrm{f}_2^{Sq}\left\{4\varepsilon K_{sol}\left[\frac{K_{sol}(\lambda_{sol}+2\mu_{sol})}{3\mu_{sol}(\lambda_{sol}+\mu_{sol})}\left(1-A(\omega_0)\right)-4\pi\gamma A(\omega_0)\right]\right.$$
$$\left.-\phi\frac{K_{sol}(\lambda_{sol}+2\mu_{sol})}{4\mu_{sol}}\left(1-9B(\omega_0)\right)\right\}, \tag{4.37}$$

$$K_{sol-s}^{Sq*} = K_{sol} + \mathrm{g}_1^{Sq}\,\mathrm{g}_2^{Sq}\left\{4\varepsilon K_{sol}\left[\frac{K_{sol}(\lambda_{sol}+2\mu_{sol})}{3\mu_{sol}(\lambda_{sol}+\mu_{sol})}\left(1-A(\omega_0)\right)-4\pi\gamma A(\omega_0)\right]\right.$$
$$\left.-\phi\frac{K_{sol}(\lambda_{sol}+2\mu_{sol})}{4\mu_{sol}}\left(1-9B(\omega_0)\right)\right\}, \tag{4.38}$$

and

$$\mu_{sol}^{Sq*} = \mu_{sol} + \frac{16}{45}\varepsilon\frac{\mu_{sol}\left(\lambda_{sol}+2\mu_{sol}\right)}{\left(3\lambda_{sol}+4\mu_{sol}\right)}\left[2+\frac{1}{1+K_c}\left(K_c+\frac{1}{1+i\omega_0\tau}\right)\right]$$
$$-\phi\frac{15\mu_{sol}\left(\lambda_{sol}+2\mu_{sol}\right)}{9\lambda_{sol}+14\mu_{sol}}, \tag{4.39}$$

where ω_0 is an arbitrary angular frequency small enough to be considered in the low-frequency range.

Correction functions f_1^{Sq} and g_1^{Sq} depend on the total porosity of the composite and are obtained with the formulas

$$\mathrm{f}_1^{Sq} = 5\phi^2 - 0.3\phi + 0.89, \tag{4.40}$$

and

$$\mathrm{g}_1^{Sq} = 29\phi^2 - 7\phi + 1.5, \tag{4.41}$$

whereas f_2^{Sq} and g_2^{Sq} are functions of the crack density ε calculated respectively as

$$\mathrm{f}_2^{Sq} = 0.69\varepsilon^2 + 0.95\varepsilon + 1.2, \tag{4.42}$$

and

$$\mathrm{g}_2^{Sq} = 0.62\varepsilon^2 + 0.2\varepsilon + 0.2. \tag{4.43}$$

The introduction of those simple correction functions allows one to compute the equivalent frequency-dependent solid bulk moduli for passing compressional and shear waves.

4.3.2.3 Calculation of Frequency-Dependent Effective Moduli

Similarly to the method for reproduction of Biot's velocities, frequency-dependent effective properties of the rock are estimated with Wu's (1966) SCA theory using K_{sol-s}^{Sq} and μ_{sol}^{Sq} (step III.a in **Figure 4.12**) as elastic properties of the solid background to model shear velocities affected by squirt flow. Fluid-saturated cracks are added into the solid matrix with the SCA theory followed by spherical pores. Resulting shear modulus of the effective medium, μ_s^{Sq}, is invoked with the bulk density in equation (2.9) to approximate the incident shear-wave velocity. S-attenuation caused by squirt flow is calculated as the inverse of the quality factor with equation (4.6).

Next, effective rock elastic properties for a propagating compressional wave are computed by using solid bulk and shear moduli, K_{sol-p}^{Sq} and μ_{sol}^{Sq}, respectively, and including fluid-filled spheroidal and spherical porous inclusions with the SCA theory into the solid background (step III.b in **Figure 4.12**). The resulting effective characteristics of the medium for a P-wave generating squirt flow are denoted K_p^{Sq} and μ_p^{Sq}. Compressional velocity and attenuation are then computed from equations (2.8) and (4.5), respectively.

4.3.3 Limitations of the Method

Limitations of the effective medium model constructed to reproduce squirt flow effects are identical to those of the model for Biot's flow. Grain bulk and shear moduli of the simulated medium should not be lower than 20 GPa and 18 GPa, respectively, and a total porosity of greater than 35% might give rise to divergences between Chapman et al.'s relations and dynamic properties estimated with the new method.

4.3.4 Application to Synthetic Cases

A synthetic rock of known lithology and fluid constituents is defined to examine the dependence of dispersion and attenuation on varying aspect ratio of cracks,

permeability, and saturating fluid. **Table 4.5** summarizes solid composition, and petrophysical and rock physics parameters assumed in the example. Because squirt flow is caused by the presence of porous heterogeneities, the synthetic case represents a shaly sandstone layer, characterized by a large density (0.23) of 40-μm-long cracks. The rock exhibits fine grains with a diameter of 45 μm, high concentrations of clay (45%) and quartz (48%), and a low concentration of calcite (7%). Total porosity and permeability are low, 11% and 30 nD, respectively, and the saturating fluid is hydrocarbon. Frequency-dependent and complex-valued solid moduli are calculated with the modified Chapman et al.'s equations for the effective medium model. **Figure 4.13** shows real and imaginary parts of the solid shear and bulk moduli. Strengthening due to squirt flow effects typically observed in a rock is modeled by the increasing of real values of the equivalent elastic properties of the solid background. The procedure described in section 4.3.2.1 also forces low-frequency values of the real parts of the equivalent moduli to tend toward the values of the static moduli of the solid matrix, K_{sol} and μ_{sol}.

For validation, wave dispersion and attenuation predicted by Chapman et al.'s (2006) equations and the new effective medium model are shown in **Figure 4.14**, where P-wave (panel a) and S-wave (panel b) velocities are plotted with their attenuation calculated as Q_p^{-1} (panel c) and Q_s^{-1} (panel d), respectively. Note the correlation between attenuation curves in **Figure 4.14** and the imaginary parts of the frequency-dependent solid moduli displayed in panels c and d of **Figure 4.13**. Percentages of dispersion for V_p and V_s obtained with both methods are almost identical (2.79% and 2.78% for P-wave velocity and 1.58% and 1.56% for S-wave velocity calculated with Chapman et al.'s and my model, respectively) indicating that the newly developed method for modeling squirt flow effects leads to accurate simulations of wave dispersion and attenuation. The extent of the range of frequency for which a continuous increase of wave speed is observed is

noticeably shorter for the squirt flow mechanism than for Biot's flow effects. There are commonly two decades of frequency between low-frequency and high-frequency limiting squirt velocities, whereas Biot's flow dispersion curves often show four orders of magnitude separating lower and upper horizontal asymptotes.

Validation of the new effective medium model for squirt flow effects is achieved by comparing simulations of velocity dispersion and attenuation implemented with Chapman et al.'s (2006) equations and my model. Different synthetic examples are defined from the example specified in **Table 4.5** where one parameter is assumed to change. Velocity and attenuation curves obtained with Chapman et al.'s equations are plotted along those simulated with the new model. Relations between parameters that have the greatest impact on dispersion mechanisms and wave velocities are also investigated, similarly to the study conducted on Biot's flow effects.

4.3.4.1 Crack Aspect Ratio Variations

Chapman et al.'s equations and the effective medium model for squirt flow are applied to two other cases where the crack aspect ratio is changed to 0.01 and 0.001. **Figure 4.15** shows compressional velocity (panel a) and attenuation (panel c) as well as shear velocity (panel b) and attenuation (panel d) for the example characterized by the flattest cracks $(\gamma = 0.001)$. Despite changes in the shape of cracks, a good qualitative match is still observed between the two methods for velocity and attenuation calculation. Additionally, **Table 4.6** compares the percentages of dispersion computed for velocities simulated with Chapman et al.'s formulas and my model for examples with three different crack aspect ratios. These results suggest that the effective medium model accurately reproduces squirt flow mechanism on velocity dispersion and attenuation a for large variety of shapes of porous heterogeneities.

Note the influence of the shape of penny-shaped cracks on the amplitude of dispersion and attenuation: flatter pores induce greater attenuation and higher increase of compressional and shear velocities. **Figure 4.16** depicts relationships between the shape of cracks and percentage of dispersion for both types of waves. Relative differences between high- and low-frequency limiting shear velocities are linked to the aspect ratio of cracks in a linear manner whereas a second-degree polynomial correlation is found between shape of cracks and magnitude of dispersion. It is worth noting the larger variations in compressional velocity than in shear velocity. Thus, estimation of crack aspect ratios would be more accurate when based on the interpretation of dispersive behavior displayed by the compressional wave.

4.3.4.2 Permeability Variations

Simulations are performed on synthetic instances defined by varying the permeability of the case described in **Table 4.5**. **Figure 4.17** shows wave velocity (panels a and b) and attenuation (panel c and d) estimations obtained with Chapman et al.'s equations and the effective medium model for three different examples: 1 nD, 0.1 μD, and 10 μD. The qualitative agreement between Chapman et al.'s theory and my model observed in **Figure 4.17** is confirmed by the similar percentages of dispersion calculated with both methods and summarized in **Table 4.7**.

Low- and high-frequency velocity limits, and attenuation curves predicted by the models are the same for all examples, only the frequency of maximum attenuation differs with permeability. **Figure 4.18** shows that modeled values of permeability and frequency of maximum attenuation scale linearly in logarithmic space, for compressional- and shear-wave velocities.

4.3.4.3 Pore Fluid Variations

Squirt flow effects on velocity and attenuation simulated with the new effective medium model are verified against results provided by Chapman et al.'s method for different saturating fluids. Simulations with water and gas are performed and results are shown in **Figures 4.19** and **4.20**, respectively. P- and S-wave velocities are plotted in panels a and b, respectively, and - and -attenuations in panels c and d, respectively. Velocity and attenuation curves obtained with my model accurately reproduce those obtained with Chapman et al.'s relations, irrespective of the nature of the saturating fluid. **Table 4.8** compares percentages of dispersion predicted by both theories for all three fluids. Similar to previous observations, Chapman et al.'s and my model are in agreement. Results in **Table 4.8** indicate that a change in pore fluid induces large variations in , whereas it almost does not affect . Another noticeable observation is the linear relationship between fluid viscosity and corresponding frequency of maximum attenuation for compressional- and shear- wave velocities shown in **Figure 4.21** where and are displayed on a log-log plot.

Several rock properties such as solid composition, total porosity, crack length, grain size, among others, also affect the squirt flow mechanism. Additional simulations (not included in this dissertation) were performed to ensure that the agreement between Chapman et al.'s model and the newly devised method was still observed when these parameters were modified, thus confirming the accuracy of the effective medium model.

4.3.4.4 Fluid Mobility Study

Figure 4.22 shows a linear increase of fluid mobility with increasing frequency at which attenuation reaches its maximum with logarithmic scales. All points lie on the same line, suggesting that mobility correlates directly with f_{att}, regardless of the relative values

of permeability and fluid viscosity. This behavior is attributed to the presence of the ratio η/κ in equation (4.29).

4.4 COMBINED BIOT/SQUIRT FLOW MODEL

An original simple procedure is formulated to simultaneously reproduce both fluid-related mechanisms of dispersion and attenuation. The new effective medium models for Biot's and squirt flow are constructed with the classical SCA theory. They depend on the calculation of frequency-dependent equivalent solid properties to account for solid/fluid interactions caused by a propagating wave. This common base allows one to conveniently integrate the two dispersion mechanisms. At each frequency, equivalent solid moduli for Biot's flow are calculated with the effective medium model described in section 4.2 (step I in **Figure 4.23**). I further define

$$\Delta K_{sol-p}^{Bi} = K_{sol-p}^{Bi} - K_{sol}, \tag{4.44}$$

$$\Delta K_{sol-s}^{Bi} = K_{sol-s}^{Bi} - K_{sol}, \tag{4.45}$$

and

$$\Delta \mu_{sol}^{Bi} = \mu_{sol}^{Bi} - \mu_{sol}. \tag{4.46}$$

Similarly, frequency-dependent moduli for squirt flow are computed with the effective medium model introduced in section 4.3, and the differences between squirt flow dynamic solid moduli and static solid moduli ΔK_{sol-p}^{Sq}, ΔK_{sol-s}^{Sq}, and $\Delta \mu_{sol}^{Sq}$, are calculated as in equations (4.44), (4.45), and (4.46) (see step II in **Figure 4.23**).

The frequency-dependent solid moduli for combined Biot/squirt flow are calculated as (step III in **Figure 4.23**)

$$K_{sol-p}^{BiSq} = K_{sol} + \Delta K_{sol-p}^{Bi} + \Delta K_{sol-p}^{Sq}, \tag{4.47}$$

for the equivalent bulk modulus for an incident P-wave,

$$K_{sol-s}^{BiSq} = K_{sol} + \Delta K_{sol-s}^{Bi} + \Delta K_{sol-s}^{Sq}, \tag{4.48}$$

for the equivalent bulk modulus for an incident S-wave, and

$$\mu_{sol}^{BiSq} = \mu_{sol} + \Delta \mu_{sol}^{Bi} + \Delta \mu_{sol}^{Sq}, \tag{4.49}$$

for the equivalent bulk modulus and where the superscript $BiSq$ identifies parameters for combined Biot's and squirt flows.

The SCA theory is invoked to estimate dynamic properties of the effective medium. Randomly-oriented fluid-filled cracks are added first into a background matrix characterized by frequency-dependent elastic features K_{sol-s}^{BiSq} and μ_{sol}^{BiSq}. Fluid-filled spherical pores are included next into the composite (step IV.a in **Figure 4.23**). The resulting effective shear modulus of the saturated rock, μ_s^{BiSq}, is invoked with the bulk density to approximate the incident shear-wave velocity. S-attenuation caused by the joint effects of Biot's and squirt flow is calculated as the inverse of the quality factor with equation (4.6). Effective elastic properties of the rock for a propagating compressional wave are computed by using solid bulk and shear moduli, K_{sol-p}^{BiSq} and μ_{sol}^{BiSq}, respectively. Fluid-filled spheroidal and spherical porous inclusions are then included into the background with the SCA theory (step III.b in **Figure 4.12**). The effective features of the medium in which a propagating P-wave causes Biot's and squirt flow are denoted K_p^{BiSq} and μ_p^{BiSq}. Compressional velocity and attenuation are then computed from equation (2.8) and (4.5), respectively.

The newly established model is applied to the synthetic cases to show simultaneous Biot/squirt effects on wave velocity and attenuation. **Figures 4.24** and **4.25** show the results obtained for the examples described in **Tables 4.1** and **4.5**, respectively. Dot-dashed lines, dashed lines, and solid lines in panels a and b of the figures identify Biot's flow velocities,

squirt flow velocities, and velocities affected by both Biot's and squirt flow mechanisms, respectively. Panels c and d show attenuation simulated with the joint model. The method accurately reproduces combined effects of Biot's and squirt flow mechanisms of dispersion. Compressional and shear velocities experience a twofold increase occurring at the same ranges of frequency predicted by individual fluid-related dispersion models, and two distinct peaks are observed for attenuation curves.

In addition to the dispersion due to Biot's flow effect that arises around 10 kHz, **Figure 4.24** shows that squirt flow dispersion and attenuation occurs at higher frequencies (10^9 Hz). This is explained by the relatively high permeability assumed in the instance described in **Table 4.1 (**refer to **Figures 4.7** and **4.18**). Biot's and squirt flow predict similar increase of dispersion and degrees of attenuation in this example. On the other hand, results in **Figure 4.25** show a first increment in velocity and attenuation at 1 kHz caused by squirt flow mechanisms and a second one induced by Biot's flow effects at frequencies too extreme even to be measured experimentally (about 10^{17} Hz). The large extent of frequencies between the dispersion and attenuation phenomena is attributed to low permeability of the synthetic rock (30 nD) and assumed high viscosity of the pore fluid (10 cP) (see **Figures 4.10** and **4.21**). Because the example in **Table 4.5** is defined with 11% of total porosity only and high crack density (0.23), squirt flow effects are much more predominant than Biot's flow effects.

4.5 SUMMARY AND DISCUSSION

The effective medium methods for modeling of Biot's and squirt flow mechanisms consist of three steps: (I) definition of low-frequency reference elastic moduli for the effective medium calculated with the self-consistent approximation; (II) estimation of two

complex-valued, frequency-dependent equivalent bulk moduli and one complex-valued, frequency-dependent equivalent shear modulus for the solid background of the composite; and (III) calculation of effective elastic dynamic properties of the rock with Wu's (1966) self-consistent approximation. The combined effects of Biot's and squirt flow are simulated with a procedure to embed porous cavities into a solid background of elastic properties calculated as the addition of changes in solid moduli predicted by both new dynamic effective medium models to the grain moduli.

As I demonstrated above, fluid-related dispersion models relate the dynamic behavior of rocks to parameters such as porosity, permeability, fluid viscosity, and shape of cracks. Thus, the development of poroelastic rock physics models is beneficial for estimating of rock physics and petrophysical parameters in addition to estimating elastic properties of a formation. Dynamic effective medium models that take fluid-related dispersion mechanisms into account should be used rather than classical static effective medium theories.

For instance, for the synthetic rock described in **Table 4.1**, velocities and variation of amplitudes measured at ultrasonic frequencies (between 10^6 Hz and 10^{10} Hz in this case as shown in **Figure 4.24**) would detect Biot's and squirt flow effects. Providing that most of parameters of the rock are known, such as mineral composition, fluid saturation, and crack density, permeability can be estimated using the frequency of maximum attenuation that corresponds to Biot's flow effect. The estimation could be obtained by simulating results with the joint model and verifying velocity estimates with measurements. If the relative increase of velocity due to the squirt flow mechanism is also observed on laboratory readings, it would confirm the assumed crack aspect ratio and ensure the accuracy of elastic properties estimation.

Dispersion and attenuation phenomena displayed in **Figure 4.25** suggest that only squirt flow velocity can be obtained with laboratory measurements because Biot's flow effects occur at frequencies above the range of ultrasonic experiments. The absence of Biot's flow reading would be, in itself, an indication that the very low permeability value (refer to **Table 4.5**) simulated with the joint Biot/squirt flow model is valid. Squirt flow effects can then be used to obtain an assessment of fluid mobility, for example.

4.6 CONCLUSIONS

I introduced two practical and efficient effective medium methods to reproduce the effects of Biot's and squirt flows on velocity and wave attenuation. The models are based on the new separate definition of complex-valued, frequency-dependent solid elastic properties for compressional and shear waves. Using Wu's (1966) classical version of the self-consistent approximation, effective elastic properties of the rock are estimated and subsequently invoked to calculate wave velocities. Extensive comparisons between results obtained with the newly developed models and original equations of Biot (1956a, 1956b) and Chapman et al. (2006) confirm that predictions for both fluid-related mechanisms are valid and can be used to describe fluid-related dispersion effects. A simple procedure was then proposed to combine Biot's and squirt flow effects on velocity. It combines the frequency-dependent solid moduli computed with the new effective medium models for reproduction of Biot's flow and squirt flow velocities to construct an equivalent rock matrix affected by both fluid-related dispersion mechanisms.

The concept of frequency-dependent bulk and shear solid moduli is used to account for dispersion and attenuation caused by Biot's and squirt flow. However, they are only equivalent properties. The objective is not to suggest that the strength of the solid matrix

of a rock is source of dispersion or that dispersion mechanisms exclusively influence the solid elastic moduli. I showed that the latter was an efficient and practical concept to use jointly with the self-consistent approximation to compute the effective properties of a poroelastic rock that undergoes dispersion.

The theories of Biot's and squirt flow assume that pores and cracks are connected and fluid can flow within the pore space for that reason. To reproduce this feature, an improved effective medium model should invoke a combination of the SCA with the DEM as described in Chapter 2. My model combines Biot's and squirt flow mechanisms, but both dispersion mechanisms are uncoupled. Dispersion and attenuation phenomena associated with pore fluid flow might be interdependent and another effective medium model would need to be proposed based on the reproduction of velocity predictions obtained with an existing coupled model (Parra, 1997; Chapman et al., 2002). Furthermore, fluid-related effects are not the only sources of wave dispersion and attenuation in porous rocks. A more complete model that combines as many dispersion mechanisms as possible would allow for cross-validation of the prediction of petrophysical properties and for further verification of rock fabric parameters describing a rock.

Properties of synthetic case for Biot's flow		
Solid background	Quartz concentration (%)	55
	Calcite concentration (%)	25
	Clay concentration (%)	20
	Grain size (mm)	0.2
Pore space	Fluid type	Water
	Total porosity (%)	20
	Crack density	0.1
	Crack length (μm)	50
	Crack aspect ratio	0.005
	Permeability (mD)	65

Table 4.1: Petrophysical and rock physics properties assumed in the synthetic case used to investigate dispersive behavior predicted by Biot's flow theory and to verify the agreement between the original Biot's (1956a, 1956b) relations and the new effective medium model for Biot's flow.

	Compressional velocity		Shear velocity	
Synthetic case	**Biot (1956) model (%)**	**New EM model (%)**	**Biot (1956) model (%)**	**New EM model (%)**
$\phi = 10\%$	0.261	0.267	0.398	0.396
$\phi = 18\%$	0.816	0.814	1.28	1.27
$\phi = 25\%$	1.48	1.45	2.49	2.46

Table 4.2: Percentages of dispersion of compressional- and shear-wave velocities calculated with Biot's (1956a, 1956b) original equations and the new effective medium (EM) method for Biot's flow modeling for the synthetic composite described in Table 4.1 with 10%, 18%, and 25% of total porosity.

	Compressional velocity		Shear velocity	
Synthetic case	**Biot (1956) model (%)**	**New EM model (%)**	**Biot (1956) model (%)**	**New EM model (%)**
$\kappa = 1\,\text{D}$	0.994	0. 987	1.59	1.57
$\kappa = 0.1\,\text{D}$	0.994	0.987	1.59	1.57
$\kappa = 1\,\text{mD}$	0.994	0. 987	1.59	1.57

Table 4.3: Percentages of dispersion for compressional- and shear-wave velocities calculated with Biot's (1956a, 1956b) original equations and the new effective medium (EM) method for Biot's flow modeling for the synthetic composite described in Table 4.1 exhibiting 1 D, 0.1 D, and 1 mD of permeability.

	Compressional velocity		Shear velocity	
Synthetic case	**Biot (1956) model (%)**	**New EM model (%)**	**Biot (1956) model (%)**	**New EM model (%)**
Water	0.994	0.987	1.59	1.57
Oil	0.692	0.697	1.11	1.1
Gas	0.153	0.158	0.185	0.183

Table 4.4: Percentages of dispersion for compressional- and shear-wave velocities calculated with Biot's (1956a, 1956b) original equations and the new effective medium (EM) method for Biot's flow modeling for the synthetic composite described in Table 4.1 saturated with water, oil, and gas.

Properties of synthetic case for squirt flow		
Solid background	Quartz concentration (%)	48
	Calcite concentration (%)	7
	Clay concentration (%)	45
	Grain size (mm)	0.045
Pore space	Fluid type	Oil
	Total porosity (%)	11
	Crack density	0.23
	Crack length (μm)	40
	Crack aspect ratio	0.005
	Permeability (nD)	30

Table 4.5: Petrophysical and rock physics properties assumed in the synthetic case defined to investigate dispersive behavior predicted by Chapman et al.'s (2006) theory for squirt flow and verify the agreement between Chapman et al.'s equations and the new effective medium model for squirt flow.

	Compressional velocity		Shear velocity	
Synthetic case	**Chapman et al. (2006) model (%)**	**New EM model (%)**	**Chapman et al. (2006) model (%)**	**New EM model (%)**
$\gamma = 0.01$	2.34	2.32	1.48	1.43
$\gamma = 0.05$	2.79	2.78	1.58	1.56
$\gamma = 0.001$	3.28	3.31	1.68	1.69

Table 4.6: Percentages of dispersion for compressional- and shear-wave velocities calculated with Chapman et al.'s (2006) equations and the new effective medium (EM) method for squirt flow modeling for the synthetic composite described in Table 4.5 with crack aspect ratios of 0.01, 0.05, and 0.001.

	Compressional velocity		Shear velocity	
Synthetic case	**Chapman et al. (2006) model (%)**	**New EM model (%)**	**Chapman et al. (2006) model (%)**	**New EM model (%)**
$\kappa = 1$ nD	2.79	2.78	1.58	1.56
$\kappa = 0.1$ μD	2.79	2.78	1.58	1.56
$\kappa = 10$ μD	2.79	2.78	1.58	1.56

Table 4.7: Percentages of dispersion for compressional- and shear-wave velocities calculated with Chapman et al.'s (2006) equations and the new effective medium (EM) method for squirt flow modeling for the synthetic composite described in Table 4.5 exhibiting 1 nD, 0.1 μD, and 10 μD of permeability.

	Compressional velocity		Shear velocity	
Synthetic case	**Chapman et al. (2006) model (%)**	**New EM model (%)**	**Chapman et al. (2006) model (%)**	**New EM model (%)**
Water	1.94	1.94	1.62	1.59
Oil	2.79	2.78	1.58	1.56
Gas	3.48	3.37	1.13	1.11

Table 4.8: Percentages of dispersion for compressional- and shear-wave velocities calculated with Chapman et al.'s (2006) equations and the new effective medium (EM) method for squirt flow modeling for the synthetic composite described in Table 4.5 saturated with water, oil, and gas.

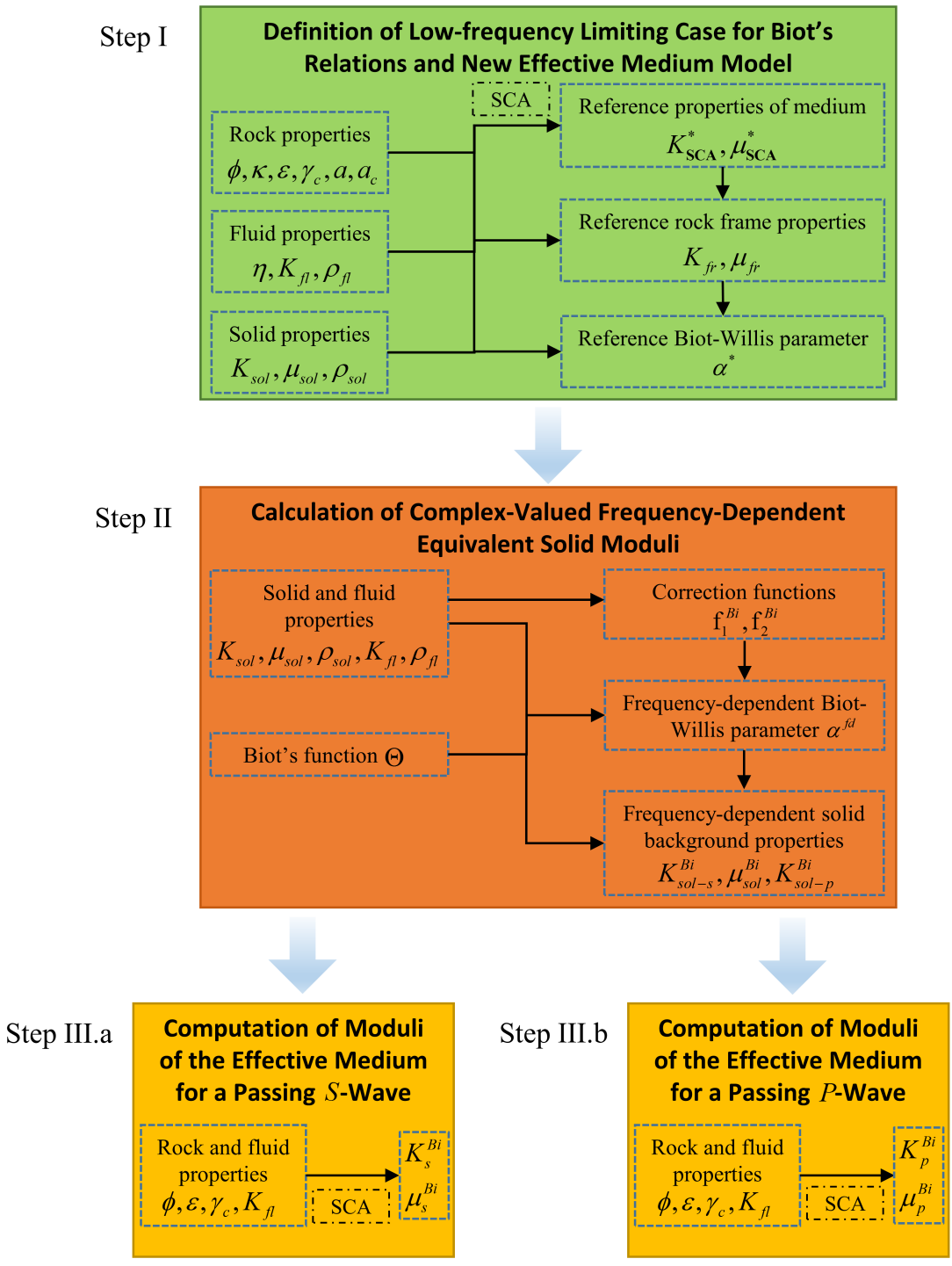

Figure 4.1: Effective medium method workflow for calculation of frequency-dependent effective moduli for reproduction of Biot's flow effects in saturated rocks.

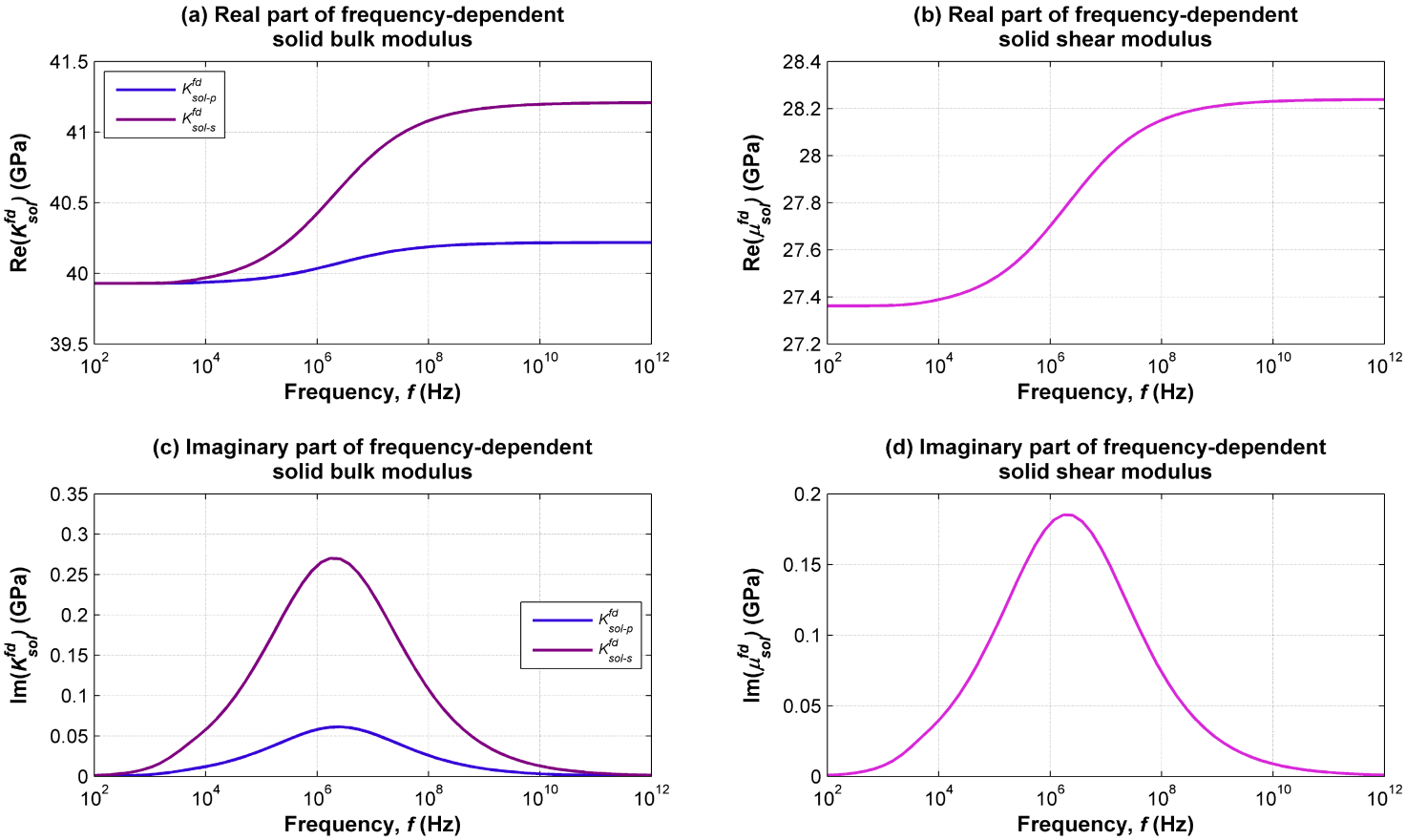

Figure 4.2: Frequency-dependent equivalent elastic moduli of the solid background of the synthetic example described in Table 4.1. Moduli are calculated with the new effective medium method for modeling Biot's flow mechanism. Panel a: real part of solid bulk moduli. Panel b: real part of solid shear modulus. Panel c: imaginary part of solid bulk moduli. Panel d: imaginary part of solid shear modulus. In panels a and c, blue and purple curves identify the bulk modulus associated with a propagating compressional and shear wave, respectively.

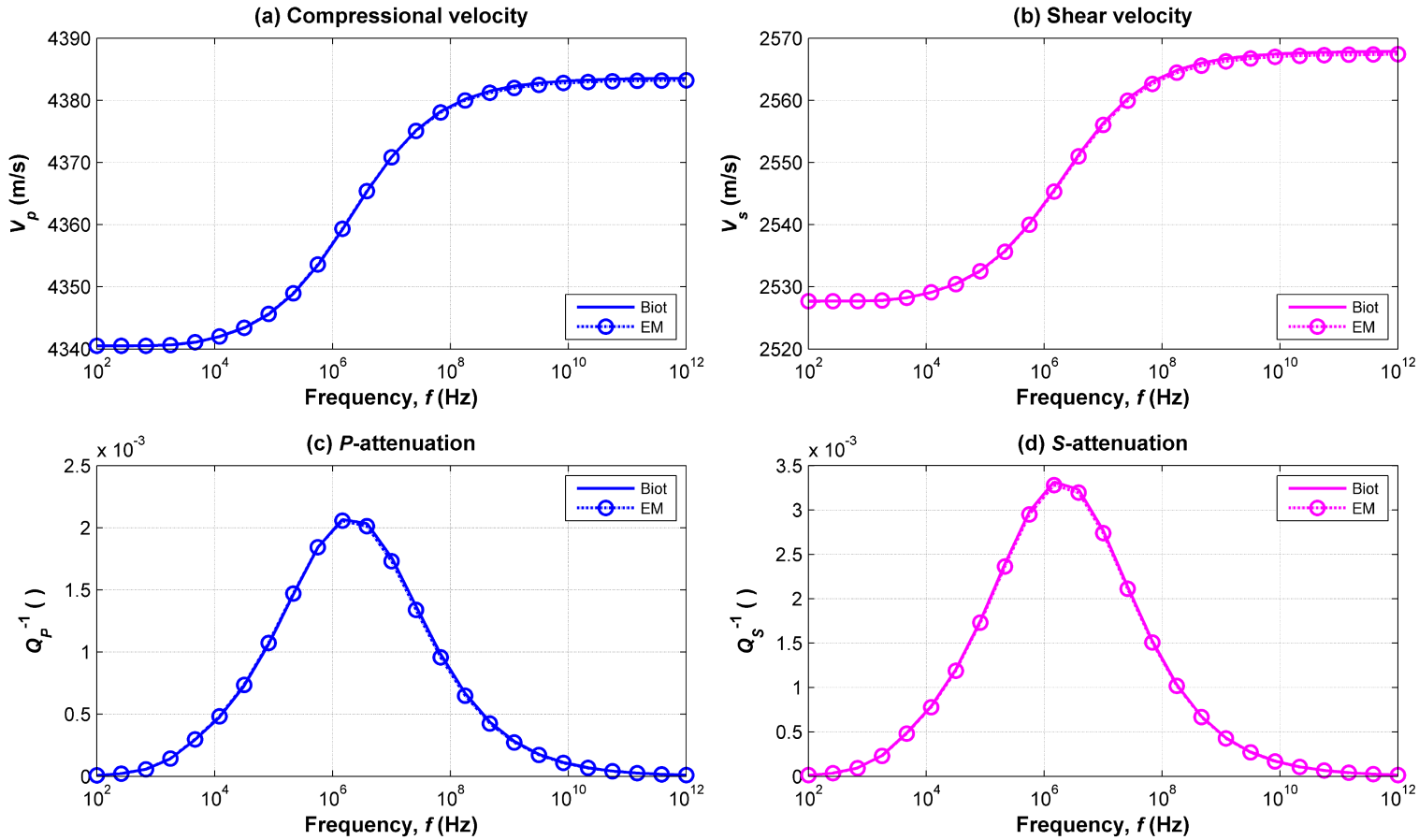

Figure 4.3: Biot's flow effects on compressional- and shear-wave velocities and attenuations for the synthetic example described in Table 4.1. Panel a: P-wave velocity. Panel b: S-wave velocity. Panel c: P-wave attenuation. Panel d: S-wave attenuation. Solid curves and dashed curves with circle markers identify velocity and attenuation calculated with Biot's equations and the new effective medium model, respectively.

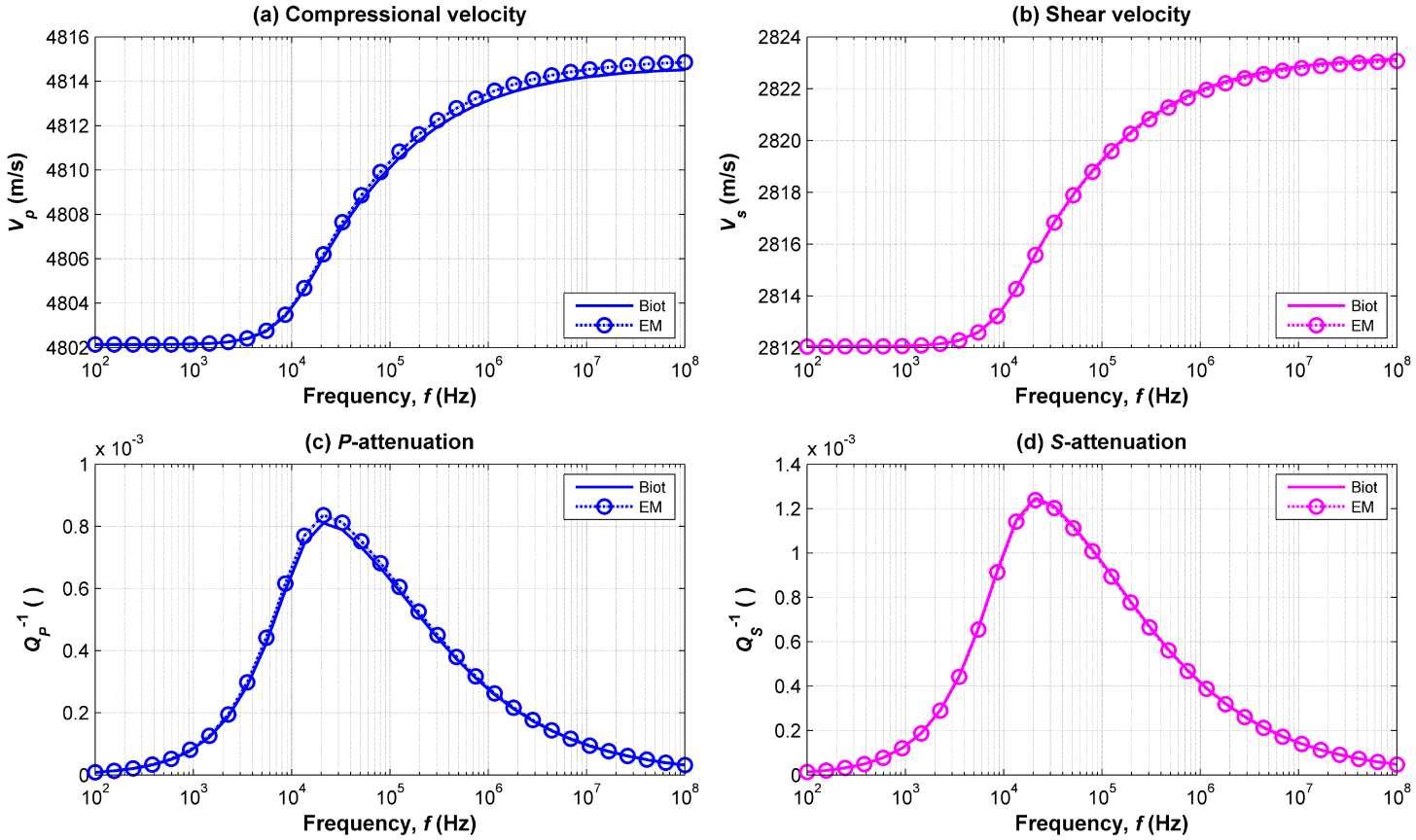

Figure 4.4: Biot's flow effects on compressional- and shear-wave velocities and attenuations for the synthetic example described in Table 4.1 with 10% of total porosity. Panel a: P-wave velocity. Panel b: S-wave velocity. Panel c: P-wave attenuation. Panel d: S-wave attenuation. Solid curves and dashed curves with circle markers identify velocity and attenuation calculated with Biot's equations and the new effective medium model, respectively.

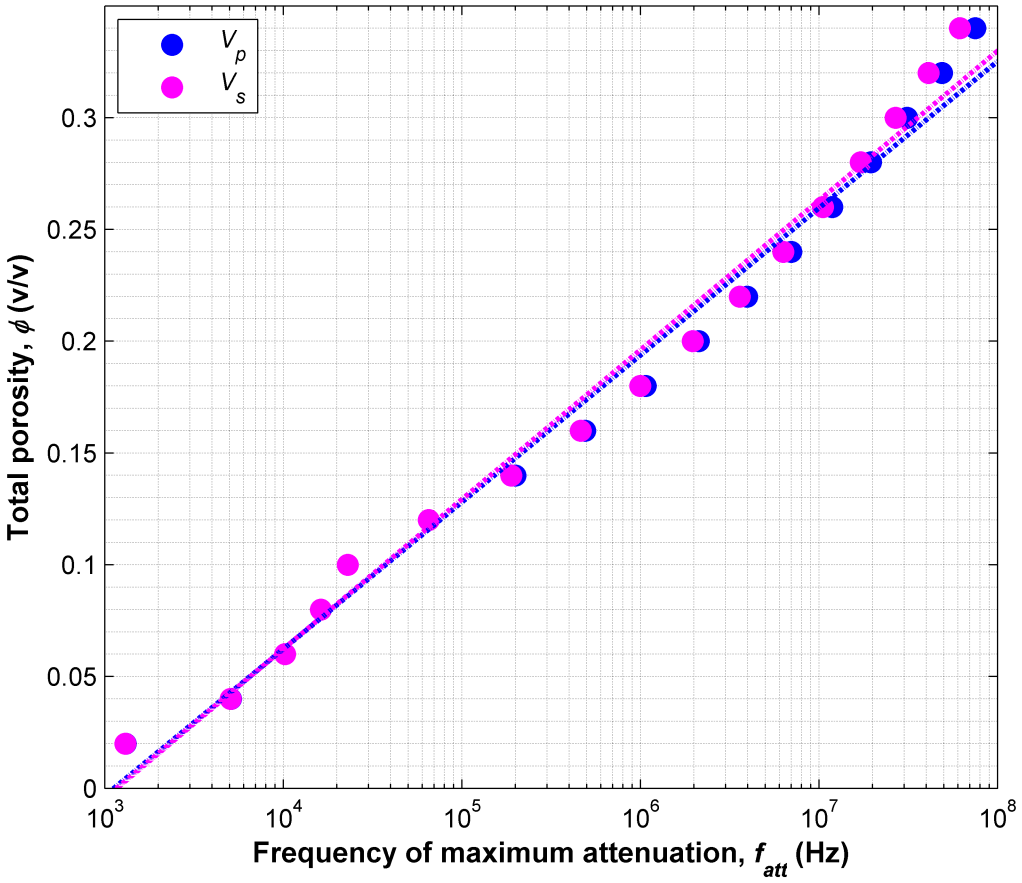

Figure 4.5: Relationship between total porosity and frequency of maximum attenuation calculated with the effective medium method for modeling Biot's flow mechanism. Blue and magenta dots identify values of frequency of maximum attenuation obtained for compressional and shear waves, respectively.

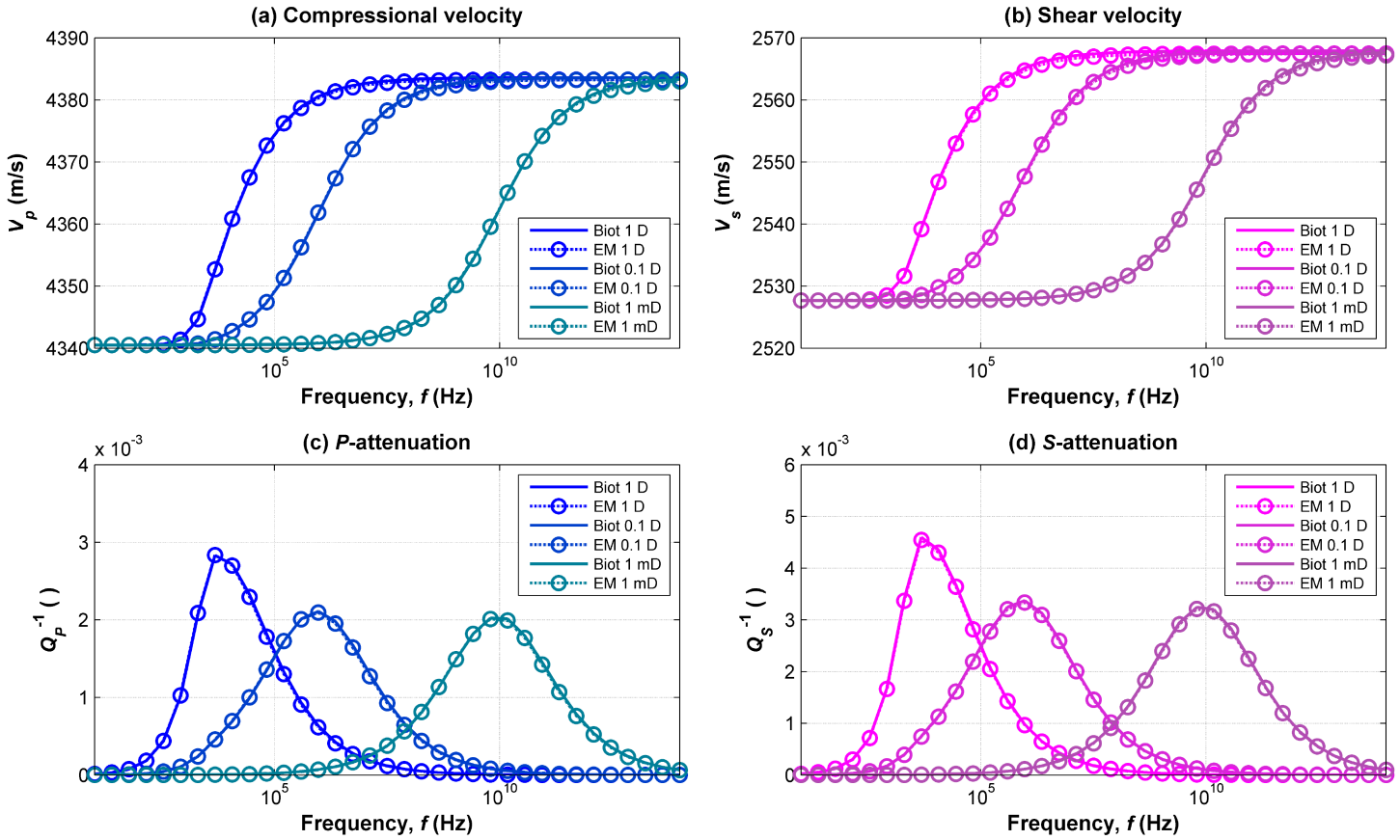

Figure 4.6: Biot's flow effects on compressional- and shear-wave velocities and attenuations for the synthetic example described in Table 4.1 with permeability of 1 D, 0.1 D, and 1 mD. Panel a: P-wave velocity. Panel b: S-wave velocity. Panel c: P-wave attenuation. Panel d: S-wave attenuation. Solid curves and dashed curves with circle markers identify velocity and attenuation calculated with Biot's equations and the new effective medium model, respectively.

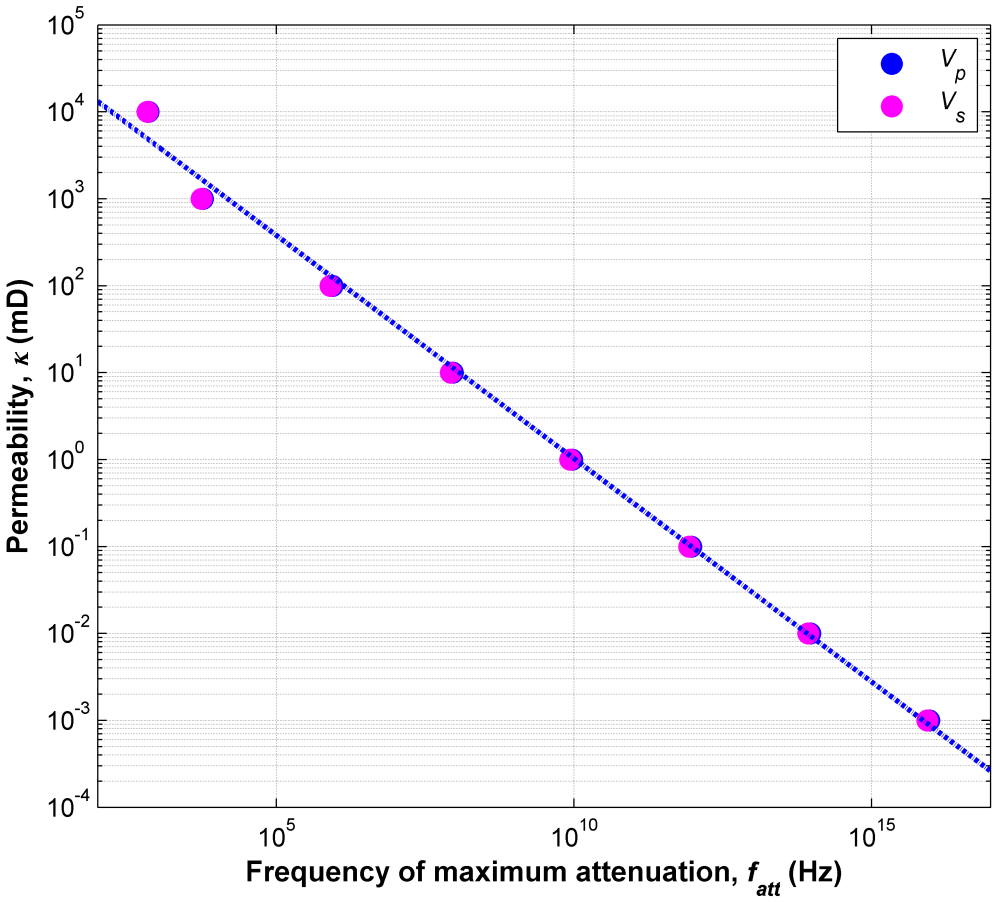

Figure 4.7: Relationship between permeability and frequency of maximum attenuation calculated with the effective medium method for modeling Biot's flow mechanism. Blue and magenta dots identify values of frequency of maximum attenuation obtained for compressional and shear waves, respectively.

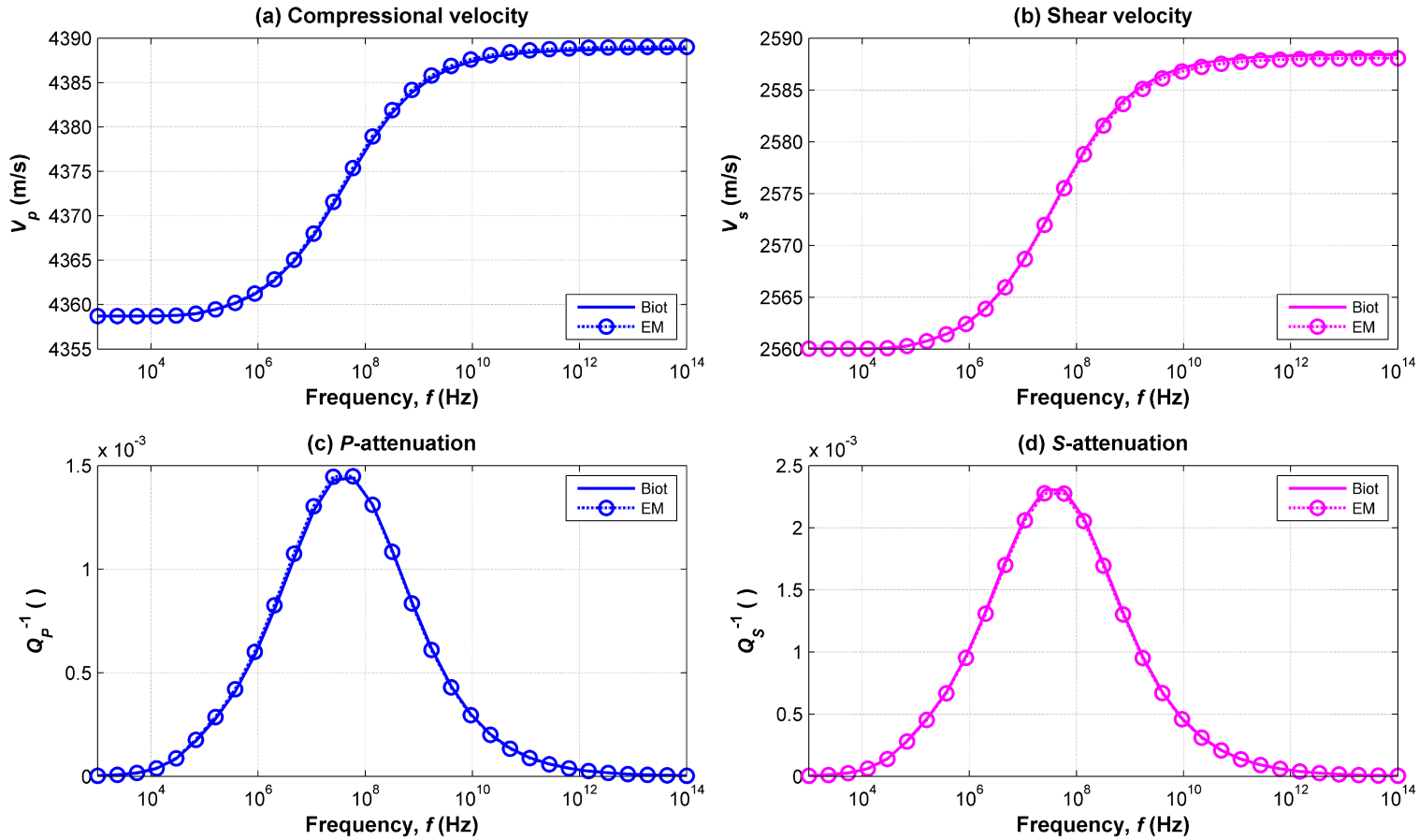

Figure 4.8: Biot's flow effects on compressional- and shear-wave velocities and attenuations for the synthetic example described in Table 4.1 saturated with oil. Panel a: P-wave velocity. Panel b: S-wave velocity. Panel c: P-wave attenuation. Panel d: S-wave attenuation. Solid curves and dashed curves with circle markers identify velocity and attenuation calculated with Biot's equations and the new effective medium model, respectively.

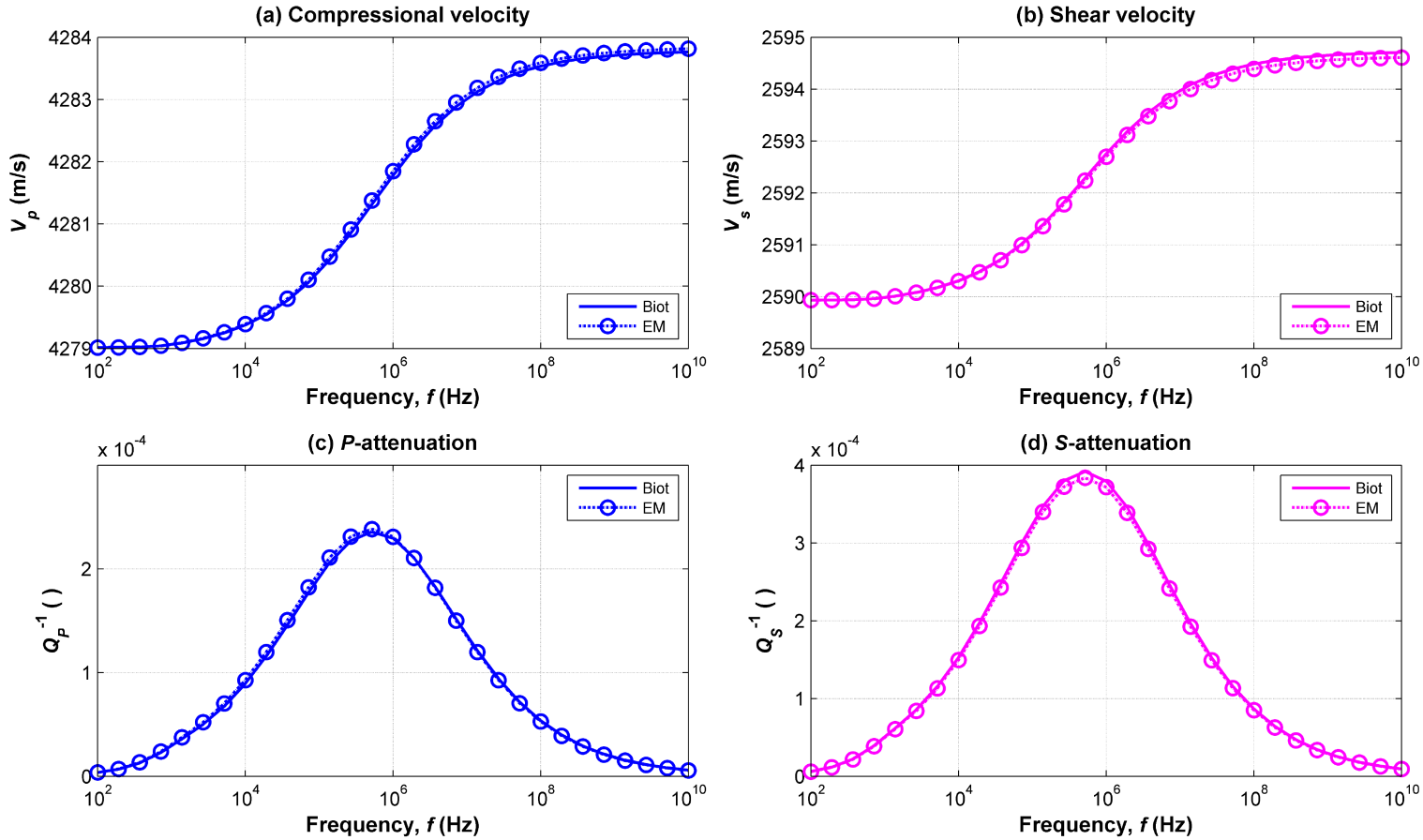

Figure 4.9: Biot's flow effects on compressional- and shear-wave velocities and attenuations for the synthetic example described in Table 4.1 saturated with gas. Panel a: P-wave velocity. Panel b: S-wave velocity. Panel c: P-wave attenuation. Panel d: S-wave attenuation. Solid curves and dashed curves with circle markers identify velocity and attenuation calculated with Biot's equations and the new effective medium model, respectively.

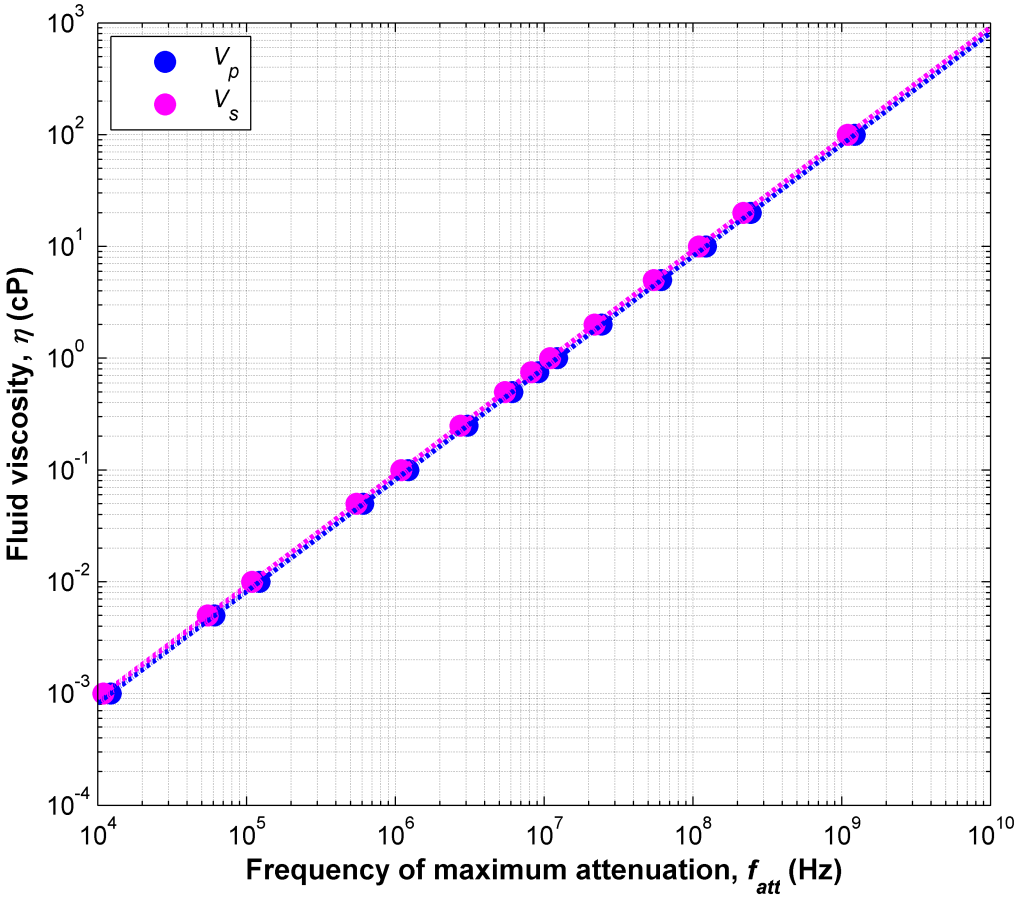

Figure 4.10: Relationship between fluid viscosity and frequency of maximum attenuation calculated with the effective medium method for modeling Biot's flow mechanism. Blue and magenta dots identify values of frequency of maximum attenuation obtained for compressional and shear waves, respectively.

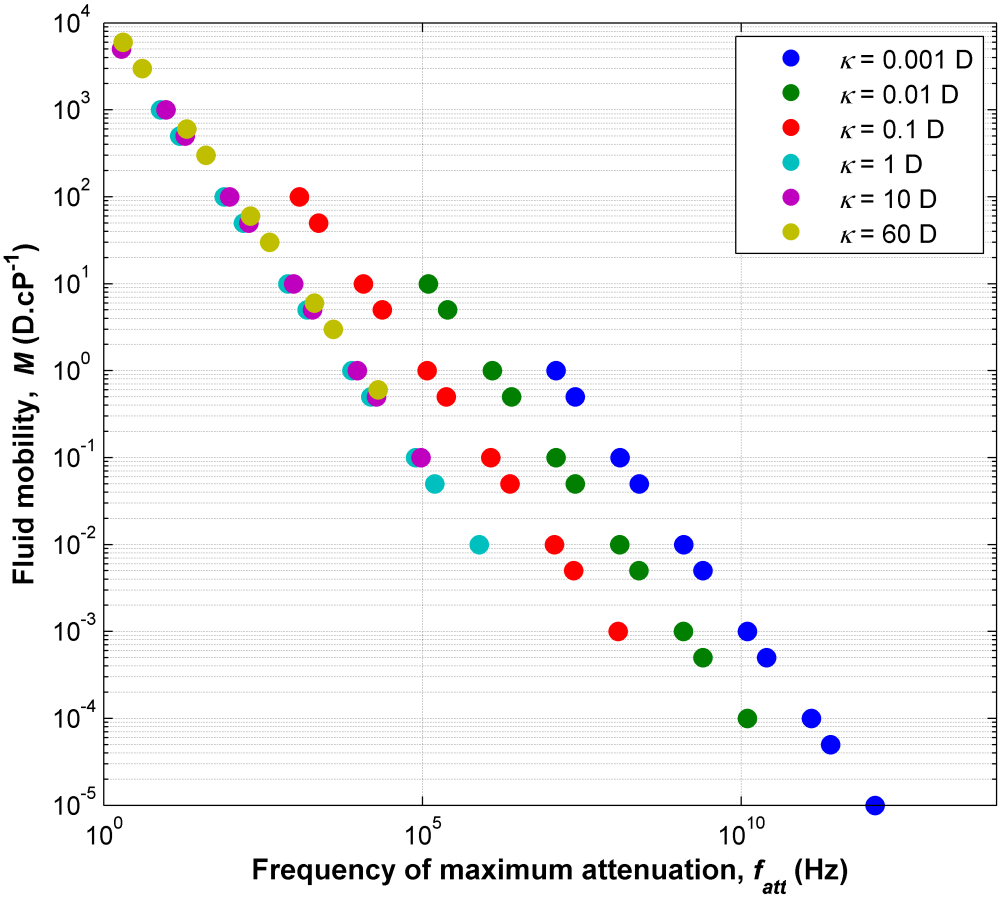

Figure 4.11: Relationship between fluid mobility and frequency of maximum attenuation for a compressional wave calculated with the effective medium method for modeling Biot's flow mechanism. Blue, green, red, cyan, magenta, and gold dots identify rock permeability of 1 mD, 10 mD, 0.1 D, 1 D, 10 D, and 60 D, respectively.

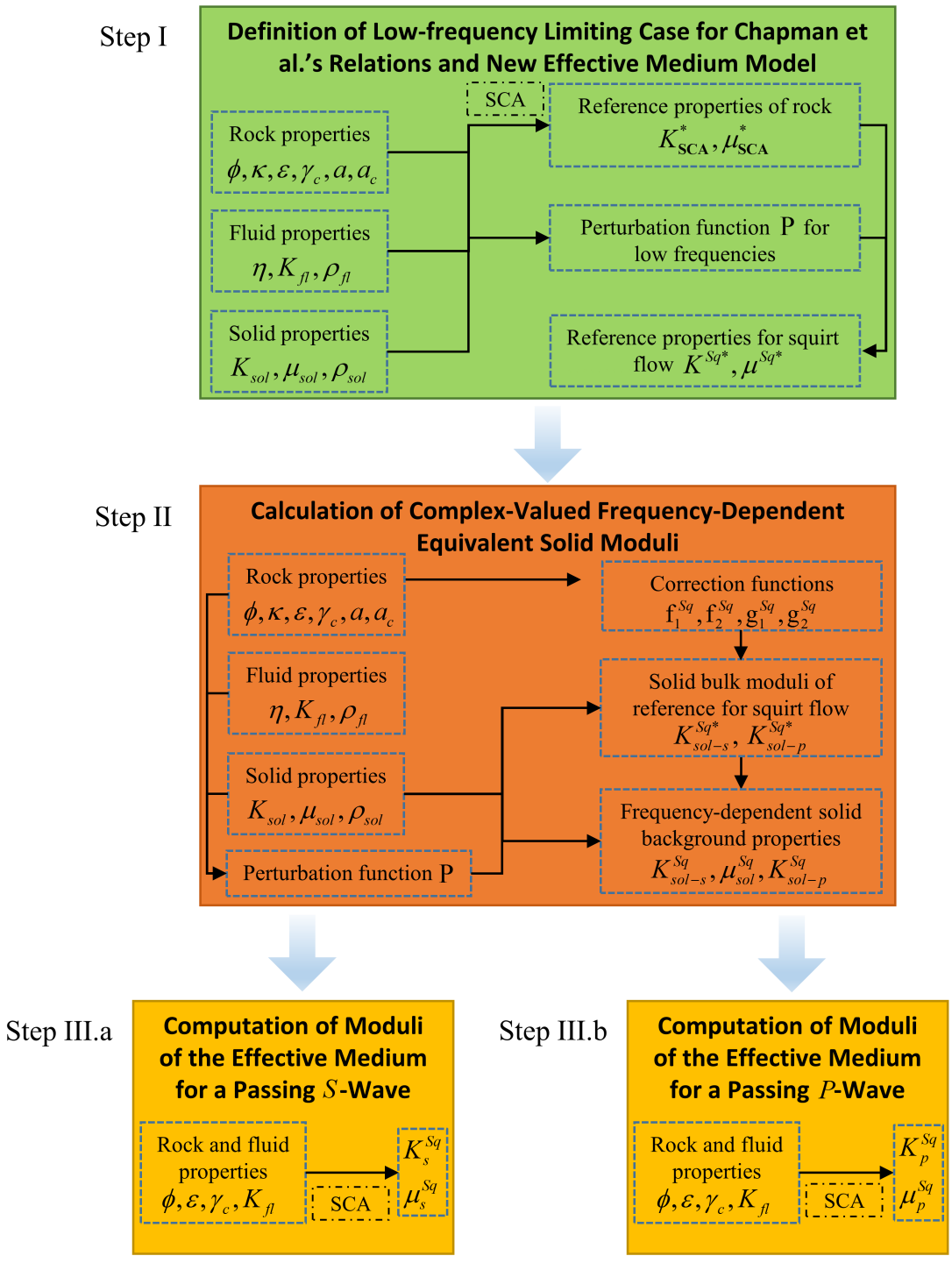

Figure 4.12: Effective medium method workflow for calculation of frequency-dependent effective moduli for reproduction of squirt flow effects in saturated rocks.

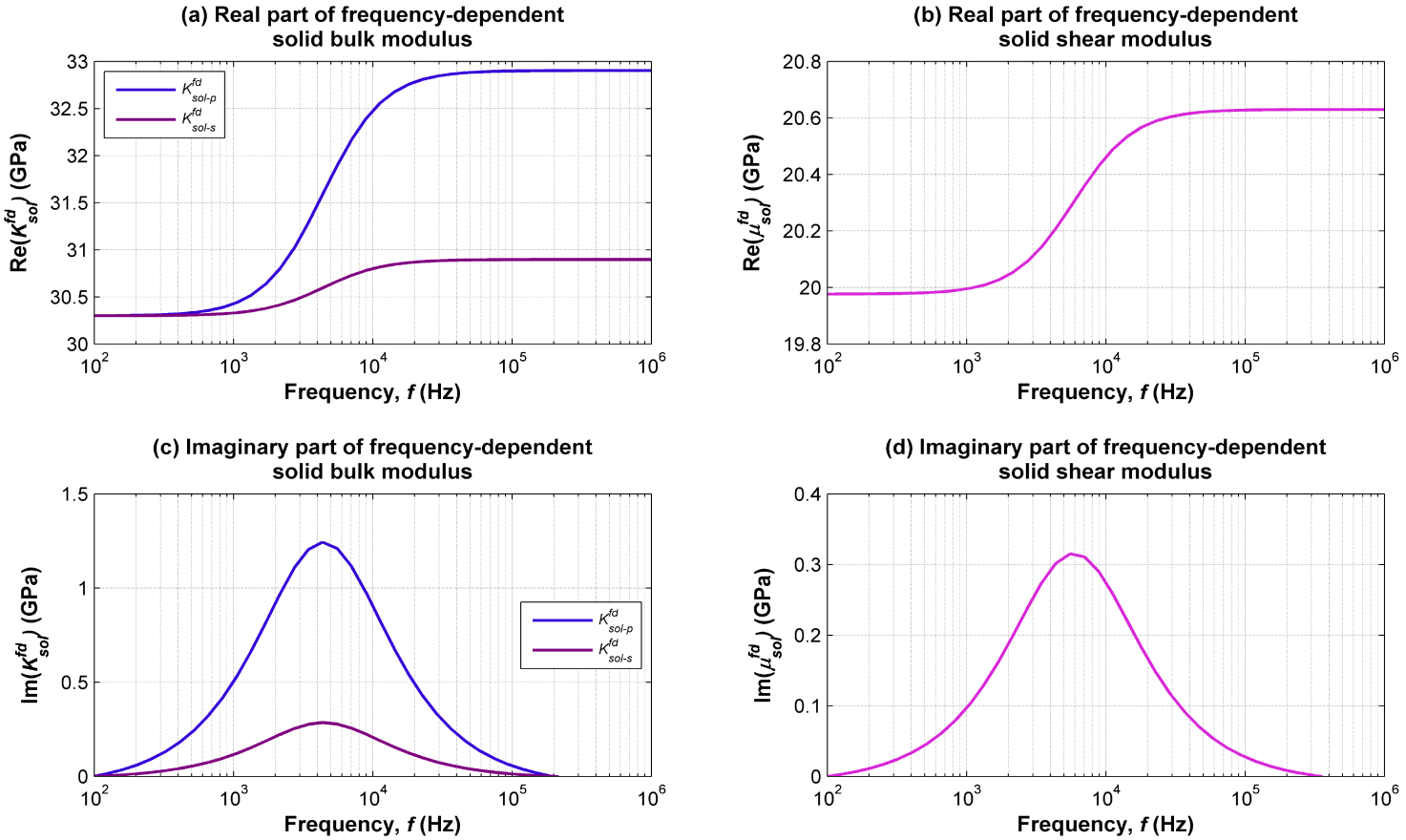

Figure 4.13: Frequency-dependent equivalent elastic moduli of the solid background of the synthetic example described in Table 4.5. Moduli are calculated with the new effective medium method for modeling the squirt flow mechanism. Panel a: real part of solid bulk moduli. Panel b: real part of solid shear modulus. Panel c: imaginary part of solid bulk moduli. Panel d: imaginary part of solid shear modulus. In panels a and c, blue and purple curves identify the bulk modulus associated with a propagating compressional and shear wave, respectively.

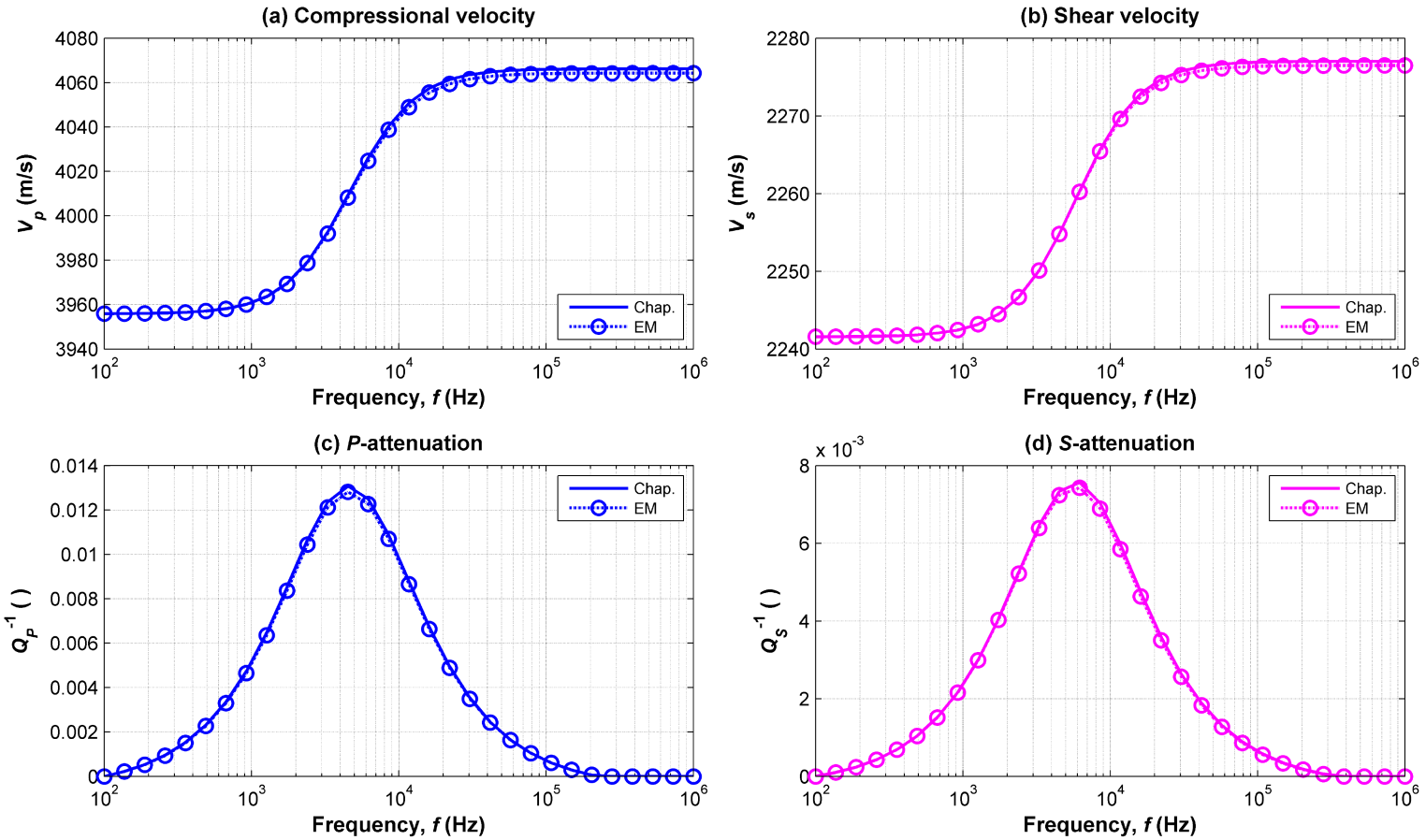

Figure 4.14: Squirt flow effects on compressional- and shear-wave velocities and attenuations for the synthetic example defined in Table 4.5. Panel a: P-wave velocity. Panel b: S-wave velocity. Panel c: P-wave attenuation. Panel d: S-wave attenuation. Solid curves and dashed curves with circle markers identify velocity and attenuation calculated with Chapman et al.'s equations and the new effective medium model, respectively.

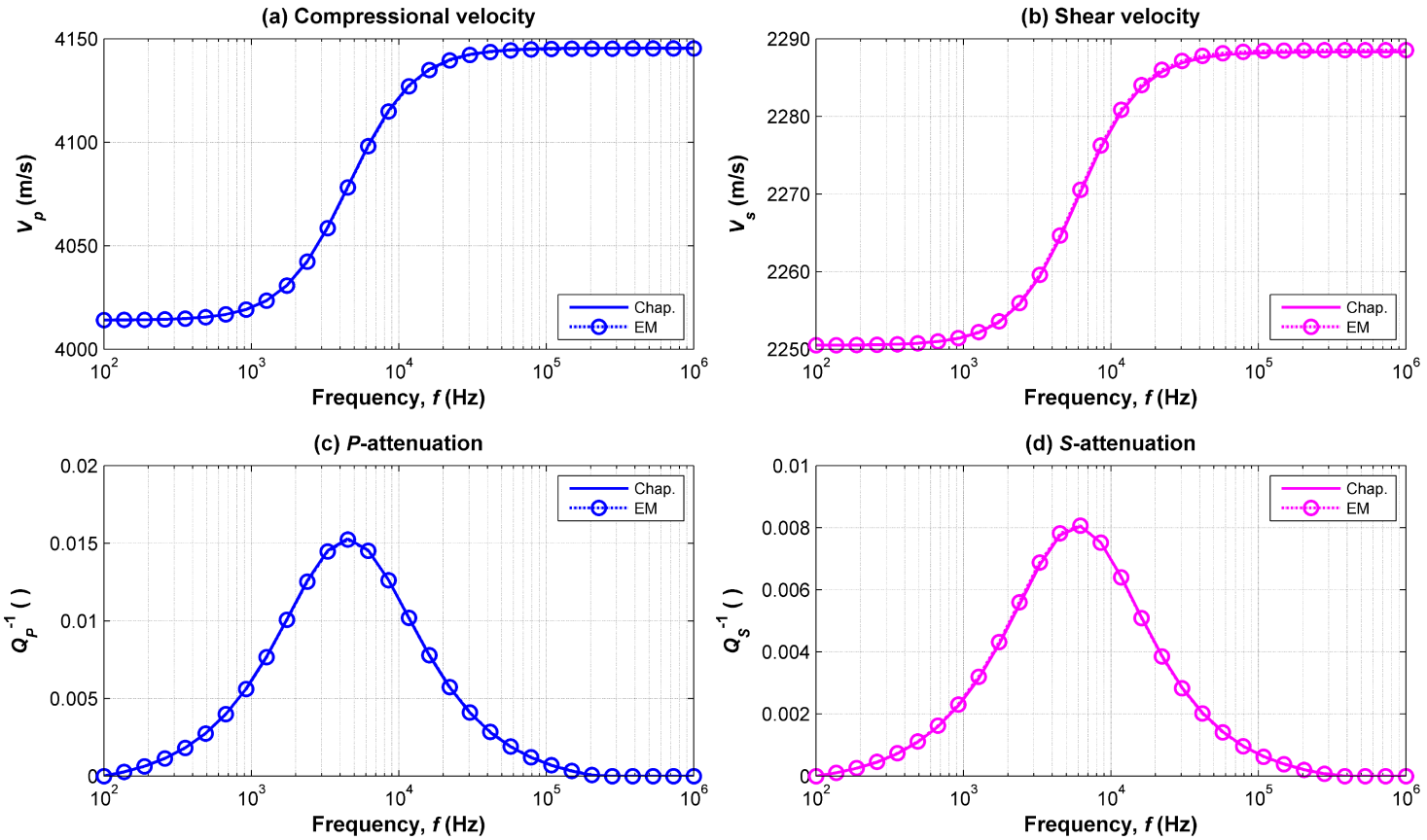

Figure 4.15: Squirt flow effects on compressional- and shear-wave velocities and attenuations for the synthetic example described in Table 4.5 exhibiting crack aspect ratio of 0.001. Panel a: P-wave velocity. Panel b: S-wave velocity. Panel c: P-wave attenuation. Panel d: S-wave attenuation. Solid curves and dashed curves with circle markers identify velocity and attenuation calculated with Chapman et al.'s equations and the new effective medium model, respectively.

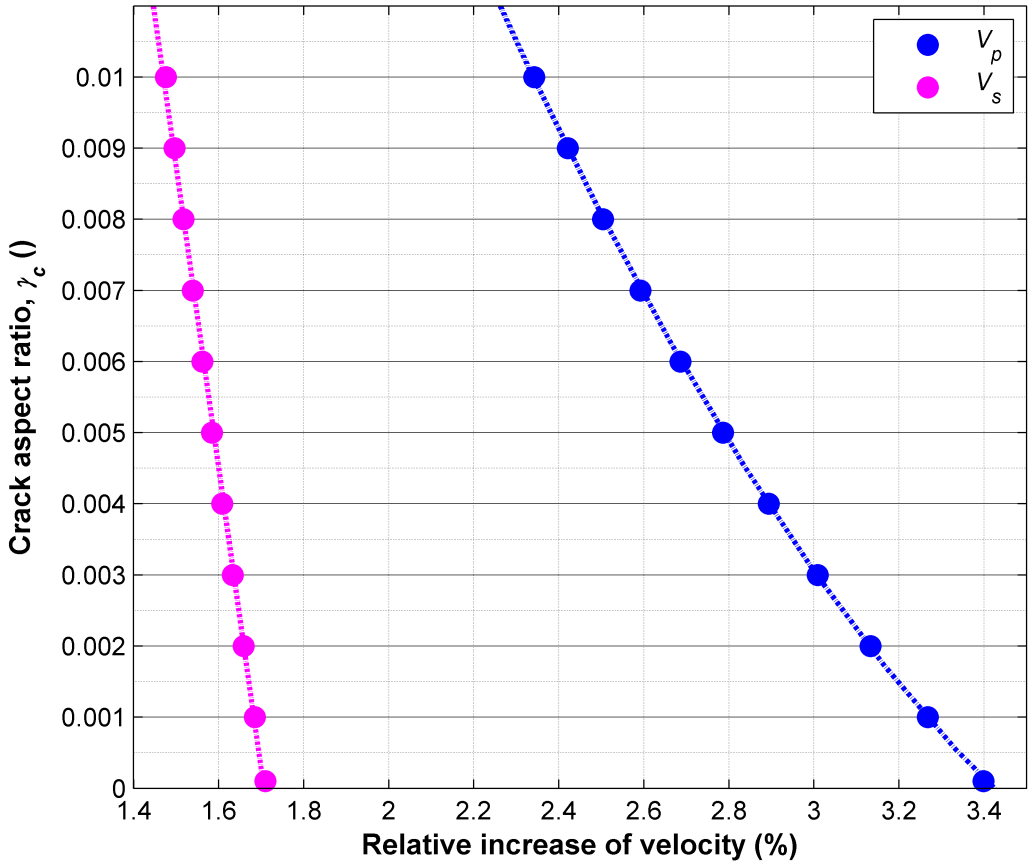

Figure 4.16: Relationships between crack aspect ratio and percentage of dispersion calculated with the effective medium method for modeling the squirt flow mechanism. Blue and magenta dots identify relative increase of velocity obtained for compressional and shear waves, respectively.

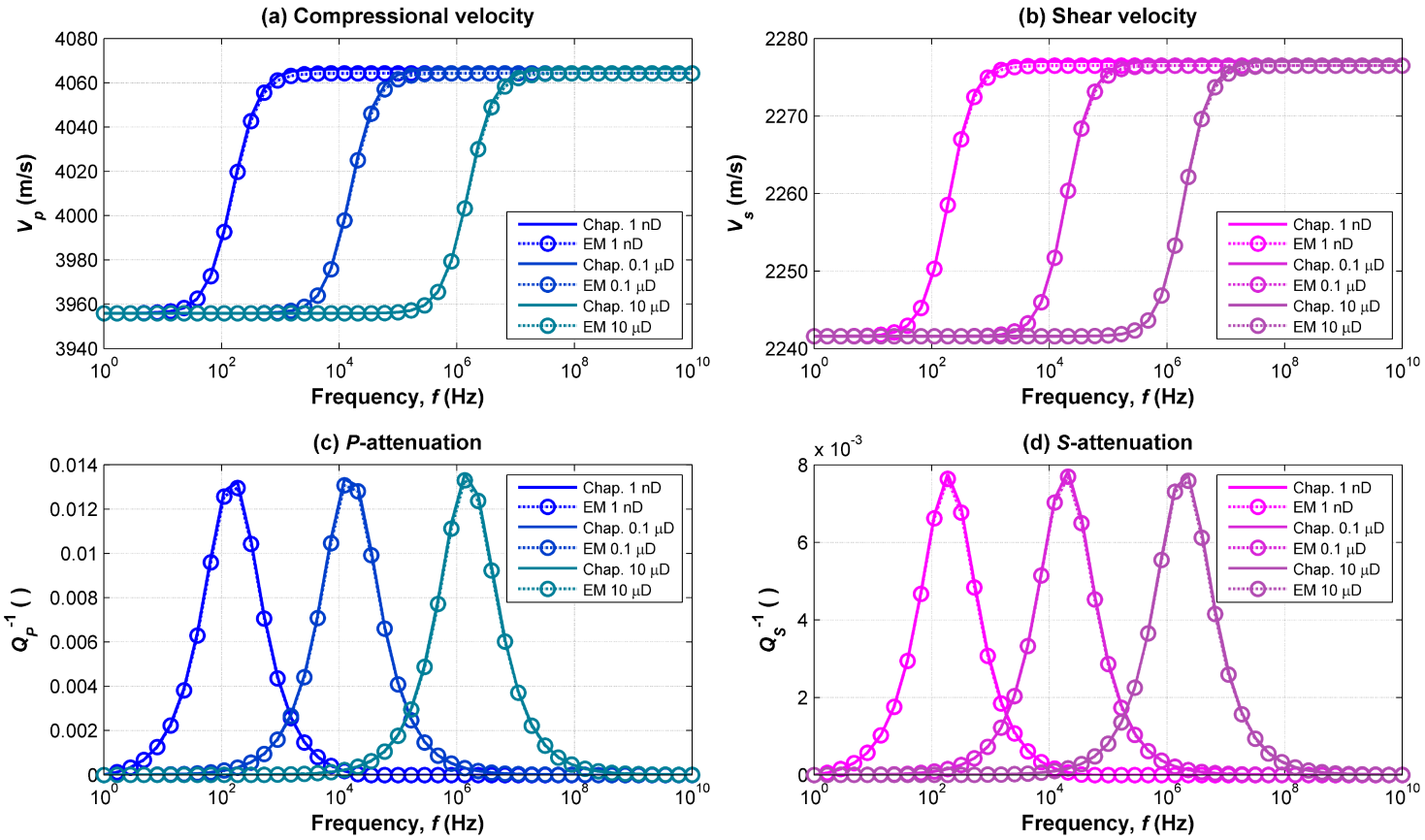

Figure 4.17: Squirt flow effects on compressional- and shear-wave velocities and attenuations for the synthetic example described in Table 4.5 with permeability of 1 nD, 0.1 μD, and 10 μD. Panel a: P-wave velocity. Panel b: S-wave velocity. Panel c: P-wave attenuation. Panel d: S-wave attenuation. Solid curves and dashed curves with circle markers identify velocity and attenuation calculated with Chapman et al.'s equations and the new effective medium model, respectively.

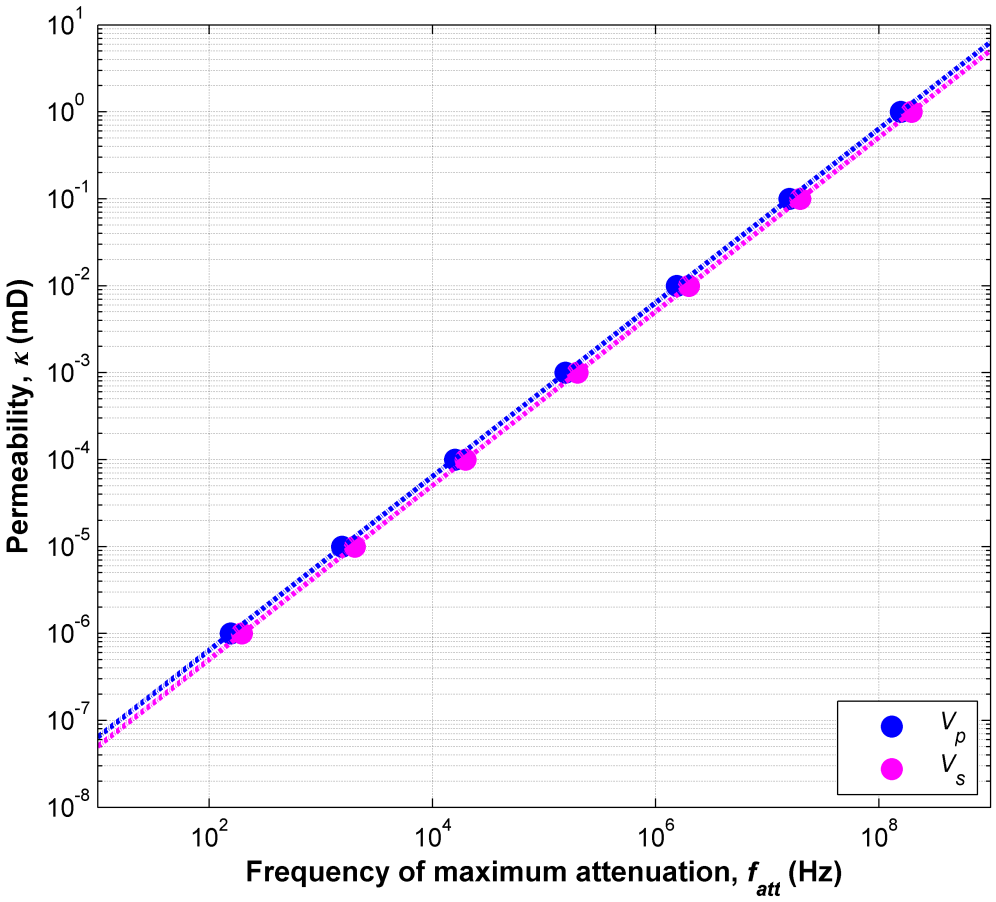

Figure 4.18: Relationship between permeability and frequency of maximum attenuation calculated with the effective medium method for modeling the squirt flow mechanism. Blue and magenta dots identify values of frequency of maximum attenuation obtained for compressional and shear waves, respectively.

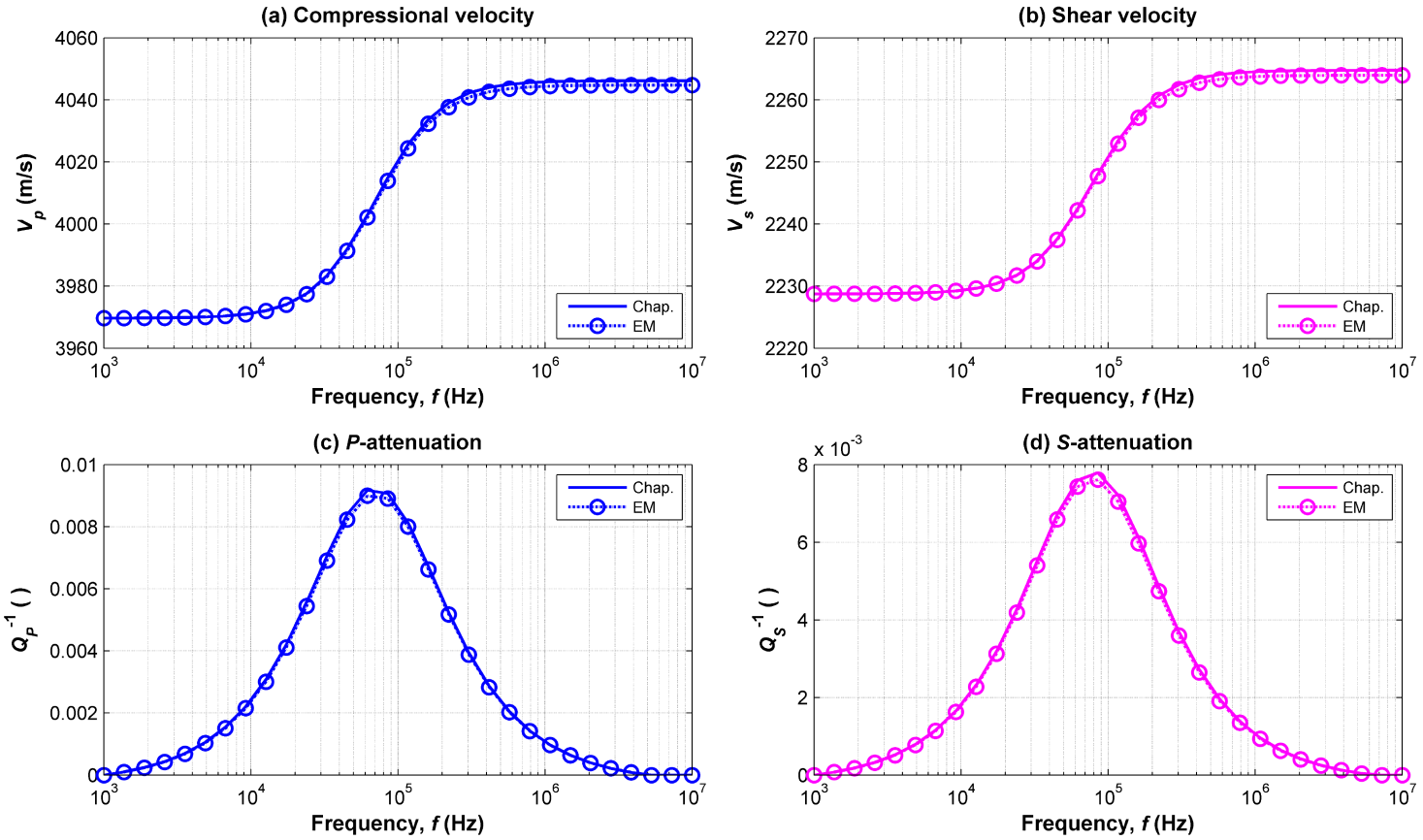

Figure 4.19: Squirt flow effects on compressional- and shear-wave velocities and attenuations for the synthetic example described in Table 4.5 saturated with water. Panel a: P-wave velocity. Panel b: S-wave velocity. Panel c: P-wave attenuation. Panel d: S-wave attenuation. Solid curves and dashed curves with circle markers identify velocity and attenuation calculated with Chapman et al.'s equations and the new effective medium model, respectively.

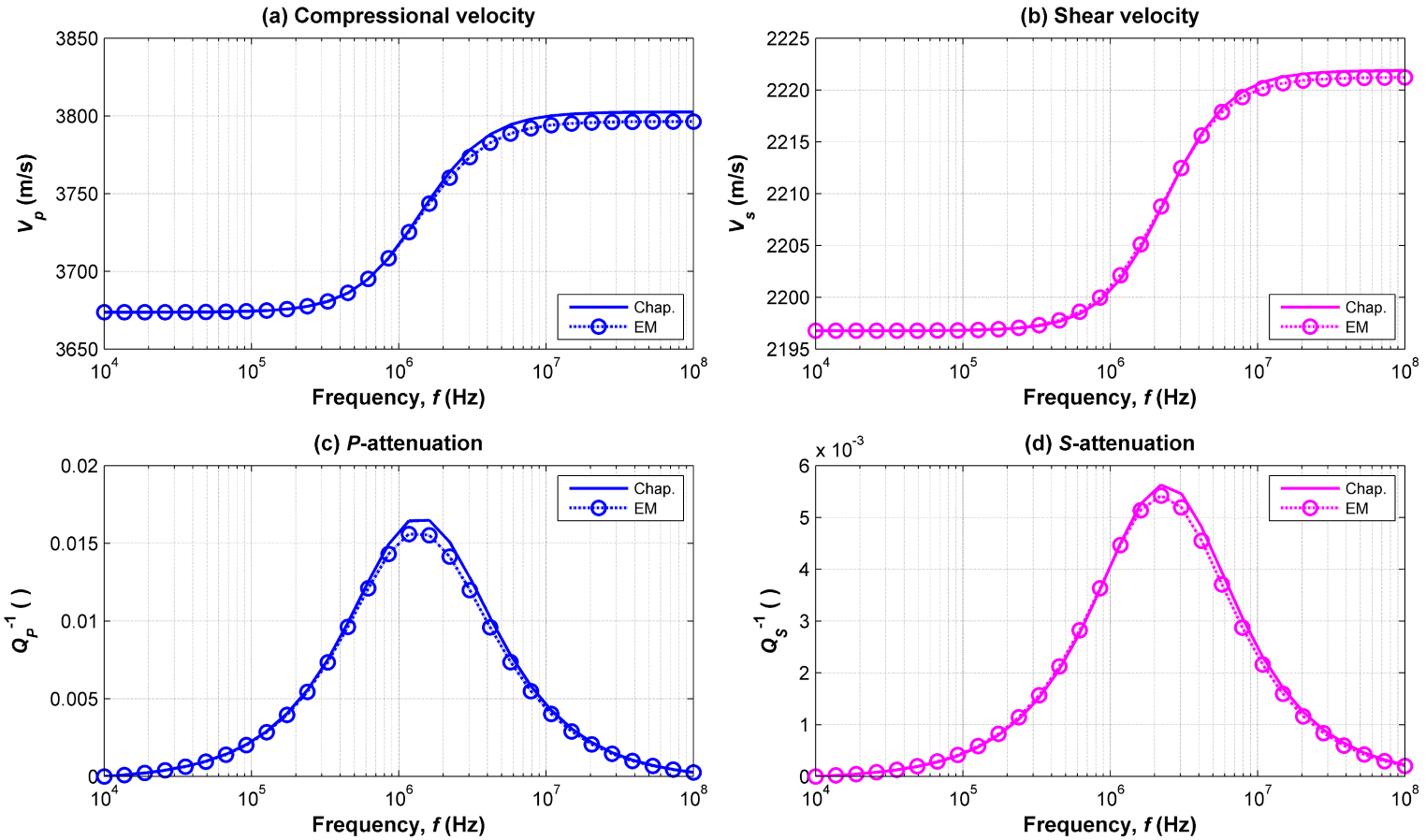

Figure 4.20: Squirt flow effects on compressional- and shear-wave velocities and attenuations for the synthetic example described in Table 4.5 saturated with gas. Panel a: P-wave velocity. Panel b: S-wave velocity. Panel c: P-wave attenuation. Panel d: S-wave attenuation. Solid curves and dashed curves with circle markers identify velocity and attenuation calculated with Chapman et al.'s equations and the new effective medium model, respectively.

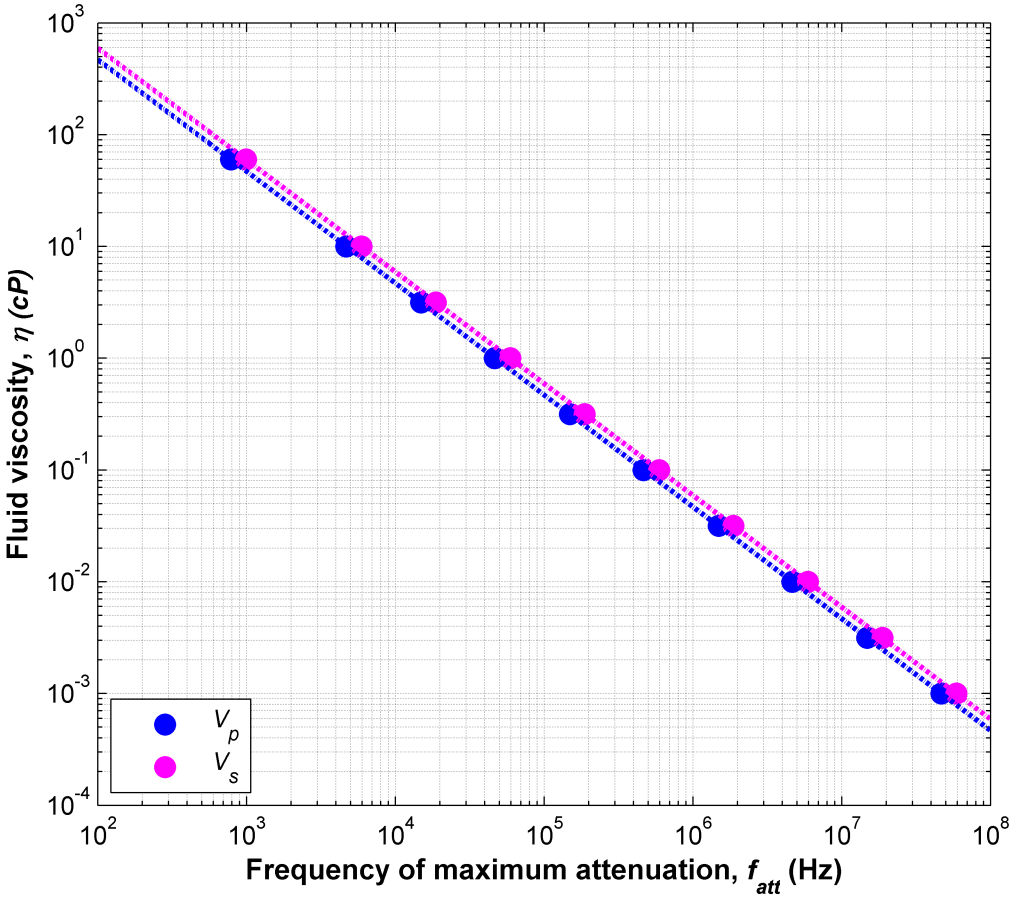

Figure 4.21: Relationship between fluid viscosity and frequency of maximum attenuation calculated with the effective medium method for modeling the squirt flow mechanism. Blue and magenta dots identify values of frequency of maximum attenuation obtained for compressional and shear waves, respectively.

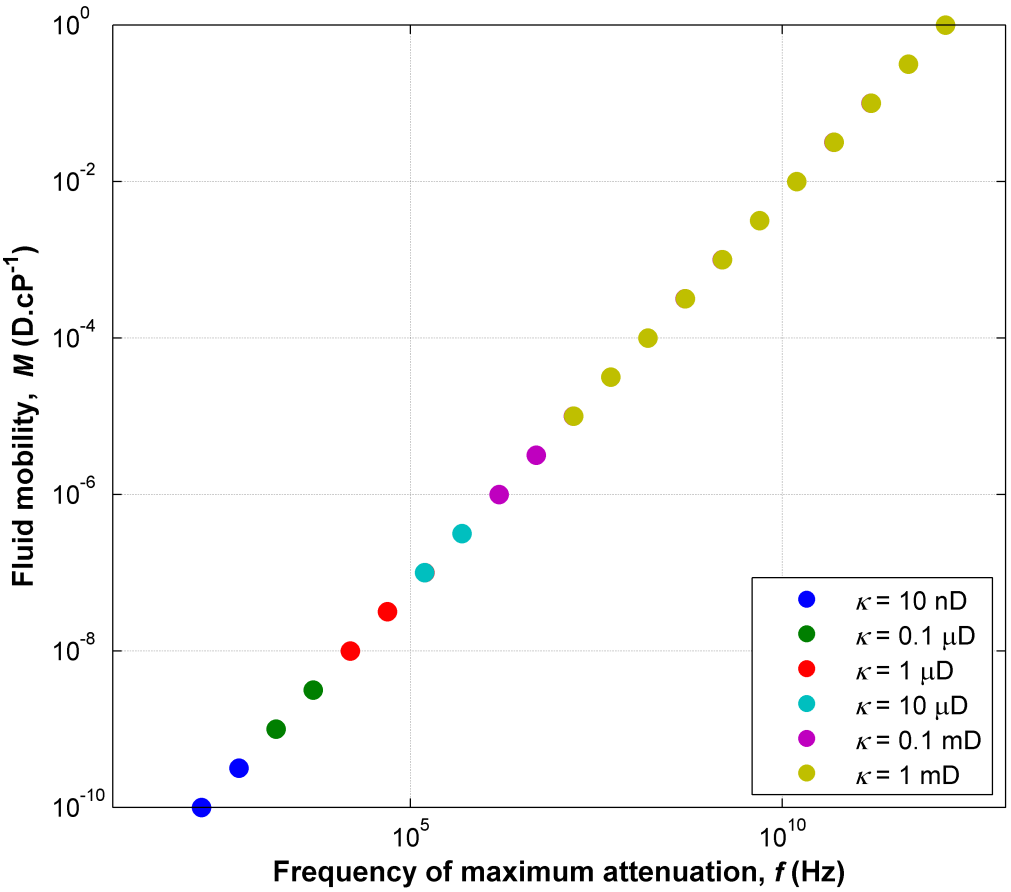

Figure 4.22: Relationship between fluid mobility and frequency of maximum attenuation for a compressional wave calculated with the effective medium method for modeling the squirt flow mechanism. Blue, green, red, cyan, magenta, and gold dots identify rock permeability of 10 nD, 0.1 μD, 1 μD, 10 μD, 0.1 mD, and 1 mD, respectively.

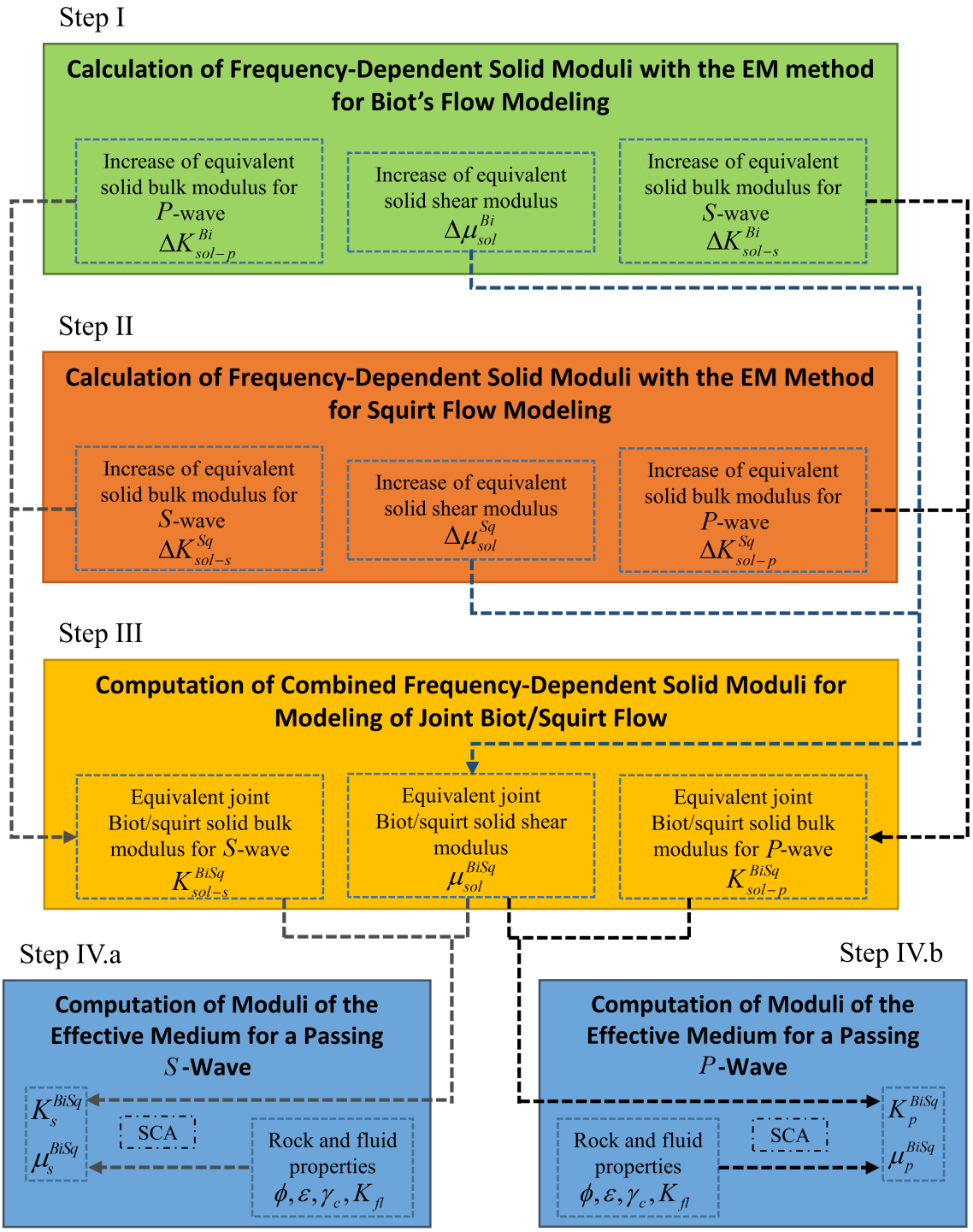

Figure 4.23: Effective medium method workflow for calculation of frequency-dependent effective moduli for simulation of combined Biot's and squirt flow effects in saturated rocks.

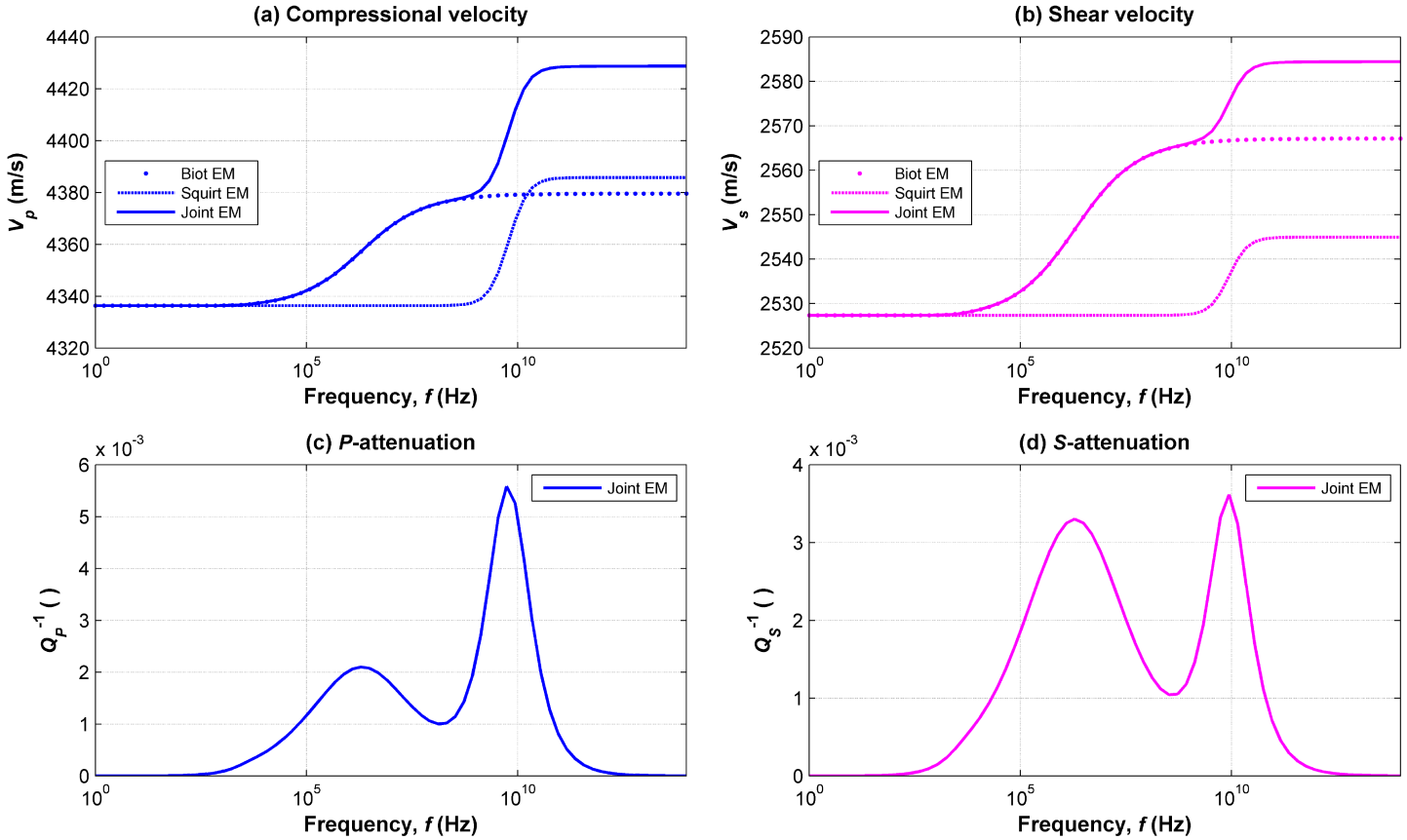

Figure 4.24: Combined Biot/squirt flow effects on compressional- and shear-wave velocities and attenuations for the synthetic example described in Table 4.1. Panel a: P-wave velocity. Panel b: S-wave velocity. Panel c: P-wave attenuation. Panel d: S-wave attenuation. In panels a and b, dot-dashed, dashed and solid curves identify velocities calculated with the effective medium method for Biot's flow, squirt flow and combined Biot/squirt flow modeling, respectively.

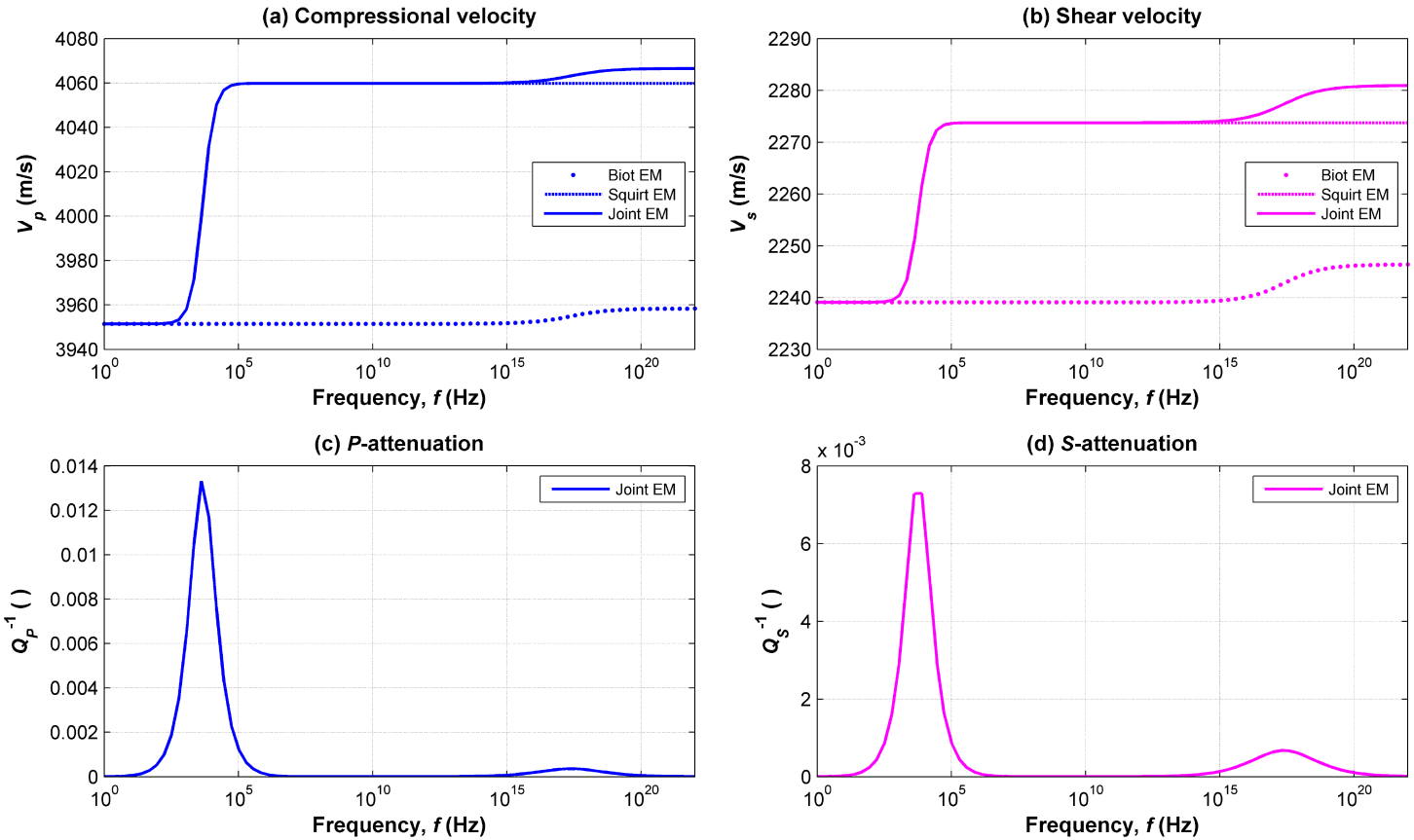

Figure 4.25: Combined Biot/squirt flow effects on compressional- and shear-wave velocities and attenuations for the synthetic example described in Table 4.5. Panel a: P-wave velocity. Panel b: S-wave velocity. Panel c: P-wave attenuation. Panel d: S-wave attenuation. In panels a and b, dot-dashed, dashed and solid curves identify velocities calculated with the effective medium method for Biot's flow, squirt flow and combined Biot/squirt flow modeling, respectively.

Chapter 5: Complete Effective-Medium Modeling of Velocity Dispersion and Attenuation in Isotropic Rocks

The prediction of velocity of waves that propagate in saturated rocks is complicated by the large number of dispersion and attenuation mechanisms. In addition to fluid-related effects, dispersion and attenuation phenomena in rocks are also induced by the presence of inhomogeneities in terms of density and elastic properties. Fluid-filled cavities typically represent large volumes of heterogeneous material in porous media. Whenever the wavelength of a passing wave is on the same scale as the size of porous inclusions, the dispersion mechanism referred to as multiple scattering of waves occurs. This chapter introduces a model that reproduces four wave-attenuation mechanisms in saturated isotropic rocks: (1) Biot's flow, (2) squirt flow, (3) acoustic scattering from spherical pores, and (4) acoustic scattering from randomly-oriented penny-shaped cracks.

First, I replicate the geometrical effect of idealized spherical and spheroidal porous inclusions on passing waves with two existing dynamic self-consistent embedding schemes. They invoke an approximate solution for scattering from a single inclusion, which allows the development of formulas similar to static self-consistent approximation theories. For the first time, equations are explicitly derived for the analysis of waves that propagate in a rock containing randomly-oriented cracks. Dependence of acoustic dispersive behavior on the size of inclusions is studied to establish the possibility of estimating rock fabric parameters from modeling of scattering dispersion mechanisms. Second, a new effective medium model is constructed using the method to approximate joint fluid-related dispersion effects described in the previous chapter. SCA theories for scattering mechanisms are alternatively employed to add cracks and stiff pores into a solid matrix with dynamic properties that reproduce dispersion effects caused by fluid flow inside the pore space. Finally, the model is applied to two synthetic cases and relationships

are established between properties assumed in the instances and frequency at which dispersion and attenuation phenomena are predicted. Based on these observations, I investigate conditions where dynamic effective medium modeling performed in parallel with acoustic measurements at multiple frequencies would be valuable.

5.1 INTRODUCTION

When generating rock physics models to determine elastic properties of potential hydrocarbon-producing zones, estimates of rock fabric parameters are typically verified by matching velocity simulations with sonic measurements. Classical effective medium theories, such as those invoked in the rock physics models described in Chapters 2 and 3, assume elastostatic properties. Under certain circumstances, wave-induced flow of the pore fluid (Sams et al., 1997; Adelinet et al., 2009), and/or the presence of large heterogeneous inclusions, such as long cracks or mesoscale fractures (Chapman, 2003; Valdiviezo-Mijangos and Nicolás-Lopez, 2014), are the source of wave dispersion and attenuation occurring at logging frequencies. Because this leads to velocity increase, it becomes essential to include dispersion mechanisms within an effective medium theory to calculate velocities that are relevant for comparison to sonic logs. When dispersive behavior is neglected, rock fabric parameters assessed with the rock physics model will differ from their actual value in order to compensate for the corresponding velocity gap. Rock fabric parameters would then produce erroneous evaluation of mechanical properties of the studied formation.

Fluid-related dispersion models pertain the dynamic behavior of a saturated rock to parameters such as porosity, permeability, fluid compressibility and viscosity (Parra, 1997), and shape of microcracks (Chapman et al., 2002). Furthermore, Valdiviezo-

Mijangos and Nicolás-Lopez (2014) showed the direct correlation between the size of inclusions and acoustic scattering. The latter mechanism occurs when the wavelength of a passing wave is comparable in size to porous inclusions, which generates dispersion in the wave speed along with attenuation effects. Hence, a detailed understanding of dissipation caused by wave-induced flow of the pore fluid and acoustic scattering associated with measurements of dispersion and attenuation from seismic, sonic measurements, and laboratory experiments is a valuable approach to quantify essential properties of hydrocarbon-bearing rocks.

Several effective medium models have been established to reproduce dispersion mechanisms caused by pore fluid flow but they are incomplete in the sense that some of the poroelastic parameters remain ignored (Berryman, 1998), only take into account one mechanism (Tod, 2003; Ghosh and Sen, 2011), or are greatly complicated (Jakobsen et al., 2003; Jakobsen and Chapman, 2009). None of these models integrate the dispersion and attenuation impact of acoustic scattering. The prediction of scattering-related wave dispersion and attenuation in effective media is a complex process due to the need to invoke the effect of multiple scattering. In fact, for composite materials with random inclusions this problem cannot be solved exactly, and only approximate solutions are available. The effective medium method is widely used for the construction of such approximate solutions of the elastic wave propagation problem (Sabina and Willis, 1988; Kanaun, 1996; Kanaun, 1997; Kanaun and Levin, 2003). All these models invoke a dynamic self-consistent method for the analysis of waves in a composite composed of a matrix with embedded inclusions. In the case of composites with spherical inclusions, predictions from effective medium models are in agreement with known experimental data (Sabina and Willis, 1988; Kim et al., 1995). To my knowledge, no effective medium model that accounts for scattering effects has ever been advanced that also includes fluid-related dispersion mechanisms.

Therefore, the technical challenge remains to devise an effective medium model to predict fluid- and scattering-related velocity dispersion and attenuation at any frequency in an isotropic fluid-saturated rock.

I first describe the simple frequency-dependent self-consistent scheme derived by Sabina and Willis (1988) for prediction of wave behavior in a composite consisting of a matrix containing spherical inclusions. Sabina et al. (1993) developed an explicit SCA theory for scattering mechanisms due to a random array of aligned spheroidal inclusions. I use their formulas and derive simplifications induced by the isotropy of an effective medium comprising cracks with no preferred orientation to be used jointly with the scattering model of Smyshlyaev et al. (1993). Linear relationships between logarithms of size of inclusions and frequency of maximum attenuation are found for both models. I also observe a remarkable dependence of percentage of dispersion on crack porosity. A complete dynamic effective medium theory is advanced for calculating wave velocity and attenuation for isotropic rocks with a homogeneous solid matrix. Randomly-oriented cracks and spherical pores are subsequently added into the solid background using the corresponding frequency-dependent SCA equations. Elastic properties of the background are computed with the joint effective medium model for dispersive behavior due to wave-induced flow of the pore fluid (formulated in Chapter 3). With the mineral matrix responsible for the simulation of fluid-related dispersion mechanisms and the dynamic self-consistent equations accountable for the modeling of scattering, the novel effective medium model simultaneously takes into account all the main sources of dispersion and attenuation of waves propagating in saturated rocks. I then examine the predictions obtained for two synthetic examples and consider the reasons that rock physics modeling would benefit from applying a dynamic effective medium model.

5.2 MODELING OF ACOUSTIC SCATTERING MECHANISMS

The main objective of the scattering theory is to determine the dependence of phase velocity and attenuation factor of waves propagating through a composite medium on the frequency of the incident field and on the details of the composite microstructure. I chose to create a new model by combining the schemes introduced by Sabina and Willis (1988) and Smyshlyaev et al. (1993) because of the simplicity of the equations easily solved by iteration, which respectively generalized to dynamics the static self-consistent approximation for spherical inclusions of Wu (1966) and Berryman (1980b) and the static self-consistent approximation for randomly-oriented spheroidal inclusions of Wu (1966) presented in Chapter 2. Their model expresses stress, strain, velocity, and momentum density in the composite, in terms of their mean values over the inclusions domain alone. These are then approximately estimated by solving a scattering problem for a single inclusion embedded in a homogeneous reference medium whose properties are chosen to be the same as those of the effective composite. For frequency-dependent problems, the single-scattering problem has no closed-form solution, but Sabina and Willis (1988) proposed an approximate solution. The simplicity of the approximation allows the development of explicit equations for multiple scattering. **Appendix D** provides further descriptions of the formulation of the general theory and the solution for the single-scattering problem.

5.2.1 Self-Consistent Equations

The requirement of self-consistency translates into the equations

$$\langle \boldsymbol{\varsigma} \rangle = \mathbf{C}_0 \langle \mathbf{e} \rangle, \text{ with } \langle \mathbf{e} \rangle = \mathbf{e}_0, \tag{5.1}$$

$$\langle \mathbf{p} \rangle = \boldsymbol{\rho}_0 \langle \mathbf{V} \rangle, \text{ with } \langle \mathbf{V} \rangle = \mathbf{V}_0, \tag{5.2}$$

where $\langle \boldsymbol{\varsigma} \rangle$, $\langle \mathbf{e} \rangle$, $\langle \mathbf{p} \rangle$, and $\langle \mathbf{V} \rangle$ are the averaged stress, strain, momentum density, and velocity tensors within the effective composite, respectively, and $\mathbf{e}_0$ and $\mathbf{V}_0$ are the strain and velocity tensors within an inclusion embedded in the effective medium, respectively. $\mathbf{C}_0$ and $\boldsymbol{\rho}_0$ represent the tensors of elastic stiffness and density of the effective medium, respectively. $\mathbf{C}_0$ and $\boldsymbol{\rho}_0$ are chosen so that the effective composite can support the mean wave of displacement $\langle \mathbf{u} \rangle$ and $\mathbf{u}_0$, the incident displacement field on the inclusion, can be taken equal to $\langle \mathbf{u} \rangle$.

The exact equations (D.7) and (D.8) therefore give, using equations (D.22) and (D.23), the frequency-dependent self-consistent conditions

$$\mathbf{C}_{\mathbf{SCA}}^{fd}\mathbf{e}_0 = \left\{ \mathbf{C}_1 + \sum_{i=2}^{n+1} x_i h_i(k\mathbf{n}) h_i(-k\mathbf{n}) (\mathbf{C}_i - \mathbf{C}_1) \left[\mathbf{I} + \overline{\mathbf{S}}_x^{(i)} \left(\mathbf{C}_i - \mathbf{C}_{\mathbf{SCA}}^{fd} \right) \right]^{-1} \right\} \mathbf{e}_0, \tag{5.3}$$

and

$$\boldsymbol{\rho}_{\mathbf{SCA}}^{fd}\mathbf{V}_0 = \left\{ \boldsymbol{\rho}_1 + \sum_{i=2}^{n+1} x_i h_i(k\mathbf{n}) h_i(-k\mathbf{n}) (\boldsymbol{\rho}_i - \boldsymbol{\rho}_1) \left[\mathbf{I} + \overline{\mathbf{M}}_t^{(i)} \left(\boldsymbol{\rho}_i - \boldsymbol{\rho}_{\mathbf{SCA}}^{fd} \right) \right]^{-1} \right\} \mathbf{V}_0, \tag{5.4}$$

where $\mathbf{e}_0$ and $\mathbf{v}_0$ are derived from the incident wave (see equation (D.9)), with

$$\left[k^2 \left(C_{SCA}^{fd} \right)_{ijkl} n_j n_l - \omega^2 \left(\rho_{SCA}^{fd} \right)_{ik} \right] m_k = 0. \tag{5.5}$$

In the self-consistent equations, $\mathbf{C}_{\mathbf{SCA}}^{fd}$ is the stiffness tensor of the effective medium that replaces $\mathbf{C}_0$ in equations (5.1) and (D.22) and $\boldsymbol{\rho}_{\mathbf{SCA}}^{fd}$ is the density tensor of the effective medium that replaces $\boldsymbol{\rho}_0$ in equations (5.2) and (D.23). The superscript fd indicates that they are frequency-dependent. $\mathbf{C}_1$ is the stiffness tensor of the background matrix of density $\boldsymbol{\rho}_1$ in which are embedded n types of inclusions, identified by the subscript i, associated with their respective volumetric concentrations x_i, stiffness tensor $\mathbf{C}_i$, and density $\boldsymbol{\rho}_i$. Definitions of all other terms in equations (5.3), (5.4), and (5.5) are given in **Appendix D**.

Hereinafter I consider a matrix containing a single population of evenly distributed porous inclusions exhibiting the same size, so that $n=1$. The frequency-dependent self-consistent equations (5.3) and (5.4), with $\mathbf{e}_0$ and $\mathbf{V}_0$ omitted, respectively become

$$\mathbf{C}_{\mathbf{SCA}}^{fd} = \mathbf{C}_1 + \phi h_2(k\mathbf{n}) h_2(-k\mathbf{n})(\mathbf{C}_2 - \mathbf{C}_1)\left[\mathbf{I} + \overline{\mathbf{S}}_x\left(\mathbf{C}_2 - \mathbf{C}_{\mathbf{SCA}}^{fd}\right)\right]^{-1}, \tag{5.6}$$

and

$$\boldsymbol{\rho}_{\mathbf{SCA}}^{fd} = \boldsymbol{\rho}_1 + \phi h_2(k\mathbf{n}) h_2(-k\mathbf{n})(\boldsymbol{\rho}_2 - \boldsymbol{\rho}_1)\left[\mathbf{I} + \overline{\mathbf{M}}_t\left(\boldsymbol{\rho}_2 - \boldsymbol{\rho}_{\mathbf{SCA}}^{fd}\right)\right]^{-1}. \tag{5.7}$$

where ϕ is the porosity, $\mathbf{C}_1$ is the stiffness tensor of the background matrix of density $\boldsymbol{\rho}_1$, and $\mathbf{C}_2$ is the stiffness tensor of the inclusion fluid of density $\boldsymbol{\rho}_2$.

5.2.2 Case of Spherical Inclusions

If the effective medium consists of an isotropic solid matrix containing spherical porous inclusions, it is also isotropic and is, therefore, characterized by its bulk modulus, $K_{\mathbf{SCA}}^{fd}$, shear modulus, $\mu_{\mathbf{SCA}}^{fd}$, and density, $\rho_{\mathbf{SCA}}^{fd}$. Expressions for $\overline{\mathbf{S}}_x$ and $\overline{\mathbf{M}}_t$ are shown in **Appendix E** and, substituting into equations (5.6) and (5.7),

$$K_{\mathbf{SCA}}^{fd} = K_1 + \frac{\phi h_2(k) h_2(-k)(K_2 - K_1)}{1 + 3\left(K_2 - K_{\mathbf{SCA}}^{fd}\right)\xi_p \Big/ \left(3K_{\mathbf{SCA}}^{fd} + 4\mu_{\mathbf{SCA}}^{fd}\right)}, \tag{5.8}$$

$$\mu_{\mathbf{SCA}}^{fd} = \mu_1 + \frac{\phi h_2(k) h_2(-k)(\mu_2 - \mu_1)}{1 + 2\left(\mu_2 - \mu_{\mathbf{SCA}}^{fd}\right)\dfrac{\left[2\mu_{\mathbf{SCA}}^{fd}\xi_p + \left(3K_{\mathbf{SCA}}^{fd} + 4\mu_{\mathbf{SCA}}^{fd}\right)\xi_s\right]}{\left[5\mu_{\mathbf{SCA}}^{fd}\left(3K_{\mathbf{SCA}}^{fd} + 4\mu_{\mathbf{SCA}}^{fd}\right)\right]}}, \tag{5.9}$$

and

$$\rho_{\mathbf{SCA}}^{fd} = \rho_1 + \frac{\phi h_2(k) h_2(-k)(K_2 - K_1)}{1 + 3\left(\rho_2 - \rho_{\mathbf{SCA}}^{fd}\right)\left(3 - \xi_p - 2\xi_s\right) \Big/ \left(3\rho_{\mathbf{SCA}}^{fd}\right)}. \tag{5.10}$$

where K_1, μ_1, and ρ_1 are the bulk and shear modulus and density of the background matrix and K_2, μ_2, and ρ_2 are the bulk and shear modulus and density of the inclusion fluid. The function h_2 for a spherical inclusion is

$$h_2(k) = \frac{3\left(\sin(ak) - ak\cos(ak)\right)}{(ak)^3}, \tag{5.11}$$

where a is the radius of the inclusions and k is the wave number which is treated here as a scalar, strictly equal to the magnitude of the wave vector. The terms ξ_p and ξ_s in the self-consistent equations (5.8) to (5.10) are calculated as

$$\xi_j = \frac{3\left(1 - iak_j\right)}{\left(ak_j\right)^3}\left[\sin\left(ak_j\right) - ak_j\cos\left(ak_j\right)\right]e^{iak_j}, \tag{5.12}$$

where

$$k_j = \omega / V_j, \tag{5.13}$$

and $j = p$ or s.

The wave number, k, is computed differently depending on the type of incident wave being considered when solving the self-consistent relations. Therefore, the alternative choices for k give rise to different equations for compressional or shear waves, and generates estimates of $K_{\mathbf{SCA}}^{fd}$, $\mu_{\mathbf{SCA}}^{fd}$, and $\rho_{\mathbf{SCA}}^{fd}$ that are the most accurate for the wave under consideration. I define $K_{\mathbf{SCA}\_p}^{fd}$, $\mu_{\mathbf{SCA}\_p}^{fd}$, and $\rho_{\mathbf{SCA}\_p}^{fd}$ as the effective bulk and shear modulus and density, respectively, used for P-waves calculations and $K_{\mathbf{SCA}\_s}^{fd}$, $\mu_{\mathbf{SCA}\_s}^{fd}$, and $\rho_{\mathbf{SCA}\_s}^{fd}$ as the effective bulk and shear modulus and density, respectively, used for S-waves calculations.

5.2.2.1 Equations for an Incident P-Wave

When considering compressional-wave dispersion due to scattering caused by spherical inclusions, the wave number is equal to k_p and calculated as

$$k = k_p = \omega\left(\left(K_{\mathbf{SCA}\_p}^{fd} + \tfrac{4}{3}\mu_{\mathbf{SCA}\_p}^{fd}\right)\Big/\rho_{\mathbf{SCA}\_p}^{fd}\right)^{-1/2}, \tag{5.14}$$

and

$$k_s = \omega\left(\mu_{\mathbf{SCA}\_p}^{fd}\Big/\rho_{\mathbf{SCA}\_p}^{fd}\right)^{-1/2}. \tag{5.15}$$

5.2.2.2 Equations for an Incident S-Wave

When considering shear-wave dispersion due to scattering caused by spherical inclusions, the wave number is equal to k_s and calculated as

$$k = k_s = \omega\left(\mu_{\mathbf{SCA}\_s}^{fd}\Big/\rho_{\mathbf{SCA}\_s}^{fd}\right)^{-1/2}, \tag{5.16}$$

and

$$k_p = \omega\left(\left(K_{\mathbf{SCA}\_s}^{fd} + \tfrac{4}{3}\mu_{\mathbf{SCA}\_s}^{fd}\right)\Big/\rho_{\mathbf{SCA}\_s}^{fd}\right)^{-1/2}. \tag{5.17}$$

Equations (5.8) to (5.10) are solved simultaneously by iteration. The iteration is usually started by taking the elastic moduli and density of the effective composite equal to the matrix values K_2, μ_2, and ρ_2, respectively. The first iteration then produces estimates of $K_{\mathbf{SCA}}^{fd}$, $\mu_{\mathbf{SCA}}^{fd}$, and $\rho_{\mathbf{SCA}}^{fd}$ used to compute a new wave number. The estimates are then injected back into the right-hand sides of equations (5.8) to (5.10), producing new values for $K_{\mathbf{SCA}}^{fd}$, $\mu_{\mathbf{SCA}}^{fd}$, and $\rho_{\mathbf{SCA}}^{fd}$ and so forth.

It is fairly simple to verify that for the low-frequency limit, $\omega = 0$, $k = 0$, $h_1(k) = 1$, and $\bar{\mathbf{M}}_t = 0$, and, taking the static limit of $\bar{\mathbf{S}}_x$, equations (5.6) and (5.7)reproduce the static self-consistent approximations of Budiansky (1965) and Hill (1965).

5.2.3 Case of Randomly-Oriented Spheroidal Inclusions

The self-consistent equations (5.6) and (5.7) are substantially more complicated to solve when reproducing the dispersion effect due to the presence of spheroidal porous inclusions. Smyshlyaev et al. (1993) applied the formulation presented in Sabina et al. (1993) for an effective medium in which are embedded aligned spheroidal inclusions to the case of a composite containing a single population of inclusions, distributed at random orientations. The difficulty is to evaluate the tensors $\overline{\mathbf{S}}_x$ and $\overline{\mathbf{M}}_t$ that appear in equations (5.6) and (5.7), respectively, when the axis of symmetry (small axis) of the spheroid inclusion takes no preferred orientation. To this end, it is convenient to define a polar angle, ϑ, between the small axis of the oblate spheroidal inclusions and the vertical x_3-axis of the effective composite, and a new coordinate system, identified by primed variables, so that the axis of symmetry of the spheroid becomes the new vertical x_3'-axis. Consider then the transversely isotropic tensor

$$\mathbf{C}' = \left(\mathbf{C}_2 - \mathbf{C}_1\right)\left[\mathbf{I} + \overline{\mathbf{S}}_x'\left(\mathbf{C}_2 - \mathbf{C}_{\mathbf{SCA}}^{fd}\right)\right]^{-1}, \tag{5.18}$$

where $\overline{\mathbf{S}}_x'$ represents the tensor $\overline{\mathbf{S}}_x$ expressed in the rotated coordinate system attached with the spheroidal inclusion and the other parameters are defined in the same manner as above. The entries of $\mathbf{C}'$ are as follows

$$\mathbf{C}' = \begin{bmatrix} c_{11}' & c_{12}' & c_{13}' & 0 & 0 & 0 \\ c_{12}' & c_{11}' & c_{13}' & 0 & 0 & 0 \\ c_{13}' & c_{13}' & c_{33}' & 0 & 0 & 0 \\ 0 & 0 & 0 & c_{44}' & 0 & 0 \\ 0 & 0 & 0 & 0 & c_{44}' & 0 \\ 0 & 0 & 0 & 0 & 0 & c_{66}' \end{bmatrix}.$$

Similarly, considering

$$\mathbf{M}' = \left(\rho_2 - \rho_1\right)\left[\mathbf{I} + \bar{\mathbf{M}}_t'\left(\rho_2 - \rho_{\mathbf{SCA}}^{fd}\right)\right]^{-1}, \tag{5.19}$$

this is also a transversely isotropic tensor whose entries are defined as

$$\mathbf{M}' = \begin{bmatrix} \mu_1' & 0 & 0 \\ 0 & \mu_1' & 0 \\ 0 & 0 & \mu_3' \end{bmatrix}.$$

The formulas for $\bar{\mathbf{S}}_x'$ and $\bar{\mathbf{M}}_t'$, from which $\mathbf{C}'$ and $\mathbf{M}'$ are respectively constructed, have never been explicitly written for a composite containing randomly-oriented cracks. I used the calculations elaborated by Sabina et al. (1993) for the case of aligned spheroidal inclusions and applied simplifications induced by the isotropy of the effective medium. The resulting equations for $\bar{\mathbf{S}}_x'$ and $\bar{\mathbf{M}}_t'$ can be found in **Appendix E.**

Because the effective medium consists of an isotropic solid matrix embedded with spheroidal porous inclusions oriented in all directions, it is isotropic, similarly to the case of spherical inclusions. Consequently, the composite is also defined by its bulk modulus, $K_{\mathbf{SCA}}^{fd}$, shear modulus, $\mu_{\mathbf{SCA}}^{fd}$, and density, $\rho_{\mathbf{SCA}}^{fd}$.

5.2.3.1 Equations for an Incident P-Wave

When considering the propagation of a compressional-wave in a composite in which randomly-oriented cracks of length a_c and aspect ratio γ are embedded, equations (5.6) and (5.7) are to be combined with equations (5.18) and (5.19) to obtain the corresponding self-consistent equations. The details of the calculations due to the transformation of coordinates are omitted, but the results at each frequency are

$$\begin{aligned} K_{\mathbf{SCA}\_p}^{fd} + \tfrac{4}{3}\mu_{\mathbf{SCA}\_p}^{fd} = K_1 + \tfrac{4}{3}\mu_1 + \phi\Big\{ & I\left(\iota_p;\left(1-u^2\right)^2\right)c_{11}' \\ & + I\left(\iota_p;\left(1-u^2\right)u^2\right)\left(2c_{13}' + 4c_{44}'\right) + I\left(\iota_p;u^4\right)c_{33}'\Big\}, \end{aligned} \tag{5.20}$$

$$K_{\mathbf{SCA}\_p}^{fd} - \tfrac{2}{3}\mu_{\mathbf{SCA}\_p}^{fd} = K_1 - \tfrac{2}{3}\mu_1 + \phi\left\{\frac{1}{2}I\left(\iota_p;\left(1-u^2\right)^2\right)\right.$$
$$\left.\left(c'_{11} - 2c'_{13} - 4c'_{44} + c'_{33}\right) + \frac{1}{2}I\left(\iota_p;1-u^2\right)\left(c'_{12} + c'_{13}\right) + I\left(\iota_p;u^2\right)c'_{13}\right\}, \tag{5.21}$$

and

$$\rho_{\mathbf{SCA}\_p}^{fd} = \rho_1 + \phi\left\{I\left(\iota_p;1-u^2\right)\mu'_1 + I\left(\iota_p;u^2\right)\mu'_3\right\}, \tag{5.22}$$

where $u = \cos(\vartheta)$, ι_p is the dimensionless angular wave number associated with the incident P-wave calculated as

$$\iota_p = a_c k_p = a_c\,\omega/V_p = a_c\omega\left(\left(K_{\mathbf{SCA}\_p}^{fd} + \tfrac{4}{3}\mu_{\mathbf{SCA}\_p}^{fd}\right)\Big/\rho_{\mathbf{SCA}\_p}^{fd}\right)^{-1/2}, \tag{5.23}$$

and I is defined as

$$I\left(\iota_j;f(u)\right) \equiv \int_0^1 \hat{h}^2\left(\iota_j\,\psi(u)\right)f(u)\,du. \tag{5.24}$$

In equations (5.20) to (5.22), K_1, μ_1, and ρ_1 are the bulk and shear modulus and density of the background matrix, respectively. $\hat{h}$ is defined by equation (E.24) and $\psi(u)$ is given by equation (E.17).

5.2.3.2 Equations for an Incident S-Wave

The treatment of S-waves follows the same pattern when considering their propagation in a composite containing randomly-oriented cracks of radius a and aspect ratio γ. The self-consistent equations then become

$$\mu_{\mathbf{SCA}\_s}^{fd} = \mu_1 + \frac{1}{2}\phi\left\{I\left(\iota_s;\left(1-u^2\right)u^2\right)\left(c'_{11} - 2c'_{13} + c'_{33}\right) + I\left(\iota_s;1-u^2\right)c'_{66}\right.$$
$$\left. + I\left(\iota_s;4u^4 - 3u^2 + 1\right)c'_{44}\right\}, \tag{5.25}$$

$$\rho_{\mathbf{SCA}\_s}^{fd} = \rho_1 + \frac{1}{2}\phi\left\{I\left(\iota_s;1+u^2\right)\mu'_1 + I\left(\iota_s;1-u^2\right)\mu'_3\right\}, \tag{5.26}$$

where ι_s is the dimensionless angular wave number associated with the incident S-wave calculated as

$$\iota_s = a_c k_s = a_c\, \omega / V_s = a_c \omega \left(\mu^{fd}_{\mathbf{SCA}\_s} / \rho^{fd}_{\mathbf{SCA}\_s} \right)^{-1/2}, \tag{5.27}$$

and all other terms are defined as above.

Equations (5.20) to (5.22) and equations (5.25) and (5.26) are solved iteratively, in the same manner as for equations (5.8) to (5.10). Moreover, for all frequency, equations (5.25) and (5.26) are solved for $\mu^{fd}_{\mathbf{SCA}\_s}$ and $\rho^{fd}_{\mathbf{SCA}\_s}$ with $K^{fd}_{\mathbf{SCA}\_s}$ chosen so that

$$K^{fd}_{\mathbf{SCA}\_s} + 4/3\, \mu^{fd}_{\mathbf{SCA}\_s} = K^{fd}_{\mathbf{SCA}\_p} + 4/3\, \mu^{fd}_{\mathbf{SCA}\_p} \tag{5.28}$$

where $K^{fd}_{\mathbf{SCA}\_p}$ and $\mu^{fd}_{\mathbf{SCA}\_p}$ are the parameters found for the propagation of P-waves.

5.3 Effects of Size and Shape of Inclusions on Scattering Mechanisms

5.3.1 Spherical Pores

Valdiviezo-Mijangos and Nicolás-Lopez (2014) showed the strong correlation between size of inclusions and the frequency at which the dispersion phenomenon due to acoustic scattering occurs. **Table 5.1** describes solid composition, petrophysical attributes, and rock physics parameters assumed in the synthetic example defined to show the scattering effects of spherical pores on velocity and attenuation curves at different frequencies. The solid background contains of 60% quartz, 20% calcite, and 20% clay. Total porosity is moderately high (18%) and is entirely made up of spherical pores (crack density is 0). The rock is fully saturated with water. Simulations are conducted for four different pore diameters, from vugs (diameter of 1 mm) to micropores (1 μm).

Equations (5.8), (5.9), and (5.10) are invoked to compute the effective elastic properties of the composite with equations (5.14) and (5.15) for an incident compressional

wave and equations (5.16) and (5.17) for an incident shear wave. Velocity and attenuation results for P-wave and S-wave are displayed in **Figures 5.1** and **5.2**, respectively. Large velocity increases, around $700\ \text{m.s}^{-1}$ for V_p and $500\ \text{m.s}^{-1}$ for V_s—which corresponds to percentage of dispersion of 16.4% and 17.9%, respectively—as shown on panels a, and narrow peaks of attenuation (see panels b), are observed in these figures. The frequency of dispersion increases with decreasing pore dimension. This result is expected as scattering effects occur when wavelength is comparable in size with the heterogeneities in the rock. **Figure 5.3** clearly depicts the linear relationship between the diameter of stiff pores and the frequency of maximum attenuation when plotted on a logarithmic scales.

5.3.2 Randomly-Oriented Spheroidal Inclusions

The frequency-dependent SCA model for randomly-oriented cracks described above can be used to simulate dispersion caused by the presence of either porous cracks or fractures. This can be done by varying the length of spheroidal inclusions within the model. **Table 5.2** summarizes characteristics of another synthetic rock composed of the same solid matrix as the example defined in **Table 5.1,** but in which are included only spheroidal inclusions. Total porosity is 0.42% and penny-shaped cavities exhibit an aspect ratio of 0.005. The rock is also fully saturated with water. **Figures 5.4** and **5.5** show compressional and shear velocities (panel a) and compressional- and shear-wave attenuation (panel b), respectively.

Three different lengths were assumed for the calculations: 1 m (to simulate fractures), 1 mm (long cracks), and 1 μm (microcracks). Because cracks represent a much lower volumetric concentration of heterogeneities than stiff pores, percentages of dispersion are commonly smaller (1.98% for V_p and 1.34% for V_s in this instance). **Figure 5.6** illustrates the linear correlation between inclusion length and frequency in logarithmic

space. The order of magnitude for the length of natural fractures lies between 0.1 m and 10 m, thus corresponding to dispersion frequencies of between 1 kHz and 10 Hz. **Figure 5.7** shows a noticeable connection between crack porosity and percentage of dispersion. Relative differences between low- and high-frequency limits of compressional and shear velocities increase linearly with volume fraction of the rock occupied by spheroidal cavities, independently of values of crack density and aspect ratio. This result suggests that the prediction of scattering effects associated with velocity measurements performed at the correct frequencies would allow one to verify the estimate of crack density obtained with classical effective medium theories.

5.4 COMPLETE NEW FREQUENCY-DEPENDENT EFFECTIVE MEDIUM MODEL

In this section, I implement a frequency-dependent self-consistent approximation workflow for combined reproduction of fluid-flow related dispersion mechanisms (Biot's flow and squirt flow) and sonic scattering mechanisms (due to stiff pores and cracks or fractures) for isotropic rocks that exhibit a homogeneous mineral background. **Figure 5.8** describes the four steps of the complete dynamic effective medium model.

5.4.1 Definition of Static Reference Case

A static case of reference is first defined (Step I in **Figure 5.8**) using the static self-consistent approximation model of Wu (1966) defined in Chapter 2. It represents the limits to which all frequency-dependent models previously described in this chapter and in Chapter 4 tend at low frequencies, ensuring consistency of the final effective medium model. The elastic properties of the reference case at low frequencies, $K^*_{\mathbf{SCA}}$ and $\mu^*_{\mathbf{SCA}}$, are calculated by adding fluid-filled spheroidal followed by spherical inclusions into the solid matrix of characteristics K_{sol} and μ_{sol}.

5.4.2 Reproduction of Biot's and Squirt Flow Effects with Frequency-Dependent Equivalent Solid Moduli

Equivalent features for the solid background of the rock are calculated to account for main fluid-related dispersion and attenuation mechanisms. Steps I to III of the model advanced in section 4.4 are invoked (step II in **Figure 5.8**) to obtain parameters K_{sol-p}^{BiSq}, K_{sol-s}^{BiSq}, and μ_{sol}^{BiSq}.

5.4.3 Calculation of Frequency-Dependent Effective Moduli for S-Wave Dispersion and Attenuation

The effect of scattering of randomly-oriented cracks or fractures on shear waves is modeled by including spheroidal fluid-filled cavities with the self-consistent equations (5.25), (5.26), and (5.28). The features of the solid background, K_1, μ_1, and ρ_1, are replaced by K_{sol-s}^{BiSq}, μ_{sol}^{BiSq}, and ρ_{sol}, respectively, for the first iteration (see step III.a in **Figure 5.8**).

Scattering mechanisms due to the presence of stiff pores and their influence on compressional- and shear-wave velocities are then simulated by adding spherical inclusions into the medium reconstructed at the end of the previous phase (step IV.a in **Figure 5.8**). Formulas (5.8) to (5.10) are used to compute the final frequency-dependent elastic properties of the effective composite with wave numbers defined in equations (5.16) and (5.17). K_1, μ_1, and ρ_1 are substituted by moduli $K_{\mathbf{SCA}\_s}^{fd}$, $\mu_{\mathbf{SCA}\_s}^{fd}$, and density $\rho_{\mathbf{SCA}\_s}^{fd}$ of the medium containing the cracks for the first operation. Shear velocity and attenuation are then computed from equations (2.9) and (4.6), respectively, using the new characteristics of the complete effective medium $K_{\mathbf{SCA}\_s}^{fd}$, $\mu_{\mathbf{SCA}\_s}^{fd}$, and $\rho_{\mathbf{SCA}\_s}^{fd}$.

5.4.4 Calculation of Frequency-Dependent Effective Moduli for P-Wave Dispersion and Attenuation

Elastic properties of the effective medium affected by crack-related acoustic scattering for a compressional wave are reproduced using the model in the same manner. Spheroidal fluid-saturated inclusions are added with equations (5.20) to (5.22) into the solid background characterized by K_{sol-p}^{BiSq}, μ_{sol}^{BiSq}, and ρ_{sol}, for the first computation (step III.b in **Figure 5.8**).

Spherical pores are included next into the resulting medium with self-consistent relations (5.8) to (5.10) to obtain the frequency-dependent bulk and shear modulus, and density of the complete effective composite, $K_{\mathbf{SCA}\_p}^{fd}$, $\mu_{\mathbf{SCA}\_p}^{fd}$, and $\rho_{\mathbf{SCA}\_p}^{fd}$, respectively (refer to step IV.b in **Figure 5.8**). Compressional velocity and attenuation for combined scattering and fluid-related dispersion are finally calculated from equation (2.8) and (4.5).

5.5 Application to Synthetic Cases and Discussion

In this section, I apply my new effective medium scheme for modeling of joint fluid-related and acoustic scattering mechanisms to two synthetic instances and examine the potential applications that the new model provides.

5.5.1 Example of a Synthetic Sandstone

Table 5.3 describes the attributes of the synthetic instance that exhibits the common solid composition, petrophysical characteristics and rock physics parameters of a highly permeable (9 D), clean water-saturated sandstone. The mineral background comprises grains with a 150 μm diameter divided between 79% quartz, 13% calcite, and only 8% clay. Most of total porosity (25%) is made up of stiff pores, and density and aspect ratio of microcracks are 0.09 and 0.01, respectively. Following the method I detailed in the above section, reference elastic moduli are calculated by incorporating penny-shaped cracks and

pores filled with water into the homogeneous solid matrix with Wu's version of the SCA. The effective medium theories for modeling of Biot's flow and squirt flow dispersion are then invoked, and frequency-dependent grain elastic properties for joint fluid-related mechanisms can be computed. Equivalent solid moduli are used as background features for the implementation of dynamic self-consistent equations for cracks and pores. I then calculate velocity and attenuation for a large range of frequency.

Figure 5.9 shows results obtained for compressional-wave velocity (panel a) and attenuation (panel b) between 100 Hz and 10^{12} Hz. The impact of the different sources of dispersion is materialized on the simulated curves by four distinct increases in the wave speed and as many peaks in the inverse quality factor. **Figures 5.10** and **5.11** display values of V_p calculated with the model restrained to frequencies in the sonic and ultrasonic spectra, respectively. Mainly because of high permeability and porosity and low crack density assumed in the synthetic case, Biot's flow occurs at logging frequencies and causes velocity to rise by 70 $m.s^{-1}$, whereas squirt flow effects are visible at much higher frequencies (above laboratory measurements) and generate a 50 $m.s^{-1}$ increase only. Both crack- and pore-related scattering mechanisms arise at ultrasonic frequencies (refer to **Figure 5.11**), at 3×10^6 Hz and 2×10^7 Hz, respectively. Amplitude of dispersion is far greater for scattering due to stiff pore (1200 $m.s^{-1}$ compared to 30 $m.s^{-1}$) on account of the negligible part occupied by crack porosity in total porosity. Similar behavior is observed on the attenuation curve.

Formations with features similar to those of the synthetic example described in **Table 5.3** exist in reality. For example, simulation of main combined dispersion mechanisms verified with wave speed experiments would enable the appraisal of rock permeability based on Biot's flow effects at sonic frequencies, crack density by measuring the relative increase of velocity at 3×10^6 Hz, and pore size according to the position of

maximum attenuation due to pore-related scattering, assuming that all other rock parameters have been quantified beforehand.

5.5.2 Example of a Synthetic Shaly Sandstone

To reproduce features of a shaly sandstone, high quartz and clay concentration, 47% and 41% of the solid background, respectively, are assumed in this synthetic case. Permeability (4 μD) and total porosity (8%) are low, and crack density is 0.15. The rock is oil-saturated. I simulate the presence of fractures with the addition of 1-m-long penny-shaped inclusions having an aspect ratio of 0.005. Properties of the synthetic example are summarized in **Table 5.4**. My method for modeling of Biot/squirt flow combined with acoustic scattering is implemented in the same manner as described above.

Compressional wave speed and an inverse quality factor, calculated between 1 Hz and 10^{10} Hz for this example, are observed in panels a and b, respectively, of **Figure 5.12**. Squirt flow effects happen at frequencies in the seismic range (see **Figure 5.13**) chiefly as a result of modeled low permeability. High crack density and the low aspect ratio explain the large dispersion, velocity increase by approximately 80 $m.s^{-1}$, due to squirt flow. **Figure 5.14** shows the impact of fractures on the scattering effects at sonic frequencies (an increase of 60 $m.s^{-1}$). Finally, dispersion mechanisms that occur in the range of laboratory frequencies, pore-related scattering, and Biot's flow are detailed in **Figure 5.15**. Because of the low concentration of stiff porosity, velocity increase due to scattering is limited to 250 $m.s^{-1}$, whereas Biot's flow effects are almost indiscernible.

Fractures present in a real formation that is similar to the synthetic shaly sandstone are visible in borehole images. Frequency-dependent elastic properties assessed with the new effective medium model incorporate scattering effects and the resulting increase of velocity. Fracture concentration could then be estimated when calculated wave speeds are

in good agreement with sonic logs. In this example, analysis of seismic data would reveal attenuation caused by squirt flow phenomenon and would help determine fluid viscosity if simulations performed with the model reproduce actual measurements. Pore-scattering effects could be used to determine pore diameter, similarly to the sandstone instance described previously.

Consequently, implementing the effective medium theory for joint fluid-related/scattering mechanisms of dispersion allows for the estimation of rock fabric parameters such as crack aspect ratio and density, as in classical static models. But also, assessments of properties would be more accurate when comparing simulated velocities with sonic logs. In the case of dispersion occurring at logging frequencies, using static effective medium theories leads to erroneous choices of rock characteristics because calculated velocities need to be overestimated to agree with sonic measurements.

Providing that most of the model inputs have *a priori* been assessed, such as total porosity (estimated with neutron and density logs), relative saturations of fluids (determined using electrical resistivity logs), and solid composition (calculated using multi-linear inversion techniques), some of the remaining rock parameters can be estimated using parallel implementation of the model and velocity and attenuation measurements.

It is of additional interest to relate dynamic behavior to in-situ effective stress. For instance, Chapman et al. (2002) introduced pressure dependence into their squirt flow model with a relationship correlating crack density and effective stress formulated as

$$\varepsilon = \varepsilon_0 e^{-c_{cr}\varsigma_{eff}} \tag{5.29}$$

where ε_0 and c_{cr} are constants, and ς_{eff} is the effective stress.

5.6 CONCLUSIONS

The dynamic effective medium model reproduces fluid-related and acoustic scattering mechanisms on wave propagation. Generation of Biot's flow and squirt flow effects was achieved through the calculation of a frequency-dependent equivalent solid background with the method explained in Chapter 4. An original procedure was developed to include geometrical dispersion caused by spherical and randomly-oriented spheroidal porous inclusions. It was shown that, depending on the rock properties, most of the main sources of dispersion can arise at sonic logging frequencies. Therefore, frequency-dependent effective medium modeling is a valuable way to improve the accuracy of assessed rock attributes obtained with static theories.

Because the saturated moduli of the effective medium are complex-valued, there is no limitation to assuming that the static solid moduli K_{sol} and μ_{sol} are also complex-valued. In doing so, one would model frame-viscoelasticity due, for example, to soft impurities such as the clay minerals within sandstones that are the cause of additional dispersion phenomena.

Although development of a joint fluid-related and scattering effective medium theory might improve the estimation of crucial rock properties for the identification of best depth zones for hydrocarbon production, implementation of the model requires parallel measurements of dispersive behavior. Relations between dispersive borehole waves such as Stoneley and flexural waves, and fluid-related dispersion effects might be worth investigating. Otherwise, seismic, sonic, and ultrasonic (in laboratory) measurements at multiple frequencies are needed to verify estimations performed using the new dynamic model.

The effective medium model I established is practical and simple to implement. It is based on the widely known self-consistent approximation theory commonly used in rock

physics modeling. The method provides estimates of acoustic wave velocity and attenuation affected by combined dispersion mechanisms that reproduce results predicted by previously developed separate theories. However, the model is applicable to isotropic rocks only, which is a significant restriction. The reliability of the new isotropic model encourages the development an anisotropic version of the theory developed in this chapter.

Properties of synthetic case for scattering caused by spherical pores		
Solid background	Quartz concentration (%)	60
	Calcite concentration (%)	20
	Clay concentration (%)	20
Pore space	Fluid type	Water
	Total porosity (%)	18
	Crack density	0

Table 5.1: Petrophysical and rock physics properties assumed in the synthetic case used to investigate dependence of dispersive behavior for pore-related scattering mechanisms on pore size.

Properties of synthetic case for scattering caused by penny-shaped cracks		
Solid background	Quartz concentration (%)	55
	Calcite concentration (%)	25
	Clay concentration (%)	20
Pore space	Fluid type	Water
	Total porosity (%)	0.42
	Crack density	0.2
	Crack aspect ratio	0.005

Table 5.2: Petrophysical and rock physics properties assumed in the synthetic case used to investigate dependence of dispersive behavior for crack-related scattering mechanism on crack length. Total porosity consists solely of penny-shaped cracks.

Properties of the synthetic sandstone		
Solid background	Quartz concentration (%)	79
	Calcite concentration (%)	13
	Clay concentration (%)	8
	Grain size (mm)	0.15
Pore space	Fluid type	Water
	Total porosity (%)	25
	Crack density	0.09
	Crack length (μm)	500
	Crack aspect ratio	0.01
	Permeability (D)	9

Table 5.3: Petrophysical and rock physics properties assumed in the synthetic sandstone defined for modeling of joint fluid-related/scattering dispersion effects.

Properties of the synthetic shaly sandstone		
Solid background	Quartz concentration (%)	47
	Calcite concentration (%)	12
	Clay concentration (%)	41
	Grain size (mm)	0.07
Pore space	Fluid type	Oil
	Total porosity	8%
	Crack density	0.15
	Crack length (μm)	1×10^{6}
	Crack aspect ratio	0.005
	Permeability (μD)	4

Table 5.4: Petrophysical and rock physics properties assumed in the synthetic shaly sandstone defined for modeling of joint fluid-related/scattering dispersion effects.

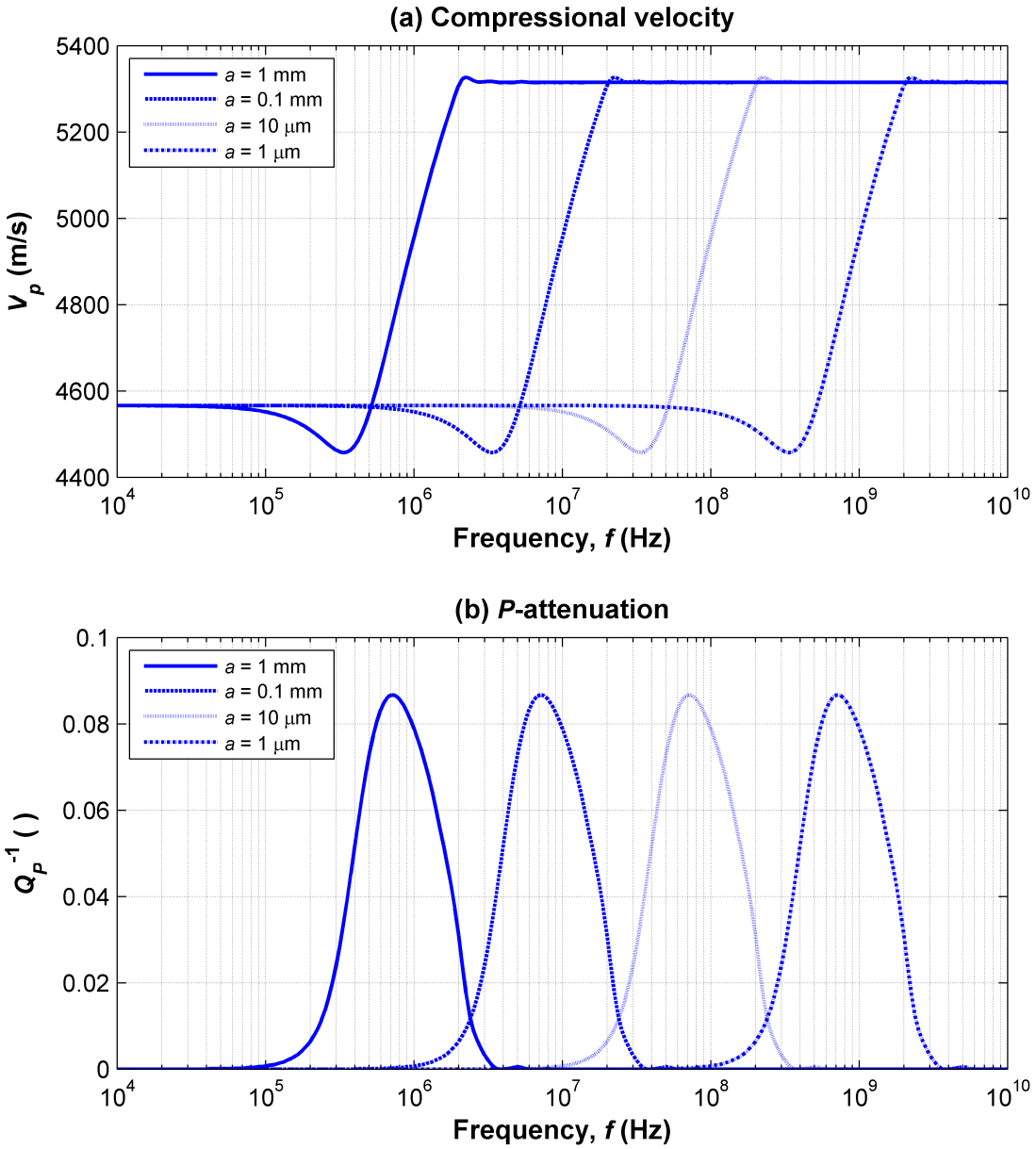

Figure 5.1: Acoustic scattering effects caused by spherical pores on compressional-wave velocity and attenuation for the synthetic example described in Table 5.1. Diameters of inclusions are 1 mm, 0.1 mm, 10 μm, and 1 μm. Panel a: P-wave velocity. Panel b: P-wave attenuation.

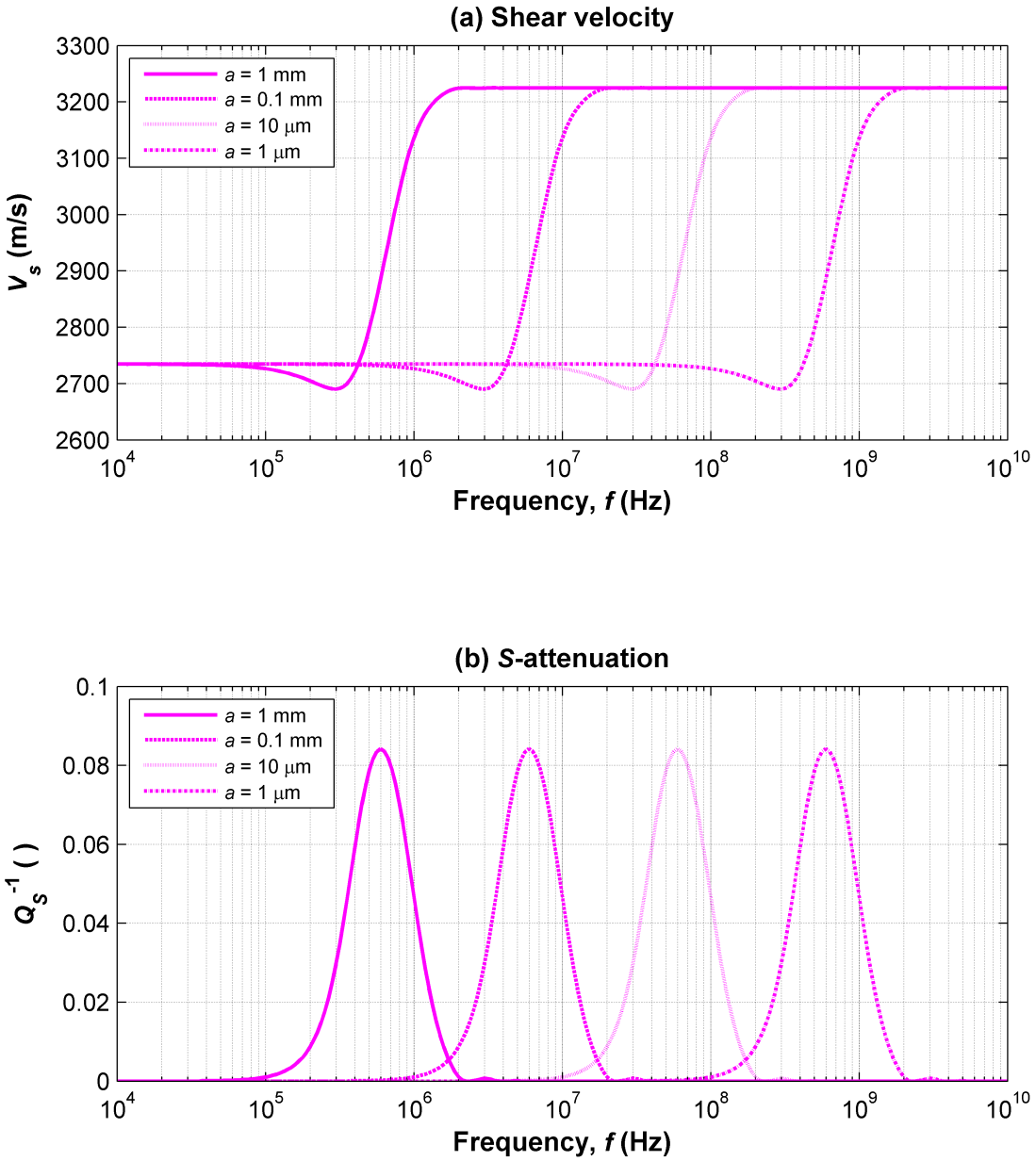

Figure 5.2: Acoustic scattering effects caused by spherical pores on shear-wave velocity and attenuation for the synthetic example described in Table 5.1. Diameters of inclusions are 1 mm, 0.1 mm, 10 μm, and 1 μm. Panel a: *S* -wave velocity. Panel b: *S* -wave attenuation.

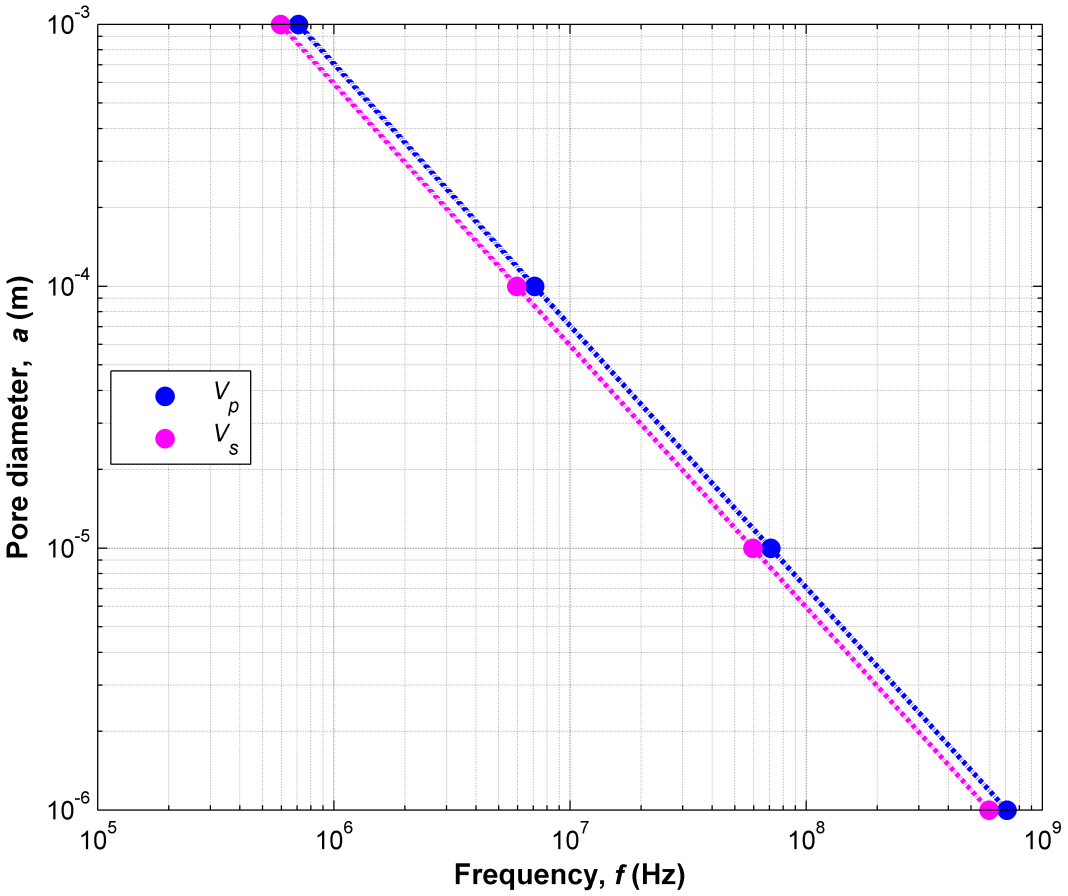

Figure 5.3: Relationship between pore diameter and frequency of maximum attenuation, as predicted by the self-consistent theory for pore-related scattering. Blue and magenta dots identify values of frequency of maximum attenuation obtained for compressional and shear waves, respectively.

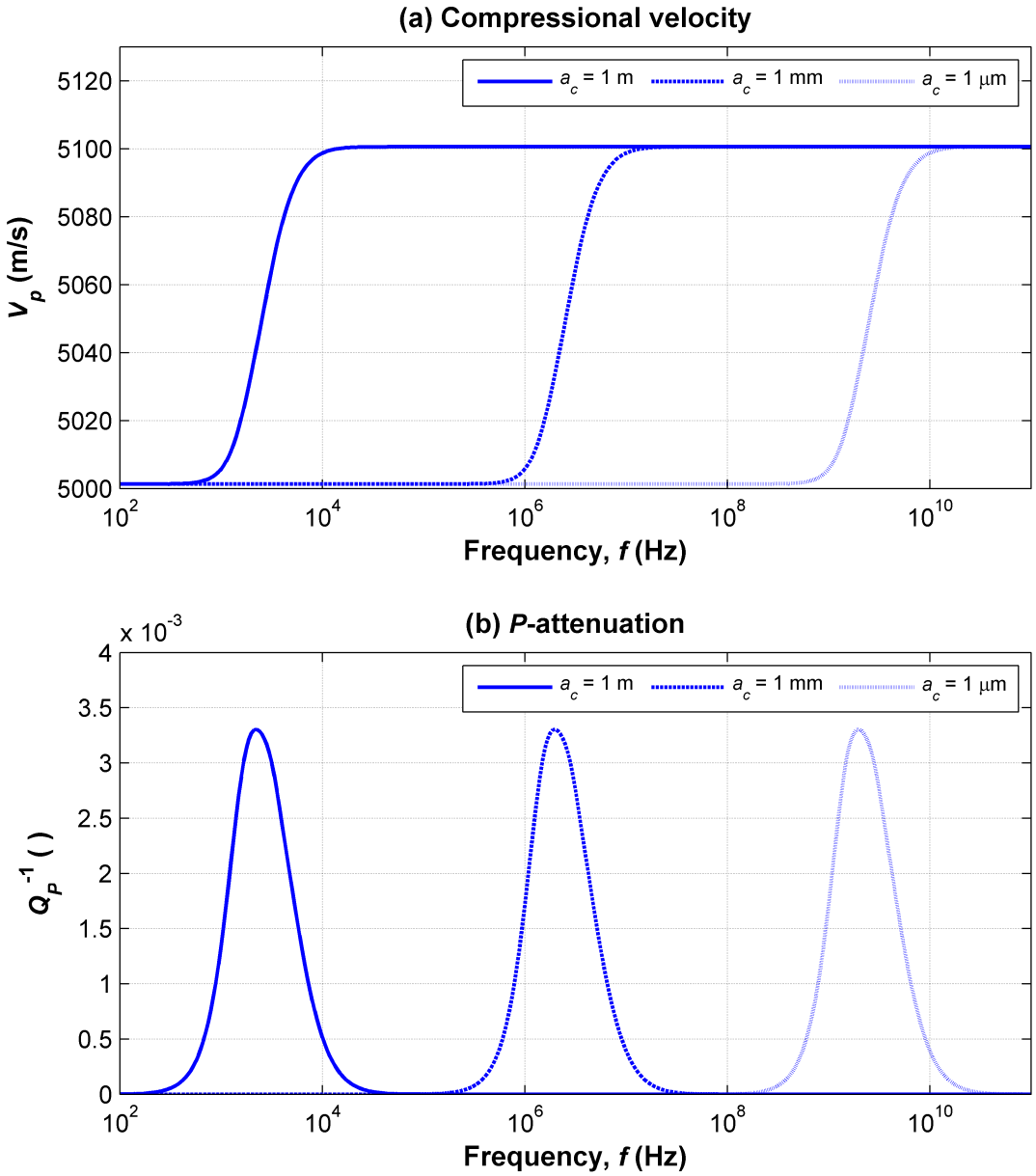

Figure 5.4: Acoustic scattering effects caused by penny-shaped fractures and cracks on compressional-wave velocity and attenuation for the synthetic example described in Table 5.2. Lengths of inclusions are 1 m, 1 mm, and 1 μm. Panel a: P -wave velocity. Panel b: P -wave attenuation.

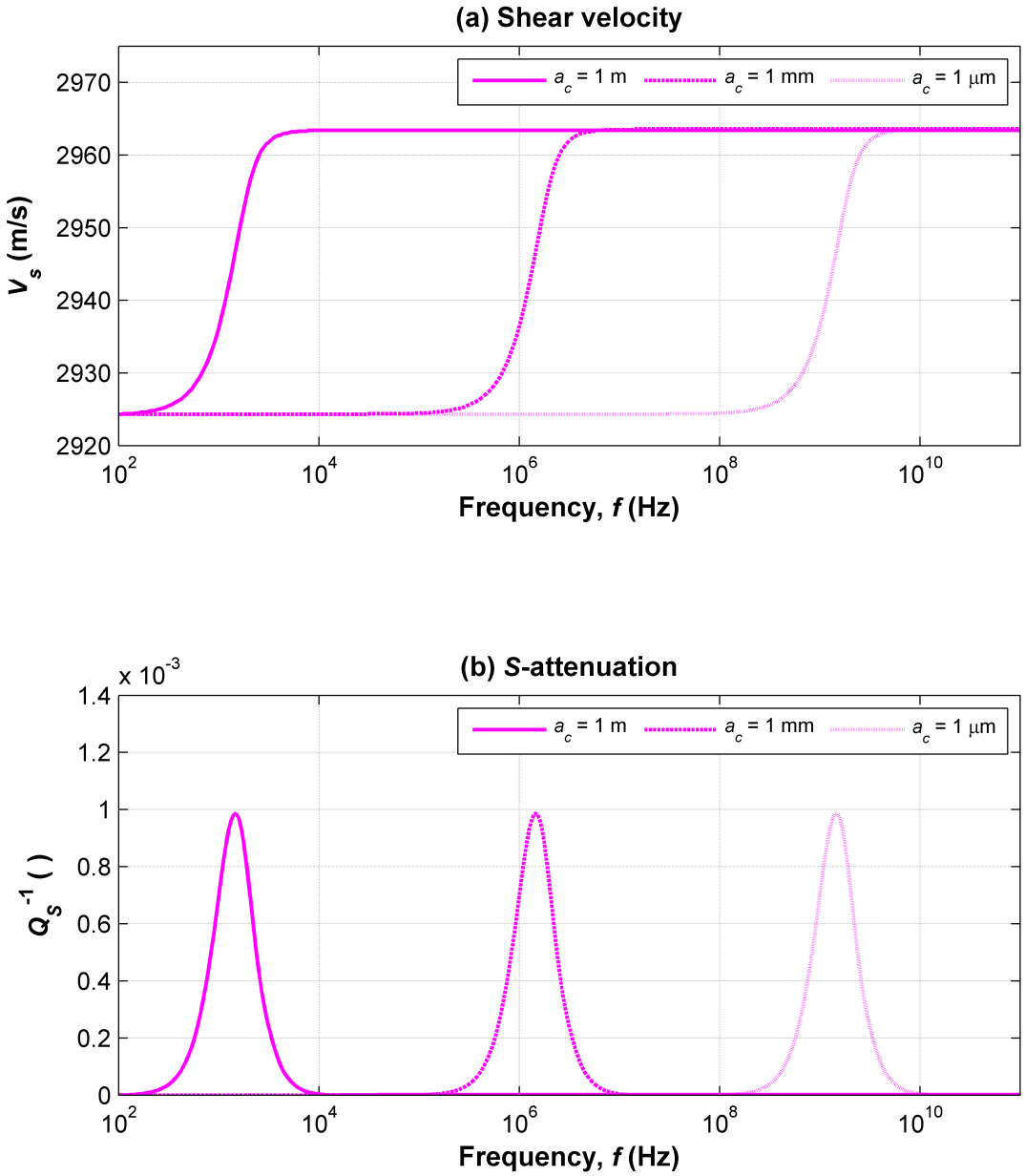

Figure 5.5: Acoustic scattering effects caused by penny-shaped fractures and cracks on shear-wave velocity and attenuation for the synthetic example described in Table 5.2. Lengths of inclusions are 1 m, 1 mm, and 1 μm. Panel a: S -wave velocity. Panel b: S -wave attenuation.

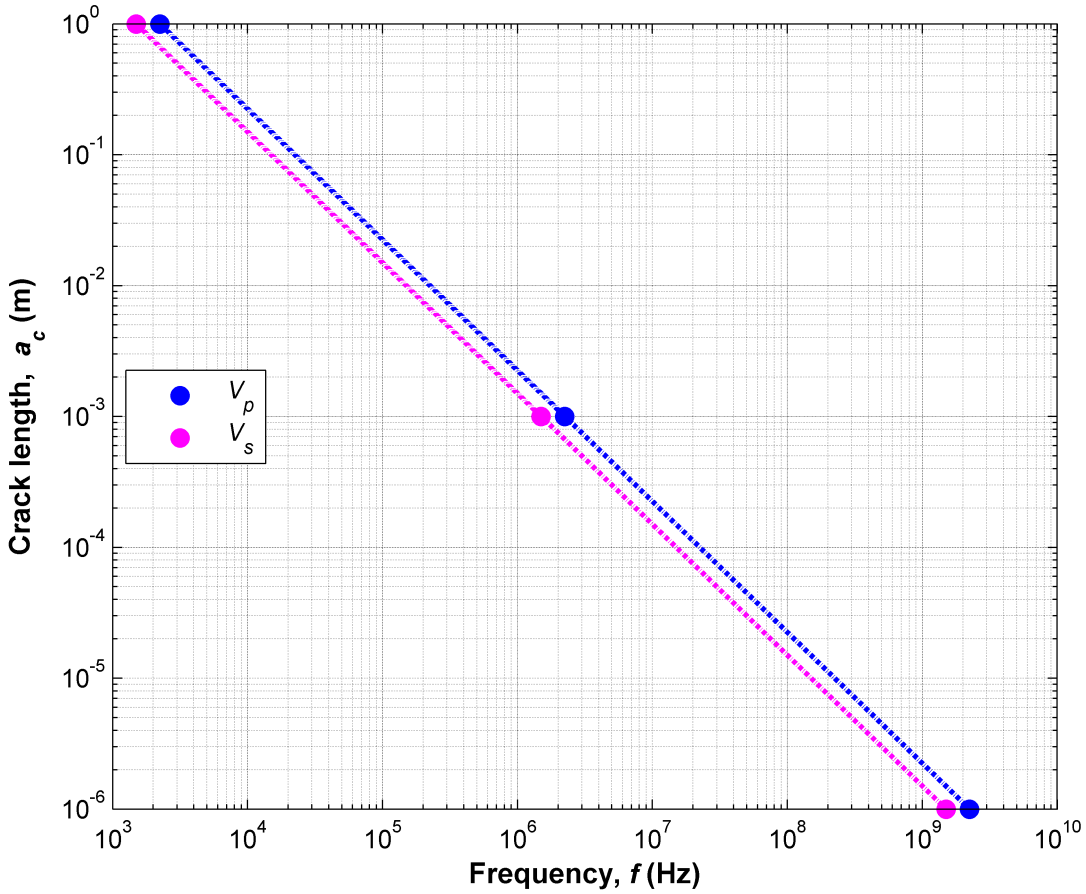

Figure 5.6: Linear relationship between logarithm of pore diameter and logarithm of frequency of maximum attenuation as predicted by the self-consistent theory for crack-related scattering. Blue and magenta dots identify values of frequency of maximum attenuation obtained for compressional and shear waves, respectively.

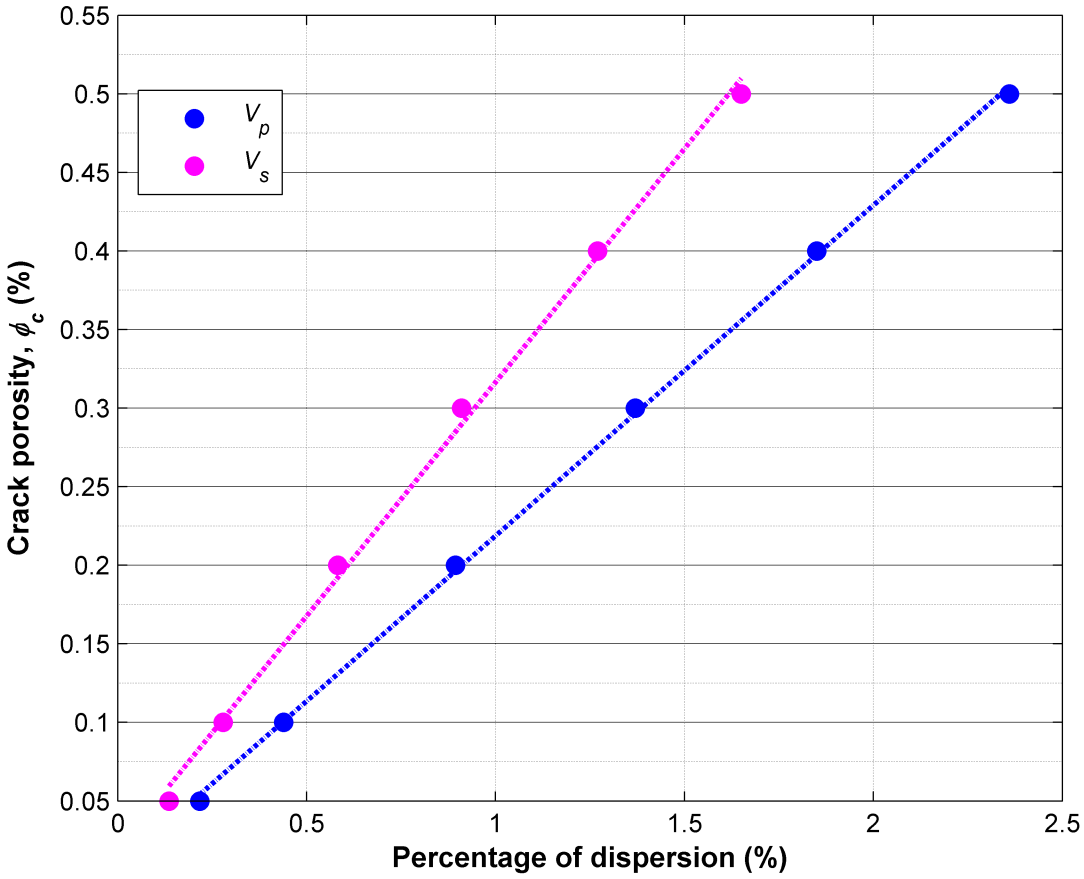

Figure 5.7: Relationships between crack porosity and percentage of dispersion for compressional and shear velocities as predicted by the self-consistent theory for crack-related scattering. Blue and magenta dots identify relative increase of velocity obtained for compressional and shear waves, respectively.

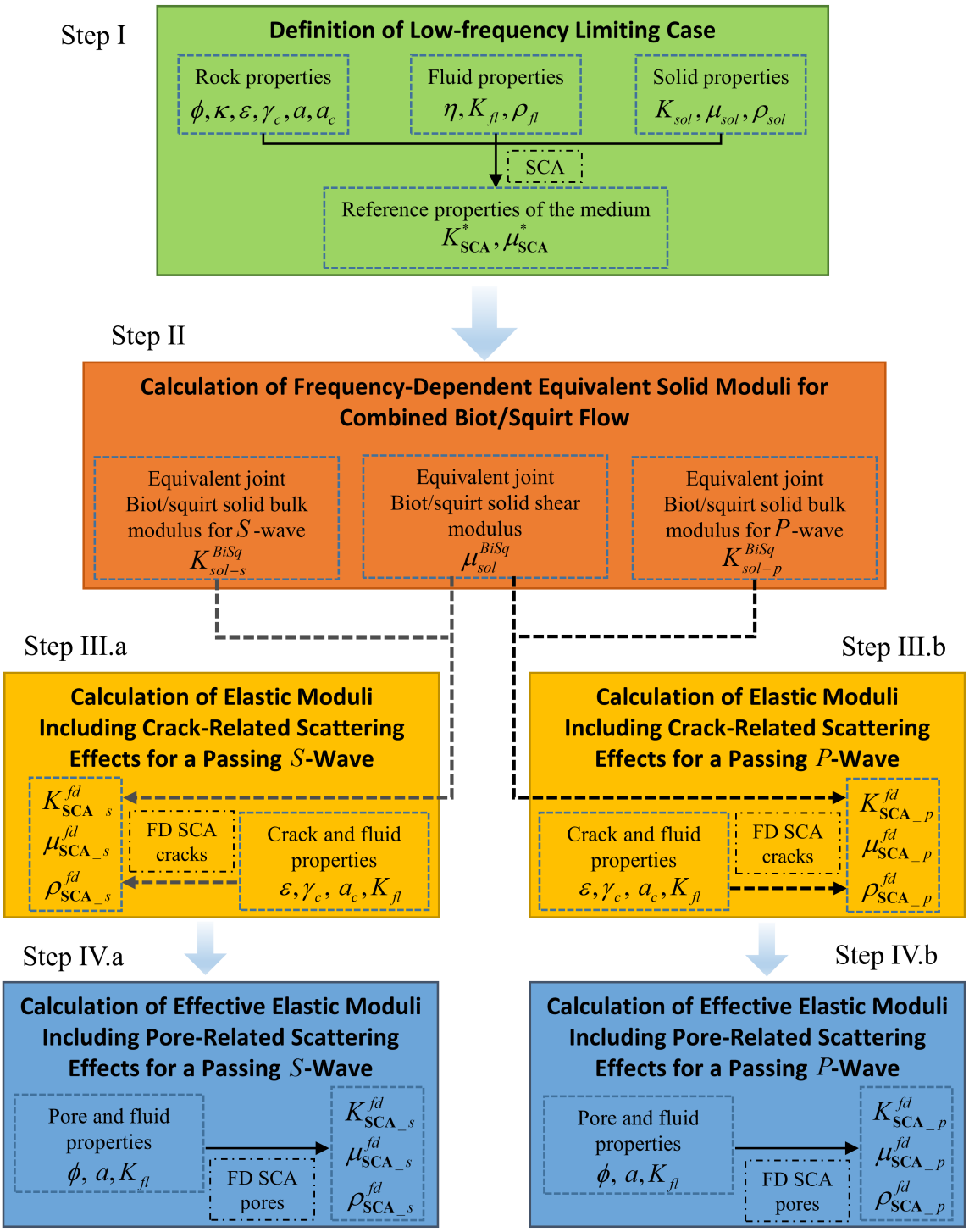

Figure 5.8: Frequency-dependent effective medium model workflow for reproduction of combined fluid-related and acoustic scattering dispersion effects on wave velocity and attenuation.

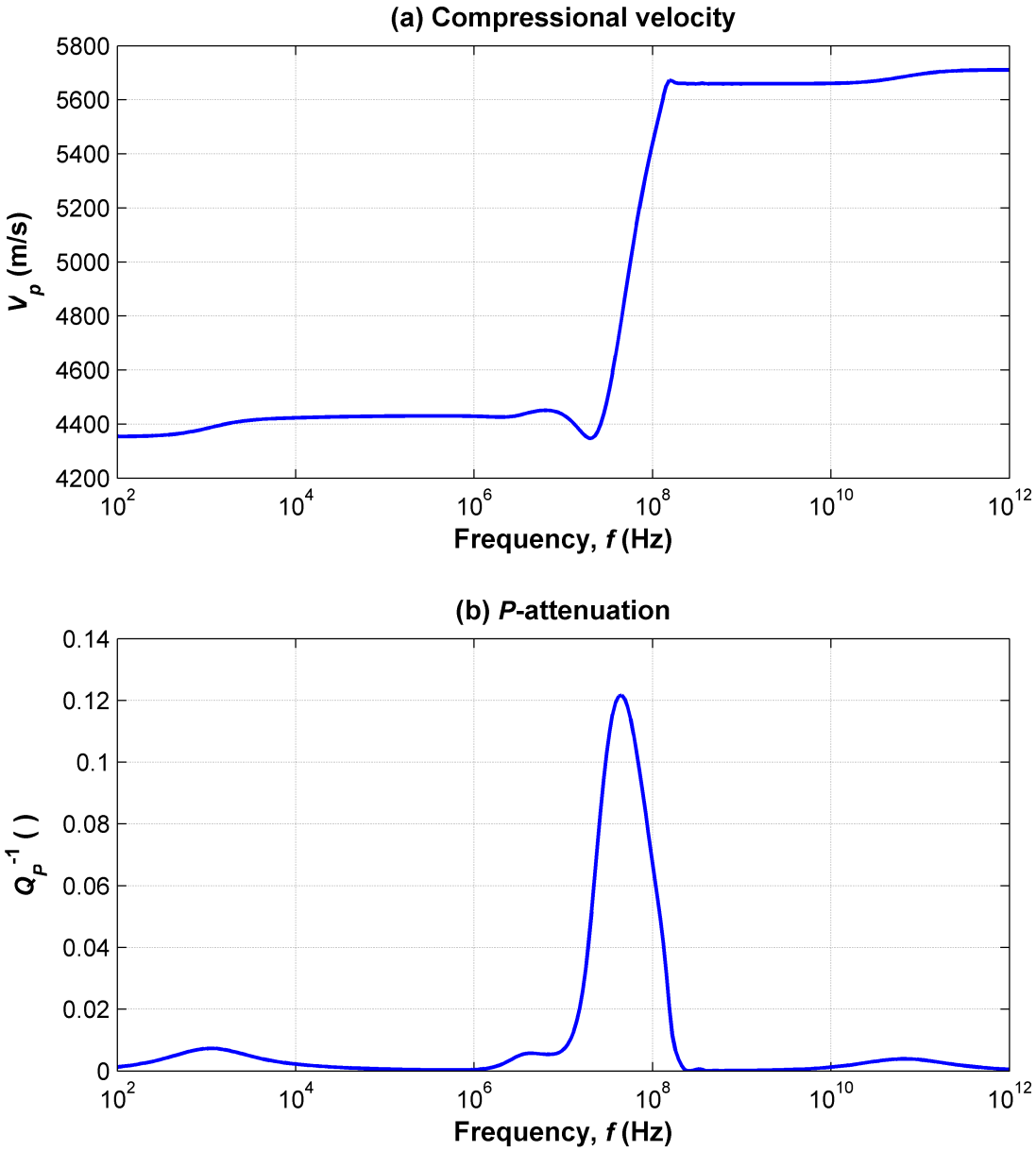

Figure 5.9: Combined pore fluid-related and acoustic scattering dispersion effects on compressional-wave velocity and attenuation for the synthetic sandstone example described in Table 4.3. Panel a: P-wave velocity. Panel b: P-wave attenuation.

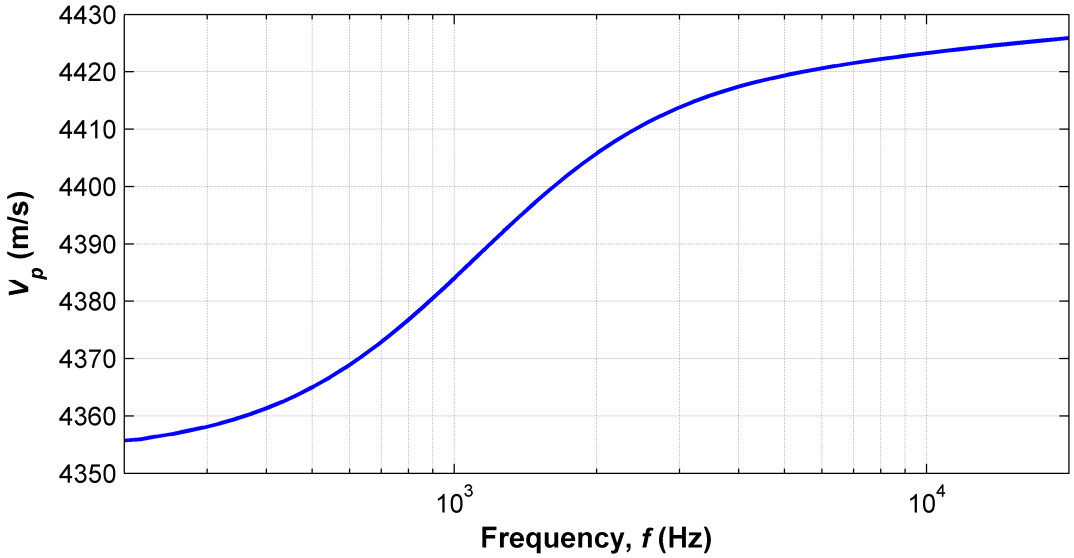

Figure 5.10: Biot's flow effects on compressional velocity at sonic frequencies for the synthetic sandstone example described in Table 4.3.

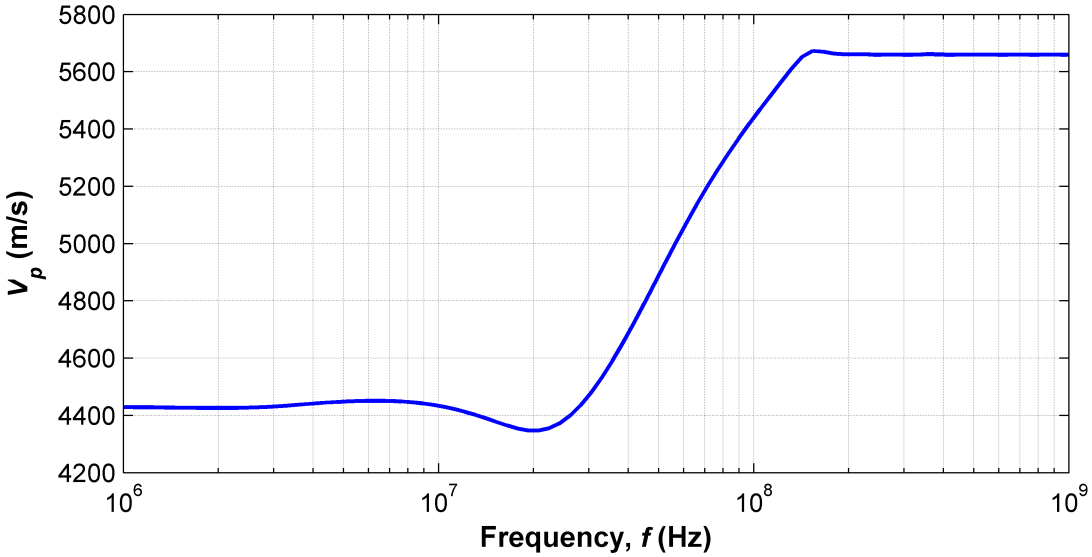

Figure 5.11: Crack- and stiff pore-related scattering effects on compressional velocity at ultrasonic frequencies for the synthetic sandstone example described in Table 4.3. The largest increase of velocity is caused by stiff pores.

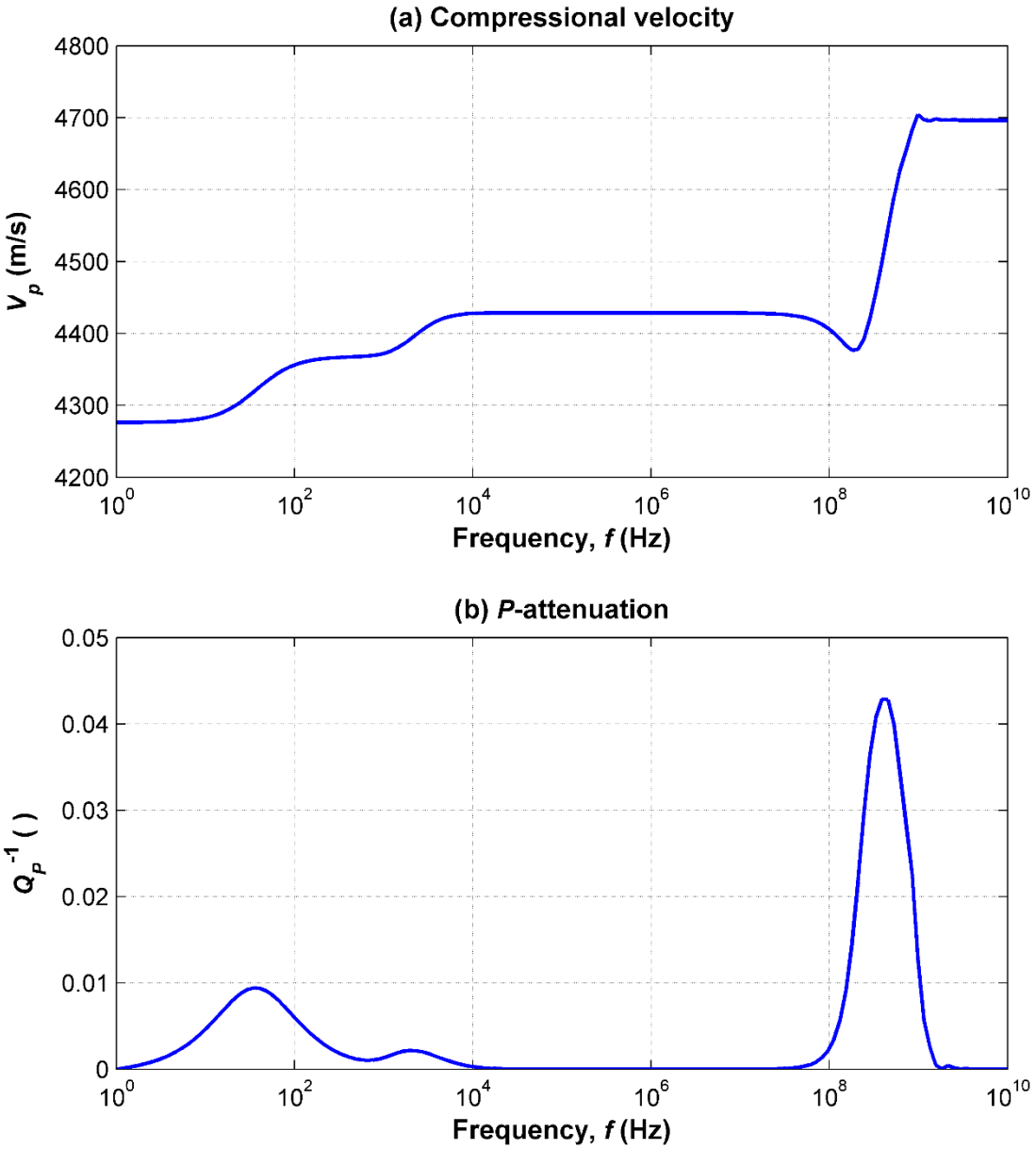

Figure 5.12: Combined pore fluid-related and acoustic scattering dispersion effects on compressional-wave velocity and attenuation for the synthetic shaly sandstone example described in Table 4.4. Panel a: P-wave velocity. Panel b: P-wave attenuation.

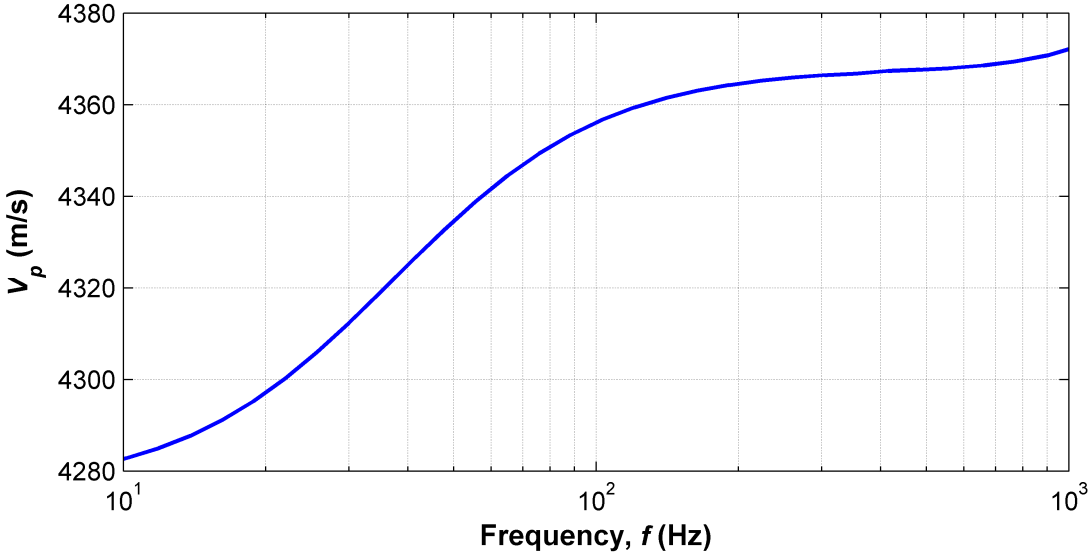

Figure 5.13: Squirt flow effects on compressional velocity at seismic frequencies for the synthetic shaly sandstone example described in Table 4.4.

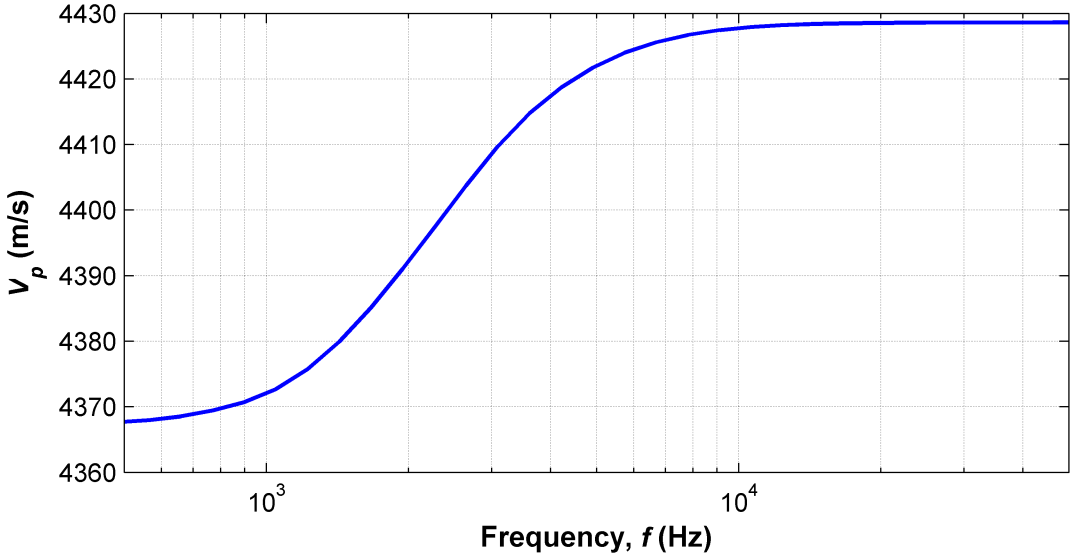

Figure 5.14: Acoustic scattering effects due to the simulated presence of fractures on compressional velocity at sonic frequencies for the synthetic shaly sandstone example described in Table 4.4.

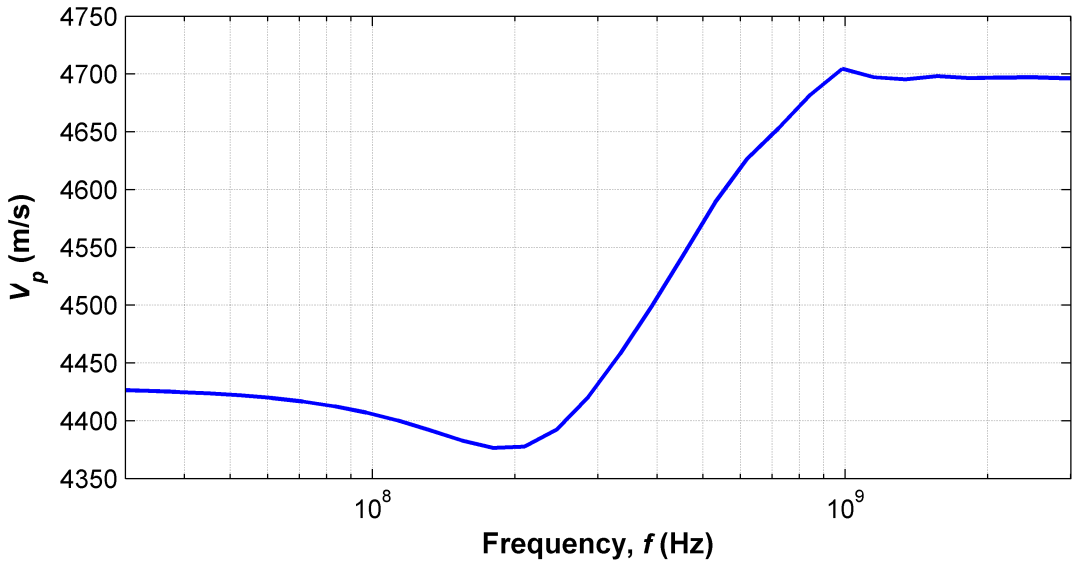

Figure 5.15: Pore acoustic scattering and Biot's flow effects on compressional velocity at ultrasonic frequencies for the synthetic shaly sandstone example described in Table 4.4. Velocity increase due to the Biot's flow mechanism occurs around 1.5×10^9 Hz and is almost imperceptible.

Chapter 6: Summary, Conclusions, and Recommendations

This final chapter summarizes the main developments and technical contributions presented in this dissertation, reiterates general conclusions from the results, and discusses recommendations for possible future research.

6.1 SUMMARY

The main objective of the dissertation was twofold: (1) to develop a rock physics model to reproduce true rock fabric parameters of laminated shales and estimate their elastic properties more accurately, and (2) to advance a dynamic rock physics model to account for principal causes of dispersion in saturated isotropic rocks. These models were constructed through combinations of two well-known and widely used effective medium theories, the differential effective medium theory and/or the self-consistent approximation. Both models aim to improve the reliability of elastic parameter calculations and to enable the assessment of supplemental parameters.

Detailed rock physics modeling techniques that reproduce the most important features of unconventional reservoirs affecting elastic properties while limiting non-uniqueness of values of input parameters had yet to be proposed. This was the main motivation behind the developments presented in the first part of the dissertation. I described previously developed isotropic and VTI versions of the SCA and DEM invoked in the model. First, isotropic theories are combined to reconstruct sand volumes composed of calcite, quartz, kerogen, and isolated and percolating sand porosity. Only part of the quartz concentration at each depth is included in sand volumes; the rest is assumed to be contained in shale volumes as silt particles along with clay grains and shale porosity divided between isolated and connected pores. Fraction of total porosity to be added into

the medium as shale porosity is inferred from readings of density porosity logs in pure shale layers. Relative concentration of silt with respect to clay is taken equal to quartz concentration of pure shale layers. This ensures that the observed properties of a specific formation are accounted for in the model. Using the VTI DEM, clay particles and porosity in shale volumes are added as penny-shaped inclusions aligned in the horizontal direction to reproduce common features causing shaly sandstones anisotropy. The effect of laminations on overall elastic properties of such formations is simulated with the Backus average. Vertical or horizontal fractures, aligned in the same direction to respect the assumed vertical transverse isotropic geometry, are added next. The reliability of most rock physics models is restricted by the larger number of inputs compared to outputs. I addressed this limitation by calculating horizontally- and vertically-polarized shear velocities in deviated wells, Stoneley velocity, and, most notably, horizontal and vertical electrical resistivity with modified SCA and DEM theories. Aspect ratio of cracks and percentage of connected porosity are rock fabric parameters that have an impact on both effective strength of the rock and electrical resistivity. Therefore, matching sonic logs and measured formation resistivity with calculated properties effectively constrained rock fabric estimates and limited non-uniqueness of solution. The joint sonic/resistivity rock physics model was applied to two wells in the Haynesville shale, more precisely to two vertical wells and one deviated section, and two portions of the same vertical well in the Barnett shale. Differences between calculated velocities and sonic logs were less than 5.4% for the simulations in the Haynesville shale and 4.3% in the Barnett shale. Qualitative agreement between computed and measured electrical resistivity was good in all studied wells.

I developed a procedure to calculate stress concentration and fracturing pressure in horizontal wells placed in laminated shales. Fracture initiation pressure is directly related to the degree of anisotropy of VTI rocks. Degree of anisotropy is expressed as the ratio of

horizontal to vertical Young's moduli calculated from the entries of the stiffness tensor. Higher Young's modulus ratio leads to lower requirements of equivalent mud weight. Using the accurate elastic properties calculated with the improved rock physics model, suitable depth zones to place horizontal wells were identified along the studied vertical wells. Retained criteria when locating optimal depths to drill horizontal wells were brittleness (high values of Young's moduli) and low fracturing pressure (high values of Young's modulus ratio).

The second part of this dissertation focused on the issue of viscoelastic behavior exhibited by most rock-like composites, but ignored by classical effective medium theory. Stiffness properties of saturated rocks are frequency-dependent and are influenced by many mechanisms of dispersion. First, I developed two models for reproduction of Biot's flow and squirt flow mechanisms. The concept of complex-valued, frequency-dependent equivalent elastic parameters for the solid background of saturated isotropic rocks was introduced to account for dispersion and attenuation effects. Dynamic solid moduli for Biot's flow were calculated with the definition of two correction functions that depend on elastic properties of the solid grains and fluid included in the rock. Dynamic solid moduli for squirt flow were calculated using the definition of correction functions that depend on total porosity and crack density of the rock. I described the results obtained with both newly developed models when applied to numerous synthetic cases for which main properties were varied over an extensive range of values. Simulated velocities and attenuation curves were plotted alongside predictions calculated with original Biot's (1956a, 1956b) and Chapman et al.'s (2006) equations for comparison purposes. The good agreement observed in each case indicates that predictions for both fluid-related mechanisms are reliable and can be used to describe fluid-related dispersion effects. Effective medium models for Biot's and squirt flow effects are valid for rocks with less than 35% porosity and characterized by

a solid matrix, with bulk and shear moduli higher than 20 GPa and 18 GPa, respectively. Next, I advanced a joint effective medium model for reproduction of Biot/squirt flow effects on velocities. The model is summarized in three steps: (1) definition of a low-frequency case of reference that corresponds to elastic properties calculated with Wu's (1966) isotropic self-consistent approximation, (2) estimation of two frequency-dependent bulk moduli and one frequency-dependent shear modulus for the solid background of the composite, computed as the sum of the dynamic moduli obtained separately with the effective medium models for Biot's and squirt flow, and (3) calculation of effective elastic dynamic properties of the rock by adding fluid-saturated cracks and spherical pores into the dynamic solid background with Wu's (1966) self-consistent-approximation.

Finally, a complete effective medium model is proposed to reproduce scattering and fluid-related mechanisms of dispersion. Self-consistent approximation methods for scattering mechanisms, developed by Smyshlyaev et al. (1993) and Sabina and Willis (1988), are alternatively invoked to add cracks and stiff pores into a solid background with dynamic elastic properties obtained with the Biot/squirt flow effective medium model. I derived the intermediate equations in Smyshlyaev et al.'s dynamic self-consistent approximations used to include randomly-oriented cracks. The model was tested on two synthetic examples defined with attributes of a sandstone and a shaly sandstone. I observed increases of velocity and peaks of attenuation occurring at various frequencies due to the four mechanisms included in the model. Relations are also investigated between rock fabric and petrophysical parameters assumed in the synthetic examples and frequencies of dispersion. Unfortunately, without any data available, predictions of velocity increase and attenuation cannot be verified, and the model remains at this point purely theoretical. The model is valid for isotropic rocks only, which is a grave limitation. Moreover, the different mechanisms of dispersion and attenuation taken into account in the model are completely

independent from each other, which probably contradicts the reality of rocks' dispersive behavior.

6.2 CONCLUSIONS

The models developed and reported in this dissertation led to the following conclusions:

i. New parameters invoked in the effective medium model were defined by readings of well logs that are not commonly used in rock physics modeling. For instance, the fraction of porosity added in the shale volumes was derived from the value of porosity logs at the depths of pure shale layers in the studied formations. Additional inputs might seem to increase complexity, but because they are estimated and set beforehand, they actually help to constrain the assessment of other rock properties with the rock physics model.

ii. Effective medium theories can reproduce true geological and petrophysical parameters of rocks, especially of unconventional reservoirs that exhibit complex rock composition and fabric. The typical features found in laminated shaly sandstones integrated in my rock physics model included the alignment of clay particles and penny-shaped cracks, the presence of natural fractures, and the distinction between connected and isolated porosity.

iii. Increasing the number of velocity outputs efficiently limited the number of solutions that originally matched compressional and shear sonic logs acquired in vertical wells drilled in VTI formations. This was done by calculating Stoneley velocity if it was measured and/or applying the model to a deviated section of a

nearby well penetrating the same geological formation to have access to a slow and a fast shear velocity.

iv. Combining elastic EMTs with EMTs for calculation of electrical resistivity allowed for the verification of two main inputs in the rock physics model: fraction of percolating porosity and crack aspect ratio. By further constraining values of some parameters, the development of a joint sonic/petrophysical parameter model contributed to the improved accuracy of the estimates of rock elastic properties.

v. When minimization of fracture initiation pressure is pursued, in-situ stress anisotropy will most likely be the parameter to consider first. In formations where horizontal stresses exhibit similar values, rock anisotropy becomes a crucial component in the choice of horizontal well placement along a vertical well. I found that rocks with a high degree of anisotropy enhance the ability to initiate hydraulic stimulation.

vi. The novel concept of frequency-dependent bulk and shear solid moduli has proved to be suitable for reproduction of dispersion and attenuation effects caused by Biot's flow and squirt flow on velocity. Dynamic equivalent elastic properties for the solid background calculated by the model represent strengthening of rocks commonly associated with dispersive behavior, but they should not be interpreted as the sources of dispersion.

vii. I developed procedures based on self-consistent approximation equations to add porous inclusions into a dynamic equivalent grain matrix calculated for Biot or squirt flow. These procedures to reconstruct a rock as a poroelastic medium are extremely simple and efficient because effective frequency-dependent elastic parameters are predicted in the same manner as static properties and all dispersion mechanisms are included into the definition of the rock's solid moduli.

viii. Providing that low-frequency limits of dynamic solid moduli are the same, equivalent properties can be calculated for combined Biot/squirt flow phenomena. Classical EMTs can be utilized in conjunction with the frequency-dependent strength parameters of a rock's matrix to numerically determine acoustic attenuation and dispersion in poroelastic systems.

ix. Because low-frequency limits of the methods developed by Sabina and Wills (1988) and Smyshlyaev et al. (1993) are the same as static results obtained with Wu's (1966) SCA, they can be combined and applied alternatively to reproduce acoustic scattering effects caused by cracks and stiff pores.

x. A model that enables the simulation of four distinct dispersion mechanisms was proposed in this dissertation. It accounts for Biot's and squirt flow and acoustic scattering due to the presence of spherical pores and randomly-oriented cracks. I demonstrated that some of the main sources of dispersion can occur at frequencies at which sonic measurements are usually conducted when logging a formation. Consequently, viscoelastic effective medium modeling can prove to be relevant in conditions where static theories would give rise to inaccurate estimates of rock fabric attributes.

xi. I found that the complete dispersion model relates the dynamic behavior of rocks to parameters such as porosity, permeability, fluid viscosity, and shape of pores and cracks. The development of viscoelastic rock physics models is valuable for the estimation of parameters in addition to estimating elastic properties of a formation.

6.3 RECOMMENDATIONS FOR FUTURE WORK

The models developed in this dissertation were based on several assumptions that represent limitations in terms of accuracy and reliability. The following is a list of recommendations to improve the contributions described in this dissertation:

i. The new rock physics model for laminated shaly sandstones could be further enhanced by the addition parameters that directly influence elastic properties of such formations such as pore pressure or temperature. Temperature affects elastic properties of minerals, notably in clay. Although the impact of temperature on rock elastic properties is probably limited compared to in-situ stress and rock fabric, integration of potential temperature effects on rock mechanical properties would be valuable when comparing core measurements to well logs.

ii. The model was developed assuming that the solid matrix of the rock was composed of only four minerals: quartz, calcite, clay, and kerogen. Results of multi-mineral inversion for estimation of rock composition could be improved by not grouping different minerals; for example, in this study calcite was grouped with dolomite. Furthermore, values for the elastic properties of individual minerals are specific to a studied formation. Having detailed knowledge of these parameters when implementing the simulation method would enable more reliable assessment of rock fabric properties.

iii. The model for estimation of rock fabric features of laminated shales should be implemented in as many wells as possible in the same formation. Extensive comparisons of calculated velocities and electrical resistivities with in-situ measurements is the recommended procedure to verify estimates of rock fabric parameters assumed in the model that influence elastic properties. Additionally,

mechanical tests performed on cores would contribute to the validation of estimations of elastic properties, provided that a reliable correlation is found between static and dynamic parameters.

iv. I introduced two new effective medium models for reproduction of Biot's and squirt flow using Wu's self-consistent equations. However, both Biot's and Chapman et al.'s models, used as reference for the elaboration of the model, assume that pores and cracks are connected and fluid can flow within the pore space for that reason. Invoking the self-consistent approximation alone does not enable one to reproduce this feature. An improved effective medium model could be built by combining the SCA with the DEM, for example, to improve consistency between original models for fluid-related dispersion and developed effective medium models.

v. Another limiting assumption made in the model for combined Biot/squirt flow mechanisms is the fact that reproduction of velocity increases and peaks of attenuation are based on two distinct models. As a result, Biot's flow and squirt flow effects are uncoupled in my model. Dispersion and attenuation phenomena associated with pore fluid flow are commonly interdependent, and I recommend a different approach based on more complex poroelastic models that simultaneously take into account Biot's and squirt flow mechanisms, such as the ones devised by Parra (1997) or Chapman et al. (2002).

vi. The frequency-dependent solid moduli and the elastic properties of the saturated effective medium are complex-valued; therefore, the dynamic effective medium model would still be applicable if the static solid moduli of minerals are assumed to be complex-valued. This characteristic would simulate dispersion mechanisms associated with the inherent viscoelasticity of the frame

of some rocks. It is sometimes stated in the literature that clay minerals should be considered viscoelastic materials (refer to Carcione, 2000). Taking viscoelastic behavior of solid minerals into account would improve the accuracy of the dispersion and attenuation predictions.

vii. The development of the new joint fluid-related and scattering effective medium theory showed that frequencies at which dispersion phenomena occur is related to properties, such as permeability and fluid viscosity, that need to be quantified when identifying the optimal depth zones for hydrocarbon production. For the assessment of these properties to be possible, the implementation of the dynamic simulation method would require parallel measurements of dispersive behavior. An experimental procedure could be developed to test the model (on core samples) in particular with ultrasonic measurements at multiple frequencies to verify estimations obtained using the model.

viii. Predictions made with the viscoelastic model are applicable to isotropic rocks only, which is a significant restriction. Effective medium models and the concept of dynamic equivalent solid moduli introduced in this dissertation for reproduction of dispersion mechanisms caused by wave-induced fluid flow could be extended to anisotropic versions of the SCA and the DEM. Future anisotropic models could then, for instance, be combined with Sabina et al.'s (1993) self-consistent approximations for acoustic scattering dispersion generated by aligned spheroidal inclusions.

Appendix A: Calculation of Mura's Fourth-Rank Tensor G Invoked in Anisotropic Versions of the DEM and SCA Methods

Both VTI versions of the SCA and DEM methods invoke a fourth-rank tensor **G** (equation 2.26) which is calculated from the response of an unbounded matrix of the effective medium. In the case of spheroidal inclusions, the entries of the tensor **G** are given by Mura (1982) as

$$G_{ijkl} = \frac{1}{8\pi}\left[\overline{G}_{ikjl} + \overline{G}_{jkil}\right], \tag{A.1}$$

where

$$\overline{G}_{ijkl} = \left(\alpha_1\alpha_1\alpha_3\right)\int_S N_{ij}\left(\boldsymbol{\xi}\right)D^{-1}\left(\boldsymbol{\xi}\right)\xi_l\xi_k\zeta^{-3}dS\left(\boldsymbol{\xi}\right), \tag{A.2}$$

$$\zeta = \left(\alpha_1^2\xi_1^2 + \alpha_1^2\xi_2^2 + \alpha_3^2\xi_3^2\right)^{1/2}, \tag{A.3}$$

$$D\left(\boldsymbol{\xi}\right) = \det\left(C_{ijkl}\xi_j\xi_l\right), \tag{A.4}$$

and

$$N_{ij} = cofactor(C_{ijkl}\xi_j\xi_l). \tag{A.5}$$

In the above equations, S is the unit sphere, $\boldsymbol{\xi}$ is the unit vector forming S, dS is the differential of the surface area on the unit sphere, α_1 and α_3 are the length of the semi-axes of the spheroid, and $\left(\xi_1,\xi_2,\xi_3\right)$ are the coordinates of the unit vector .

For a transversely isotropic system, the non-zero entries of tensor **G**, G_{ijkl}, are given by a definite integral of polynomial functions from 0 to 1. If the principal axes of the spheroidal inclusion coincide with the orientation of the effective medium, in other words, if the semi-axes of same length $\left(\alpha_1\right)$ lie in the plane of isotropy and the third semi-axis is parallel to the medium's axis of symmetry, the inclusion domain can be described as

$$\frac{x_1^2}{\alpha_1^2}+\frac{x_2^2}{\alpha_1^2}+\frac{x_3^2}{\alpha_3^2}\le 1. \tag{A.6}$$

Then, the non-zero entries G_{ijkl} are given by

$$\begin{aligned}\overline{G}_{1111}=\overline{G}_{2222}=\frac{\pi}{2}\int_0^1\Delta\left(1-x^2\right)\Big\{\Big[f\left(1-x^2\right)+h\gamma^{-2}x^2\Big]\\ \Big[\left(3e+d\right)\left(1-x^2\right)+4f\gamma^{-2}x^2\Big]-g^2\gamma^{-2}x^2\left(1-x^2\right)\Big\}dx,\end{aligned} \tag{A.7}$$

$$\overline{G}_{3333}=4\pi\int_0^1\Delta\gamma^{-2}x^2\Big[d\left(1-x^2\right)+f\gamma^{-2}x^2\Big]\Big[e\left(1-x^2\right)+f\gamma^{-2}x^2\Big]dx, \tag{A.8}$$

$$\begin{aligned}\overline{G}_{1122}=\overline{G}_{2211}=\frac{\pi}{2}\int_0^1\Delta\left(1-x^2\right)\Big\{\Big[f\left(1-x^2\right)+h\gamma^{-2}x^2\Big]\\ \Big[\left(3e+d\right)\left(1-x^2\right)+4f\gamma^{-2}x^2\Big]-3g^2\gamma^{-2}x^2\left(1-x^2\right)\Big\}dx,\end{aligned} \tag{A.9}$$

$$\begin{aligned}\overline{G}_{1133}=\overline{G}_{2233}=2\pi\int_0^1\Delta\gamma^{-2}x^2\Big\{\Big[\left(d+e\right)\left(1-x^2\right)+2f\gamma^{-2}x^2\Big]\\ \Big[f\left(1-x^2\right)+h\gamma^{-2}x^2\Big]-g^2\gamma^{-2}x^2\left(1-x^2\right)\Big\}dx,\end{aligned} \tag{A.10}$$

$$\begin{aligned}\overline{G}_{3311}=\overline{G}_{3322}=2\pi\int_0^1\Delta\left(1-x^2\right)\Big[d\left(1-x^2\right)+f\gamma^{-2}x^2\Big]\\ \Big[e\left(1-x^2\right)+f\gamma^{-2}x^2\Big]dx,\end{aligned} \tag{A.11}$$

$$\overline{G}_{1212}=\frac{\pi}{2}\int_0^1\Delta\left(1-x^2\right)^2\Big\{g^2\gamma^{-2}x^2-\left(d-e\right)\Big[f\left(1-x^2\right)+h\gamma^{-2}x^2\Big]\Big\}dx, \tag{A.12}$$

and

$$\overline{G}_{1313}=-2\pi\int_0^1\Delta g\gamma^{-2}x^2\left(1-x^2\right)\Big[e\left(1-x^2\right)+f\gamma^{-2}x^2\Big]dx, \tag{A.13}$$

where

$$\begin{aligned}\Delta^{-1}=\Big[e\left(1-x^2\right)+f\gamma^{-2}x^2\Big]\Big\{\Big[d\left(1-x^2\right)+f\gamma^{-2}x^2\Big]\\ \Big[f\left(1-x^2\right)+h\gamma^{-2}x^2\Big]-g^2\gamma^{-2}x^2\left(1-x^2\right)\Big\},\end{aligned} \tag{A.14}$$

$$d = c_{11}, \tag{A.15}$$

$$e = (c_{11} - c_{12}) / 2, \tag{A.16}$$

$$f = c_{44}, \tag{A.17}$$

$$g = c_{13} + c_{44}, \tag{A.18}$$

$$h = c_{33}, \tag{A.19}$$

and

$$\gamma = \frac{\alpha_3}{\alpha_1}. \tag{A.20}$$

Appendix B: Calculation of Backus Average for an Effective Medium Constituted by Alternating Isotropic and VTI Layers

An effective VTI medium with its axis of symmetry perpendicular to alternating fine layers is associated with an averaged stiffness tensor with the form

$$\mathbf{C_{av}} = \begin{bmatrix} c_{11\_av} & c_{12\_av} & c_{13\_av} & 0 & 0 & 0 \\ c_{12\_av} & c_{11\_av} & c_{13\_av} & 0 & 0 & 0 \\ c_{13\_av} & c_{13\_av} & c_{33\_av} & 0 & 0 & 0 \\ 0 & 0 & 0 & c_{44\_av} & 0 & 0 \\ 0 & 0 & 0 & 0 & c_{44\_av} & 0 \\ 0 & 0 & 0 & 0 & 0 & \frac{1}{2}\left(c_{11\_av} - c_{12\_av}\right) \end{bmatrix}. \tag{B.1}$$

Elastic properties of the individual layers are averaged to calculate the elastic constants of the effective medium as (Backus, 1962)

$$c_{11\_av} = \left\langle c_{11} - {c_{13}}^2 / c_{33} \right\rangle + \left\langle 1/c_{33} \right\rangle^{-1} \left\langle c_{13}/c_{33} \right\rangle^2, \tag{B.2}$$

$$c_{12\_av} = \left\langle c_{12} - {c_{13}}^2 / c_{33} \right\rangle + \left\langle 1/c_{33} \right\rangle^{-1} \left\langle c_{13}/c_{33} \right\rangle^2, \tag{B.3}$$

$$c_{33\_av} = \left\langle 1/c_{33} \right\rangle^{-1}, \tag{B.4}$$

$$c_{13\_av} = \left\langle 1/c_{33} \right\rangle^{-1} \left\langle c_{13}/c_{33} \right\rangle^2, \tag{B.5}$$

and

$$c_{44\_av} = \left\langle 1/c_{44} \right\rangle^{-1}. \tag{B.6}$$

Brackets $\langle . \rangle$ indicate averages of the enclosed properties weighted by their volumetric proportions. The c_{ij_av} are the averaged entries of the stiffness tensor of the effective medium, and the c_{ij} are the entries of the stiffness tensor of the individual thin layers.

Appendix C: Definition of Terms Used in Biot's Velocity Equations

The different terms invoked in Biot wave equations (4.1) and (4.2) are defined by

$$H = K_{fr} + \frac{4}{3}\mu_{fr} + \frac{\left(K_{sol} - K_{fr}\right)^2}{\left(D - K_{fr}\right)}, \tag{C.1}$$

$$C = \frac{\left(K_{sol} - K_{fr}\right)K_{sol}}{\left(D - K_{fr}\right)}, \tag{C.2}$$

$$M = \frac{K_{sol}^2}{\left(D - K_{fr}\right)}, \tag{C.3}$$

and

$$D = K_{sol}\left[1 + \phi\left(\frac{K_{sol}}{K_{fl}} - 1\right)\right], \tag{C.4}$$

where K_{fr} and μ_{fr} are the effective bulk and shear moduli of the rock frame, respectively, K_{sol} is the bulk modulus of the mineral background composing the rock, K_{fl} is the effective bulk modulus of the pore fluid, and ϕ is the total porosity.

The viscodynamic operator $F(z)$ that appears in equation (4.3) is defined as

$$F(z) = \frac{1}{4}\left(\frac{zT(z)}{1 + 2iT(z)/z}\right), \tag{C.5}$$

where

$$T(z) = \frac{e^{i3\pi/4}J_1\left(ze^{-i\pi/4}\right)}{J_0\left(ze^{-i\pi/4}\right)}, \tag{C.6}$$

$$z = \left(\frac{\omega a^2 \rho_{fl}}{\eta}\right)^{1/2}, \tag{C.7}$$

and J_n is the Bessel function of order n, and a is the pore-size parameter corresponding to the radius of the spherical pores.

When the solid matrix is composed of spherical grains, Hovem and Ingram (1979) obtained

$$a = \frac{\phi d}{3(1-\phi)}, \tag{C.8}$$

where d is the characteristic grain diameter.

Appendix D: Formulation of the Scattering Problem and Approximate Solution of the Single-Scattering Problem

This appendix provides descriptions about the formulation of the general theory behind dispersive behavior due to scattering and the solution for the single-scattering problem that leads the frequency-dependent self-consistent equations (5.3) and (5.4) as given by Sabina et al. (1993).

D.1 GENERAL THEORY

The effective composite that is being reconstructed with the dynamic self-consistent method developed by Sabina and Willis (1988) and Sabina et al. (1993) consists of a matrix with tensors of elastic stiffness and mass density $\mathbf{C}_1$ and $\boldsymbol{\rho}_1$, respectively, in which are embedded n different types of inclusions positioned randomly. An inclusion of type i has a stiffness tensor $\mathbf{C}_i$ and mass density $\boldsymbol{\rho}_i$. It occupies a domain $\mathbf{x}' + \Omega_i$ where Ω_i contains the origin. Each inclusion of type i thus has the same shape, size, and orientation; $\mathbf{x}'$ will be referred to as the center of the inclusion in question. The composite will be taken to occupy a domain Ω, large enough to contain many inclusions.

The field within the composite satisfies the equation of motion

$$\operatorname{div}(\boldsymbol{\varsigma}) = \dot{\mathbf{p}}, \tag{D.1}$$

where stress $\boldsymbol{\varsigma}$ and momentum density $\mathbf{p}$ are related to strain $\mathbf{e}$ and velocity $\mathbf{V}$ through the constitutive relations

$$\boldsymbol{\varsigma} = \mathbf{C}\mathbf{e}, \quad \mathbf{p} = \boldsymbol{\rho}\mathbf{V}, \tag{D.2}$$

with strain $\mathbf{e}$ and velocity $\mathbf{V}$ related to displacement $\mathbf{u}$ through

$$e_{ij} = \frac{1}{2}\left(u_{i,j} + u_{j,i}\right) \text{ and } V_i = \dot{u}_i. \tag{D.3}$$

The objective is to deduce from equations (D.1), (D.2), and (D.3), augmented with initial and boundary conditions, the averaged fields $\langle \boldsymbol{\varsigma} \rangle, \langle \mathbf{e} \rangle, \langle \mathbf{p} \rangle, \langle \mathbf{V} \rangle$, and $\langle \mathbf{u} \rangle$. The equation of motion (D.1) is linear and so immediately yields

$$\operatorname{div} \langle \boldsymbol{\varsigma} \rangle = \langle \dot{\mathbf{p}} \rangle. \tag{D.4}$$

The relations (D.3) can be averaged similarly. Moreover, the following relations exists:

$$\langle \mathbf{e} \rangle = \sum_{i=1}^{n+1} x_i \langle \mathbf{e} \rangle_i \text{ and } \langle \mathbf{V} \rangle = \sum_{i=1}^{n+1} x_i \langle \mathbf{V} \rangle_i, \tag{D.5}$$

where x_i represents the probability of finding material i at a position $\mathbf{x}$ inside the effective composite and $\langle \mathbf{e} \rangle_i$, $\langle \mathbf{V} \rangle_i$ represent, respectively, the expectation values of $\mathbf{e}$, $\mathbf{V}$ at $\mathbf{x}$, conditional upon finding material of type i at $\mathbf{x}$. The probabilities x_i, are uniform, and equal to volume fractions, if the material is statistically uniform, as assumed in Chapter 4. Furthermore, we have

$$\langle \boldsymbol{\varsigma} \rangle = \sum_{i=1}^{n+1} x_i \langle \boldsymbol{\varsigma} \rangle_i = \sum_{i=1}^{n+1} x_i \mathbf{C}_i \langle \mathbf{e} \rangle_i, \tag{D.6}$$

and hence, by elimination of $\langle \mathbf{e} \rangle_1$ between (D.5) and (D.6),

$$\langle \boldsymbol{\varsigma} \rangle = \mathbf{C}_1 \langle \mathbf{e} \rangle + \sum_{i=2}^{n+1} x_i (\mathbf{C}_i - \mathbf{C}_1) \langle \mathbf{e} \rangle_i. \tag{D.7}$$

Similarly,

$$\langle \mathbf{p} \rangle = \boldsymbol{\rho}_1 \langle \mathbf{V} \rangle + \sum_{i=2}^{n+1} x_i (\boldsymbol{\rho}_i - \boldsymbol{\rho}_1) \langle \mathbf{V} \rangle_i. \tag{D.8}$$

The problem would thus be solved if the mean fields $\langle \mathbf{e} \rangle_i$ and $\langle \mathbf{V} \rangle_i$ could be expressed in terms of $\langle \mathbf{e} \rangle$ and $\langle \mathbf{V} \rangle$. Exact calculation would require complete knowledge of the composite. This information is unavailable, and the problem would in any case be

too difficult. Approximate expressions are found, instead, by solving the problem of a single inclusion of type i, centered at $\mathbf{x}'$, embedded in a uniform reference medium with stiffness tensor $\mathbf{C}_0$ and density $\boldsymbol{\rho}_0$. The field incident on the inclusion is $\mathbf{u}_0$; contact with the original problem is made by selecting $\mathbf{C}_0$ and $\boldsymbol{\rho}_0$ so that the reference medium can support the mean wave $\langle \mathbf{u} \rangle$ and $\mathbf{u}_0$, the incident displacement field on the inclusion, can be taken equal to $\langle \mathbf{u} \rangle$.

D.2 THE SINGLE-SCATTERING PROBLEM

Attention is focused on plane mean waves, which a composite of infinite extent can support. Therefore, the single-scattering problem is considered, for an incident plane wave of the form

$$u_0(\mathbf{x}, t) = \mathbf{m} e^{i(k\mathbf{n}\cdot\mathbf{x} - \omega t)}, \tag{D.9}$$

this representing a wave that can propagate freely in the reference medium. Here, $\mathbf{n}$ is a unit vector defining the direction of the wave and k is the wave number. If the total stress and strain fields are denoted $\boldsymbol{\varsigma}$ and $\mathbf{e}$, respectively, it follows that

$$\boldsymbol{\varsigma} = \mathbf{C}_0 \mathbf{e} + \boldsymbol{\tau}, \tag{D.10}$$

where $\boldsymbol{\tau}$, referred to as the stress polarization, is zero outside the inclusion and satisfies

$$\boldsymbol{\tau} = (\mathbf{C}_i - \mathbf{C}_0)^{-1} \mathbf{e}, \tag{D.11}$$

within it. A momentum polarization can be defined similarly:

$$\mathbf{p} = \boldsymbol{\rho}_0 \mathbf{V} + \boldsymbol{\pi}, \tag{D.12}$$

where

$$\boldsymbol{\pi} = (\boldsymbol{\rho}_i - \boldsymbol{\rho}_0)^{-1} \mathbf{V}, \tag{D.13}$$

within the inclusion. If equations (D.10) and (D.12) are substituted into the equation of motion (D.1), it follows that the resulting total displacement field $\mathbf{u}$ is identical to one in the uniform reference medium, driven by the body-force $\left(\operatorname{div}\boldsymbol{\tau}-\dot{\boldsymbol{\pi}}\right)$, and hence may be represented in terms of a convolution integral involving the Green's function for the reference medium. Strain and velocity then follow by differentiation. As discussed by Sabina and Willis (1988), these fields can be represented in the forms

$$\mathbf{e}=\mathbf{e}_0-\mathbf{S}_x*\boldsymbol{\tau}-\mathbf{M}_x*\boldsymbol{\pi} \quad \text{and} \quad \mathbf{V}=\mathbf{V}_0-\mathbf{S}_t*\boldsymbol{\tau}-\mathbf{M}_t*\boldsymbol{\pi}. \tag{D.14}$$

The functions $\mathbf{S}_x$, $\mathbf{S}_t$, $\mathbf{M}_x$, and $\mathbf{M}_t$ are obtained from differentiating the Green's function G. The symbol $*$ represents the operation of convolution over space and time in general, or over space only in the time-reduced case when, as in equation (D.9), all fields contain a factor, which may be suppressed.

Integral equations for $\boldsymbol{\tau}$ and $\boldsymbol{\pi}$ now follow by combining (D.11) and (D.13) with (D.14):

$$\left(\mathbf{C}_i-\mathbf{C}_0\right)^{-1}\boldsymbol{\tau}+\mathbf{S}_x*\boldsymbol{\tau}+\mathbf{M}_x*\boldsymbol{\pi}=\mathbf{e}_0, \tag{D.15}$$

$$\left(\boldsymbol{\rho}_i-\boldsymbol{\rho}_0\right)^{-1}\boldsymbol{\pi}-\mathbf{S}_t*\boldsymbol{\tau}-\mathbf{M}_t*\boldsymbol{\pi}=\mathbf{V}_0. \tag{D.16}$$

These are hard to solve exactly, so instead a simple approximation is adopted, by taking $\boldsymbol{\tau}$ and $\boldsymbol{\pi}$ constant over the inclusion (but still dependent upon the position $\mathbf{x}'$ of its center) and satisfying equations (D.15) and (D.16) in the mean sense

$$\left(\mathbf{C}_i-\mathbf{C}_0\right)^{-1}\boldsymbol{\tau}+\overline{\mathbf{S}}_x^{(i)}*\boldsymbol{\tau}+\overline{\mathbf{M}}_x^{(i)}*\boldsymbol{\pi}=\overline{\mathbf{e}}_0^{(i)}, \tag{D.17}$$

$$\left(\boldsymbol{\rho}_i-\boldsymbol{\rho}_0\right)^{-1}\boldsymbol{\pi}+\overline{\mathbf{S}}_t^{(i)}*\boldsymbol{\tau}+\overline{\mathbf{M}}_t^{(i)}*\boldsymbol{\pi}=\overline{\mathbf{V}}_0^{(i)}, \tag{D.18}$$

where the overbar represents mean value over the inclusion, the superscript indicating that the inclusion is of type i.

In the case that the inclusion has a center of symmetry, it can be verified that $\bar{\mathbf{M}}_x^{(i)} = \bar{\mathbf{S}}_t^{(i)} = 0$. Then, equations (D.17) and (D.18) uncouple, and their solution can be given in the form

$$\boldsymbol{\tau} = \left[\left(\mathbf{C}_i - \mathbf{C}_0 \right)^{-1} \boldsymbol{\tau} + \bar{\mathbf{S}}_x^{(i)} \right]^{-1} \bar{\mathbf{e}}_0^{(i)} \quad \text{and} \quad \boldsymbol{\pi} = \left[\left(\boldsymbol{\rho}_i - \boldsymbol{\rho}_0 \right)^{-1} \boldsymbol{\pi} + \bar{\mathbf{M}}_t^{(i)} \right]^{-1} \bar{\mathbf{V}}_0^{(i)}, \tag{D.19}$$

taking time-reduction for granted. Approximations for the strain $\mathbf{e}$ and velocity $\mathbf{V}$ now follow from equations (D.11) and (D.13):

$$\mathbf{e} = \left[\mathbf{I} + \bar{\mathbf{S}}_x^{(i)} \left(\mathbf{C}_i - \mathbf{C}_0 \right) \right]^{-1} \bar{\mathbf{e}}_0^{(i)} \quad \text{and} \quad \mathbf{V} = \left[\mathbf{I} + \bar{\mathbf{M}}_t^{(i)} \left(\boldsymbol{\rho}_i - \boldsymbol{\rho}_0 \right) \right]^{-1} \bar{\mathbf{V}}_0^{(i)}. \tag{D.20}$$

Finally, specializing to the incident wave (D.9), define

$$h_i \left(k\mathbf{n} \right) = \frac{1}{\left| \Omega_i \right|} \int_{\Omega_i} e^{(ik\mathbf{n} \cdot \mathbf{x})} dx. \tag{D.21}$$

The required conditional means $\left\langle \mathbf{e} \right\rangle_i$ and $\left\langle \mathbf{V} \right\rangle_i$ then follow as

$$\left\langle \mathbf{e} \right\rangle_i \left(\mathbf{x} \right) = h_i \left(k\mathbf{n} \right) h_i \left(-k\mathbf{n} \right) \left[\mathbf{I} + \bar{\mathbf{S}}_x^{(i)} \left(\mathbf{C}_r - \mathbf{C}_0 \right) \right]^{-1} \mathbf{e}_0 \left(\mathbf{x} \right), \tag{D.22}$$

and

$$\left\langle \mathbf{V} \right\rangle_i \left(\mathbf{x} \right) = h_i \left(k\mathbf{n} \right) h_i \left(-k\mathbf{n} \right) \left[\mathbf{I} + \bar{\mathbf{M}}_t^{(i)} \left(\boldsymbol{\rho}_i - \boldsymbol{\rho}_0 \right) \right]^{-1} \mathbf{V}_0 \left(\mathbf{x} \right). \tag{D.23}$$

Appendix E: Kernel Functions for the Scattering Problem

The frequency-dependent self-consistent equations for a two-phase composite (5.6) and (5.7) invoke the tensors $\bar{\mathbf{S}}_x$ and $\bar{\mathbf{M}}_t$. This appendix summarizes the formulas that are required to calculate these tensors.

E.1 SPHERICAL INCLUSIONS

For a composite containing spherical inclusions, the second-rank tensor $\bar{\mathbf{S}}_x$ is written as

$$\bar{\mathbf{S}}_x = \begin{bmatrix} S_{11} & S_{12} & S_{12} & 0 & 0 & 0 \\ S_{12} & S_{11} & S_{12} & 0 & 0 & 0 \\ S_{12} & S_{12} & S_{11} & 0 & 0 & 0 \\ 0 & 0 & 0 & S_{44} & 0 & 0 \\ 0 & 0 & 0 & 0 & S_{44} & 0 \\ 0 & 0 & 0 & 0 & 0 & S_{44} \end{bmatrix}, \tag{E.1}$$

where

$$S_{11} = \frac{\xi_p}{3\left(3K_{\mathbf{SCA}}^{fd} + 4\mu_{\mathbf{SCA}}^{fd}\right)} + \frac{2}{15}\left[\frac{2\xi_p}{3K_{\mathbf{SCA}}^{fd} + 4\mu_{\mathbf{SCA}}^{fd}} + \frac{\xi_s}{\mu_{\mathbf{SCA}}^{fd}}\right], \tag{E.2}$$

$$S_{12} = \frac{\xi_p}{3\left(3K_{\mathbf{SCA}}^{fd} + 4\mu_{\mathbf{SCA}}^{fd}\right)} - \frac{2}{15}\left[\frac{2\xi_p}{3K_{\mathbf{SCA}}^{fd} + 4\mu_{\mathbf{SCA}}^{fd}} + \frac{\xi_s}{\mu_{\mathbf{SCA}}^{fd}}\right], \tag{E.3}$$

and

$$S_{44} = \frac{1}{10}\left[\frac{2\xi_p}{3K_{\mathbf{SCA}}^{fd} + 4\mu_{\mathbf{SCA}}^{fd}} + \frac{\xi_s}{\mu_{\mathbf{SCA}}^{fd}}\right]; \tag{E.4}$$

and the tensor $\bar{\mathbf{M}}_t$ is computed as

$$\bar{\mathbf{M}}_t = \frac{3 - \xi_p - 2\xi_s}{3\rho_{\mathbf{SCA}}^{fd}} \begin{bmatrix} 1 & 0 & 0 \\ 0 & 1 & 0 \\ 0 & 0 & 1 \end{bmatrix}. \tag{E.5}$$

E.2 RANDOMLY-ORIENTED SPHEROIDAL INCLUSIONS

For a composite containing randomly-oriented spheroidal inclusions, it is easier to express the tensors $\overline{\mathbf{S}}_x$ and $\overline{\mathbf{M}}_t$ in the coordinate system attached with an inclusion. In the inclusion coordinate system, $\overline{\mathbf{S}}_x$ and $\overline{\mathbf{M}}_t$ are transversely isotropic and are denoted by $\overline{\mathbf{S}}'_x$ and $\overline{\mathbf{M}}'_t$, respectively.

The tensor $\overline{\mathbf{S}}'_x$ is written as

$$\overline{\mathbf{S}}'_x = \begin{bmatrix} S'_{11} & S'_{12} & S'_{13} & 0 & 0 & 0 \\ S'_{12} & S'_{11} & S'_{13} & 0 & 0 & 0 \\ S'_{13} & S'_{13} & S'_{33} & 0 & 0 & 0 \\ 0 & 0 & 0 & S'_{44} & 0 & 0 \\ 0 & 0 & 0 & 0 & S'_{44} & 0 \\ 0 & 0 & 0 & 0 & 0 & S'_{66} \end{bmatrix}, \tag{E.6}$$

where

$$S'_{11} = \frac{1}{8\rho_{\mathbf{SCA}}^{fd}} \int_0^1 \left(1-u^2\right) \left[3m_1^2 H_p\left(\psi(u)\right) + \left(1+3m_3^2\right) H_s\left(\psi(u)\right) \right] du, \tag{E.7}$$

$$S'_{13} = \frac{1}{2\rho_{\mathbf{SCA}}^{fd}} \int_0^1 u\left(1-u^2\right)^{1/2} m_1 m_3 \left[H_p\left(\psi(u)\right) - H_s\left(\psi(u)\right) \right] du, \tag{E.8}$$

$$S'_{33} = \frac{1}{\rho_{\mathbf{SCA}}^{fd}} \int_0^1 u^2 \left[m_3^2 H_p\left(\psi(u)\right) - m_1^2 H_s\left(\psi(u)\right) \right] du, \tag{E.9}$$

$$\begin{aligned} S'_{44} = \frac{1}{8\rho_{\mathbf{SCA}}^{fd}} \int_0^1 \Bigg\{ & \left[u^2 m_1^2 + \left(1-u^2\right) m_3^2 + 2u\left(1-u^2\right)^{1/2} m_1 m_3 \right] H_p\left(\psi(u)\right) \\ & + \left[u^2\left(1+m_3^2\right) + \left(1-u^2\right) m_1^2 - 2u\left(1-u^2\right)^{1/2} m_1 m_3 \right] H_s\left(\psi(u)\right) \Bigg\} du, \end{aligned} \tag{E.10}$$

$$S'_{66} = \frac{1}{8\rho_{\mathbf{SCA}}^{fd}} \int_0^1 \left(1-u^2\right) \left[m_1^2 H_p\left(\psi(u)\right) + \left(1+m_3^2\right) H_s\left(\psi(u)\right) \right] du, \tag{E.11}$$

and

$$S'_{12} = S'_{11} - 2S'_{66}. \tag{E.12}$$

In the above equations, $\rho_{\mathbf{SCA}}^{fd}$ is the density of the effective composite and the different functions are calculated as

$$m_1(u) = \rho_{\mathbf{SCA}}^{fd\,1/2}\left[\left(K_{\mathbf{SCA}}^{fd} - \mu_{\mathbf{SCA}}^{fd}/3\right)\left(1-u^2\right)\right]D^{-1/2}, \tag{E.13}$$

$$m_3(u) = \rho_{\mathbf{SCA}}^{fd\,1/2}\left[\left(K_{\mathbf{SCA}}^{fd} - \mu_{\mathbf{SCA}}^{fd}/3\right)u\left(1-u^2\right)^{1/2}\right]D^{-1/2}, \tag{E.14}$$

with

$$D = \rho_{\mathbf{SCA}}^{fd}\left[\left(K_{\mathbf{SCA}}^{fd} - \mu_{\mathbf{SCA}}^{fd}/3\right)^2\left(1-u^2\right)\right], \tag{E.15}$$

where $K_{\mathbf{SCA}}^{fd}$ and $\mu_{\mathbf{SCA}}^{fd}$ are the bulk modulus and shear modulus of the effective medium, respectively; and as

$$H_j(\psi) = \gamma V_j^{-2}\psi^{-3}\xi\left(a_c k_j \varsigma\right), \tag{E.16}$$

with

$$\psi(u) = \left[1+\left(\gamma^2-1\right)u^2\right]^{1/2}, \tag{E.17}$$

$$\xi(z) = \frac{3(1-iz)}{z^3}\left[\sin(z) - z\cos(z)\right]e^{iz}, \tag{E.18}$$

$$k_j = \omega/V_j, \tag{E.19}$$

and γ and a_c are the aspect ratio and length of the inclusions, respectively, and $j = p$ or s.

The tensor $\bar{\mathbf{M}}_t'$ is written as

$$\mathbf{M}' = \begin{bmatrix} M_1' & 0 & 0 \\ 0 & M_1' & 0 \\ 0 & 0 & M_3' \end{bmatrix}, \tag{E.20}$$

where

$$M_1' = \frac{1}{2\rho_{\mathbf{SCA}}^{fd}} \int_0^1 \left[m_1^2 F_p\left(\psi(u)\right) + \left(1 + m_3^2\right) F_s\left(\psi(u)\right) \right] du, \tag{E.21}$$

and

$$M_3' = \frac{1}{\rho_{\mathbf{SCA}}^{fd}} \int_0^1 \left[m_3^2 F_p\left(\psi(u)\right) + m_1^2 F_s\left(\psi(u)\right) \right] du, \tag{E.22}$$

where $\rho_{\mathbf{SCA}}^{fd}$ and the functions ψ, m_1, and m_3 are defined in the same manner as above, and F_j is calculated as

$$F_j(\psi) = \gamma \left[1 - \xi\left(a_c k_j \psi\right) \right] \psi^{-3}, \tag{E.23}$$

with $j = p$ or s.

Finally, the function $\hat{h}$ used in equation (5.24) is defined as

$$\hat{h}(z) = \frac{3\left[\sin(z) - z\cos(z)\right]}{z^3}. \tag{E.24}$$

List of Symbols

α	$(\ )$	Biot-Willis parameter
γ	$(\ )$	Aspect ratio of solid and porous inclusions
ε	$(\ )$	Crack density
η	$\left(\text{Pa.s}^{-1}\right)$	Fluid viscosity
θ	$(^\circ)$	Deviation angle of the well
ϑ	$(^\circ)$	Angle between small axis of spheroidal inclusion and vertical axis of effective medium
ι_j	(rad)	Dimensionless angular wave number associated with a j-wave
κ	$\left(\text{m}^2\right)$	Effective permeability
λ	(Pa)	Lamé parameter
μ	(Pa)	Shear modulus
ν	$(\ )$	Poisson's ratio
$\boldsymbol{\rho}$	$\left(\text{kg.m}^{-3}\right)$	Density tensor
ρ	$\left(\text{kg.m}^{-3}\right)$	Density
σ	$\left(\text{S.m}^{-1}\right)$	Electrical conductivity
σ_h	$\left(\text{S.m}^{-1}\right)$	Horizontal electrical conductivity
σ_v	$\left(\text{S.m}^{-1}\right)$	Vertical electrical conductivity
$\boldsymbol{\varsigma}$	(Pa)	Stress tensor
ς_{ij}	(Pa)	Entry of the stress tensor
ς_φ	(Pa)	Effective hoop stress
τ	$\left(\text{s}^{-1}\right)$	Timescale parameter for squirt flow
T	$(\ )$	Tortuosity

ϕ	(v/v)	Total porosity
ϕ_c	(v/v)	Porosity composed of cracks
ϕ_p	(v/v)	Porosity composed of spherical pores
φ	$(^\circ)$	Angle around horizontal wellbore (from horizontal plane)
ψ	$(^\circ)$	Angle between orientation of horizontal well and direction of maximum horizontal stress
ω	(rad.s^{-1})	Angular frequency
a	(m)	Pore radius
a_c	(m)	Crack length
c_{ij}	(Pa)	Entry of the stiffness tensor in Voigt's notation
$\mathbf{C}$	(Pa)	Stiffness tensor
d	(m)	Characteristic grain size
$\mathbf{e}$	$(\ )$	Strain tensor
e_{kl}	$(\ )$	Entry of the strain tensor
E	(Pa)	Young's modulus
f	(Hz)	Frequency
$\mathbf{I}$	$(\ )$	Identity tensor
k	(rad.m^{-1})	Angular wave number
k_j	(rad.m^{-1})	Angular wave number associated with j-wave
K	(Pa)	Bulk modulus
K_c	$(\ )$	Crack-space compressibility parameter
K_p	$(\ )$	Pore-space compressibility parameter
M	$(\text{m}^2.\text{Pa}^{-1}.\text{s}^{-1})$	Fluid mobility
P_ϕ	(Pa)	Pore pressure

P_{bor}	(Pa)	Borehole pressure
P_{frac}	(Pa)	Fracture initiation pressure
Q	$(\ )$	Quality factor
R	$(\Omega.\mathrm{m})$	Simulated electrical resistivity
R_t	$(\Omega.\mathrm{m})$	True deep electrical resistivity
s_w	$(\mathrm{v/v})$	Water saturation
S_φ	(Pa)	Total hoop stress
S_h	(Pa)	Total minimum horizontal stress
S_H	(Pa)	Total maximum horizontal stress
S_V	(Pa)	Total vertical stress
$\mathbf{V}$	$(\mathrm{m.s^{-1}})$	Velocity tensor
V	$(\mathrm{m.s^{-1}})$	Wave velocity
x	$(\mathrm{v/v})$	Volumetric concentration

Subscripts

att	Maximum attenuation
b	Background
bor	Borehole
DEM	Differential effective medium
fl	Fluid
fr	Frame
h	Horizontal
i	i^{th} inclusion phase in a mixture

j	j -wave
mud	Borehole fluid
p	Compressional
s	Shear
SCA	Self-consistent approximation
sh	Horizontally-polarized shear
sv	Vertically-polarized shear
sol	Solid/Matrix
$sol-p$	Solid parameter defined in case of incident compressional-wave velocity
$sol-s$	Solid parameter defined in case of incident shear-wave velocity
Sto	Stoneley
v	Vertical

Superscripts

*	Low-frequency case of reference
¯	Average over inclusion
Bi	Biot's flow
BiSq	Combined Biot's and squirt flows
fd	Frequency-dependent
Sq	Squirt flow

References

Adelinet, M., J. Fortin, and K. T, Lewallen, 2009, Seismic wave attenuation in carbonates: Journal of Geophysical Research, **114**, B06208.

Adiguna, H., 2012, Comparative study for the interpretation of mineral concentrations, total porosity, and TOC in hydrocarbon-bearing shale from conventional well logs: M.S. Thesis, The University of Texas at Austin.

Ahmadov, R., T. Vanorio, and G. Mavko, 2009, Confocal laser scanning and atomic-force microscopy in estimation of elastic properties of the organic-rich Bazhenov formation: The Leading Edge, **28**, 18–23.

Amadei, B., 1983, Rock anisotropy and the theory of stress measurements: Springer-Verlag.

Aplin, A. C., I. F. Matenaar, D. K. McCarty, and B. A. van der Pluijm, 2006, Influence of mechanical compaction and clay mineral diagenesis on the microfabric and pore-scale properties of deep-water Gulf of Mexico mudstones: Clays and clay minerals, **54**, no. 4, 500–514.

Backus, G., 1962, Long-wave elastic anisotropy produced by horizontal layering: Journal of Geophysical Research, **76**, 4427–4440.

Bandyopadhyay, K., 2009, Seismic anisotropy: geological causes and its implications to reservoir geophysics: Ph.D. dissertation, Stanford University.

Banik, N. C., 1984, Velocity anisotropy in shales and depth estimation in the North Sea basin: Geophysics, **49**, 1411–1419.

Berryman, J. G., 1980a, Confirmation of Biot's theory: Applied Physics Letters, **37**, 382–384.

Berryman, J. G., 1980b, Long-wavelength propagation in composite elastic media: Journal of the Acoustical Society of America, **68**, 1809–1831.

Berryman, J. G., 1981, Elastic wave propagation in fluid-saturated media: Journal of the Acoustical Society of America, **69**, 416–424.

Berryman, J. G., 1992, Single-scattering approximations for coefficients in Biot's equations of poroelasticity: Journal of Acoustic Society of America, **91**, 551-571.

Berryman, J. G., 1995, Mixture theories for rock properties, *in* T. J. Ahrens, eds., Rock Physics and Phase Relations: a Handbook of Physical Constants: American Geophysical Union, 205–228.

Berryman, J. G., 1998, Rocks as poroelastic composites: *in*, J.-F. Thimus, Y. Abousleiman, A. H.-D. Cheng, O. Coussy, and E. Detournay, eds., Poromechanics: A. A. Balkema, 11–16.

Biot, M. A., 1956a, Theory of propagation of elastic waves in a fluid saturated porous solid, I. Low frequency range: Journal of the Acoustical Society of America, **28**, 168–178.

Biot, M. A., 1956b, Theory of propagation of elastic waves in a fluid saturated porous solid, II. Higher frequency range: Journal of the Acoustical Society of America, **28**, 179–191.

Biot, M. A., 1962, Mechanics of deformation and acoustic propagation in porous media: Journal of Applied Physics, **33**, 1482–1498.

Britt, L. and J. Schoeffler, 2009, The geomechanics of a shale play: What makes a shale prospective!, Paper 125525: Presented at the 2009 Eastern Regional Meeting, SPE.

Bruggeman, D. A. G., 1935, Berechning verscherdener physikalischer konstaten von heterogenen substanzen I. Dielecktrizitätskonstanten und leifähigigkeiten der mischkörper aus isotropen substanzen: Ann. Phys., **24**, 636–679.

Budiansky, B., 1965, On the elastic moduli of some heterogeneous materials: Journal of the Mechanics and Physics of Solids, **13**, 223–227.

Carcione, J. M., 2000, A model for seismic velocity and attenuation in petroleum source rocks: Geophysics, **65**, 1080–1092.

Chapman, M., 2003, Frequency-dependent anisotropy due to meso-scale fractures in the presence of equant porosity: Geophysical Prospecting, **51**, 369–379.

Chapman, M., E. Liu and X-Y. Li, 2006, The influence of fluid-sensitive dispersion and attenuation on AVO analysis: Geophysical Journal International, **167**, 89–105.

Chapman, M., S. V. Zatsepin, and S. Crampin, 2002, Derivation of a microstructural poroelastic model: Geophysical Journal International, **151**, 427–451.

Chi, S. and X. M. Tang, 2003, Accurate approximations to Qsv and Qp wave speeds in TIV media and Stoneley wave speed in general anisotropic media: Presented at the 44th Annual Logging Symposium, Society of Petrophysicists and Well Log Analysts.

Dvorkin, J. and A. Nur, 1993, Dynamic poroelasticity: a unified model with the squirt flow and the Biot mechanisms: Geophysics, **58**, 524–533.

Dvorkin, J., G. Mavko, and A. Nur, 1995, Squirt flow in fully saturated rocks: Geophysics, **60**, 97–107.

Dvorkin, J., R. Nolen-Hoeksema, and A. Nur, 1994, The squirt-flow mechanism: Macroscopic description: Geophysics, **59**, 428–438.

Eshelby, J. D., 1957, The determination of the elastic field of an spheroidal inclusion and related problems: Proceedings of the Royal Society of London, Series A, **241**, 376–396.

Fairhurst, C., 1968, Methods of determining in-situ rock stresses at great depths: Conducted for Missouri River Division, Corps of Engineers.

Farmer, C. L., 2002, Upscaling: A review: International Journal for Numerical Methods in Fluids, **40**, 63–78.

Fjar, E., R. M. Holt, A. M. Raaen, R. Risnes, and P. Horsrud, 2008, Petroleum related rock mechanics, Second edition: Elsevier B.V.

Frydman, M., 2010, Determinations of the dynamic elastic constants of a transverse isotropic rock based on borehole dipole sonic anisotropy in deviated wells: Presented at the biennial 15th Rio Oil and Gas Conference.

Gaede, O., F. Karpfinger, J. Jocker, and R. Prioul, 2012, Comparison between analytical and 3D finite elements solutions for borehole stresses in anisotropic elastic rock: International Journal of Rock Mechanics and Mining Science, **51**, 53–63.

Gale, J. F. W., S. E. Laubach, J. E. Olson, P. Eichhubl, and A. Fall, 2014, Natural fractures in shale: A review and new observations: American Association of Petroleum Geologists Bulletin, **98**, no. 11, 2165–2216.

Gassmann, F., 1951, Über die Elastizität poröser Medien: Vierteljahrsschrift der naturforschenden, Gesellschaft in Zürich, **96**, 1–23.

Ghosh, R. and M. K. Sen, 2011, Effective medium modeling of fluid-filled fractured-porous medium: Presented at the 82nd Annual International Meeting, SEG.

Hammes, U., H. S. Hamlin, and T. E. Ewing, 2011, Geologic analysis of the upper Jurassic Haynesville shale in east Texas and west Louisiana: American Association of Petroleum Geologists Bulletin, **95**, no. 10, 1643–1666.

Hashin, Z. and S. Shtrikman, 1963, A variational approach to the elastic behavior of multiphase materials: Journal of the Mechanics and Physics of Solids, **11**, 127–140.

Heidari, Z., C. Torres-Verdín, and W. E. Preeg, 2012, Improved estimation of mineral and fluid volumetric concentrations from well logs in thinly bedded and invaded formations: Geophysics, **77**, no. 3, WA79–WA98.

Hill, R., 1952, The elastic behavior of crystalline aggregate: Proceedings of the Physical Society, A **65**, 349–354.

Hornby, B. E., L. M. Schwartz, and J. A. Hudson, 1993, Effective medium modeling of the electrical and elastic properties of anisotropic porous media: 63rd Annual International Meeting, SEG, Extended Abstracts, 786–791.

Hornby, B. E., L. M. Schwartz, and J. A. Hudson, 1994, Anisotropic effective-medium modeling of elastic properties of shales: Geophysics, **59**, 1570–1583.

Hill, R., 1965, A self-consistent mechanics of composite materials: Journal of the Mechanics and Physics of Solids, **13**, 213–222.

Hossain, M. M., M. K. Rahman, and S. S. Rahman, 2000, Hydraulic fracture initiation and propagation: roles of wellbore trajectory, perforation and stress regimes: Journal of Petroleum Science and Engineering, **27**, 129–149.

Hovem, J. M. and G. D. Ingram, 1979, Viscous attenuation of sound in saturated sand: Journal of the Acoustical Society of America, **66**, 717–722.

Hudson, J. A., 1980, Overall properties of a cracked solid, Mathematical Proceedings: Cambridge Philosophical Society, **88**, 371–384.

Hudson, J. A., 1994, Overall properties of materials with inclusions or cavities: Geophysical Journal International, **117**, 555–561.

Hudson, J. A. and E. Liu, 1999, Effective elastic properties of heavily faulted structures: Geophysics, **64**, 479–485.

Hudson, J. A., E. Liu, and S. Crampin, 1996, The mechanical properties of materials with interconnected cracks and pores: Geophysical Journal International, **124**, 105–112.

Jakobsen, M., and J. A. Hudson, 2003, Visco-elastic waves in rock-like composites, Studia Geophysica et Geodaetica, **47**, no. 4, 793–826.

Jakobsen, M., J. A. Hudson, T. A. Minshull, and S. C. Singh, 2000, Elastic properties of hydrate-bearing sediments using effective medium theory: Journal of Geophysical Research, **105**, 561–577.

Jakobsen, M., and M. Chapman, 2009, Unified theory of global and squirt flow in cracked porous media: Geophysics, **74**, no. 2, WA65–WA76.

Jakobsen, M., T. A. Johansen, and C. McCann, 2003, The acoustic signature of fluid flow in complex porous media: Journal of Applied Geophysics, **54**, 219–246.

Johnston, J. E. and N. I. Christensen, 1995, Seismic anisotropy of shales: Journal of Geophysical Research, **100**, no. B4, 5991–6003.

Jones, L. E. A. and H. F. Wang, 1981, Ultrasonic velocities in Cretaceous shales from the Williston basin: Geophysics, **46**, 288–297.

Jones, T., 1986, Pore fluids and frequency-dependent wave propagation in rocks: Geophysics, **51**, 1939–1953.

Jones, T. and A. Nur, 1983, Velocity and attenuation in sandstone at elevated temperatures and pressures: Geophysics Research Letters, **10**, 140–143.

Kanaun, S. K., 1996, Propagation of elastic waves through polycrystalline materials: European Journal of Mechanics A/Solids, **15**, 859–881.

Kanaun, S. K., 1997, Propagation of scalar waves through matrix composite materials: effective medium approach: European Journal of Mechanics A/Solids, **16**, 1041–1066.

Kanaun, S. K. and V. M. Levin, 2003, Effective medium method in the problem of axial elastic shear wave propagation through fiber composites: International Journal of Solids and Structures, **40**, 4859–4878.

Kim, J.-Y., 2010, Effective medium theories for wave propagation in two-dimensional random inhomogeneous media: Journal of Mechanics of Materials and Structures, **5**, no. 4, 567–581.

Kim, J.-Y., I. Jeong-Guon, and L. Byung-Ho, 1995, Dispersion of elastic waves in random particulate composites: Journal of the Acoustical Society of America, **97**, 1380–1388.

King, G. E., 2010, Thirty years of gas shale fracturing: what have we learned?, Paper 133456: Presented at the Annual Technical Conference and Exhibition, SPE.

Kirsch, G., 1898, Die Theorie der Elastizität und die Bedürfnisse der Festigkeitslehre: Journal of the Association of German Engineers, **42**, 797–807.

Kümpel, H.-J., 1991, Poroelasticity: parameters reviewed: Geophysical Journal International, **105**, 783–799.

Kuster, G. T., and Toksöz, M. N., 1974, Velocity and attenuation of seismic waves in two-phase media: Geophysics, **39**, 587–618.

Lekhnitskii, S. G., 1981, Theory of elasticity of an anisotropic body: Mir Publications.

Manger, G. E., 1963, Porisity and bulk density of sedimentary rocks: U.S. Geological Survey Bulletin, **1144-E**, 34–40.

Mavko, G., and A. Nur, 1975, Melt squirt in asthenosphere: Journal of Geophysical Research, **80**, 1444–1448.

Mavko, G. and D. Jizba, 1991, Estimating grain-scale fluid effects on velocity dispersion in rocks: Geophysics, **56**, 1940–1949.

Mavko, G., T. Mukerji, and J. Dvorkin, 2009, The rock physics handbook, Second edition: Tools for seismic analysis of porous media: Cambridge University Press.

Montaut, A., 2012, Detection and quantification of rock physics properties for improved hydraulic fracturing in hydrocarbon-bearing shales: M.S. Thesis, The University of Texas at Austin.

Montaut, A., P. Sayar, and C. Torres-Verdín, 2013, Detection and quantification of rock physics properties for improved hydraulic fracturing in hydrocarbon-bearing shale: Presented at the 54th Annual Logging Symposium, Society of Petrophysicists and Well Log Analysts.

Montgomery, S. L., D. M. Jarvie, K. A. Bowker, and R. M. Pollastro, 2005, Mississippian Barnett shale, Fort Worth basin, north-central Texas: Gas-shale play with multi–trillion cubic foot potential: American Association of Petroleum Geologists Bulletin, **89**, no. 2, 155–175.

Müller, T. M., B. Gurevich, and M. Lebedev, 2010, Seismic wave attenuation and dispersion resulting from wave-induced flow in porous rocks — A review: Geophysics, **75**, no. 5, 75A147–75A164.

Mura, T., 1982, Micromechanics of defects in solid: Martinus Nijhoff Publications.

Nishizawa, O., 1982, Seismic velocity anisotropy in a medium containing oriented cracks: Transversely isotropic case, Journal of Physics of the Earth, **30**, 331–347.

Norris, A. N., 1990, The speed of a tube wave: Journal of Acoustic Society of America, **87**, 414–417.

O'Connell, R. J. and B. Budiansky, 1978, Measures of dissipation in viscoelastic media: Geophysical Research Letters, **5**, 5–8.

O'Connell, R. J. and B. Budiansky, 1977, Viscoelastic properties of fluid-saturated cracked solids: Journal of Geophysical Research, **82**, 5719–5740.

Parra, J. O., 1997, The transversely isotropic poroelastic wave equation including the Biot and the squirt mechanisms: Theory and application: Geophysics, **62**, 309–318.

Pommer, M. and K. Milliken, 2015, Pore types and pore-size distributions across thermal maturity, Eagle Ford Formation, Southern Texas: American Association of Petroleum Geologists Bulletin, doi: 10.1306/03051414151.

Pride, S. R., J. G. Berryman, and J. M. Harris, 2004, Seismic attenuation due to wave induced flow: Journal of Geophysical Research, **109**, no. B1, 2156–2202.

Reed, R. M., R. G. Loucks, and K. Milliken, 2012, Heterogeneity of shape and microscale spatial distribution in organic-matter-hosted pores of gas shales, Annual Convention, American Association of Petroleum Geologists, Abstract 1236631.

Reuss, A., 1929, Berechnung der Fliessgrenzen von Mischkristallen auf Grung der Plastizitätsbedingung für Einkristalle: Zeitschrift für Angewandte Mathematik und Mechanik, **9**, 49–58.

Sabina, F. J. and J. R. Willis, 1988, A simple self-consistent analysis of wave propagation in particulate composites: Wave Motion, **10**, 127–142.

Sabina, F. J., V. P. Smyshlyaev, and J. R. Willis, 1993, Self-consistent analysis of waves in a matrix-inclusion composite, I. Aligned spheroidal inclusions: Journal of the Mechanics and Physics of Solids, **41**, no. 10, 1573–1588.

Sams, M. S., J. P. Neep, and M. H. Worthington, 1997, The measurement of velocity dispersion and frequency-dependent intrinsic attenuation in sedimentary rocks: Geophysics, **62**, 1456–1464.

Serajian, V. and A. Ghassemi, 2011, Hydraulic fracture initiation from a wellbore in transversely isotropic rock: Presented at the 45th U.S. Rock Mechanics/Geomechanics Symposium, American Rock Mechanics Association.

Sheng, P., 1990, Effective-medium theory of sedimentary rocks: Physical Review, **B41**, 4507–4512.

Sheng, P., 1991, Consistent modeling of the electrical and elastic properties of sedimentary rocks: Geophysics, **56**, 1236–1243.

Smyshlyaev, V. P., J. R. Willis, and F. J. Sabina, 1993, Self-consistent analysis of waves in a matrix-inclusion composite, II. Randomly oriented spheroidal inclusions: Journal of the Mechanics and Physics of Solids, **41**, no. 10, 1589–1598.

Stoll, R. D., 1977 Acoustic waves in ocean sediments: Geophysics, **42**, 715–725.

Thomsen, L., 1986, Weak elastic anisotropy: Geophysics, **51**, 1954–1966.

Tod, S. R., 2003, An anisotropic fractured poroelastic effective medium theory, Geophysical Journal International, **155**, 1006–1020.

Valdiviezo-Mijangos, O. C. and R. Nicolás-Lopez, 2014, Dynamic characterization of shale systems by dispersion and attenuation of P-wave and S-waves considering their mineral composition and rock maturity: Journal of Petroleum Science and Engineering, **122**, 420–427.

Walsh, J., B. Sinha, and A. Donald, 2006, Formation anisotropy parameters using borehole sonic data: Presented at the 47th Annual Logging Symposium, Society of Petrophysicists and Well Log Analysts.

Wang, Z., 2002, Seismic anisotropy in sedimentary rocks: Part 2 – Laboratory data: Geophysics, **67**, 1423–1440.

Willis, J. R., 1977, Bounds and self-consistent estimates for the overall properties of anisotropic composites, Journal of the Mechanics and Physics of Solids, **25**, 185–202.

Wu, T. T., 1966, The effect of the inclusion shape on the elastic moduli of a two-phase material: International Journal of Solids and Structures, **2**, 1–8.

Wyllie, M. R. J., Gregory, A. R., and Gardner, L. W., 1956, Elastic wave velocities in heterogeneous and porous media: Geophysics, **21**, 41–70.

Wyllie, M. R. J., Gregory, A. R., and Gardner, G. H. F., 1958, An experimental investigation of factors affecting elastic wave velocities in porous media: Geophysics, **23**, 459–493.

Xu, S. and R. E. White, 1995, A new velocity model for clay-sand mixtures: Geophysical Prospecting, **43**, 91–118.

Yao, Q., D.-H. Han, F. Yan, and L. Zhao, 2015, Modeling attenuation and dispersion in porous heterogenous rocks with dynamic fluid modulus, Geophysics, **80**, no. 3, D183–D194.

Zoback, M. D., 2007, Reservoir geomechanics: Cambridge University Press.